Pattern formation through lateral inhibition mediated by Notch signaling

Pau Formosa-Jordan,

Pattern formation through lateral inhibition mediated by Notch signaling

Pau Formosa-Jordan

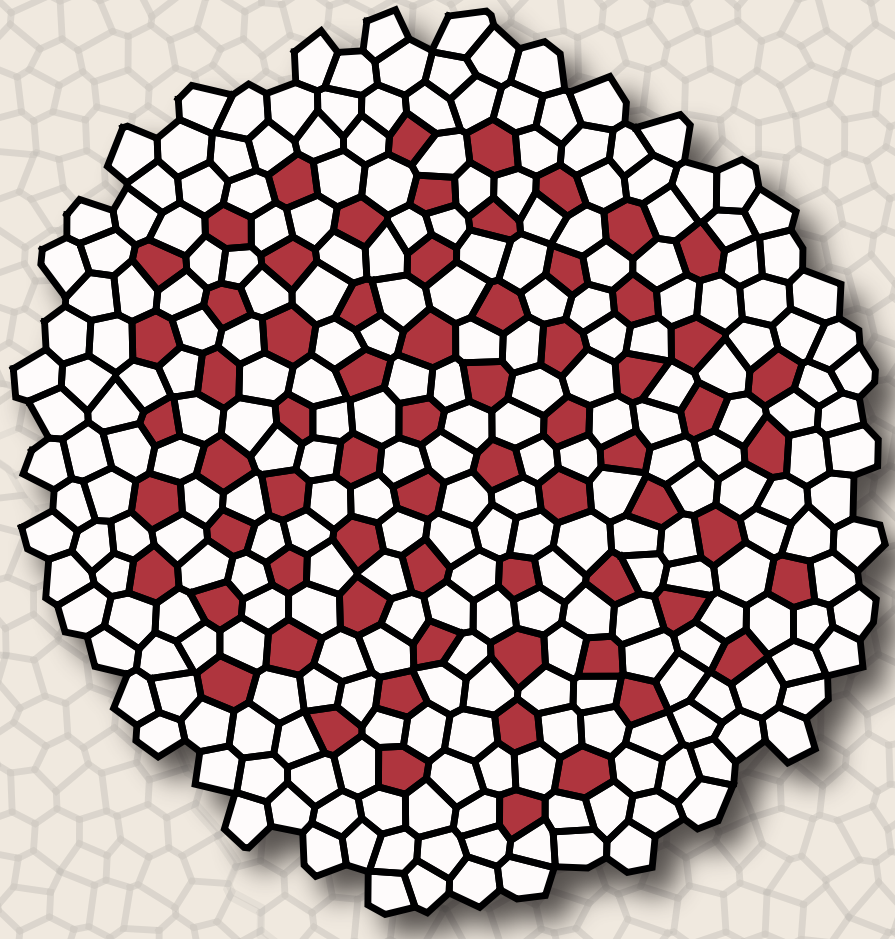

Pattern formation through lateral inhibition mediated by Notch signaling

Programa de doctorat: *Física*

Línia d'investigació: Física de la matèria condensada

Directors de Tesi:
Dr. Marta Ibañes Miguez
Prof. José María Sancho Herrero

Memòria presentada per Pau Formosa Jordan per a optar al títol de Doctor en Física (15 de Març de 2013)

Facultat de Física
Departament d'Estructura i Constituents de la Matèria

About the images at the front and back covers:
Artistic representation of a neurogenic tissue (white and red cells) invading a non-neurogenic tissue (light brown cells) in wild-type conditions (front cover) and in a mutant case where the invaded tissue has not inhibitory capacity. Red cells represent the first differentiated neurons, white cells represent cells undergoing lateral inhibiton dynamics.

Al meu pare
A la meva mare

Acknowledgements

This period of my life has been a great gift to me, in a very wide sense. Doing this Thesis has been an opportunity to learn, to create something by doing Science, to meet great people, to grow.

My first acknowledgement is for Marta Ibañes, who has advised my Thesis. Gràcies Marta per tota la confiança dipositada en mi, i tota la dedicació que has tingut aquests anys. Saps que sempre t'estaré agraït per tot aquest període de temps en que m'has estat ajudant contínuament. Gràcies a tu he après molta ciència, i també a "fer ciència" amb la humanitat que et caracteritza. Em sento molt afortunat d'haver-te tingut com a directora de tesis, has set i seràs un referent per a mi. Gràcies.

Also I want to acknowledge all the support form José María Sancho Herrero, who has also advised my Thesis. Muchas gracias José María por todo este tiempo, por toda tu ayuda, por tu confianza en mí, por toda la ciencia que he podido aprender gracias a ti.

I would like to thank Dr. David Sprinzak and Dr. Luis G. Morelli for being the referees of this Thesis. Also, I am thankful to Dr. Jaume Casademunt, Dr. Aneta Koseska and Prof. Jordi García-Ojalvo for being the committee for the Thesis defense.

A special acknowledgement for the PhD students of the Department during these years that belong to the Nonlinear Physics group. Thanks for creating this great ambience and great community in the Department, for the labmeetings, for the lunches, for the discussions... I would like to mention some names: Javier Orlandi and Rubén Pérez. I am really in debt with them, cause they have helped me so much during all this time in all kind of stuff, specially in computational

issues, and most importantly, they have been great office mates! I also want to acknowledge the nice times spent with other office mates: Maria Khoury, Àlex Gómez, Daniel Dagnino, Fèlix Campelo, Sara Teller and Claudia Trejo. I would like to mention some more PhD students in our Department: Carles Blanch, Laura Casanelles, Xavier Clotet, and Elisenda Tibau.

Also, all these years I had great times with other PhD students that are from our neighboring Department of Física Fonamental. Among other people, I would like to mention María Aznar, Paolo Malgaretti, Martin Goethe, Cristina Ciornei, Guillem Pérez, Nidal Haddad, Paco Alarcón, Valentino Bianco and Nico Geisel. I have to say that Nico Geisel has been a reference for me, because of his passion for Science and the way he understood it. I still remember when we had those informal seminars between us, supposed to be just for one hour and often ended up in ... three hours? That was great actually! Well, and even better all times we had fun with not-so-academic things!

There are other PhD students that have also been very influential, helpful and a reference for me during these years. Among them, Oriol Canela, Marc Weber and Pau Rué, thanks for everything!

Also, a great acknowledgment to extraordinary people I have shared a long journey during my Physics studies and my PhD years, that make it just unforgettable. Toni Luque, David López Val, Jose María Escartín and Jordi Salvadó, among others. It was from high school that Toni and me we both shared the passion of Physics, we have spent so many things together... David has been as a guide for me all these years. Also other people I had the luck to meet during my studies in Physics: Jordi Valls, Daniel Oliu, Artur Latorre, Albert Saragossa, Belén Sancristóbal, Olivia Jordi, and much more lovely people. Sento que aquest camí sense tots vosaltres no hauria estat el mateix, gràcies.

During this Thesis I was gifted with great collaborators and I would like to say few words about them.

The first one was Saúl Ares, who I met in a poster session in a Fises Conference. After an intense discussion about Notch and Delta, he suggested me to think about the problem of a neurogenic wavefront. It ended up in an intense and fascinating collaboration, directed by Jose María Frade by Cajal Institute (CSIC, Madrid), and also Saúl Ares and Marta Ibañes.

Thanks to this collaboration I also had the great chance to go twice to the

Max Planck Institue for the Physics of Complex Systems (MPI-PKS), in Dresden, Germany. The time I spent there has given me a keystone perspective of the Biological Physics discipline, and this is still a reference for me. There, I had the chance to interact and learn from great scientists. Among them, Prof. Frank Jülicher, Prof. Andrew Oates, Dr. Luis G. Morelli, Dr. Ernesto Nicola, Dr. Manuel Matías, Dr. Koichiro Uriu and Bo-Kai, among much more people I met in MPI-PKS and in the Max Planck Institute of Molecular Cell Biology and Genetics (MPI-CBG). The labmeetings of the Biological Physics group at MPI-PKS and the Oates labmeetings at MPI-CBG ... that was a great luck for me, really, I am grateful for that. Also I would like to thank to Saúl the special "care" inside and outside the Institute he had with me when I was in Dresden. Saúl has been a scientific reference for me, and the chance to work with him has provided me very important scientific insights.

Another very intense collaboration has been with Ana Caño Molecular and Genetics Lab (CSIC-IRTA). I would like to thank to all of them all the shared moments, all the labmeetings we had all these years, all the discussions and nice moments we spent together. The multiple labmeetings we had, they have incredibly helped to learn how to communicate to people from other disciplines. Collaborating with Ana Caño Lab has always been very motivating and inspiring. A special thanks to Norma Fàbregas and also to Ana Confrarias for the exciting project we are involved in (and of course to Ana Caño, and Marta!). And once more, special thanks to Norma, I have learned a lot working with you. Also, the other members of the Lab: Irina, Pep, Mary-Paz, Reinhardt and Kostas. Thanks to all this Lab to get me to know the Plant's world!!!

In the last two years there has been a new collaboration with the group of Prof. Fernando Giraldez (UPF-PRBB, Barcelona, Spain). Together with Joana Neves, Jelena Petrovic, Juan Camilo and Marta, this has been a big excursion in the inner ear of mice. In all the discussions we had, the time always went away incredibly fast... I guess that it is because all the passion we all have in this project. Thanks for this big quality time that we have had together.

Also, a recent joined project with David Palau, Jose María Sancho and Marta has lead to new ways of studying patterning in a perspective I would not have imagined! I am amazed from the brainstorming meetings we have and all the work from David... Definitively, I am learning also a lot from this experience.

Last spring I had the chance to do an internship at David Sprinzak Lab (Tel Aviv, Israel). This Lab brought me the opportunity to experience a day-to-day dialog on Notch from both experimental and theoretical perspectives, which was like a dream for me. I really want to thank David Sprinzak and the rest of the members of the Lab for the exciting months I had in this internship. Their names are Liat Amir-Zilberstein, Oren Shaya, Tslil Rotbert, Olga Loza, Sheila Weinreb and Itzhak Khait (Tsuky). During this internship I had the chance to have also very exciting discussions with people of the Elowitz Lab (Caltech, USA), and specially Michael Elowitz, Sandy and Leah. Their work and previous outstanding articles from this Lab have been very influential to me.

I want to acknowledge other PhD students in our group for all the nice time spent together, for the discussions, for the lunch times, for the experience of being close to you. Again, Juan Camilo and David Palau, and also David Frigola, Irina Parvelescu, and Elisa, the newcomer of the group. I have learned from all of you lots of things. Specially more recently, from the intense collaborations with David Palau and Juan Camilo.

Thanks to Paul Tondelier, Dr. Jaume Casademunt and Marta for the intense collaboration we had on the auxin project. This story has allowed me to go deeper in the nonlinear world, and I can't wait for keeping on learning about that!

Also, I am grateful for meeting during these years Javier Buceta and Jordi García-Ojalvo. In multiple times they have taught me, in their lectures and seminars, with their papers, in our discussions...

I am fortunate for having interacted and learned from other researchers like Prof. Uri Alon, Prof. Naama Barkai, Prof. François Schweisguth, Dr. Richard Smith, Prof. Jordi Ortín, Dr. Jordi Soriano, Dr. Otger Campàs, Prof. Fèlix Ritort, Prof. Marco Milán, Prof. James Sharpe, Dr. Joannes Jaegger, Dr. Isaac Salazar-Ciudad, among others.

I feel the necessity to thank the teachers that have taught to me during my whole life, in the primary school, high school, and at the Degree and Master level.

Also, I would like to acknowledge all teachers I had from music and dance, my main hobbies that did this journey more amenable, and provided me a lot of sources of creativity.

I also want to acknowledge to all my friends their support, this journey would

not have been the same without them. I can't wait to see those ones that I haven't met for so long time! Another great chance I had during these years is to live with some of them. Especialment, vull mencionar els noms amb els que he pogut viure i compartir més temps plegats: Anton, Marion, Nico i Gonzalo.

My biggest acknowledgement to my family and to my life partner, Janialy, who has been all this time sharing this journey with me.

Pels amics de l'ànima, per la familia, para Janialy. Per l'Ivan i la Nerea, els més petits de la familia. Per l'avi Joan, la Vicenta i els avis que ja no hi són. Pels estimats tiets, tietes i cosins i cosines. Per a la meva germana Anna i en Toni. Per a la familia de Puerto Rico. Para Janialy. Gràcies per ensenyar-me a viure amb aquesta intensitat aquesta vida, pel vostre suport, la vostra música, la vostra alegria, la vostra confiança, el vostre amor. Gràcies.

The realization of this Thesis would not have been possible without the financial support I had during these years. Most importantly, the FI fellowship, funded by the Generalitat de Catalunya for a few months (March 2009-July 2009), and afterwards the FPU fellowship (FPU-AP2008-03325) supported by the Ministry of Education (2009-2011) and the Ministry of Education, Culture and Sports (2011-2013). Two additional grants from the Ministry of Education from Spain also covered an internship at MPI-PKS (Dresden, Germany) and an internship at Sprinzak Lab (Tel Aviv, Israel). Other financial support was essential for me during all these years (FIS2006-11452-C03-01, Ministerio de Ciencia e Innovación; 2005SGR00507, Generalitat de Catalunya; FIS2009-13360-C03-01, Ministerio de Ciencia y Educación; 2009SGR14, Generalitat de Catalunya; traveling grants of the Physics Faculty of the University of Barcelona). For obtaining all this funding, the help of my PhD advisors Dr. Marta Ibañes Míguez and Prof. José María Sancho Herrero has been crucial.

The Max Planck Society also allowed me to do my first research stay at MPI-PKS (Dresden, Germany). Also during my internship at Sprinzak Lab (Tel Aviv, Israel), financial support coming from Sprinzak Lab covered different fees for me, and I am very thankful for that too.

I am grateful to have spent these years for doing the PhD in the Nonlinear Physics Group in the Department of Estructura i Constituents de la Matèria, which belongs to the Physics building of the Universitat de Barcelona. I would like to acknowledge all the Physics I have learned in this institution, during my degree in Physics and in my Master Degree in Biophysics.

Preface

During these years of my PhD in Physics at the University of Barcelona I have been studying from a theoretical and computational perspective how patterns are formed in tissues of living beings. In particular, I have focused on the salt-and-pepper patterns emerging in different kind of animal tissues mediated by the Notch signaling pathway.

My intention in this Thesis is two-fold. On one side, I try to provide valuable results in relation to pattern formation in spatially extended dynamical systems. On the other side, I want to bring useful knowledge into the biological context of Notch signaling pathway. Because of this double intention, the reader will often find the alternation of more biologically-based paragraphs with other more physically-motivated paragraphs.

All the central questions that you will find in the following pages come from recent experimental findings in the Notch pathway that pose new puzzles to dechiper. We will address these questions through the formulation of simple non-linear dynamic models. In particular, we will use coupled ordinary and stochastic differential equations to simulate the evolving concentration variables in different cells in a tissue. To understand the pattern formation capabilities of our models, we will make use of analytic tools and computer simulations. In every chapter, based on our results, we will formulate specific predictions of the systems under study.

This Thesis will start with an introductory chapter (Chap. 1) where we will present the general biological and theoretical context we want to dig in. The following Chap. 2 is devoted to present the general methodology that has been used in this Thesis. This chapter is very important, since next chapters of the

Thesis are built up assuming the knowledge of the methodological framework presented herein. Next, there are four chapters, which are the core projects of the Thesis.

Chap. 3 will deal with a differentiation wave leaving on its wake a salt-and-pepper pattern. The main addressed question is how differentiation front progression will depend on the state of the tissue being invaded. This project has been a collaboration with Dr. Saúl Ares, at that time being a Postdoc Researcher at Max Planck Institute for the Physics of Complex Systems (Dresden, Germany), and now being at Logic of Genomic Systems Laboratory, Centro Nacional de Biotecnología, CSIC (Madrid, Spain) and Dr. José María Frade, a Group Leader of an experimental Lab at Cajal Institute from CSIC (Madrid, Spain). In such collaboration I had the great chance to do two internships at Max Planck Institute for the Physics of Complex Systems, hosted by the Biological Physics group directed by Frank Jülicher, in Dresden. This allowed me to intensively work together with Saúl Ares on this project, who is an expert on theoretical aspects of Notch signaling. The question we dealt with was motivated by Dr. Frade and at this stage it can only be addressed theoretically and computationally. Our work poses specific predictions that hopefully will be tested in future years. The main fruits of this joint project has been published in Development recently (see List of publications in Sec. 7.3). In Chap. 3 the reader will find the published work presented from a slightly different scope, and also some new material that came afterwards.

The following Chap. 4 arises as a theoretical question based on experimental data: how diffusible ligand transport can influence salt-and-pepper patterning. Nowadays, diffusible ligands are not a "hot topic" in the Notch literature out from the scientific community studying the *C. Elegans* organism. Though, there are increasing evidences that diffusible ligands and other molecules similar to such ligands might have a significant role. This study started as a part of my Master Thesis in Biophysics, and ended up later on being an important project in my Thesis. This work allowed me to become familiar with the different modeling techniques. This work has already been published (see Sec. 7.3).

Next, in Chap. 5 we examine theoretically a question that has been a "hot topic" in the Notch community and has been studied by different groups in the last few years: how the interaction of receptors and ligands inside the same cell,

what is called cis-interactions, can affect Notch signaling and patterning. This was also a project I started in my Master Thesis, and I am still involved in it. Actually, such simple question can lead to an incredible amount of different phenomena to look at. This project has brought us, among other things, the concept of competition in the context of gene regulation, that has been pivotal for the last central chapter of the Thesis.

In the last central chapter of the Thesis, Chap. 6, we study the effects of two different ligands for understanding a pattern emergence in the inner ear of chick embryos. In particular, we address the question of how two opposite roles of Notch are orchestrated: first lateral induction and then lateral inhibition. This last project has been a collaboration with the group of Prof. Fernando Giraldez, from the Universitat Pompeu Fabra and Parc de Recerca Biomèdica de Barcelona (Barcelona, Spain). I have started being involved on that at a late stage of my PhD. This new story gave me the chance to meet closer with other characters in the Notch pathway (Jagged, Hey1, Hes5), among other things.

After the central chapters, the general conclusions are presented followed by the references, three technical appendices and an additional appendix with a brief summary of the Thesis in Catalan, my mother language.

In the last years there has been a lot of publications focusing on theoretical aspects of such salt-and-pepper patterns mediated by Notch. Also new papers have brought new experimental data accounting for the different phenomena we were focused on. Because of these two factors, our questions, goals and ways to proceed have been highly shaped by the exciting scientific evolving context.

The reader coming from a Biophysics background will probably miss numbers, or a more quantitative approach. In this Thesis, we address some quantitative aspects, but mostly, our phenomenological models provide qualitative behaviors that are very robust in the parameter space. The lack of "numbers" in this Thesis comes from the complexity of the Notch pathway and its context-dependent nature, what makes complicate to bridge our work with specific quantitative predictions. Nowadays, new approaches brought from Synthetic Biology and new live-imaging techniques have just started to provide numbers and more dynamical data that will facilitate a deeper link between theory and experiments in the next few years.

At the end of my PhD I have started a collaboration with the Lab of David

Sprinzak, from Tel Aviv University (Tel Aviv, Israel). David Sprinzak has been extensively studying the Notch signaling pathway from a multidisciplinary approach. Last Spring I had the chance to do an internship in his Lab to work on different aspects of the Notch pathway. This is still an ongoing collaboration, and such work is not present in this Thesis. This collaboration has brought me new theoretical insights in relation of how cis-interactions can affect Notch signaling pathway. Also, I had the opportunity to do image analysis of time-lapse microscopy images of some experiments performed at Sprinzak Lab.

Another important focus during all my PhD has been on the formation of the vascular pattern in the shoot of *Arabidopsis thaliana* plant. This project has been done in collaboration with the group of Ana Caño Delgado, an experimental group on Molecular Genetics at Centre de Recerca en Agrigenòmica, a CSIC-IRTA consortium (Bellaterra, Spain). This collaboration brought me the opportunity to study another pattern formation mechanism, which is due to the transport and accumulation of a very important plant hormone, auxin. This project has lead me to the study of a longer wavelength pattern with a very rich phenomenology. This project gave rise to another project in collaboration with Dr. Jaume Casademunt, who is an expert in nonlinear phenomena in our Department, and with the Master student Paul Tondelier, from the École Normale Supérieure (Paris, France). For time constraints we have finally not included all this work in the Thesis.

There are several manuscripts under revision and in process in relation with my PhD (see List of Publications in Sec. 7.3). I hope to publish them soon to share it with the rest of the scientific community.

Finally, I wish the reader a fruitful and pleasant reading of the Thesis.

Barcelona, March 2013.

Contents

Chapter 1

Introduction

How living beings are formed? How a single cell, the fertilized egg, can give rise to a multicellular organism?

Complex multicellular organisms are made of tissues and organs, all constituted by different kinds of cells [1]. Cells are the structural unit of life, being composed by different organelles and soluble molecules [2]. The development of a full organism is a very complex phenomenon, occurring at different spatial and time scales. In the last decades, experimental efforts have brought an enormous progress in understanding the way an organism is built. Also, mathematical and computational approaches have brought different insights that have contributed to its understanding [3]. Specially, previous knowledge on pattern formation [4,5] and deterministic [6] and stochastic [7] dynamical systems has been widely applied to different questions in Developmental Biology [8]. In the last decade, different groups with strong experimental and theoretical backgrounds have made a step forward in the understanding of the dynamics of living matter from a multidisciplinary approach [9]. This emerging multidisciplinary perspective has already enormously contributed in the understanding of developmental phenomena.

In this Thesis, we adopt a theoretical scope to decipher different aspects of the early development of animal tissues. We make use of mathematical dynamical models to understand how cells differentiate and give rise to ordered salt-and-pepper patterns of different cell types [10], always with a link with experimental evidences and, in some occasions, with a direct connection with experiments

performed by our collaborators.

This chapter introduces the reader to the subject we will deal with throughout this Thesis. In Sec. 1.1 we sketch some general biological aspects, and in Sec. 1.2 we outline some theoretical landmarks that have been pivotal in this field. In Sec. 1.3 we present the type of pattern we are interested in and we also introduce the main actor responsible for the formation of the studied patterns: the Notch signaling pathway. Afterwards, in Sec. 1.4 we learn about a key dynamical effect of this pathway that has been proposed as a trigger of pattern emergence: lateral inhibition. In Sec. 1.5 we present different models that have dealt with lateral inhibition. Last, in Sec. 1.6 several challenges around lateral inhibition are presented. These challenges provide the different aspects and questions that have motivated this Thesis.

1.1 General biological aspects

1.1.1 Central dogma, genetic regulation and cell differentiation

Cells have encoded the same information in their genetic code, which is made of the DNA. In animal and plant cells, the DNA is well packed and protected in the nucleus of every cell. The DNA contains different information units, called genes. Each gene is transcribed into its mRNA, and afterwards is translated into a protein. Such linear process is what is called the central dogma of Molecular Biology [2].

How initially equivalent embryonic cells in a tissue get differentiated into different kinds of cells? Genes are differentially expressed, what means that just a part of their genetic code is active and it can be different from cell to cell [1]. For doing so, there is what is called genetic regulation at transcriptional, translational and even post-translational levels. For instance, a protein can act as a transcription factor and bind to a promoter of another gene, which is a DNA region that is responsible for starting the transcription of a gene. The binding of a transcription factor to a gene promoter will enhance or inhibit the transcriptional rate for such gene [2]. Genetic regulation creates feedback loops at different levels. These feedback loops turn the simplicity and linearity of the

central dogma to a much more intricate and nonlinear process.

Genetic regulation enables cells to become distinct from one another, leading to different patterns of gene expression [11]. These different patterns are ultimately related to specific cell types. Cells start reversibly adopting certain fate decisions, a process known as cell specification, and afterwards, cells perform and irreversibly fate commitment, what is known as cell differentiation.

During the process of cell differentiation, different external physicochemical signals alter the cell decisions. For instance, extracellular molecules present around the cell can be endocyted, leading to a cascade of phenomena that ends up in the activation or inhibition of the promoter of a gene. These external signals often come from other cells, what makes that cell decisions can occur in a non-cell autonomous way [12].

1.1.2 Pattern formation in multicellular organisms

Multicellular organisms are constituted by different kind of cells which are arranged in a particular way, forming tissues with specific functions. The organization of these different cells can give rise to regular spatiotemporal patterns [1, 8].

For instance, in plants, branches are born along the main shoot in an ordered way, giving rise to a variety of different phyllotactic patterns [13]. In animal early embryonic development, a series of segments along its main axes can be identified in both vertebrates and in invertebrates. In vertebrates, coupled genetic oscillations result in the formation of the somites, which are the precursors of the vertebras [14]. In *Drosophila melanogaster* fruit fly, one of the most studied invertebrate organisms, body segmentation occurs along the anterior-posterior axis, leading to the creation of different body parts [1]. Patterns in which few alternated cell types appear are also ubiquitous in very different tissues in plants and animals [15]; for instance, the spines of the cactus, the pores found in the epidermis of plants' leaves called stomata [16], the photoreceptors in the fruit fly eye [17], the sensory cells in the inner ear of vertebrates (Fig. 1.1) [18], and the hairs and feathers in the epidermis of animals [19]. We will refer to these patterns as fine-grained patterns, and more specifically as salt-and-pepper patterns when we deal with two types of cells.

In many cases, patterns emerge in homogeneous tissues made of equivalent

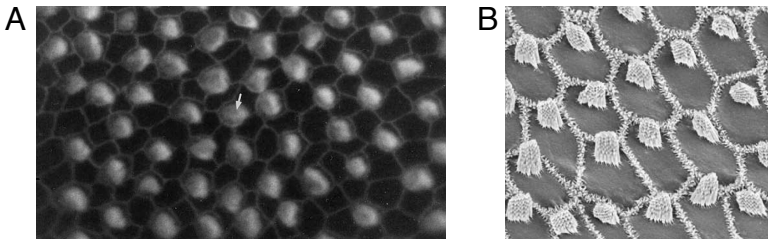

Figure 1.1: Example of a salt-and-pepper pattern of two cell types in the mouse (A) and chick (B) embryonic inner ear. (A) Snapshot extracted from [20] showing a cellular pattern of two cell types in a developing portion of the inner ear of mouse embryos. Sensory cells, which are called hair cells, are marked in white and are surrounded by supporting cells. Arrow points to a central hair cell. (B) Snapshot extracted from [21] showing a portion of chick inner ear in which the pattern is in a more advanced stage. Hair cells — the large hexagonal cells with a hair bundle above them — are surrounded by narrow, microvillus-bearing supporting cells.

cells, so how these patterns are formed? In the 20th century the concept of morphogen has been pivotal to start answering this question [1]. A morphogen is a diffusible chemical that elicits different cellular responses depending on its local concentration. This concept has been fundamental for understanding different developmental processes, like the segmentation of the *Drosophila* body [1].

Nowadays, it is known that in addition to morphogens, different transport mechanisms inside and outside cells and cell-to-cell signaling processes are key elements for cellular organization, and ultimately for cellular patterning.

After the Molecular Genetics revolution in the last decades there is a great amount of experimental data that brings quantitative information at cellular, subcellular and even molecular levels. Mathematical and computational modeling can facilitate the understanding of the different studied phenomena, and most importantly, it enables the possibility to formulate specific predictions that can be posteriorly validated or rejected with further experiments.

In the next section we will mention some general theoretical ideas that have persisted until nowadays and have brought useful knowledge into the field of Developmental Biology.

1.2 Theoretical aspects in Biology: from cell differentiation to biological pattern formation

In 1940, Waddington proposed the epigenetic landscape metaphor for the cell differentiation process [22], an idea that has been used afterwards. The classical conception of the Waddington landscape, more established in the next decade, is a ball rolling downhill the landscape, what represents a developing cell, passing through different valleys that represent alternative cell states [23]. When the ball encounters a bifurcation valley, this means that at that point a cell decision fate needs to be made, and the ball will continue through one of the valleys. This metaphor and variants of it have been widely used until nowadays, bringing new ideas of how cells differentiate and drive cellular patterning (see for instance [24]).

A few years after, a seminal paper by Alan Turing came into the light, providing a *de novo* mechanism for pattern formation from a homogeneous tissue of equivalent cells [25]. In 1951, Turing proposed that the diffusion of interacting chemical species, what he also called morphogens, would be the factor that could unstabilize a homogeneous precursor state, leading to a patterned solution [25]. He showed that if two interacting chemicals were distributed homogeneously, small differences in the initial conditions in space could be amplified if diffusion was considered. This was a revolutionary idea, since diffusion by that time was associated to a homogenizing mechanism. A typical Turing pattern would resemble the skin pigment patterns of different animals, like the stripes in zebra's skin or the spots of a leopard.

In 1971, Koch and Meinhardt [26] studied in depth Turing's systems and established some fundamental principles leading to patterning. Most importantly, they proposed that the combination of a short range activator with a long range inhibitor was a fundamental mechanism for patterning [27]. Meinhard's works have been applied to very different phenomena, ranging from the vein formation in plants leaves to axis formation in animals. One big challenge of all these Turing-based models has been to identify the diffusing morphogens with the corresponding real molecular entities of the studied cases.

In the late sixties, Kauffman proposed different network models, whose nodes would connect dynamic evolving variables, for studying the emerging dynamical

behaviors from genetic networks [28,29]. He found that even very large networks of thousands of genes lead to a few ordered and stable dynamic behaviors.

Recently, gene regulatory networks have been shown to be built from some recurrent simple building blocks, what has been termed network motifs [9,30,31]. The proposal and mathematical study of these network motifs and small genetic networks have been pivotal for understanding the relation between topology and function of different regulatory networks [9,11]. For instance, a positive feedback loop is known to lead to multistability, while a negative feedback loop drives homeostasis or oscillations (see for instance review [32]).

In this last decade, the advance of genetic tools and new visualization techniques in combination with theoretical approaches is enabling a clear synergy between modeling and experimental approaches that tries to decipher developmental phenomena from a more holistic perspective. We will refer to this multidisciplinary and holistic perspective as the Systems Biology approach[1].

Such joined experimental and theoretical efforts have shown that Turing patterns and more general reaction-diffusion systems do occur in real biological systems [33–36]. For instance, periodic stripe formation in the mammalian palate [35] and also the digits formation in mice have been shown to be controlled by a Turing-like mechanism [36].

Combined genetic approaches and theoretical work have established new ways of pattern formation, different from Turing's idea. A clear example is the advances in the last decade for the understanding of pattern formation in plants. Works coming from different groups have shown that concentration peaks of the hormone auxin drives the formation of new organs. Auxin is a very small molecule that is being transported by diffusion and through transporters that actively pump auxin in and out of the cell. Such recent works have proposed that the active transport of auxin is the triggering agent leading to a patterned distribution of such hormone, and that this model is able to explain phyllotactic [13,37,38] and vascular pattern formation [39,40] in *Arabidopsis* plant.

Also, other recent multidisciplinary works have proposed that mechanics is also important for patterning [3,12,41]. Interestingly, in some cases it has been supported that an interplay between signaling and mechanics is pivotal for the

[1]Herein we do not pretend to give a precise definition of Systems Biology. Some people would disagree with this definition.

pattern generation [42, 43].

In the last few years, the new multidisciplinary field of Synthetic Biology has emerged. Among other things, Synthetic Biology is trying to built up small genetic networks for ultimately understanding the natural genetic circuits [44, 45] with the help of mathematical modeling. Recent works have already achieved to construct oscillating genes that can be used as synthetic biological clocks [46]. Also, Synthetic Biology has started being applied to cell-to-cell communication processes [47]. Recently, it has been designed a synthetic intercellular feedback that is able to propagate a signal from cell to cell [48].

1.3 Our focus: salt-and-pepper patterns due to the Notch signaling pathway

1.3.1 Salt-and-pepper patterns

One ubiquitous phenomena of pattern formation in tissues is the case of salt-and-pepper patterns, where two different kinds of cells are mixed. This Thesis mainly focuses on this kind of pattern appearing in animal tissues, in which one cell type is always surrounded by cells adopting a different cell fate, leading to very regular and periodic patterns (Fig. 1.1).

Salt-and-pepper patterns are typical of tissues where neurons and sensory organs are born. Several paradigmatic examples can be found in the *Drosophila* fruit fly, like the arrangement of bristles in its thorax [49, 50], or the perfect arrangement of photoreceptor cells in its eyes [17]. Numerous examples can be found in vertebrates, like in the vertebrate retina [51–54], where each new born neuron is surrounded by non-differentiated cells, and the vertebrate inner ear, where the sensory cells, which are called hair cells, are surrounded by its supporting cells [18, 55–57]. Also, other salt-and-pepper patterns can be found in other tissues with non-sensory functions, like the distribution of ionocytes in the epidermis of zebrafish embryos, which are related to ion transport [58], or the distribution of secretory cells in the mouse intestine, which are surrounded by absorptive cells [59, 60].

How these patterns are formed? Is there an underlying mechanism driving

the patterning process? Salt-and-pepper patterns involve spatial scales of few cells, so these kinds of patterns can be expected to be based on short-range interactions. Indeed, nowadays it is known that cell-to-cell communication between adjacent cells enables this particular cellular arrangement. This cellular spatial coupling does not involve the classical diffusion of a molecular species, but rather the cell-to-cell direct contact mediated by proteins that are anchored to the cell membrane, the so-called transmembrane proteins. Some of these proteins, the ligands, bind to another kind of transmembrane proteins anchored to the membrane of neighboring cells, the receptors, enabling direct cell-to-cell communication. It has been proposed from theoretical grounds that this cell-to-cell coupling with other downstream events can create intercellular positive feedbacks between cells [10]. This cell-to-cell communication process and its downstream events belong to what is called the Notch signaling pathway.

Next, we review some aspects of the Notch signaling pathway, what will be fundamental for the study of the mechanism leading to salt-and-pepper patterning.

1.3.2 The Notch signaling pathway

The Notch signaling pathway is one of the "six major and universal signal transduction devices in the cell" [61]. Notch is present in all metazoans and it has been conserved through evolution. This universal device influences cell fate specification, cell proliferation and apoptosis in almost all vertebrate and invertebrate tissues and organs [62, 63]. Indeed, Notch pathway is involved in different aspects of the developing embryo at different stages. This encompasses a wide variety of processes, ranging from the creation of the somites along the body in vertebrates [14], angiogenesis, which is the creation of red blood vessels [64], neurogenesis [54, 65], boundary determination in tissues [66] and so on. Moreover, such pathway is directly related to different important diseases, like cancer [67].

The firsts studies involving the Notch pathway were performed on invertebrates, being first in *Drosophila*, and then in the worm *C. elegans*. Later on, a homolog was found in the *Xenopus* frog, and finally it was also found in humans.

The Notch term comes from a story that happened around $1913 - 1914$. On March 1913, a *Drosophila* mutant exhibited several serrations or notches on its

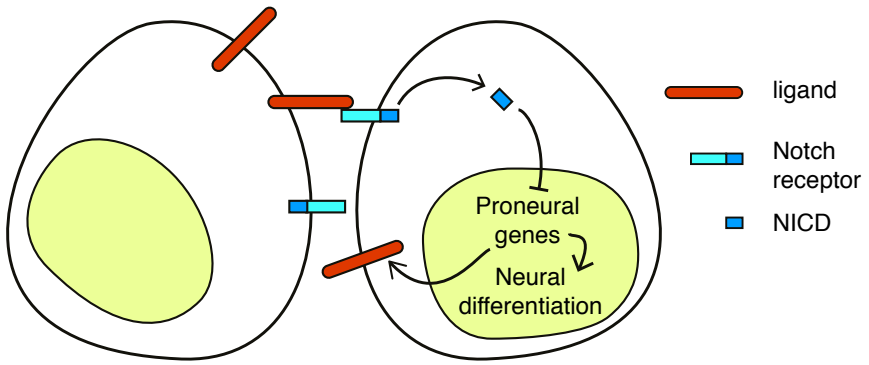

Figure 1.2: Simplified cartoon of the Notch signaling pathway. A Notch ligand (*e.g.* Delta) (left cell) binds to the Notch receptor in a neighboring cell (right cell). Then, a series of proteolytic cleavages (not shown) releases the Notch intracellular domain (NICD) towards the cell that is harboring the receptor. NICD ultimately inhibits the proneural genes expression, which drive the expression of further ligand and neural differentiation. Note that in this cartoon we omit the Hes/Hey Notch targets and therefore its direct regulation on the Notch ligands.

wings [68]. Such phenotype was firstly reported on 1914 [69] and it was shown to be a dominant effect of a sex-linked mutation in the X-chromosome [68, 70]. In 1937 Poulson showed that deficiencies in the X-chromosome in *Drosophila* lead to altered embryos with a prominent nervous system [71], what would correspond to a massive production of neurons, a feature that is named neurogenic phenotype [62]. Almost 50 years later, the group of Artavanis-Tsakonas discovered the *locus* of the Notch gene and cloned it, revealing that it was related to a surface membrane receptor [63]. Later on, in 1990, Fehon *et al.* showed that cells expressing the Delta ligand formed aggregates with Notch expressing cells, indicating a specific interaction for Notch with Delta anchored in neighboring membranes [72]. Afterwards, many works have shown this interaction and have focused on its downstream events (see for instance reviews [73, 74]).

Nowadays, the Notch pathway is a very active field of research, and new elements of this pathway are still being revealed [63].

Notch protein is a transmembrane receptor that binds to its ligands that are

anchored on the membrane of neighboring cells (Fig. 1.2) [72]. These intercellular or 'trans-interactions' result in a complex that undergoes a series of proteolytic cleavages, leading to the release of the Notch intracellular domain (NICD) towards the cell that is harboring the receptor. NICD translocates to the cell nucleus, where it forms a complex with the so-called CLS transcription factor and a co-activator called Mastermind/Lag-3. Then, such ternary complex binds to specific DNA regulatory sequences, activating the transcription of different Notch target genes (see reviews [73, 74] for a detailed explanation of this process). Among these genes there are the family of Hes/Hey genes [75, 76]. Hes/Hey genes are transcriptional inhibitors of the Notch ligands genes itself and a group of genes named proneural genes, which are essential for cell differentiation into the neural and other cellular fates. Proneural genes expression also inhibits the Notch ligands genes [77]. For understanding salt-and-pepper patterning, the fact that Notch receptor, upon binding with its ligand on a neighboring cell, inhibits the production of ligand is crucial, as will be described below.

Notch receptor has different canonical ligands. In vertebrates these ligands are Delta and Jagged (in *Drosophila*, the Jagged homologous ligand is Serrate). In worms, the Notch homolog receptors are called GLP and LIN, and its ligands LAG and APX. In vertebrates, receptor and ligand types can present different subtypes (paralogs). Specifically, in vertebrates four Notch receptor subtypes have been characterized (Notch1-4) and six ligands, four belonging to Delta family (Delta-like 1-4, homologous to Delta) and two to Jagged family (Jagged 1-2, homologous to Serrate). In *Drosophila* there is just one Notch receptor and two different ligands, Delta and Serrate. Moreover, there are numerous non-canonical factors that can modulate Notch pathway. For instance, the non-canonical Notch ligands Delta-like homologs Dlk1/2, which are similar to the canonical ligands but lack the DSL domain contained by the canonical ligands [78, 79].

There are additional aspects of the Notch pathway that appear to be pivotal for its regulation at transcriptional and post-transcriptional levels [80]. Some of the most studied are ligand endocytosis [81], ligand regulated degradation [82] and receptor modifications through Fringe glycosiltransferases [83, 84]. Moreover, Notch pathway coexists with other signaling pathways in the cell. Though, these pathways do not act independently, but there is crosstalk among them [63]. For instance, the Notch pathway shares some elements with the Wingless/Int1

(Wnt) [61] and the Hedgehog (Hh) [63] pathways, being both of them two other important pathways in metazoan development. Hence, Notch pathway is very complex, and the context in which is acting will drive to very distinct phenomena.

Notch pathway has been reported to function in two different operating modes: lateral inhibition and lateral induction (Fig. 1.3). In lateral inhibition, a cell heading for a particular fate inhibit its neighbors to adopt such fate. Thus, a cell that is expressing high ligand amount will inhibit its neighboring cells to express such ligand. This kind of behavior will be essential for the creation of salt-and-pepper patterns in a wide variety of sensory and non-sensory tissues, like in the vertebrate and invertebrate eyes, the vertebrate inner ear, and the epidermis of zebrafish. Lateral induction acts in the opposite way, driving nearby cells to adopt the same fate. Lateral induction has been proposed to occur in lens formation, in pancreas development, in angiogenesis and in inner ear development, among others [18].

Notch signaling can also undergo synchronous and asynchronous oscillations in the tissue [85]. One of the most studied phenomena where genetic oscillations have been observed is in somitogenesis, where synchronous oscillations and delays are of paramount importance [14, 86–88].

In this Thesis we mainly focus on lateral inhibition, since we are mostly interested in salt-and-pepper patterns and how different elements in the Notch pathway modify them. Moreover, lateral inhibition has been a subject of study by biologists in the last thirty years, so there is enough literature regarding this patterning mechanism for doing a theoretical work with a strong motivation in previous experimental observations. In Chap. 6 we also deal with lateral induction, which is a less studied phenomenon.

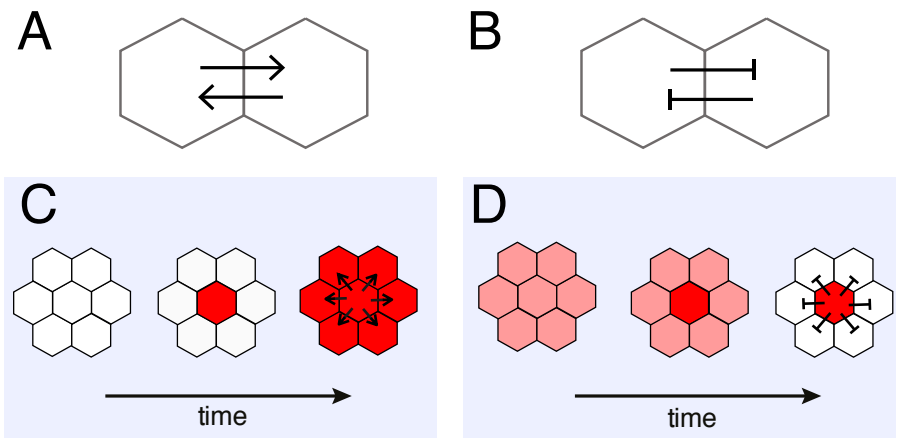

Figure 1.3: Notch can act in two different operating modes. (A) Lateral induction, in which a cell induce its neighboring cells to adopt the same fate and (B) lateral inhibition, in which a cell inhibits its neighboring cells to adopt the same fate. We illustrate this phenomenon in terms of ligand expression. (C,D) Possible dynamical outputs for (C) lateral induction and (D) lateral inhibition. Red intensity is related to the amount of ligand concentration: high ligand cells are red, while cells without ligand are white. Arrows in the last panel of (A,C) and (B,D) indicate activation and inhibition, respectively.

1.4 Lateral inhibition: a biological introduction

As explained above, lateral inhibition is a dynamical behavior in which a cell that is heading for a particular fate inhibits its surrounding cells to adopt the same fate.

The first formulation of this concept in animals was proposed by Wigglesworth in 1940 [89,90]. In this work he was studying the bristles spacing in the *Rhodnius Prolixus* bug. He hypothesized that there was an essential factor for the activity of the bristle-forming centers. When a new bristle was formed, it acted as a sink of such factor, depleting its concentration in its surroundings and hence inhibiting the neighboring cells from becoming new bristle-forming centers. This is reminiscent of the lateral inhibition that was proposed in plants by Schoute in 1913 [91] and posterior works in the thirties where the plant hormone auxin in plants was proposed to be the mediator of such inhibition [92].

Over 50 years had to pass to make a link of lateral inhibition with the Notch signaling pathway. In 1983 Lehmann *et al.* found that mutations of genes related to neurogenesis in *Drosophila* — now called the proneural genes — lead to a neurogenic phenotype, *i.e.* an excess of neural cells at the expenses of epidermal cells [93], what was reminiscent of the experiments performed by Poulson in the forties [71]. In 1990, Simpson and Carteret found that in the same organism, neural precursors were formed in equivalence groups, *i.e.* clusters of cells having the same developmental potential [94]: the mutation of the *shaggy* gene in *Drosophila*, mediator of the bristles development in the epidermis, would lead all cells in the cluster adopt the neural fate, developing into new bristles. In 1991, Heitzler and Simpson suggested that Notch protein was participating as a receptor from an inhibitory signal emanating from neural precursors, since Notch mutations in proneural clusters lead to cell-autonomous neurogenesis [95]. Along the nineties it has been accepted the model in which the interaction of Notch with its ligands together with downstream Notch signaling processes mediate the lateral inhibition effect.

Nowadays, a simplified view of lateral inhibition process for reaching a certain fate would be the following: initially there is a competent field of equivalent cells, in which all cells are trying to adopt a particular desired fate and express a Notch ligand. In particular, we will mostly refer to the Delta ligand given that

this has been the most studied Notch ligand in relation to lateral inhibition. Delta expression inhibits neighboring cells to adopt the desired fate by binding to Notch protein in such cells, eliciting a signal that ultimately inhibits the proneural genes and the differentiation into the initially desired fate (Fig. 1.2).

Lateral inhibition occurs in very different tissues and therefore it can occur in very different conditions. For instance, the initial equivalent group of cells where lateral inhibition takes place can be very different in size; it can occur either in smalls group of cells, like the proneural clusters in *Drosophila*, or it can happen in a few rows of cells, like in the vertebrate inner ear, or it can take place in larger cell populations, like in *Drosophila* eye. Also, lateral inhibition patterning may also depend of cell proliferation, apoptosis and cell movements, being therefore a more morphogenetic process in which signaling and other mechanism and more mechanical phenomena are coupled [12]. Pattern emergence dynamics can be very diverse, occurring simultaneously in the whole tissue of cells, like the beautiful pattern of scale cell precursors in the butterfly's wing [96] (Fig. 1.4 (A)), or for instance nucleating first in one part of the tissue and after spreading over the rest of the tissue [50, 54], like in the vertebrate retina or in the *Drosophila* eye (Fig. 1.4 (B)), forming what is called a differentiation wavefront. Notch pathway has been shown to be very context dependent [79], so different elements of the Notch pathway may be involved in each particular case, like the downstream targets of Notch and the particular ligands involved in the process. Conversely, some general processes are conserved in the pathway, like the trans-interactions mediated by ligands and receptors anchored in neighboring cells.

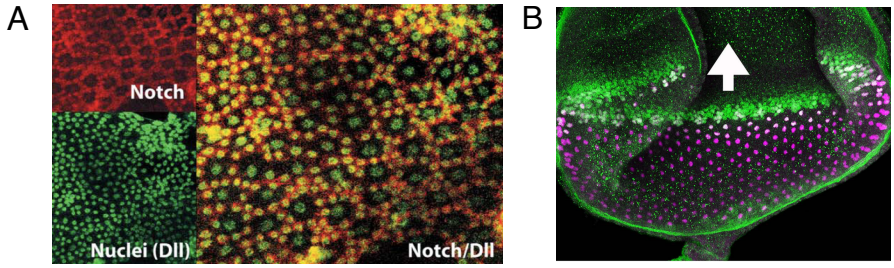

Figure 1.4: Examples of salt-and-pepper patterns of two cell types in (A) the butterfly's wing and (B) in the *Drosophila* eye. In both processes, the Notch pathway is important for the resulting patten. (A) Snapshot adapted from [96] showing a cellular pattern of two cell types in the butterfly's wing that emerges simultaneously in all the tissue. Left panels show (up) Notch expressing cells in red and (bottom) the nuclei marked in green. Right panel is a superposition of these two channels, what reveals the order of cells that do not express Notch (and then would have high Delta levels) surrounded by cells expressing Notch (with low Delta levels). (B) Snapshot adapted from [97] showing the progression of a differentiation wavefront in the embryonic *Drosophila* eye invading a non differentiated tissue marked in green. Arrow indicates the direction of the wavefront progression. The purple cells are the precursor cells of the R8 cells, which are the first photoreceptors that differentiate.

1.5 Models for lateral inhibition patterning

How is it possible to start from an initial equivalent tissue of cells without any spatial order, and ending up in a mosaic of cells with such regular and periodic pattern? In the last twenty years, computational and theoretical approaches have started playing a role in the understanding of this complex phenomenon.

The first theoretical studies were purely computational models [98, 99]. In these models, a lateral inhibition rule was applied to a line of cells and a bidimensional hexagonal array of cells for being selected to differentiate. These works provided quantitative values of the ratios of differentiated cells. Interestingly, they showed that if the lateral inhibition rule was applied successively to all cells in the tissue but cells were picked randomly, there was a ratio of 0.23 differentiated cells in the tissue. If cell picking was performed systematically in the tissue (for instance, from left to right) such ratio varied from 1/3 to 1/7. Such kind of models were also applied to disordered arrays of cells through a Voronoi tessellation (see Sec. 2.9.2) with periodic and fixed boundary conditions. In more disordered patterns it could be observed that slightly more differentiated cells could be obtained than in the perfect hexagonal array [99].

Later on, a first formulation of such pattern formation emergence in terms dynamical equations was proposed by Collier *et al.* [10], based on the Notch signaling pathway. In their paper they theoretically showed that the fate choice is spatially regulated through lateral inhibition with an intercellular positive feedback loop [10]. Feedback arises from the fact that (i) all cells can potentially express the Notch receptor and the Delta ligand and then each cell can perform lateral inhibition to its neighboring cells, and (ii) Delta expression itself can be inhibited by Notch signaling (Fig. 1.5).

They proposed two coupled ordinary differential equations per cell accounting phenomenologically with the dynamics of what they called the "Notch activity" and the "Delta activity". In this model, the Delta activity in a cell i is repressed by the Notch activity, and this in turn is activated by the averaged levels of ligand activity in the neighboring cells. The model equations read

$$\frac{\mathrm{d}s_i}{\mathrm{d}t} = f\left(\langle l_i \rangle\right) - s_i \tag{1.1a}$$

$$\frac{\mathrm{d}l_i}{\mathrm{d}t} = v\left\{g(s_i) - l_i\right\} \quad , \tag{1.1b}$$

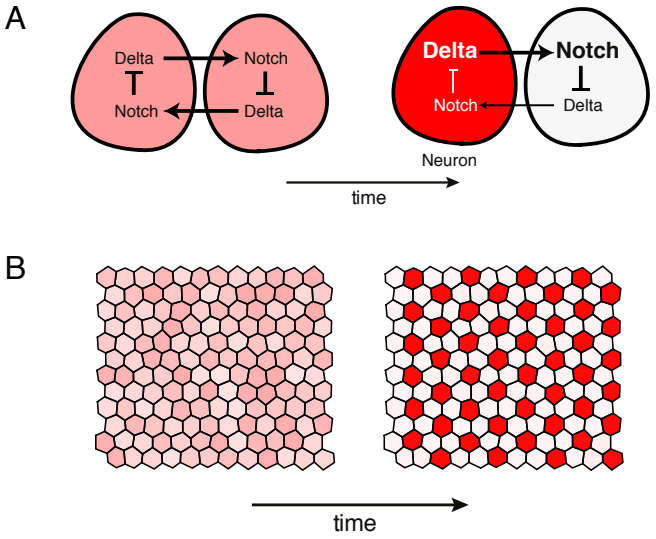

Figure 1.5: Fine-grained patterning through lateral inhibition. (A) Mutual lateral inhibition between neighboring cells drives an intercellular positive feedback loop. The positive feedback amplifies small initial differences between cells that are initially equivalent (left) leading to two mutually exclusive fates (right). Bigger (smaller) size of the letters inside cells refer to higher (lower) amount of activity. Red intensity is related to the amount of ligand concentration: high ligand cells are red, while cells without ligand are white. (B) Lateral inhibition acting on a tissue of equivalent precursors with small variability (left) leads to an ordered salt-and-pepper pattern of two cell types (right). Snapshots from simulation results showing the emergence of the pattern. Simulation results from the Collier model (Eqs. 1.1) in an irregular array of cells (Eq. 2.9) with periodic boundary conditions. At the onset of differentiation all cells have equivalent amounts of Notch and Delta activity levels (left), what results in a pattern of high-Delta and low-Notch fated cells surrounded by low-Delta and high-Notch fated cells (right). We call this the normal lateral inhibition pattern because this is the one typically found in nature.

where l_i and s_i are the Delta and Notch activity levels in the i-cell, $\langle l_i \rangle$ is the cell-to-cell coupling term, and it stands for the averaged ligand activity in cells neighboring cell i,

$$\langle l_i \rangle = \frac{1}{\omega} \sum_{j \in nn(i)} l_j \quad , \tag{1.2}$$

being ω the coordination number, *i.e.* the number of first neighbors in the cell array ($\omega = 6$ in a hexagonal array), and $j \in nn(i)$ refers to all j cells neighboring to cell i. The regulatory functions g and f are Hill functions defined as

$$f\left(\langle l_i \rangle\right) = \frac{\langle l_i \rangle^k}{a + \langle l_i \rangle^k}, \quad g(s_i) = \frac{1}{1 + b s_i^h} \quad . \tag{1.3}$$

a is related to the ligand activity required in neighboring cells for Notch activity activation in cell i, b controls the strength of Delta activity inhibition by the Notch activity (the higher b, the stronger the inhibition), k and h are the Hill exponents accounting for the cooperativities for the activation due to f and repression due to g, respectively, and v is the ration between the degradation rate of the Delta activity divided by the degradation of Notch activity.

In this model, small differences in activity between neighboring cells are amplified through the intercellular positive feedback (Fig. 1.5 (A)). As a consequence, if cell-to-cell coupling is strong enough, cells with high Delta activity (and low Notch) are surrounded by cells with low Delta activity (and high Notch), resulting in an ordered salt-and-pepper pattern (Fig. 1.5 (B)), what we call the normal lateral inhibition pattern. This model showed for the first time the lateral inhibition patterning as a linear instability of a homogeneous precursor state (Sec. 1.1.2).

After Collier model, other theoretical models have been proposed for studying lateral inhibition [100–112], addressing different kinds of theoretical questions, *e.g.* the effect of delays [108, 113] or the effect of noise [110] in lateral inhibition dynamics. Some of these studies were based on a model proposed by Owen *et al.* [100] in which the kinetics of receptors and ligands are taken into account. This model has three dynamical equations per cell, where the free Notch receptor, the free ligand and the complex are modeled [101, 103, 104, 106–108, 110]. Following this theoretical scope, it has been recently found that both Collier and Owen models admit patterned traveling waves as solutions [104, 109]. Recently, some theoretical papers have focused on this aspect [**?**, 111, 112].

Just recently, other works have presented a stronger link with experiments, addressing more specific questions of the pathway and being more quantitative. For instance, Cohen *et al.* with a variation of the Collier model have found that that dynamic filopodia are pivotal for refinement in pattern formation of the bristles in *Drosophila* [114]. Sprinzak *et al.* have studied from a more Synthetic Biology perspective Notch signaling. In particular, they address the question of what happens if Notch and Delta bind in the same cell [47]. In this work they propose different kinetic models that allow to reproduce the dynamical behavior of their engineered Notch-Delta circuits. Some of their models are reduced to three equations per cell, in which the dynamics of the ligand, the receptor, and the Notch intracellular domain (NICD) are modeled, and in some cases there is also a variable accounting for the response of the NICD.

Other theoretical works have addressed different pattern formation phenomena — different from the salt-and-pepper patterning — in which Notch mediated cell-to-cell communication is also important. For instance, mathematical models have been proposed for studying boundary formation [47, 66], and somitogenesis [8, 14, 86, 87, 115].

1.6 New challenges in lateral inhibition

The lateral inhibition model by Collier and colleagues provides a key mechanism for salt-and-pepper patterning. Though, different elements participating in the Notch pathway also seem to have an important role in the pattern formation emergence, challenging the classical mechanism proposed by Collier *et al.* [10] and making this phenomenon a richer and more variate process, as we pointed out in Sec. 1.4. In this section we mention some of these challenges that have motivated the different works addressed in this Thesis.

The particular dynamics of the pattern emergence is something that has started being studied. One of the most well studied cases is the differentiation of the first neural types in the retina of vertebrate and invertebrate embryos (Fig. 1.4 (B)). In these cases, pattern emergence starts in a localized and well defined part of the tissue and spreads towards the rest of the tissue, defining what is called a differentiation wavefront. Genetic studies have already revealed different key points of how these differentiation wavefronts are regulated. In par-

ticular, it is known that diffusible morphogens have an important regulatory role on how these patterns progressively move forward in the tissues. There is a lot less known about specific mechanisms that confer robustness to these wavefronts, and in particular it is not known what makes so robust the lateral inhibition process at the edges of the wavefronts. In this Thesis we address this question in the context of neurogenesis in the embryonic vertebrate retina and invertebrate eye (Chap. 3).

There are several elements and interactions taking place in the Notch pathway whose roles still remain obscure and could have a high impact on patterning. In particular, it is known that ligands can also travel through the extracellular space [74, 116–120], what suggests another way of cell-to-cell communication. Also, there are numerous evidences that ligands can bind with receptors inside the same cell, a phenomenon that has been named as cis-interactions [47,121–129], while its particular function is starting to be unveiled [47, 49, 90, 105, 130]. These two different aspects rise the questions of whether a diffusible transport and cis-interactions can modify the pattern formation capabilities of the system. These two aspects are treated in depth in Chaps. 4 and 5.

Notch appears to have antagonistic roles in some systems. For instance, in the sensory organs of vertebrate embryos, it is known that Notch first has a lateral inductive role, leading patches of cells being competent for differentiating into a sensory cell type, and afterwards has a lateral inhibitory role, in which just some of the cells are finally selected for differentiating into such sensory type. The precise mechanism of how lateral induction and lateral inhibition are achieved in the vertebrate inner ear still remains elusive, and also, how in the same system the two operating modes can sequentially take place. In this Thesis we do not focus on how precisely these two antagonistic operating modes are regulated, but we study the transition between them in the context of the chick embryonic inner ear (Chap. 6).

For addressing all these questions, we use a phenomenological model of a few ordinary differential equations per cell. In particular, we extend the Collier model through the inclusion of the different components of interest. For doing that, we combine phenomenological Hill functions and other terms with a more direct chemical-based kinetics. Our simple models enable some analytical treatment. The low dimensionality and number of parameters facilitates the performance of

simulations across the parameter space. We include some more realistic aspects into our models for checking its robustness: dynamical noise and irregularity on the cellular array. We expect to have robust effects of the observed behaviors, without the necessity of fine-tuning in the parameter space.

Before addressing our particular questions, we start with a methodological chapter (Chap. 2), in which we present in depth the different technical aspects that are going to be used in this Thesis.

Chapter 2

Methods

Throughout this Thesis we deal with different models accounting for the lateral inhibition phenomena. For avoiding repetition, this chapter introduces the bases of the analytical and numerical methods used in these models. This will enable a more direct application of the methodology in the following chapters, facilitating the focus on the achieved results and on the discussions.

This chapter is structured as follows. First, in Sec. 2.1 we provide an interpretation of the Collier model that will enable to extend the model properly for addressing the different aspects we are interested in relation to Notch signaling and patterning. In Sec. 2.2 we define the regulatory roles between different components in a genetic regulatory network. In Sec. 2.3 we show how we introduce dynamical noise in these kind of deterministic models. Next, in Sec. 2.4 we introduce the linear stability analysis technique (LSA), which enables to predict when a pattern spontaneously emerge from a homogeneous state of equivalent cells. This technique is standard and has already been described in the kind of models we are interested in, but still it is instructive to rewrite it in our own way, stressing the points that are important for us. Afterwards, in Sec. 2.5 a new method we developed is presented, which enables to compute the exact solutions of the forming patterns. We will frequently refer to that as the reduced model. In Sec. 2.6 we sketch the methods that we have been using for finding the solution of algebraic equations, what has been used for computing the steady states of the dynamics and for compute the pattern solutions in a systematic way. In

Sec. 2.7 we present how stability of the pattern solutions is determined. Then, in Sec. 2.8 we describe two different tools we use for the characterization of the pattern emergence: an order parameter, and the structure function. In Sec. 2.9, we briefly explain some issues regarding the numerical simulations. Last, Sec. 2.10 is used for revising the Collier model by using the techniques presented in this chapter, what leads to new results necessary for a better understanding of the following chapters.

2.1 Model interpretation

Collier model was proposed as a phenomenological model to describe the dynamics of Delta and Notch activities. As we show in Secs. 1.5 and 2.10, this simplified model already captures some fundamental aspects of the lateral inhibition dynamics.

Herein we present an interpretation of the Collier model that facilitates its generalizations in a consistent way for studying other components of the pathway that can contribute to Notch signaling. In this Thesis, the Collier model is generalized by including a diffusible ligand in the dynamics (Chap. 4), by including cis-interactions between ligands and receptors within the same cell (Chap. 5), and by integrating two Notch ligands in the model (Chap. 6).

A dimensional equation of the Notch signal concentration, what would correspond to the NICD (Sec. 1.3.2), can be understood as a production term minus a typical linear degradation term of the signal concentration. If we assume that the production term is proportional to the equilibrium concentration of the complex formed due to trans-interactions (*i.e.* the interactions resulting from the binding and unbinding between receptors and ligands anchored in neighboring cells) and that the total Notch receptor amount is conserved in this process, we obtain the equation for the Notch signal proposed by Collier.

Specifically, let's assume the Notch receptor in a i-cell, whose concentration is denoted by N_i, can reversibly trans-interact with the Notch ligand (Delta or Jagged) in the j neighboring cell L_j (Eq. 2.1), forming a complex whose concentration is denoted by C_i. The resulting complex elicit the Notch signal S_i towards the cell that is harboring the receptor (Eq. 2.1). Thus, the chemical

reactions accounting for these processes would be

$$N_i + L_j \underset{k_{-b}}{\overset{k_b}{\rightleftharpoons}} C_i \xrightarrow{k_s} S_i + C_i \quad . \tag{2.1}$$

Note that in these reactions, we assume that both Notch receptor and ligand are conserved[1]. We hypothesize that the total receptor concentration per cell is equal for all the cells, so a conservation equation can be written as

$$N_{tot} \equiv N \quad = \quad N_i + C_i \quad , \tag{2.2}$$

being N the total amount of receptor concentration in every i-cell. If we assume that the ligand is homogeneously distributed in the cell, the equilibrium concentration of the complex due to trans-interactions reads

$$C_i \quad = \quad K_b N_i \langle L_i \rangle \quad , \tag{2.3}$$

where $K_b = k_b/k_{-b}$ is the equilibrium constants of the kinetics of binding-unbinding of the receptor-ligand placed in two neighboring cells, what we call trans-affinity constant. By using the conservation Eq. 2.2 and Eq. 2.3 we get

$$C_i \quad = \quad \frac{K_b N \langle L_i \rangle}{1 + K_b \langle L_i \rangle} \quad , \tag{2.4}$$

where $\langle L_i \rangle$ is the average of ligand concentration in neighboring cells (*i.e.* the dimensional version of Eq. D.2). By using the Mass Action law, the equation of the Notch signal in a i-cell can be written as

$$\frac{\mathrm{d}S_i}{\mathrm{d}\tau} \quad = \quad k_s C_i - \nu_s S_i \quad , \tag{2.5}$$

where τ is the dimensional time, ν_s is the signal degradation rate, and C_i is the equilibrium complex concentration, so by plugging 2.4 into 2.5 we obtain the dimensional equation for the Notch signal,

$$\frac{\mathrm{d}S_i}{\mathrm{d}\tau} \quad = \quad \frac{k_s N K_b \langle L_i \rangle}{1 + K_b \langle L_i \rangle} - \nu_s S_i \quad . \tag{2.6}$$

[1]Notch conservation does not happen in real conditions since the trans-complex is cleaved when it releases the Notch signal, but this simplification helps us to obtain a more treatable model. The Notch proteolytic cleavage is considered in a more realistic model (Sec. 5.3.7) and we see that this simplification does not affect our main results.

For the dynamics of the ligand concentration, we use the Collier dimensional version of the ligand equation, in which there is a linear degradation term and a production term that is modulated due to the Notch signal in the same cell, what inhibits the production of further ligand. In particular, such ligand production term in the i-cell can be represented by a decreasing Hill function of the signal in such cell. Overall, the dimensional equation for the ligand can be written as

$$\frac{\mathrm{d}L_i}{\mathrm{d}\tau} = \frac{\beta_l}{1+K_p S_i^h} - \nu_l L_i \quad , \tag{2.7}$$

where β_l the effective basal production of the ligand when it is not inhibited, h is what is called a cooperativity exponent, accounting with the nonlinearity that represents the multistep process from NICD release until ligand inhibition (see Sec. 1.3.2), and K_p is related to the threshold for ligand inhibition, being K_p^{-h} the signal amount required for decreasing ligand production to a half.

We adimensionalize our dynamical equations by doing $S_i = S_0 s_i$, $L_i = L_0 l_i$, $\tau = T_0 t$ where s_i, l_i are the new non-dimensional variables for the signal and the ligand, and t is the adimensional time. Herein we choose S_0, L_0 and T_0 as $S_0 = \frac{k_s N}{\nu_s}$, $L_0 = \beta_l/\nu_l$ and $T_0 = 1/\nu_s$. Then, the system reads

$$\frac{\mathrm{d}s_i}{\mathrm{d}t} = \frac{r_t \langle l_i \rangle}{1+r_t\langle l_i\rangle} - s_i \tag{2.8a}$$

$$\frac{\mathrm{d}l_i}{\mathrm{d}t} = v\left\{\frac{1}{1+b s_i^h} - l_i\right\} \quad , \tag{2.8b}$$

being $r_t = K_b L_0$, $b = K_p S_0^h$, and $v = \nu_l/\nu_s$. Note that we completely recover the Collier model but with Michaelis-Menten dynamics in the equation for the Notch activity instead of a Hill function with a certain degree of cooperativity [10]. Throughout this Thesis we do not consider cooperativity in the equation for the signal production, since our formulation is more consistent with a scenario in which the trans-interactions consist on one ligand binding to one receptor. Moreover, recent experimental results by Sprinzak *et al.* showed that a gradual increase of trans-interactions elicits a graded response in a Notch reporter, what is consistent with this modeling approach [47]. Our r_t parameter is equivalent to $1/a$ defined in the Collier model (see Eqs. 1.1, D.3). In this chemical derivation we find that r_t is related to the ligand to receptor affinity and gives the strength of trans-interactions. For simplicity, we call r_t as the trans-interactions strength

parameter, or more explicitly, ligand-mediated trans-interaction parameter. b now is related to the amount of dimensional signal elicited by trans-interactions, and the ligand inhibition strength. For this reason b is called signaling strength or inhibition strength parameter.

Since cells generally present more irregular shapes than regular hexagons, it's worth studying lateral inhibition patterning in an irregular array of cells. Additionally, this is a way to check the robustness of our results. As a first approximation to deal with more realistic tissues, we make use of the Voronoi tesselation for the construction of such arrays (see Sec. 2.9.2 for details) [98, 99]. In this context, the cell-to-cell coupling term in an irregular array of cells reads

$$\langle l_i \rangle \quad = \quad \sum_{j \in nn(i)} \alpha_{ij} l_j \quad , \tag{2.9}$$

where α_{ij} is the cell-to-cell coupling coefficient in an irregular cell lattice and is defined as

$$\alpha_{ij} = \frac{e_{ij}}{\sum_{j \in nn(i)} e_{ij}} \quad , \tag{2.10}$$

being e_{ij} the length of the edge shared by adjacent cells i and j [131]. Eq. 2.9 assumes that the ligand is distributed homogeneously along the cell membranes and takes into account that trans-interactions between two adjacent cells is proportional to the contact length of the membrane between such adjacent cells.

A more chemical-based approach can be adopted in which one assumes a transcriptional activation of the ligand promoter through a reversible binding of the signal with the promoter. In this case, a rigorous adiabatic reduction would lead to Eq. 2.6 with an additional prefactor on its right hand side that would also depend on the signal concentration. Though, in this more elaborated formulation we would still find the steady state of the dynamics for our Eq. 2.6. This approach would also naturally lead to a decreasing Michaelis Menten function in the equation of the ligand.

On the other side, the binding-unbinding kinetics due to the trans-interactions can be also included in the ligand equation and in a dynamical equation for the complex. In Sec. 5.3.7 we see that the inclusion of such kinetics does not affect our main results. Note that a more rigorous adiabatic reduction taking into account the full binding-unbinding kinetics would not result in the Collier model, but in a much more complicated model difficult to handle with.

2.2 Characterization of inhibitory/activatory regulatory roles

Regulation between different chemical species is ubiquitous within the cell. For instance, the rise of a certain protein can trigger the extinction or the overproduction of another protein. Herein we formalize the definition of the two basic regulatory roles: activation and inhibition

Generally speaking, the evolution of any molecular species x can be written as

$$\frac{\mathrm{d}x}{\mathrm{d}t} = F_x \quad , \tag{2.11}$$

where F_x is the regulatory function associated to the chemical species x, what usually depends on different variables. We say that a variable has an activatory or inhibitory role on x if this enhances or depletes the production rate F_x.

In order to characterize this aspect, we define the the role of y on x, $\mathscr{R}$, as the partial derivative of the production of x with respect to y:

$$\mathscr{R}_{x,y} = \frac{\partial}{\partial y}\frac{\mathrm{d}x}{\mathrm{d}t} = \frac{\partial F_x}{\partial y} \quad . \tag{2.12}$$

Then, $\mathscr{R}_{x,y} > 0$ denotes activation of x by y, while $\mathscr{R}_{x,y} < 0$ denotes inhibition. Often, F_x depends on x trough the typical linear term denoting degradation. In these cases, $\mathscr{R}_{x,y} \propto \frac{\partial}{\partial y} x_{st}$ being x_{st} the steady state solution for the x species, meaning that activation or inhibition can be also understood of as an enhancement or depletion of the steady state of x when y is increased.

During this Thesis, we address both intracellular and intercellular regulation roles. Then, the regulatory roles with respect to a chemical species x in a cell i are characterized by

$$\mathscr{R}_{x_i,y_k} = \frac{\partial}{\partial x_k}\frac{\mathrm{d}y_i}{\mathrm{d}t} \quad , \tag{2.13}$$

where $k = i$ in the case of intracellular interactions and $k \neq i$ in the case of intercellular interactions. With respect to trans-interactions, we say that y trans-activates or trans-inhibits x if $\mathscr{R}_{x_i,y_k} > 0$ or $\mathscr{R}_{x_i,y_k} < 0$ respectively, being k the index of a neighboring cell to cell i.

We typically evaluate the role of different regulatory elements at the onset of the pattern formation when the precursor state exhibits low variability, and therefore at the homogeneous steady state of the system.

The state of the other regulatory elements in the network can modify the type of regulatory effect of the x species over y. Then, the regulation of x_i by y_i can change in the presence of a third species z_i, so that $\mathscr{R}_{x_i,y_i}(z_i = 0)$ and $\mathscr{R}_{x_i,y_i}(z_i > 0)$ do not forcely have the same sign. For this reason, we call the effective role of x over y. We use this concept of effective regulation in Chaps. 5 and 6.

2.3 Adding noise to lateral inhibition dynamics

Throughout the study of Notch signaling in this Thesis, stochastic nature of gene expression arising from low copy number molecules has been included by extending the deterministic dynamics for its molecular species to the Langevin dynamics in the Itô interpretation [132–134]. Note that the modeling equations for ligand (l_i) and the signal (s_i) consist of a production (synthesis) term minus a degradation term. For these kind of modeling equations, the stochastic version for any molecular species x_i whose dynamics consist on a production and degradation term, what we write as F^+_{xi} and F^-_{xi}, would read

$$\frac{\mathrm{d}x_i}{\mathrm{d}t} = F^+_{xi} - F^-_{xi} + \sqrt{\frac{F^+_{xi} + |F^-_{xi}|}{2V}}\eta_{xi}(t) \quad , \tag{2.14}$$

where V is an effective volume of the cell and $x_i(t)$ are stochastic variables of mean zero and variance $\langle \eta_{xi}(t)\eta_{x'j}(t')\rangle = 2\delta_{xx'}\delta_{ij}\delta(t-t')$ (i.e., uncorrelated Gaussian white noises), being $\delta_{xx'}$ the Kronecker delta and $\delta(t-t')$ the delta functions [132–134]. In this approach where noise appears as a multiplicative term, the size of the fluctuations depends on the level of the state variables, instead of what happens when an additive noise is included.

The coefficient of variation of the modeled variables, which is defined as its standard deviation divided by its mean, decreases as the effective cell volume V is increased, recovering the deterministic limit.

Applying Eq. 2.14 formulation to the Collier model (Eqs. 2.8), the resulting equations read

$$\frac{\mathrm{d}s_i}{\mathrm{d}t} = \frac{r_t\langle l_i\rangle}{1+r_t\langle l_i\rangle} - s_i + \sqrt{\left(\frac{r_t\langle l_i\rangle}{1+r_t\langle l_i\rangle} + s_i\right)\frac{1}{2V}}\eta_{s_i} \tag{2.15a}$$

$$\frac{\mathrm{d}l_i}{\mathrm{d}t} = v\left\{\frac{1}{1+bs_i^h} - l_i\right\} + \sqrt{v\left\{\frac{1}{1+bs_i^h} + l_i\right\}\frac{1}{2V}}\eta_{l_i} \quad . \tag{2.15b}$$

Recent works have treated other ways to implement noise in the lateral inhibition dynamics [110,114,130]. For instance, Rudge and Burrage accounted with dynamic noise coming from either the stochastic nature of the chemical reactions or in the variable production rates of the genetic products [110], while Sprinzak et al. used spatial static noise in the production rates [130] and [114]. In our approach, spatial static noise has been also effectively included in our equations when we deal with irregular arrays, and dynamic noise has been included in a more generic way, without dealing in particular with the chemical equations and the production rates of every molecular species. This more generic approach will be enough for checking the robustness of some of our main results.

2.4 Linear stability analysis (LSA)

The classical view of lateral inhibition is that patterning starts emerging in a field of equivalent undifferentiated cells [10]. Therefore, the initial state of the modeled tissue, what we also refer as the precursor state, can be understood as a tissue having all cells exhibiting more or less the same phenotype in terms of its concentration variables. For this reason, we set the initial state across the modeled tissue to be homogeneous with small fluctuations, accounting for the cell-population variability.

Linear stability analysis (LSA) over the homogeneous state[2] allows us to make analytic predictions about how this homogeneous precursor state becomes unstable to small fluctuations, enabling spontaneous patterning. On one side, LSA will tell us in which regions of the parameter space spontaneous patterning occurs.

[2]When we refer just to LSA, by default we mean it is performed over the homogeneous state, and not over the pattern state.

These regions are going to be delimited by what we call LSA critical lines. On the other side, LSA indicates which is the typical spacing between the cells with high ligand expression, what we call the characteristic length of the pattern or pattern wavelength. Such predicted pattern feature comes from the identification of the mode that has a fastest growing rate when the homogeneous mode is unstabilized, what is called the fastest growing mode. The fastest growing mode will be indicative of the resulting pattern when the system behaves linearly in the parameter space[3].

Herein we describe the general method of LSA in a discrete cell lattice with periodic boundary conditions, that is going to be used through this Thesis. This methodology can be found in different resources [10, 25, 106, 135] and more generally in its continuous version in space [3, 5, 25]. Herein we focus on the regular hexagonal cell lattice, but it can be easily generalized to other regular lattices.

Let's define a dynamical system over a regular array of cells with periodic boundary conditions and isotropic interactions to first neighbors, having $n = 2$ variables per each i-cell, x_i and y_i. Our dynamical system with first neighbor interactions can be written as

$$\frac{\mathrm{d}x_i}{\mathrm{d}t} = F_x(x_i, \{x_{i'}\}, y_i, \{y_{i'}\}) \tag{2.16a}$$

$$\frac{\mathrm{d}y_i}{\mathrm{d}t} = F_y(x_i, \{x_{i'}\}, y_i, \{y_{i'}\}) \quad , \tag{2.16b}$$

where i' is referring to the first neighbors of the cell i, being $\{x_{i'}\}$ and $\{y_{i'}\}$ the set of all the variables defined in such i'-neighboring cells. F_x and F_y are specific functions of these variables. In a system of $N \times M$ cells, we are dealing with $n \times N \times M$ coupled ordinary differential equations, being $n = 2$ variables per cell in this case.

The first thing to be done is to find the homogeneous steady state of the system (x_0, y_0), what represents the precursor undifferentiated state. This corresponds to find the solution of the system 2.16 by imposing $\frac{\mathrm{d}x_i}{\mathrm{d}t} = \frac{\mathrm{d}y_i}{\mathrm{d}t} = 0$ and $x_i = x_0$

[3]Normally, the pattern wavelength is well predicted by LSA if we are close to the critical line predicted from LSA, and if the pattern formation transition is supercritical [5], *i.e.* the pattern amplitude gradually grows at the critical line. Even if we are not in these situations, LSA can be a starting point.

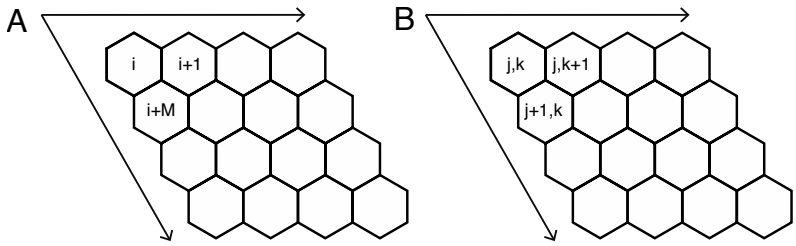

Figure 2.1: Arrays of $N \times M$ perfect hexagonal cells with the subindex labeling schemes used that number each cell along the array. In (A) one subindex is used, while in (B) we use two subindices. The two main spatial directions of the cellular array are depicted.

and $y_i = y_0$ for every i-cell, *i.e.*

$$0 = F_x(x_0, \{x_0\}, y_0, \{y_0\}) \tag{2.17a}$$
$$0 = F_y(x_0, \{x_0\}, y_0, \{y_0\}) \quad . \tag{2.17b}$$

Normally, this can not be solved analytically, and one has to use a root-finding algorithm for doing so [136] (Sec. 2.6).

Then, we linearize the dynamical system around these solutions, *i.e.* we perform a Taylor expansion of the dynamical system around the homogeneous point until first order. Thus, we do the change of variables $x_i = x_0 + \widetilde{x_i}$ and $y_i = y_0 + \widetilde{y_i}$ into Eqs. 2.16, where $\widetilde{x_i}$ and $\widetilde{y_i}$ are small, what leads to

$$\begin{aligned} &\frac{\mathrm{d}}{\mathrm{d}t}\begin{pmatrix} x_0 \\ y_0 \end{pmatrix} + \frac{\mathrm{d}}{\mathrm{d}t}\begin{pmatrix} \widetilde{x_i} \\ \widetilde{y_i} \end{pmatrix} \simeq \\ &\simeq \begin{pmatrix} f(x_0, \{x_0\}, y_0, \{y_0\}) \\ g(x_0, \{x_0\}, y_0, \{y_0\}) \end{pmatrix} + J_0 \begin{pmatrix} \widetilde{x_i} \\ \widetilde{y_i} \end{pmatrix} + J_1 \begin{pmatrix} \sum_{i'} \widetilde{x_{i'}} \\ \sum_{i'} \widetilde{y_{i'}} \end{pmatrix} , \end{aligned} \tag{2.18}$$

where J_0 and J_1 are the matrices

$$J_0 = \left.\begin{pmatrix} \frac{\partial F_x}{\partial x_i} & \frac{\partial F_x}{\partial y_i} \\ \frac{\partial F_y}{\partial x_i} & \frac{\partial F_y}{\partial y_i} \end{pmatrix}\right|_{x_0, y_0} , \quad J_1 = \left.\begin{pmatrix} \frac{\partial F_x}{\partial x_{i'}} & \frac{\partial F_x}{\partial y_{i'}} \\ \frac{\partial F_y}{\partial x_{i'}} & \frac{\partial F_y}{\partial y_{i'}} \end{pmatrix}\right|_{x_0, y_0} , \tag{2.19}$$

where i' refers to first neighbors to the cell i. Note that this can be done because we are dealing with a dynamical system defined in a regular array of cells

with periodic boundary conditions with isotropic cell-to-cell interactions to first neighbors. From the definition of (x_0, y_0) and using Eqs. 2.17-2.18 it leads to

$$\frac{\mathrm{d}}{\mathrm{d}t}\begin{pmatrix}\widetilde{x_i}\\ \widetilde{y_i}\end{pmatrix} \simeq J_0\begin{pmatrix}\widetilde{x_i}\\ \widetilde{y_i}\end{pmatrix} + J_1\begin{pmatrix}\sum_{i'}\widetilde{x_{i'}}\\ \sum_{i'}\widetilde{y_{i'}}\end{pmatrix} \quad . \tag{2.20}$$

In the particular case of a hexagonal array of $N \times M$ cells (Fig. 2.1), the perturbations $\widetilde{x_i}$ and $\widetilde{y_i}$ can be written as a discrete Fourier series

$$\widetilde{x_i} \equiv \widetilde{x_{j,k}} = \sum_{\bar{q}}\sum_{\bar{p}} \sigma^x_{\bar{q},\bar{p}} e^{2\pi\mathrm{i}(\bar{q}j+\bar{p}k)+\alpha_{\bar{q},\bar{p}}t} \tag{2.21a}$$

$$\widetilde{y_i} \equiv \widetilde{y_{j,k}} = \sum_{\bar{q}}\sum_{\bar{p}} \sigma^y_{\bar{q},\bar{p}} e^{2\pi\mathrm{i}(\bar{q}j+\bar{p}k)+\alpha_{\bar{q},\bar{p}}t} \quad , \tag{2.21b}$$

where two subindexes j, k have been used to refer to the spatial position of cell i within the two-dimensional hexagonal cell lattice (Fig. 2.1). $\bar{q}$ and $\bar{p}$ are proportional to the wavenumbers along the natural axis in a two-dimensional hexagonal lattice, and are defined as $\bar{q} = q/N$, $\bar{p} = p/M$ being $q = 1, ..., N$ and $p = 1, ..., M$, so the first and second sums are performed over $\bar{q} = 1/N, 2/N, ..., 1$ and $\bar{q} = 1/M, 2/M, ..., 1$. Note that the ansatz solutions 2.21 contain an exponential growth in time of these modes at rate $\alpha_{\bar{q},\bar{p}}$. We refer to the couple of indices $(\bar{q}, \bar{p})$ as a particular Fourier mode. The inverted transform is

$$\sigma^x_{\bar{q},\bar{p}} = \frac{1}{NM}\sum_j\sum_k \widetilde{x_{j,k}} e^{-2\pi\mathrm{i}(\bar{q}j+\bar{p}k)-\alpha_{\bar{q},\bar{p}}t} \tag{2.22a}$$

$$\sigma^y_{\bar{q},\bar{p}} = \frac{1}{NM}\sum_j\sum_k \widetilde{y_{j,k}} e^{-2\pi\mathrm{i}(\bar{q}j+\bar{p}k)-\alpha_{\bar{q},\bar{p}}t} \quad . \tag{2.22b}$$

In the Fourier space, the first neighbors contribution can be written as[4]

[4]By doing

$$\sum_{i'}\widetilde{x_{i'}} = \widetilde{x_{j,k+1}} + \widetilde{x_{j,k-1}} + \widetilde{x_{j+1,k}} + \widetilde{x_{j-1,k}} + \widetilde{x_{j-1,k+1}} + \widetilde{x_{j+1,k-1}} =$$

$$\sum_{\bar{p}}\sum_{\bar{q}} \sigma^x_{\bar{q},\bar{p}} \left(e^{2\pi\mathrm{i}(\bar{q}j+\bar{p}(k+1))+\alpha_{\bar{q},\bar{p}}t} + e^{2\pi\mathrm{i}(\bar{q}j+\bar{p}(k-1))+\alpha_{\bar{q},\bar{p}}t} + e^{2\pi\mathrm{i}(\bar{q}(j+1)+\bar{p}k)+\alpha_{\bar{q},\bar{p}}t} + \right.$$

$$\left. e^{2\pi\mathrm{i}(\bar{q}(j-1)+\bar{p}k)+\alpha_{\bar{q},\bar{p}}t} + e^{2\pi\mathrm{i}(\bar{q}(j-1)+\bar{p}(k+1))+\alpha_{\bar{q},\bar{p}}t} + e^{2\pi\mathrm{i}(\bar{q}(j+1)+\bar{p}(k-1))+\alpha_{\bar{q},\bar{p}}t}\right)$$

, taking out the common factor and doing likewise for the y variable we get to Eqs. 2.23.

$$\sum_{i'} \widetilde{x_{i'}} = \sum_{\bar{p}} \sum_{\bar{q}} \omega \Omega_{\bar{q},\bar{p}} \sigma^{x}_{\bar{q},\bar{p}} e^{2\pi \mathrm{i}(\bar{q}j+\bar{p}k)+\alpha_{\bar{q},\bar{p}}t} \tag{2.23a}$$

$$\sum_{i'} \widetilde{y_{i'}} = \sum_{\bar{p}} \sum_{\bar{q}} \omega \Omega_{\bar{q},\bar{p}} \sigma^{y}_{\bar{q},\bar{p}} e^{2\pi \mathrm{i}(\bar{q}j+\bar{p}k)+\alpha_{\bar{q},\bar{p}}t} \quad , \tag{2.23b}$$

being $\omega = 6$ the number of first neighbors in a hexagonal cell lattice, and $\Omega_{\bar{q},\bar{p}}$ the function that takes into account the isotropic spatial coupling terms within the hexagonal cell lattice [5]

$$\Omega_{\bar{q},\bar{p}} = \frac{1}{3}\left\{\cos(2\pi\bar{q}) + \cos(2\pi\bar{p}) + \cos(2\pi(\bar{p}-\bar{q}))\right\} \quad . \tag{2.24}$$

Given that our system is discrete and finite, $\Omega_{\bar{q},\bar{p}}$ takes discrete values within the interval $[-0.5, 1]$. Moreover, $\Omega_{\bar{q},\bar{p}}$ is a surjective function, *i.e* different $(\bar{q},\bar{p})$ modes can give rise to the same Ω[6]. For this reason, any function $F(\Omega_{\bar{q},\bar{p}})$ can be equivalently written as $F(\Omega)$. Thus, we refer to a certain Ω as the family of all the couples $(\bar{q},\bar{p})$ having the same Ω. Note that $\Omega = 0$ would correspond to the homogeneous mode, while $-0.5 \leq \Omega < 1$ would correspond to non-homogeneous mode families. This Ω function will be widely used through this Thesis.

The linearized system of differential equations 2.20 can be rewritten in the Fourier space as

$$\sum_{\bar{p}} \sum_{\bar{q}} \alpha_{\bar{q},\bar{p}} e^{2\pi \mathrm{i}(\bar{q}j+\bar{p}k)+\alpha_{\bar{q},\bar{p}}t} \sigma_{\bar{\mathbf{q}},\bar{\mathbf{p}}} = \sum_{\bar{p}} \sum_{\bar{q}} (J_0 + \omega J_1 \Omega_{\bar{q},\bar{p}}) e^{2\pi \mathrm{i}(\bar{q}j+\bar{p}k)+\alpha_{\bar{q},\bar{p}}t} \sigma_{\bar{\mathbf{q}},\bar{\mathbf{p}}} \quad , \tag{2.25}$$

being $\sigma_{\bar{\mathbf{q}},\bar{\mathbf{p}}} = \begin{pmatrix} \sigma^{x}_{\bar{q},\bar{p}} \\ \sigma^{y}_{\bar{q},\bar{p}} \end{pmatrix}$. Notice that different modes are not coupled because of linearization, so we can end up in just two coupled algebraic equations per each

[5] See Fig. 2.1 for the cell labeling scheme. If the orientation of one of the axis is inverted with respect to Fig. 2.1 we obtain the equivalent function $\Omega_{\bar{q},\bar{p}} = \frac{1}{3}\left\{\cos(2\pi\bar{q}) + \cos(2\pi\bar{p}) + \cos(2\pi(\bar{p}+\bar{q}))\right\}$.

[6] For a one line of cells with periodic boundary conditions it can be shown that Eqs. 2.23 are also valid with $\omega = 2$ but with a different Ω function given by $\Omega_{\bar{q}} = \cos(2\pi\bar{q})$, so in the line of cells $\Omega \in [-1, 1]$.

existing $(\bar{q},\bar{p})$-mode[7] :

$$\alpha_{\bar{q},\bar{p}}\sigma_{\bar{\mathbf{q}},\bar{\mathbf{p}}} \quad = \quad \mathscr{M}\sigma_{\bar{\mathbf{q}},\bar{\mathbf{p}}} \quad , \tag{2.26}$$

where matrix $\mathscr{M}$ reads

$$\mathscr{M} \quad = \quad J_0 + \omega J_1 \Omega_{\bar{q},\bar{p}} \quad . \tag{2.27}$$

In order to solve the system of Eqs. 2.26, we have to diagonalize the $\mathscr{M}$ matrix, what will uncouple the two equations. For doing so, we have to find the roots of the characteristic polynomial by solving $P(\alpha_{\bar{q},\bar{p}},\Omega) = \det\left(\mathscr{M} - I\alpha_{\bar{q},\bar{p}}\right) = 0$, being I the identity matrix and $\alpha_{\bar{q},\bar{p}}$ the eigenvalues of $\mathscr{M}$. We refer to the expression of the eigenvalues $\alpha_{\bar{q},\bar{p}}$ with respect to $(\bar{q},\bar{p})$ or Ω as dispersion relation.

In a system with two variables per cell, the characteristic polynomial is of second order. As a consequence, each couple $(\bar{q},\bar{p})$ has two eigenvectors and eigenvalues. In this case, the perturbations grow as

$$\begin{pmatrix} \widetilde{x_{j,k}} \\ \widetilde{y_{j,k}} \end{pmatrix} = \sum_{\bar{p}}\sum_{\bar{q}} e^{2\pi(\bar{q}j+\bar{p}k)} \times \left\{ \begin{pmatrix} A^{+}_{\bar{q},\bar{p}} \\ B^{+}_{\bar{q},\bar{p}} \end{pmatrix} e^{\alpha^{+}_{\bar{q},\bar{p}}t} + \begin{pmatrix} A^{-}_{\bar{q},\bar{p}} \\ B^{-}_{\bar{q},\bar{p}} \end{pmatrix} e^{\alpha^{-}_{\bar{q},\bar{p}}t} \right\}, \tag{2.28}$$

where $\begin{pmatrix} A^{\pm}_{\bar{q},\bar{p}} \\ B^{\pm}_{\bar{q},\bar{p}} \end{pmatrix}$ and $\alpha^{\pm}_{\bar{q},\bar{p}}$ are the eigenvectors and eigenvalues associated to $(\bar{q},\bar{p})$ of the matrix $\mathscr{M}$. In case that at least one family of modes Ω grows exponentially fast (*i.e*, the real part of its eigenvalue is bigger than zero, $Re(\alpha_\Omega) > 0$), it linearly unstabilizes the homogeneous solution. In this case, the fastest family of growing modes, what we denote by Ω^*, dominates over the rest at short times, giving rise to a periodic pattern with the $(\bar{q},\bar{p})$-wavenumbers forming such Ω^*-family.

In a system with higher n number of variables per cell than two, $n > 2$, the roots of the characteristic polynomial may be more difficult to find. In these cases the application of the Routh-Hurwitz stability criterion can be helpful [3]. In particular, a system of three variables per cell yields a characteristic polynomial of third order that can be written as

$$P(\alpha,\Omega) = \alpha^3 + a_1(\Omega)\alpha^2 + a_2(\Omega)\alpha + a_3(\Omega) \quad . \tag{2.29}$$

[7] If the system is not linearized, the amplitudes of the modes would be coupled and therefore the growth of one mode will also depend on other modes.

This criterion establishes that the homogeneous solution is linearly unstable if any of the following conditions is not fulfilled [3]:

$$a_1 > 0, \quad a_1 a_2 - a_3 > 0, \quad a_3 > 0 \quad . \tag{2.30}$$

The violation of these conditions determines the fastest family of growing modes Ω^* [8].

In the following chapters we do not detail the LSA procedure for each of the specific models under study, but instead we show the specific matrix $\mathscr{M}$ of the studied models and infer the condition for spontaneous pattern formation. We usually get 2×2 matrices $\mathscr{M}$ whose eigenvalues are easily determined. In Chaps. 4 and 6 we obtain 3×3 matrices $\mathscr{M}$, and in the first case the Routh-Hurwitz criterion facilitates the analysis, while in Chap. 6 the roots of the eigenvalues are easily obtained.

In order to determine the region of the parameter space where pattern emerges, we usually perform a systematic evaluation of the conditions for patterning.

2.5 Exact pattern solutions (reduced model)

In this section we present a method that we have developed [135] and we use throughout this Thesis. This method consists on reducing the dimensionality of the system by imposing the symmetry of the resulting pattern into the steady state equations of the model of interest, specially into the spatial coupling term. This leads to what we call a reduced model, whose solutions give the exact solutions of the pattern. LSA over the pattern solutions and simulations will provide the stability of such solutions. This method is reminiscent of what Collier proposed for finding the pattern solution of two cell types in a line of cells [10], in which there is a perfect alternate pattern every two cells.

Let's define a dynamical system in a regular array of cells with one variable x_i per cell that can be written as

$$\frac{\mathrm{d}x_i}{\mathrm{d}t} = F_x(x_i, \langle x_i \rangle) = F_x^+(\langle x_i \rangle) - x_i \quad , \tag{2.31}$$

[8] Note though that a_1 a_2 and a_3 are nontrivially related to the roots of Eq. 2.29 [3]. In our case, the roots α_1, α_2 and α_3 and these coefficients are related by $a_1 = -(a_1 + a_2 + a_3)$, $a_2 = -(a_1 a_2 + a_2 a_3 + a_3 a_1)$ and $a_3 = -a_1 a_2 a_3$.

where $\langle x_i \rangle = \frac{1}{\omega} \sum_{k \in nn(i)} x_{i'}$ and F_x^+ is the regulatory function mediating trans-interactions. The steady state solutions are given by

$$x_i = F_x^+(\langle x_i \rangle) \tag{2.32}$$

for every i-cell. If we have a system of N cells, we have to solve N algebraic equations. Our method proposes that if the system presents a final pattern of two different cell types defined by x_A and x_B, we can reduce the dimensionality of the system into two algebraic equations, each one for every cell type:

$$x_A = F_x^+(\langle x_A \rangle), \quad x_B = F_x^+(\langle x_B \rangle) \quad . \tag{2.33}$$

Now we introduce the periodicity and symmetry of the pattern whose solution we are looking for:

$$\langle x_A \rangle = c_A x_A + (1 - c_A) x_B \tag{2.34a}$$

$$\langle x_B \rangle = c_B x_B + (1 - c_B) x_A \quad , \tag{2.34b}$$

where $c_{A,B}$ is the ratio of A, B-like cells neighboring to the A, B-cell type. The pattern symmetries determine the set of c_A and c_B values. We say that two patterns have the same symmetry if they have the same c_A and c_B values. The resulting system of Eqs. 2.33-2.34 is what we call reduced model. Different examples of reduced models can be found in Secs. 2.10.1 and 5.3.6. Note that the homogeneous state is always solution of these equations, *i.e.* $x_A = x_B$. Moreover, additional solutions with $x_A \neq x_B$ can be expected for specific parameter values, possibly representing stable pattern solutions. Thus, the existence of a pattern solution and its main characteristics can be studied from solving Eqs. 2.33-2.34 with a simple algorithm of root finding (see next Sec. 2.6). The presented methodology can be easily applied to more complicated dynamical systems than the one presented in Eq. 2.31, as we will see throughout this Thesis.

Our method provides a numerical tool that can be used for finding the exact solution of more complex patterns. For instance, this method can be easily extended for more than two cell types, although the roots of the system can be more difficult to find. The systematic computation of the reduced model's roots provides an easy way for finding what we define as the critical lines of the pattern, which are the lines enclosing the parameter regions where a certain patterned solution exists.

2.6 Root-finding algorithms for stationary solutions

In different occasions, we need to compute homogeneous or pattern solutions for our dynamical system systematically. In particular, these solutions are necessary for computing the regions at which the pattern solution exists, for studying the bifurcations, and for providing the initial conditions for the simulations.

We use the function NSolve provided by Mathematica 8.0 and also the root-finding algorithms by the GNU Scientific libraries (GSL). Several difficulties sometimes arise with these algorithms. Mathematica is too slow for doing systematic explorations across the parameter space, and sometimes fails to find certain roots near function discontinuities. GSL does not easily allow to find multiple roots at the same point in the parameter space.

For these reasons, we use our own custom-made program with a root-finding algorithm that can be adjusted to our necessities. Our program can find the solutions of an algebraic equation, which represents the steady states of the dynamical system of interest. Therefore, we can apply this methodology when the expression for the steady state under study can be reduced to a single equation, having just one independent variable. The root-finding algorithm consists on two successive applications (*i.e.* embedded loops) of the bisection method for acquiring better resolution. In some occasions, a very high precision is needed to find multiple roots that are very closed to each other. In these cases, the bisection method is applied using a logarithmic spaced partition grid along the interval where the root solutions are found. Our custom-made methodology is useful for finding single or multiple homogeneous solutions (see Eqs. 2.17) and also for finding exact solutions of two cell type patterns (see Eqs. 2.33-2.34).

2.7 Stability analysis of pattern solutions

In the cases were pattern solutions are found, we are often interested in determining its stability. During this Thesis we evaluate the stability of pattern solutions numerically and/or theoretically. Numerical methods consist on simulations with patterned initial conditions performed with custom-made programs (Sec. 2.9.1).

Also we numerically evaluate pattern states with Xpp-Aut software in small cellular arrays. In some occasions, we use a theoretical approach in which we perform LSA over the pattern solutions. Up to our knowledge, some stability arguments over lateral inhibition pattern solutions have just been formulated [112, 137]. In this Thesis we study pattern stability in a different way. In particular, we combine our reduced model approach, some adiabatic reductions, and the LSA analysis over the pattern solutions. We apply this methodology to different patterns and perform systematic explorations of pattern stability across the parameter space.

LSA over a pattern solution can be performed as follows. Once the pattern solution is found through the reduced model (Sec. 2.5), the Jacobian of the full dynamical system can be evaluated around the pattern solution in a system of $\mathscr{N}$ hexagonal cells, what we also refer as $\mathscr{M}$. The Jacobian is a matrix of dimensions $n \times \mathscr{N}$ being n the number of variables per cell, and its eigenvalues determine the stability of the pattern, as described in the LSA over the homogeneous state (Sec. 2.4). Adiabatic reductions and the application of this method in small cell arrays lead to smaller Jacobians, and simplify the study of the stability. Particular examples of LSA over pattern solutions can be found in Sec. 2.10 and App. C.

2.8 Pattern characterization

Herein we describe how we characterized the spatial distribution of any of the molecular species x in the cellular array.

2.8.1 Order parameter

To distinguish whether the species x is distributed according to a pattern and not homogeneously, we defined the order parameter η_x for the x species, which is $\eta_x > 0$ when x is patterned, and $\eta_x = 0$ when it is homogeneously distributed:

$$\eta_x = \frac{1}{NM} \sum_i \frac{1}{\omega} \sum_{j \in nn(i)} |x_i - x_j| \quad . \tag{2.35}$$

The first sum in Eq. 2.35 is performed over the whole $N \times M$ cells in the tissue, and the second sum is performed only over the ω nearest neighbor cells to cell i. For an irregular array of cells it reads

$$\eta_x = \frac{1}{\mathscr{N}} \sum_{i=1}^{\mathscr{N}} \sum_{j \in nn(i)} \alpha_{ij} |x_i - x_j| \quad , \tag{2.36}$$

where α_{ij} is the cell-to-cell coupling coefficient in an irregular lattice (Eq. 2.10) and $\mathscr{N}$ is the cell number of the lattice.

The theoretical order parameter of a perfectly periodic pattern in a regular array can be easily determined. To obtain it we take into account (i) the fraction of cells of each cell type, (ii) the exact solutions of the pattern given by Eqs. 2.33-2.34 and (iii) the kinds of neighbors each cell type has. Accordingly, the theoretical order parameter for our studied pattern of just two cell types A and B would be

$$\eta_x^{th} = q_A \eta_{x_A}^{th} + q_B \eta_{x_B}^{th} \quad , \tag{2.37}$$

where $q_{A,B}$ is the cell fraction adopting the A, B-type and $\eta_{x_{A,B}}^{th}$ is the theoretical local order parameter for cell type A, B, which reads

$$\eta_{x_{A,B}}^{th} = (1 - c_{A,B})|x_A - x_B|. \tag{2.38}$$

2.8.2 Structure function

Sometimes we are interested not only to distinguish between a patterned and a homogeneous state, but also to know which periodicity underlies the pattern. For this reason, we make use of the structure function [7]. This function provides the amplitude spectrum of the modes participating in a pattern. In this section we describe how we obtain it.

Firstly, we subtract a constant background x_b from the pattern under study for the variable x and then we perform its Fourier transform:

$$\sigma'_{\bar{q},\bar{p}} = \sum_{k=1}^{M} \sum_{j=1}^{N} (x_{j,k} - x_b) e^{-2\pi \mathrm{i}(\bar{q}j + \bar{p}k)} \quad . \tag{2.39}$$

We set the background $x_b \equiv (x_A + 2x_B)/3$ with x_A and x_B being the stationary x-state values for the lateral inhibition pattern obtained from equations 2.33-2.34 applied to the dynamical model under study. This value of x_b has been chosen

such that no contribution arises in the structure function for $\Omega_{\bar{q},\bar{p}} = 1$ ($\bar{q} = 1$, $\bar{p} = 1$) (see App. B). Then, the structure function for the chemical species x in a system of $N \times M$ can be defined as the normalized scalar product of the Fourier transform of the pattern:

$$\mathbb{S}(\bar{q},\bar{p}) \quad = \quad \frac{1}{NM}\sigma'_{\bar{q},\bar{p}}\sigma'_{-\bar{q},-\bar{p}} \quad . \tag{2.40}$$

Note that this expression can be written in an equivalent form:

$$\mathbb{S}(\bar{q},\bar{p}) \quad = \quad \frac{1}{MN}\sum_{j,k}\sum_{j',k'}(x_{j,k}-x_b)(x_{j',k'}-x_b)e^{-2\pi \mathrm{i}(\bar{q}(j-j')+\bar{p}(k-k'))}, \tag{2.41}$$

where we have used every summatory for referring to a double sum in space, *e.g.* $\sum_{j,k} = \sum_{j=1}^{N}\sum_{k=1}^{M}$. We can define the structure function in terms of Ω, what reads

$$\mathbb{S}(\Omega) \quad = \quad \sum_{(\bar{q},\bar{p})\in\Omega}\frac{1}{C(\Omega)}\mathbb{S}(\bar{q},\bar{p}) \quad , \tag{2.42}$$

with $C(\Omega_{\bar{q},\bar{p}})$ being the number of $\bar{q}$,$\bar{p}$ modes that yield the same Ω value (Eq. 2.24). For the sake of simplicity, we use the $\mathbb{S}(\Omega)$ function instead of $\mathbb{S}(\bar{q},\bar{p})$[9].

2.9 Numerical simulations

During this Thesis, we use numerical simulations for integrating the whole nonlinear models. Numerical simulations are going to be used to corroborate the predictions performed by LSA. Note that the emerging pattern is not necessarily the one predicted by LSA over the homogeneous state, given that nonlinear effects may take place. Herein we detail some technical aspects regarding the numerical simulations.

2.9.1 Numerical integration of the model

Throughout this Thesis, we use a Runge-Kutta fourth-order algorithm [136] for the integration of the deterministic models.

[9] In the linear approximation, each Ω-family of modes grows at the same exponential rate, so the modes yielding the same Ω are present in the emerging pattern in a similar way.

Stochastic simulations are performed using a variation of Heun algorithm for the Itô interpretation [138] with a time step of $\mathrm{d}t = 0.001$, unless otherwise stated. Gaussian random numbers are generated according to Toral and Chakrabarti [139].

We use three types of initial conditions: uniformly distributed random perturbations, $x_i(t = 0) = U_i^x$, being U_i^x a uniform random number between 0 and 1, homogeneous and patterned initial conditions, both of them with small random uniformly distributed perturbations with amplitude δ, $x_i(t = 0) = x_{0,patt}(1 + \delta(U_i^x - 0.5))$ being x_0 the homogeneous steady state for the specie x x_{patt} the patterned solution. Unless otherwise stated, we normally use $\delta = 0.1$.

Simulations are stopped when the steady state is achieved. Simulations are considered to reach the steady state when a certain function of the order parameters (see Eq. 2.36) evolve less than a threshold $\Delta\eta^{steady}$ in a certain period of time Δt (*e.g.* $\Delta t \sim 10 - 100$). For every x species it could be defined

$$\Delta\eta_x \quad = \quad \mathscr{N}|\eta_x(t + \Delta t) - \eta_x(t)| \quad , \tag{2.43}$$

being $\mathscr{N}$ the number of cells and η_x given by Eq. 2.36. Then, our system reaches the steady state when an order parameter for a species x fulfills [10]

$$(\Delta\eta_x) \quad < \quad \Delta\eta^* \quad , \tag{2.44}$$

being $\Delta\eta$ a very small value ($\Delta\eta^* << 1$) or being more restrictive, when a combination of order parameters reach its steady state, *e.g.*

$$(\Delta\eta_x(\Delta t) + \Delta\eta_y(\Delta t)) \quad < \quad \Delta\eta^* \tag{2.45}$$

with $\Delta\eta^* << 1$. We typically use $\Delta\eta^* = 10^{-5} - 10^{-7}$ values.

2.9.2 Irregular tissue layouts

To construct the spatial layout of cells we generate an irregular distribution of points on a plane starting from a perfect triangular lattice and displacing the position $\mathbf{r}$ of each point to a new position $\mathbf{r}'$ given by

[10] Since this criterion has to be used either in the pattern and homogeneous situation, so $\eta_x \geq 0$, we can not use a criterion expression in which the actual order parameter appears multiplying or dividing it.

$$\mathbf{r}' \quad = \quad \mathbf{r} + \frac{\gamma}{\Gamma}\left\{(v_x - 0.5)\mathbf{x} + (v_y - 0.5)\mathbf{y}\right\} \quad , \tag{2.46}$$

where Γ is the distance between first nearest neighbor nodes on the triangular lattice, v_x and v_y are random numbers drawn from an uniform distribution between 0 and 1 and $\mathbf{x}$ and $\mathbf{y}$ are unitary vectors along the x and y axis. γ sets the magnitude of irregularity of the resulting lattice such that the resulting field is composed of equal perfectly hexagonal cells for $\gamma = 0$, and irregularity increases with increasing γ. This irregularity affects two aspects: the sides of the cells (cell-to-cell coupling coefficient, α_{ij}, Eq. 2.10) and the number of neighbors, being the former first distorted (Fig. 2.2). A Voronoi tessellation is created around these points [140] by using Mathematica's Computational Geometry Package (Wolfram Research, Inc. (2008), Mathematica, Version 7.0, Champaign, IL, USA). In some cases we set periodic boundary conditions (Fig. 2.3). Periodicity in the boundary conditions can be achieved by (i) surrounding the initial array of nodes with equivalent arrays, (ii) computing the associated Voronoi tesselation and (iii) taking the resulting Voronoi tesselation associated with the initial array of nodes.

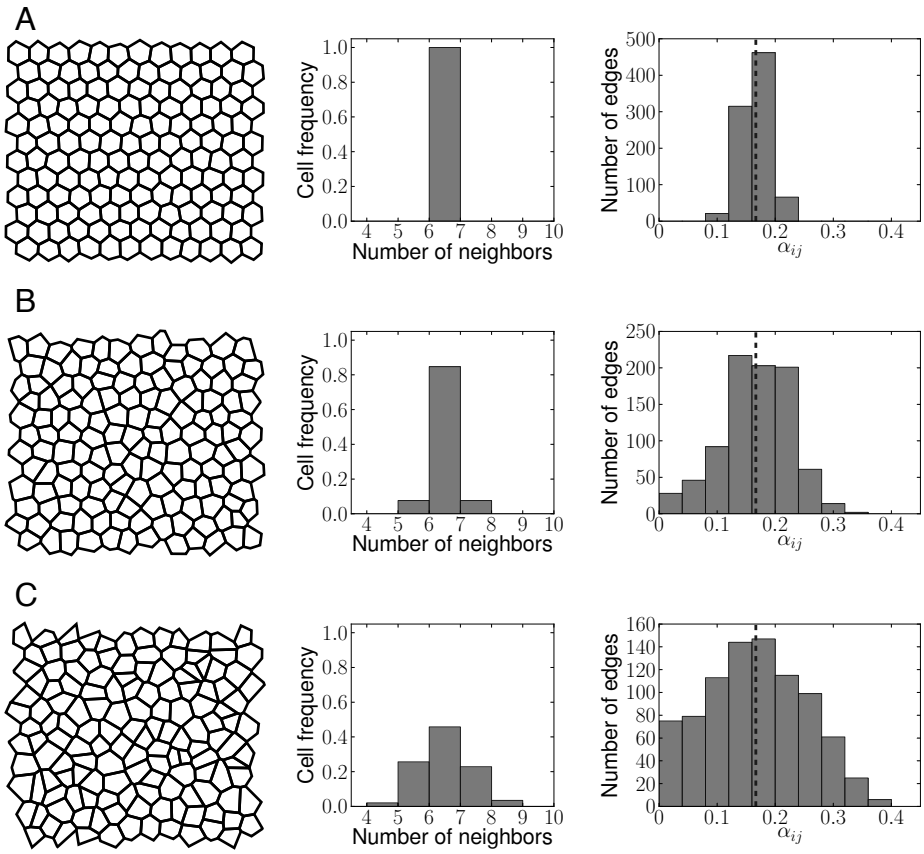

Figure 2.2: Characterization of irregular cell arrays. Examples of constructed cell arrays (left) with lattice irregularity parameters (A) $\gamma = 0.67$, (B) $\gamma = 1.6$ and (C) $\gamma = 2.67$ with a characterization of the number of of neighbors per cell (middle) and a bar diagram with the cell-to-cell coupling coefficients α_{ij} (Eq. 2.10) (right). The right panels contain a vertical dashed line at $\alpha_{ij} = 1/6$ as a reference for the perfect hexagonal array. Although for $\gamma = 0.67$ all cells have six neighbors, cell side lengths (and, accordingly, the strength of the ligand-receptor interaction) are not regular.

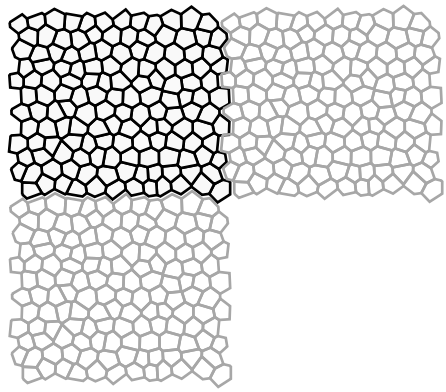

Figure 2.3: Irregular cell arrays are built with periodic boundary conditions. Herein we show two additional gray copies of the same cell array juxtaposed, showing the periodic nature of the cell array.

2.10 A particular example: the Collier model revisited

In this section we study the pattern formation capabilities of the Collier model (Eqs. 2.8a-2.8b), what helps to exemplify some of the material presented in the precedent sections. We start by doing a theoretical analysis, and afterwards we present simulation results. Emphasis is made on new results about this model.

2.10.1 Theoretical analysis of the Collier model

For simplicity, we rewrite the dynamical system of Collier *et al.* as

$$\frac{\mathrm{d}s_i}{\mathrm{d}t} = f(\langle l_i \rangle) - s_i \tag{2.47a}$$

$$\frac{\mathrm{d}l_i}{\mathrm{d}t} = v\left\{g(s_i) - l_i\right\} \quad , \tag{2.47b}$$

with

$$g(s_i) = \frac{1}{1+bs_i^h}, \quad f(\langle l_i \rangle) = \frac{r_t \langle l_i \rangle}{1 + r_t \langle l_i \rangle} \quad . \tag{2.48}$$

From these equations, the shape of the regulatory functions f and g already inform us about the effective role of both species s and l in the regulatory network

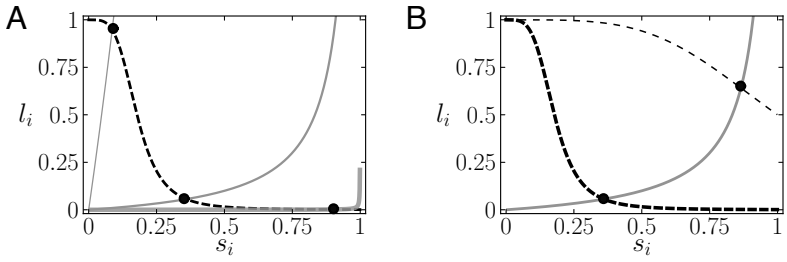

Figure 2.4: Nullclines of Collier model for different (A) trans-activation and (B) ligand-inhibition strengths. Black dashed and gray solid represent the l-nullclines and the s-nullclines, respectively (Eq. 2.49). Intersections between the nullclines are marked with filled dots, and denote homogeneous steady state solutions (s_0, l_0). Parameters values: (A) $r_t = 0.1$ (thin line), $r_t = 10$ (medium line) and $r_t = 5000$ (thick line) with $b = 1000$, and (B) $b = 1$ (thin line) and $b = 1000$ (thick line) with $r_t = 10$. $h = 4$ was used for both panels.

(see Sec. 2.2, Fig. 1.5). Specifically, the ligand trans-activates the signal (f is a monotonic increasing function of the ligand), while the signal inhibits the production of ligand in the same cell (g is a monotonic decreasing function of the signal).

The homogeneous fixed point (s_0, l_0) can be found by setting $\langle l_i \rangle = l_i$ and finding the intersection of the nullclines $s_i = f(l_i)$ and $l_i = g(s_i)$. This can be rewritten as

$$\frac{1}{1 + b s_i^h} = \frac{s_i}{r_t(1 - s_i)} \quad , \tag{2.49}$$

where the left-hand side corresponds to the l-nullcline, and the right-hand side to the s-nullcline. The nullclines diagram (Fig. 2.4) can easily help us to check how are the homogeneous modes at different parameter regimes. On one side, by increasing the trans-interactions strength parameter r_t we reach higher Notch signal and lower ligand homogeneous concentrations. On the other side, by increasing ligand inhibition b, we decrease both ligand and signal homogeneous concentrations. Hence, weak trans-interactions or ligand inhibition by Notch would rise the ligand levels, while strong trans-interactions or ligand inhibition by Notch would deplete ligand levels.

Now we can proceed with the LSA analysis over the homogeneous state. Tak-

ing into account the dynamics of both species, the $\mathscr{M}$ matrix (Eq. 2.27) for such a system reads

$$\begin{pmatrix} -1 & \mathscr{A}\Omega \\ v\mathscr{B} & -v \end{pmatrix} \quad . \tag{2.50}$$

$\mathscr{A}$ and $\mathscr{B}$ are related to the partial derivatives of the signal and ligand production, *i.e.*

$$\mathscr{A} = \omega \left.\frac{\partial}{\partial l_{i'}} \frac{\mathrm{d}s_i}{\mathrm{d}t}\right|_{s_0,l_0}, \quad \mathscr{B} = \left.\frac{1}{v}\frac{\partial}{\partial s_i}\frac{\mathrm{d}l_i}{\mathrm{d}t}\right|_{s_0,l_0}, \tag{2.51}$$

where i' is referred to first neighbors of cell i, $\mathscr{A} = \frac{\mathrm{d}f(\langle l_i\rangle)}{\mathrm{d}\langle l_i\rangle}|_{s_0,l_0} = \frac{r_t}{(1+r_t l_0)^2}$ and $\mathscr{B} = \frac{\mathrm{d}g(s_i)}{\mathrm{d}s_i}|_{s_0,l_0} = -\frac{bhs_0^{h-1}}{(1+bs_0^h)^2}$. The sign of these derivatives confirms us the effective role of both species in the regulatory network: $\mathscr{A} > 0$ denotes signal trans-activation by the ligand and $\mathscr{B} < 0$ denotes ligand inhibition by the signal[11].

After diagonalizing the $\mathscr{M}$ matrix, we find the following dispersion relation:

$$\alpha_\Omega^\pm = \frac{1}{2}\left\{-(1+v) \pm \left((1+v)^2 - 4v(1-\mathscr{A}\mathscr{B}\Omega)\right)^{1/2}\right\}. \tag{2.52}$$

The homogeneous steady state is unstable if $Re(\alpha_\Omega^\pm) > 0$. For Eq. 2.52, this condition leads to $1 < \mathscr{A}\mathscr{B}\Omega$. Given that $\mathscr{A}\mathscr{B} < 0$ and $\Omega \in [-0.5, 1]$, the fastest growing family of modes correspond to $\Omega^* = -0.5$, that is formed by the two couples of modes $(\bar{q}, \bar{p}) = (1/3, 2/3)$ and $(\bar{q}, \bar{p}) = (2/3, 1/3)$. Therefore, the homogeneous state in a regular hexagonal array is unstable to these modes if

$$2 > \mathscr{A}\mathscr{B} \quad , \tag{2.53}$$

and then spontaneous patterning is expected to emerge. The perturbed solution of the linearized Collier model gives rise to the patterned state around the homogeneous solution given by

$$\begin{pmatrix} \widetilde{s}_{j,k} \\ \widetilde{l}_{j,l} \end{pmatrix} \sim \begin{pmatrix} C_1 \\ C_2 \end{pmatrix} \left(e^{2\pi i(j+2k)/3} + e^{2\pi i(2j+k)}\right) \quad , \tag{2.54}$$

[11] The activatory and inhibitory role can be defied out of the homogeneous solution. Specifically, it can be shown that for the Collier model the signal is always inhibiting ligand production and the ligand is always trans-activating the signal given that $\mathscr{R}_{l_i,s_i} < 0$ and $\mathscr{R}_{s_i,l_i} < 0$ for the Collier model (in Sec. 2.2 we defined $\mathscr{R}_{x_i,y_i} = \frac{\partial}{\partial y_i}\frac{\mathrm{d}x_i}{\mathrm{d}t}$).

being C_1 and C_2 two constants. Indeed, this kind of solution leads to a lateral inhibition pattern (Fig. 2.5 (A)). Some aspects of this analysis can be found in more detail in the original article by Collier et al. [10]. A systematic computation of Eq. 2.53 in the parameter space will provide the spontaneous pattern forming region, delimited by a LSA critical line ($2 = \mathscr{A}\mathscr{B}$) (we will see this critical line afterwards in Fig. 2.6).

Now we want to compute the exact pattern solutions of the lateral inhibition pattern (Fig. 2.5 (A)) (Sec. 2.5). First, we name the cell type being in minor proportion (1/3 of cells in the tissue) as the cell type A, and the cells being in major proportion (2/3 of cells in the tissue) as the cell type B. In this pattern, all neighbors of cell type A are type B cells, while half of the neighbors of type B cells are also type B and the remaining half are cell type A (Fig. 2.5 (A)). This periodicity corresponds to $c_A = 0$ and $c_B = 1/2$ in Eqs. 2.34. By applying it to the Collier model, the reduced model described in Sec. 2.5 results in

$$s_A = f(l_B), \quad l_A = g(s_A), \quad s_B = f\left(\frac{l_A + l_B}{2}\right), \quad l_B = g(s_B) \quad . \tag{2.55}$$

These equations could also lead to an inverted phenotype, what we refer as the inverted pattern, so the cell type A would be with low ligand (high signal). Also, these equations provide the exact solution of an equivalent pattern with the same symmetry properties (*i.e.* the same c_A and c_B values) in a line of cells (Fig. 2.5 (B)). We can easily reduce Eqs. 2.55 into one algebraic equation, *i.e.*

$$g\left(f(l_B)\right) = \frac{1}{2} f^{-1}\left(g^{-1}(l_B) - \frac{1}{2} l_B\right) \quad , \tag{2.56}$$

where g^{-1} and f^{-1} refer to the inverse functions of g and f respectively. In Chaps. 4 and 5 we use this method for different extended versions of Collier model systematically, and with the help of simulations we compute different bifurcation diagrams. Also, in Chap. 5 we apply this method to other regular patterns of two cell types[12]. By applying the bisection method to Eq. 2.56 the exact solution of the pattern is found. By solving this equation in the parameter space, we find

[12]Notice that we mathematically define a "cell type" as the molecular state of a cell and of its neighbors. Indeed, two apparently equivalent cells having different neighborhoods will attain different exact solutions. This is a mathematical definition, and the biological interpretation of a cell type or a cell fate will not rely on that.

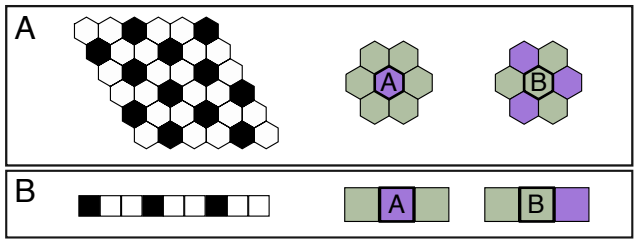

Figure 2.5: Representation of lateral inhibition patterns (left) and its spatial symmetry (right) for its two cell types for (A) a regular hexagonal array of cells and (B) a cell line with periodic boundary conditions. Cell type A, corresponding to the cell type present in minor proportion, is all surrounded by cells belonging to the cell type in major proportion, the cell type B, so $c_A = 0$. Cell type B has half of its neighbors being of cell type A and the other half of cell type B, so $c_B = 1/2$. The represented lateral inhibition patterns (left) have cell type A with high ligand and low signal, while cell type B with low ligand and high signal. Black corresponds to high levels ($l_i = 1$), white to low ligand levels ($l_i = 0$). In the right panel, colors represent the cell type, being violet for cell type A and green for cell type B. Both lateral inhibition patterns share the same proportions in terms of ratios of types of neighbors, and consequently both patterns have the same exact solutions.

the critical line of the lateral inhibition pattern, *i.e.* a line enclosing the region where the lateral inhibition pattern solution exists (we will see this critical line afterwards in Fig. 2.6).

Once the pattern solutions are found, we can compute if such solutions are linearly stable to small perturbations. To do so, we make use of the equivalence of the lateral inhibition pattern in a regular hexagonal array with a lateral inhibition pattern in the line of cells (Fig. 2.5), and we consider a system of three cells with periodic boundary conditions. For the sake of simplicity, we consider fast ligand variables[13], so the system reads

[13]This adiabatic reduction is performed for simplifying the stability calculation and does not obey a real timescales motivation of the ligand *versus* the Notch signal. In App. C we show that the resulting theoretical stability criterion agrees with simulation results where both ligand and signal variables are governed by the same timescales (*i.e.* $v = 1$).

$$\frac{\mathrm{d}s_1}{\mathrm{d}t} = f\left(\frac{g(s_2)+g(s_3)}{2}\right) - s_1 \tag{2.57a}$$

$$\frac{\mathrm{d}s_2}{\mathrm{d}t} = f\left(\frac{g(s_1)+g(s_3)}{2}\right) - s_2 \tag{2.57b}$$

$$\frac{\mathrm{d}s_3}{\mathrm{d}t} = f\left(\frac{g(s_1)+g(s_2)}{2}\right) - s_3 \quad . \tag{2.57c}$$

If we assume that cell 1 is adopting cell fate A and cells 2 and 3 adopt fate B, the $\mathscr{M}$ matrix for this system is

$$\mathscr{M} = \left.\begin{pmatrix} \frac{\partial}{\partial s_1}\frac{\mathrm{d}s_1}{\mathrm{d}t} & \frac{\partial}{\partial s_2}\frac{\mathrm{d}s_1}{\mathrm{d}t} & \frac{\partial}{\partial s_3}\frac{\mathrm{d}s_1}{\mathrm{d}t} \\ \frac{\partial}{\partial s_1}\frac{\mathrm{d}s_2}{\mathrm{d}t} & \frac{\partial}{\partial s_2}\frac{\mathrm{d}s_2}{\mathrm{d}t} & \frac{\partial}{\partial s_3}\frac{\mathrm{d}s_2}{\mathrm{d}t} \\ \frac{\partial}{\partial s_1}\frac{\mathrm{d}s_3}{\mathrm{d}t} & \frac{\partial}{\partial s_2}\frac{\mathrm{d}s_3}{\mathrm{d}t} & \frac{\partial}{\partial s_3}\frac{\mathrm{d}s_3}{\mathrm{d}t} \end{pmatrix}\right|_{s_A,s_B} = \begin{pmatrix} -1 & \mathscr{A}_A\mathscr{B}_B & \mathscr{A}_A\mathscr{B}_B \\ \mathscr{A}_B\mathscr{B}_A & -1 & \mathscr{A}_B\mathscr{B}_B \\ \mathscr{A}_B\mathscr{B}_A & \mathscr{A}_B\mathscr{B}_B & -1 \end{pmatrix}, \tag{2.58}$$

where $\mathscr{A}_A = \frac{\frac{r_t}{2}}{(1+r_t l_B)^2}$, $\mathscr{A}_B = \frac{\frac{r_t}{2}}{(1+\frac{r_t}{2}(l_B+l_A))^2}$ and $\mathscr{B}_{A,B} = -\frac{bhs_{A,B}^{h-1}}{(1+bs_{A,B}^h)^2}$.
The three eigenvalues $\alpha_{1,2,3}$ read

$$\alpha_1 = -(1+\mathscr{A}_B\mathscr{B}_B) \tag{2.59a}$$

$$\alpha_{2,3} = \frac{1}{2}\left\{-(2+\mathscr{A}_B\mathscr{B}_B) \pm \left(\mathscr{A}_B\mathscr{B}_B\left(8\mathscr{A}_A\mathscr{B}_A + \mathscr{A}_B\mathscr{B}_B\right)\right)^{1/2}\right\} . \tag{2.59b}$$

A pattern is stable in a point of the parameter space if these three eigenvalues are negative ($\alpha_{1,2,3} < 0$)[14]. This criterion will not forcely match with simulations in larger systems in the case the pattern is linearly unstable to longer wavelengths than the size of the studied system. We refer to this issue in more detail and make use of this method in Chap. 5 and App. C.

Now we want to evaluate these theoretical results in the parameter space r_t–b (r_t and b are the trans-interactions strength and ligand inhibition strength parameters respectively) (Fig. 2.6).

Our results show that intermediate values of trans-interactions strength r_t and above a threshold of ligand inhibition by Notch (b) the homogeneous state is linearly unstable to inhomogeneous perturbations (solid line in Fig. 2.6). This

[14]The stability condition that can be extracted from $\alpha_1 < 0$ leads to the expression obtained by O'Dea and King (2011) [112].

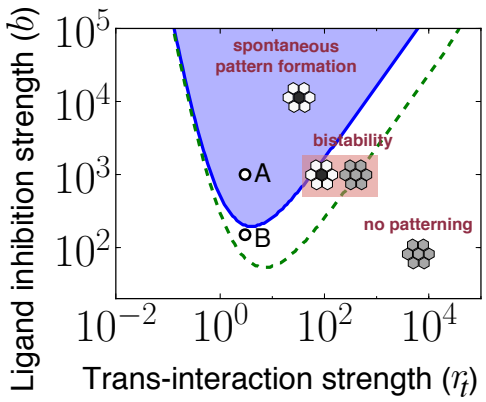

Figure 2.6: Phase diagram analysis show that Collier model is robust for salt-and-pepper patterning. The blue region delimited by the solid line indicates where spontaneous pattern formation occurs. This is computed by LSA (Eq. 2.53). The region below the green dashed line indicates where the patterned solution exists and is linearly stable, enlarging the region provided by LSA. This has been computed through the reduced model (Eqs. 2.56-2.55) and through LSA over the pattern solutions (Eqs. 2.59 should be negative for pattern stability). Lateral inhibition patterning is robust in the parameter space and occurs at intermediate trans-interactions strengths (r_t) and above a threshold of ligand inhibition by Notch (b). Points (A) and (B) inside the diagram correspond to simulations shown in Figs. 2.6-2.12 and 2.15 respectively. Also, in Fig. 2.7 we show the dispersion relation of the model and the nullclines for finding the exact pattern solutions at points (A) and (B). This diagram has been computed for cooperativity $h = 4$.

dependence on parameters r_t and b can be intuitively understood as follows: for small enough values of r_t the ligand concentrations cannot activate the signal s_i (*i.e.* $f(\langle l_i \rangle >> r_t) \approx 0$, so $\mathscr{A} \approx 0$ and for small values of b the ligand is not sensible to the signal (*i.e.* $\mathscr{B} \approx 0$ since $g(s_i << b^{-1/h}) \approx 1$). Hence, small values of r_t or b break the feedback of lateral inhibition, forbidding pattern formation. The feedback is also broken for large values of r_t, since the signal is saturated and becomes independent of the ligand concentrations (*i.e.* $\mathscr{A} \approx 0$ since $f(\langle l_i \rangle << r_t) \approx 1$). Accordingly, we find that the homogeneous state becomes linearly stable again to inhomogeneous perturbations for large values of r_t.

The reduced model shows us that the pattern formation region is significantly larger than the region predicted by LSA over the homogeneous state. Indeed, with the help of LSA over the pattern state and simulations (see Chap. 4 for an exhaustive numerical analysis) we find a region outside the spontaneous patterning zone where both the homogeneous state and the pattern exist and are both linearly stable (Fig. 2.6). Through this Thesis, we refer to this phenomenon as bistability, or coexistence of the pattern and homogeneous state, and we call such region as the bistable region. In Chap. 4 we see that such bistability is consistent with the subcritical behavior we find in the bifurcation diagrams, also involving that the emerging pattern has a finite amplitude at the transition zone between the homogeneous state and the pattern state[15].

The plot of the dispersion relation for the Collier model (Fig. 2.7 (A)) clearly shows a monotonic tendency, in which the fastest growing mode is the one having the minimal possible Ω, being $\Omega = -0.5$ for the perfect hexagonal array of cells and then corresponding to the lateral inhibition pattern[16]. The nullclines for the reduced model (Eqs. 2.55, Fig. 2.7 (B)) together with the LSA over the pattern solutions show that in this model cell type A, *i.e.* the cell fate in minor proportion, has a high ligand (low signal) phenotype and that cell type B has a low ligand (high signal) phenotype (Fig. 2.5 (A)). Hence, in the Collier model

[15] In a line of cells or in a squared bidimensional array of cells, the transition is supercritical, meaning that the amplitude of the pattern gradually grows around the critical line indicating pattern formation. Hence, in such different cell lattices, the bistable region does not exist.

[16] It can be easily shown that for the line of cells, the fastest growing mode is $\Omega = -1$ and it corresponds to a wavelength of two cells [10].

with no cooperativity in the equation of the signal ($k = 1$ in Eqs. 1.1-D.3), just the normal lateral inhibition pattern is found, while the inverted pattern (the cell fate in minor proportion being cells with low ligand) do not appear. We study and discuss this aspect in more detail in Chap. 5.

In summary, these results show that lateral inhibition patterning occurs in a wide region of the parameter space, exhibiting a robust behavior (Fig. 2.6).

2.10.2 Simulation results

Herein we present some simulation results to verify the pattern formation capabilities obtained in the precedent section.

Simulation results in the spontaneous pattern formation region can lead to the perfectly regular lateral inhibition pattern (Fig. 2.8). Apart from visualizing the concentration levels in an array of cells representation, we also make use of the structure function $\mathbb{S}$ to see the amplitudes of the modes participating in the pattern (Fig. 2.8 (B)). In App. B we derive a theoretical prediction of the amplitudes of the structure function for a perfect lateral inhibition pattern. We also check that the attained states by the simulations correspond to solutions predicted by the reduced model (Fig. 2.9 (A)). Such attained states are stable solutions, while the three solutions in between the attained solutions correspond to unstable states, being the central one the homogeneous state. In our simulations we track the numerical order parameter to figure out whether the system reaches the steady state (Fig. 2.9 (B)). A theoretical prediction of the order parameter of a perfectly regular lateral inhibition pattern can be made, so that we can compare it with the numerical order parameter (see Sec. 2.8.1). In particular, by using Eq. 2.37 one can see that the theoretical order parameter for the x species in a perfect lateral inhibition pattern reads $\eta_x^{th} = \frac{2}{3}|x_A - x_B|$ with x_A and x_B being the corresponding patterned state solutions for the cell types A and B respectively.

In the spontaneous pattern formation zone, pattern simultaneously starts at different points of the tissue, and then defects may emerge due to the collision of different patterning growing domains (Fig. 2.10). In general, defects are going to be more likely to appear when other modes besides the fastest growing mode can linearly unstabilize homogeneous fixed point. Defects more likely appear in larger systems, and also far from the critical line set by LSA, inside the spontaneous

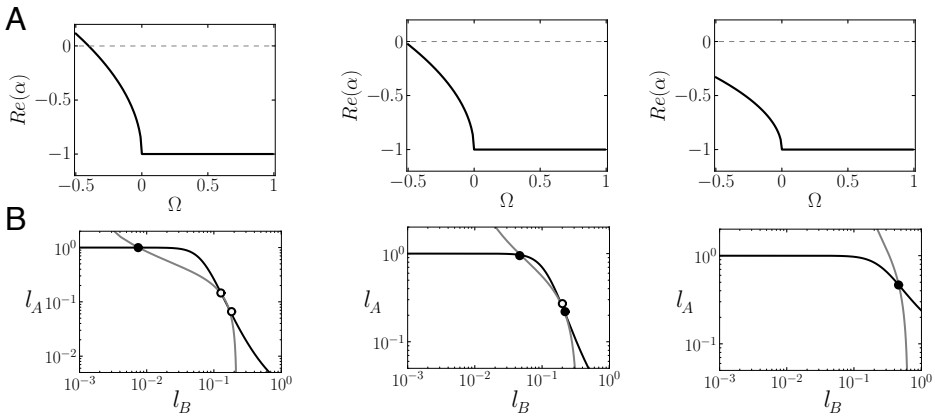

Figure 2.7: Theoretical results of the Collier model for strong ligand inhibition (left panels, $b = 1000$), moderate (middle panels, $b = 150$) and weak ligand inhibition ($b = 10$). (A) Real part of the exponential growing rates of the modes perturbing the homogeneous fixed point. This is also called the dispersion relation (Eq.2.52). At strong inhibition strengths (left) the dispersion relation is over zero for some range of Ω values, meaning that the associated modes are able to linearly unstabilize the homogeneous fixed point. The fastest growing mode is for $\Omega^* = -0.5$, what means that the final pattern state is probably dominated by the characteristic length set by $\Omega^* = -0.5$. (B) Nullclines of the reduced model (Eq. 2.56) whose intersections, marked with dots, represent the exact solutions of the reduced model. Empty dots are unstable solutions, while filled dots are stable solutions. The black line corresponds to the left-hand side of Eq. 2.56, while the gray line to its right-hand side. For both stronger (left) and weaker (middle) inhibition strengths, three solutions are found, being one of them the homogeneous solution ($l_A = l_B$), and the other two are pattern solutions leading to the normal lateral inhibition pattern, for which cells with high ligand are all surrounded by cells with low ligand ($l_A > l_B$). LSA over the pattern state and simulation results tell us the stability of the patterned solutions. The pattern solution with intermediate ligand concentration values is unstable, and the other pattern solution is the stable one. Parameter values: $h = 4$, $r_t = 3$, $v = 1$ for all panels.

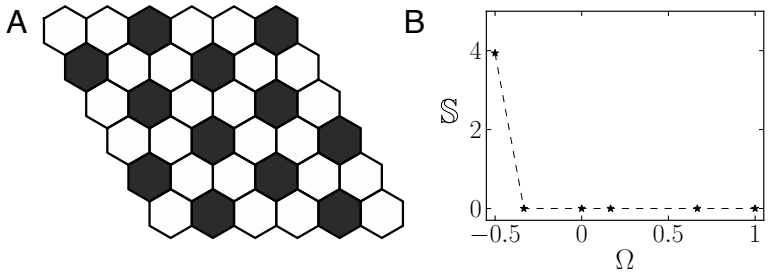

Figure 2.8: Normal lateral inhibition pattern in a perfect hexagonal array of cells composed by the two modes $(\bar{q}, \bar{p}) = (1/3, 2/3)$ and $(\bar{q}, \bar{p}) = (2/3, 1/3)$ belonging to $\Omega^* = -0.5$. (A) Stationary snapshot of a simulation of the Collier model on a perfect hexagonal array starting from homogeneous initial conditions with small fluctuations. The pattern of the ligand (l) levels is shown. Dark gray correspond to high ligand concentration, while light gray correspond to low ligand concentration (black was used for $l = 1$ and white for $l = 0$). The Notch signal representation will be normally omitted, since the corresponding pattern is the opposite with respect to the ligand pattern; high (low) ligand cells correspond to low (high) Notch signal cells. (B) Structure function for such pattern (Eqs. 2.39, 2.40, 2.42). Asterisks correspond to the amplitudes of the existing modes in a 6×6 system of cells, dashed line is a guide to the eye. Its expression agrees with the theoretical computation of the structure function in a perfect hexagonal array (see Sec. 2.8.2 and App. B). Simulations performed in point A of the diagram presented in Fig 2.6. Parameter values: $b = 1000$, $r_t = 3$, $h = 4$ and $v = 1$.

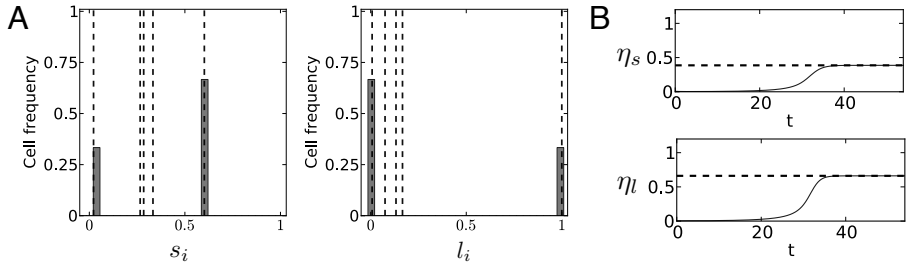

Figure 2.9: The exact solution method matches with the simulation results. (A) Histogram of the attained solutions in the simulation shown in Fig. 2.8. Vertical lines are the theoretical solutions of the pattern. The vertical lines corresponding to the highest and lowest level of signal and ligand correspond to the stable pattern solutions. The three vertical lines in between the stable pattern solutions correspond to unstable solutions, being the central one the homogeneous solution. (B) Evolution of the order parameters for such simulation. Horizontal lines correspond to the theoretical order parameters for a perfect normal lateral inhibition pattern. Parameter values as in Fig. 2.8.

pattern formation region. Our numerical simulations show that these defects are very stable (deterministic numerical simulations in regular hexagonal arrays of cells show they do not evolve for times 100 times longer than those required to reach the steady state). In Chaps. 4 and 5 we study in more detail the emergence of pattern defects. We will see that variations of the Collier model can increase or reduce the nonlinearity of the system under study, what promotes pattern regularity or driving the appearance of more irregular patterns respectively.

Variations in the regularity of the lattice also lead to quite regular patterns that conserve the characteristic wavelengths (Fig. 2.11), being consistent with other previous results [107].

The implementation of dynamical multiplicative noise, with intensity inversely proportional to an effective cellular volume, to the Collier dynamics (Sec. 2.3) leads to equivalent results, driving pattern formation emergence with the expected wavelength (Fig. 2.12). Remarkably, at moderate noise intensities the dynamics of patterning is accelerated. This is consistent with recent theoretical results, where it is shown that multiplicative and additive noise in a similar model for lateral inhibition accelerate the lateral inhibition dynamics [110]. Surprisingly,

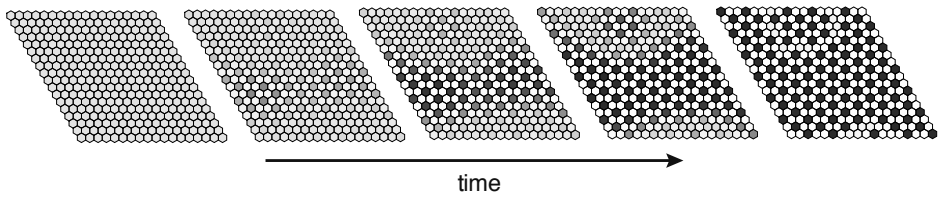

Figure 2.10: Collier model enables spontaneous pattern formation. Snapshots of the ligand levels from deterministic simulations of the Collier model on a regular array of cells starting from the homogeneous fixed point with small random perturbations (see Sec. 2.9.1). From left to right, the time points of the panels are $t = 8, 16, 18, 20, 42$. The pattern emergence is initiated at different parts of the tissue. The collision of the pattern growing domains lead to the creation of very stable defects, which can be identified in the panels on the right. Parameter values as in Fig. 2.8.

our simulations show that defects can also persist to such noise. However, too high noise intensities destroy the pattern (Fig. 2.12 (C)).

The attained pattern states in our simulations agreed well the theoretical prediction for the exact solutions (Fig. 2.9 (A)) also when the pattern had some defects (Fig. 2.14 (A)). Remarkably, our theoretical solutions are a good approximation even when stochasticity and cell irregularity are taken into account (see Figs. 2.13 and 2.14 (B-C)).

Simulation results confirm that in the bistable region it is possible to unstabilitze the homogeneous state, driving pattern emergence. In particular, patterning can occur due to a more heterogeneous initial condition that nonlinearly unstabilizes the homogeneous state. Also, dynamical noise or more irregular cell geometries can easily lead to patterning in such region (Fig. 2.15)[17]. In Chap. 3 we see that in such region patterning can also occur in a more complex model where lateral inhibition dynamics is regulated through a diffusible morphogen.

In this section we have seen that the phenomenological model of Collier – and therefore similar models to this model – can be studied analytically, providing

[17]In the case of dynamical noise or irregular cell arrays, it is not clear anymore if both homogeneous and patterned states are linearly stable. For simplicity however, we will still use the bistability nomenclature for referring to the region outside the spontaneous pattern formation zone in which the pattern solution exists.

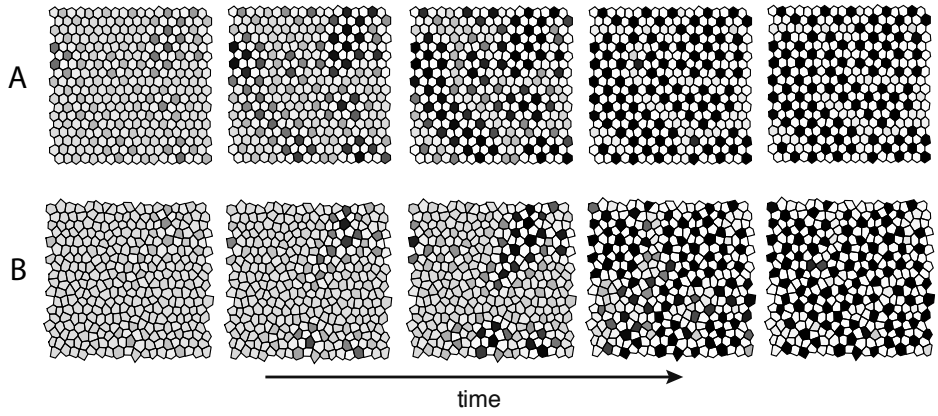

Figure 2.11: Collier model in irregular cellular arrays enables spontaneous pattern formation. Snapshots of the ligand levels from deterministic simulations of the Collier model on (A) less irregular and more irregular (B) arrays of cells starting from the homogeneous fixed point with small random perturbations (see Sec. 2.9.1). From left to right, the time points of the panels are $t = 16, 18, 20, 36, 66$ for (A) and $t = 8, 10, 14, 18, 60$ for (B). In panel (A) we can clearly see the pattern emergence being initiated at different parts of the tissue. The collision of the pattern growing domains lead to the creation of very stable defects, which can be identified in the panels on the right. Irregularity parameters are (A) $\gamma = 0.67$ and (B) $\gamma = 1.6$. Parameter values as in Fig. 2.8.

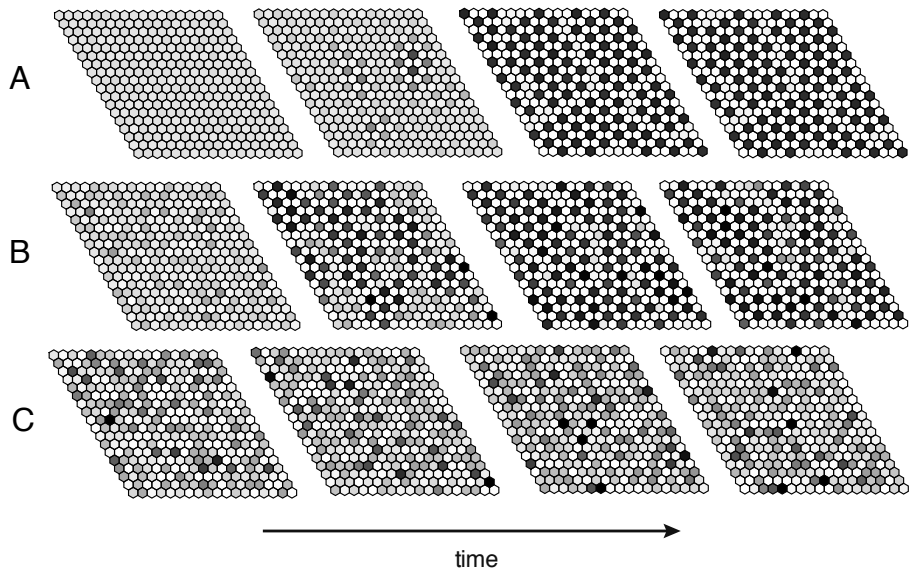

Figure 2.12: A stochastic version of Collier model (Eqs. 2.15) also enables stable pattern formation. Snapshots of the ligand levels showing the time courses of simulation results for (A) low ($V = 2000$), (B) moderate ($V = 100$) and (C) high ($V = 10$) noise intensities. Note that at low and moderate noise intensities defects are still present. At these noise intensities, after an initial transient, cellular states steadily fluctuate around the patterned solutions (see Figs. 2.13 (B-C)). Higher noise intensities like in (C) destroys the pattern given that cells do not keep the same state over time. From left to right, the time points of the panels are $t = 2, 6, 78, 118$ from left to right. Parameter values as in Fig. 2.8.

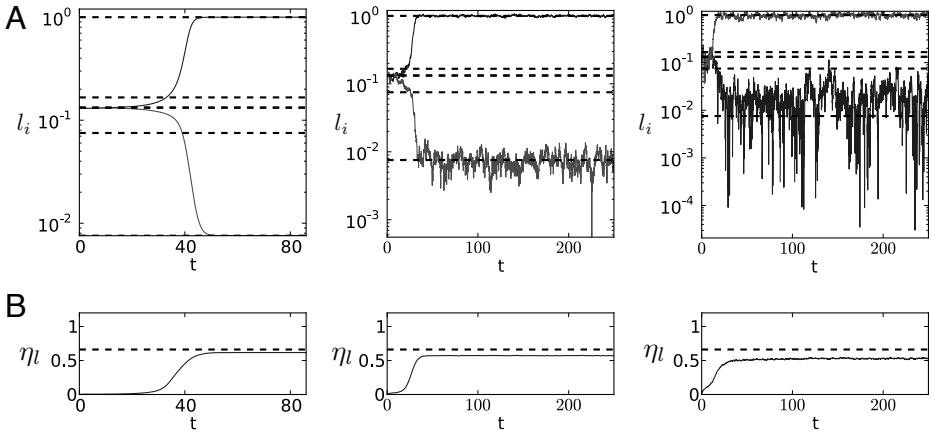

Figure 2.13: Comparing deterministic (left) and stochastic (middle and right) simulation results. Stochastic simulations are performed for low noise (middle, $V = 2000$) and high noise (right, $V = 50$) intensities. (A) Ligand time evolution for two cells and (B) ligand order parameter. Horizontal dashed lines represent the theoretical pattern solutions in (A) and the theoretical order parameter in (B) for a perfect normal lateral inhibition pattern. The ligand order parameter does not reach the theoretical value (calculated for a perfect pattern) because of the presence of defects in the spontaneously formed simulated patterns. Left, middle and right panels correspond to simulations presented in Figs. 2.10, 2.12 (A) and (B) respectively.

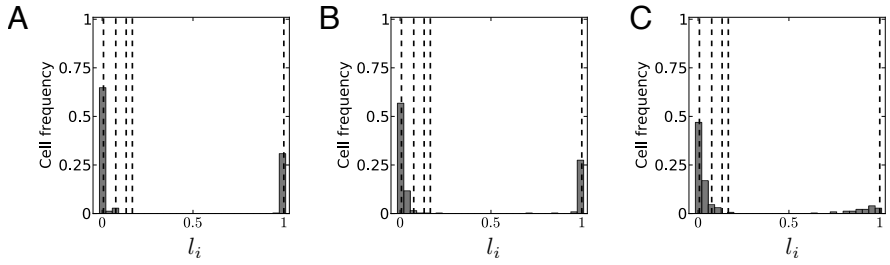

Figure 2.14: Simulation results showing the histograms of the attained cellular fates for (A-B) deterministic simulations on a (A) regular hexagonal array of cells and (B) irregular array of cells (with an irregularity parameter $\gamma = 1.6$), and for (C) a stochastic simulation at moderate noise intensity ($V = 100$) on a regular array of cells. Vertical lines correspond to the theoretical exact solutions for the lateral inhibition pattern. Panels (A), (B) and (C) correspond to simulations presented in Figs. 2.10, Fig. 2.11 (B) and Fig. 2.12 (B) respectively. Defects drive the presence of additional cell states.

not just the classical pattern formation region in which the homogeneous state is linearly unstabilized, but also a larger region where the lateral inhibition pattern solution exists. Simulation results in Fig. 2.15 confirm that in such region lateral inhibition patterns can emerge. Then, during this Thesis we apply both LSA and the reduced model methodology for studying the pattern formation capabilities of different models. Simulation results are performed to confirm our analytical results. In some occasions, simulation results also inform us about nonlinear effects that could not be detected through our analytical tools. During most part of the Thesis we perform simulations on irregular lattices in order to check the robustness of our results. We refer in more detail to some effects of regular *versus* irregular arrays of cells in Chap. 3. In Chap. 3 we discuss in more detail the impact of noise on lateral inhibition dynamics.

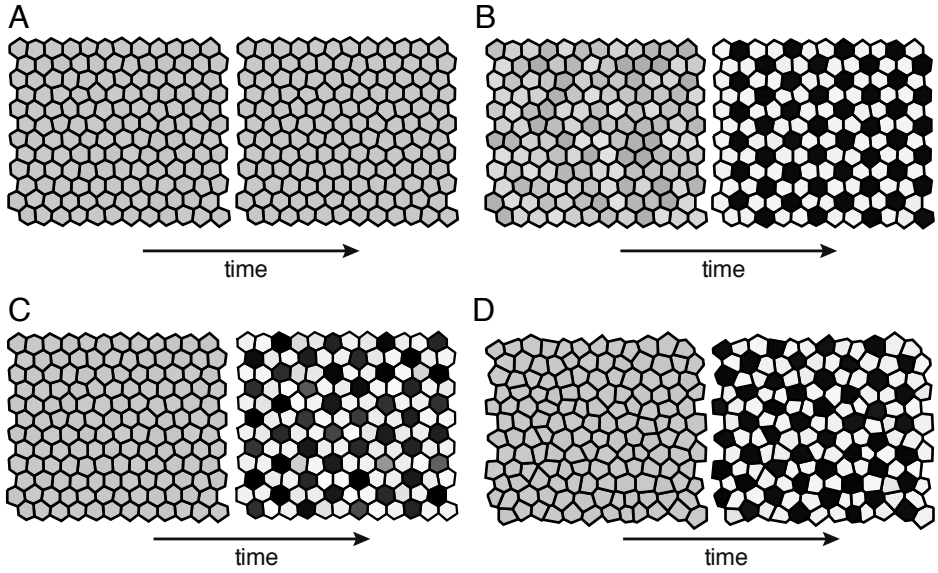

Figure 2.15: Simulation results confirm Collier model is bistable, enabling stable homogeneous and patterned solutions at the same point in the parameter space. Snapshots of the ligand levels showing deterministic simulations (A-B,D) and stochastic simulations (C) results in irregular arrays of cells. (A) Homogeneous initial conditions with small fluctuations ($\delta = 0.1$) lead to homogeneous pattern. (B) Homogeneous state can still be unstabilized by using larger fluctuations at the initial conditions ($\delta = 1$) (C) dynamical noise ($V = 100$) and (D) more irregular arrays. Simulations performed in point B of the diagram presented in Fig 2.6. Parameter values as in Fig. 2.8 but with $b = 150$; irregularity parameter $\gamma = 0.67$ for (A-C) and $\gamma = 1.6$ for (D).

Chapter 3

Dynamics of neurogenic wavefront progression and its interplay with the state of the invaded tissue

3.1 Introduction

In the classical Collier model [10] and in most of the theoretical works on lateral inhibition patterning it is considered that pattern emergence is occurring more or less simultaneously in the whole tissue. For instance, this is the case of the pattern of differentiating scales in the butterfly's wing [96]. Sometimes the fine-grained pattern starts nucleating in a region of the tissue and spreads out to the rest of the tissue. The embryonic vertebrate retina is a paradigmatic example for studying this phenomenon (Fig. 3.1 (A)).

In the retina of vertebrate embryos, the pattern emerges first in the centre of this tissue and spreads out defining a differentiation wavefront which divides the retina in two areas: a differentiating inner domain and a surrounding undifferentiated region [54, 141, 142]. In the inner domain the lateral inhibition process

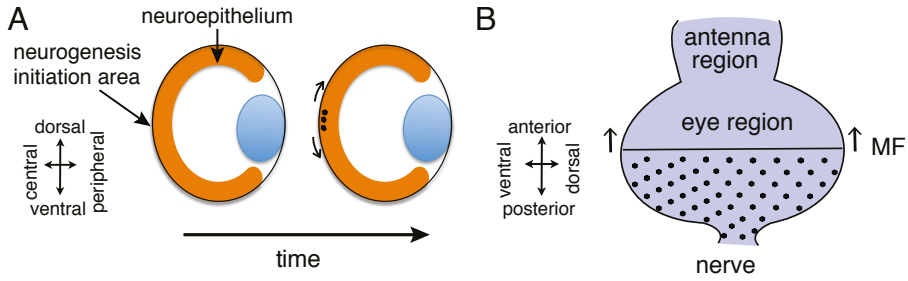

Figure 3.1: Cartoons of neurogenic wavefronts on (A) the vertebrate retina and (B) the eye-antennal imaginal disc of *Drosophila* fruit fly. (A) Eye section cartoons before (left) and after (right) neurogenesis initiation. (B) Cartoon illustrating the progression of the morphogenetic furrow (MF) in *Drosophila* eye-antennal imaginal disc. In both panels, black dots represent neural differentiated cells and black arrows beside them denote wavefront progression.

takes place and it starts the differentiation of the first neurons to be born in this tissue, the differentiated retinal ganglion cells (RGCs) [51, 143–145]. We will refer to this region as the neurogenic domain. In the undifferentiated tissue the proneural genes are not expressed, so lateral inhibition can not be mediated [54]. We call this undifferentiated tissue the non-neurogenic domain. The boundary between both domains moves forward when cells nearby in the neurogenic tissue get differentiated into neurons as a result of lateral inhibition dynamics. These newly differentiated neurons secrete the morphogen Sonic hedgehog (Shh) [142]. In this regard, Shh has been observed to diffuse from differentiated RGCs in chick [143], mouse [146] and zebrafish [51]. Such morphogen expressed by newly differentiated neurons spreads into the non-neurogenic tissue and activates in turn the lateral inhibition circuitry in its cells, converting the invaded non-neurogenic tissue into new neurogenic tissue. This scenario is what we call a self-regulated wavefront.

This morphogen-dependent spreading of neurogenesis is reminiscent of the progression of photoreceptor differentiation in the *Drosophila* larval eye [147], which is placed in the eye-antennal imaginal disc (Fig. 3.1 (B)). Photoreceptor differentiation occurs in a straight indentation, the so-called morphogenetic furrow (MF), that moves from the posterior to the anterior part of the imaginal

disc (Fig. 3.1 (B)). In such indentation there is the expression of the proneural gene *Atonal* (*ato*), driving photoreceptors differentiation. MF progression is also dependent on the release of the morphogen Hedgehog (Hh) which is secreted by the newly differentiated photoreceptors [147]. Furthermore, *hairy* (*h*), a proneural gene repressor, and *extra macrochaetae* (*emc*), an antagonist of the proneural gene products, are both expressed just ahead of the MF [148], an area that, in the lack of such two genes, it would have potential neurogenic capacity due to the indirect influence of MF-derived Hh [149]. Therefore, MF progression is another paradigmatic example for studying the progression of a neurogenic self-regulated wavefront, invading a non-neurogenic tissue.

Cells located at the neurogenic wavefront are in direct contact with cells in the non-neurogenic tissue, which are not undergoing lateral inhibition. The initial value of the Delta ligand in non-neurogenic cells sending inhibitory signal in the border might be important for regulating the state of the cells at the neurogenic wavefront, and therefore its progression. If Delta values in such non-neurogenic cells is Notch-dependent, then Notch values will be also relevant.

Indeed, generalized *Delta* expression is often observed in prospective neural tissues and neurogenic boundary regions. For instance, in the early zebrafish embryo, strong *deltaD* expression delineates the whole developing retina a few hours before the initiation of neurogenesis in this tissue [150, 151]. In both the avian and murine retina, *Delta-like 1* (*Dll1*) is expressed more peripherally than its homolog *Dll4*, being detected in a high proportion of mitotically-active progenitor cells [152–154]. In *Drosophila*, *Delta* (*Delta*) expression has been shown to precede achaete protein accumulation in microchaeta proneural stripes [155]. Within the eye imaginal discs of *Drosophila*, on the surfaces of unpatterned cells ahead of the MF [156–159], both Delta and Notch expression have been described in the absence of proneural gene expression [148]. As in other neural structures, generalized *Delta* expression ahead of the MF seems to be independent of canonical Notch signaling [160] since *h* and *emc*, two regulatory genes known to respectively prevent proneural gene expression and function, are both expressed in this region [148].

Overall, these observations suggest that generalized *Delta* expression ahead of the neurogenic wavefront could be relevant in the process of lateral inhibition during neurogenesis. This is indicative that initial conditions ahead of the domain

where lateral inhibition is occurring might be relevant.

The goal of this study is to decipher the role of this high *Delta* expression in the invaded undifferentiated area for proper pattern emergence. The lack of knowledge of how Delta is regulated ahead of the wavefronts makes difficult to design any experiment with the current available techniques. Therefore, we adopt a theoretical and computational approach to unravel this question.

Theoretical studies on moving wavefronts of lateral inhibition have recently come to attention [97,104,109,111,112,161]. These studies addressed the problem of how a wavefront can sweep across a field of identical cells and leave behind a fine-grained pattern of different cell types. Most of them addressed general theoretical aspects of the traveling waves solutions in the Collier model [109, 111, 112] or in a more general model of three equations per cell [104] proposed by Owen [100]. For instance, Plahte and Oyehaung [109] focused on aspects regarding pattern initiation and featured the kind of propagation (pulled *versus* pushed fronts). Owen [104] studied the velocity and propagation failure of moving fronts generated by its model and simpler models on discrete cell lattices.

More recently, a couple of theoretical works revealed different aspects of the wavefront of photoreceptor differentiation in *Drosophila* eye-antennal disc, in collaboration with experiments [97,161]. The authors focused on a simplified model of the genetic network, without dealing with the cell-to-cell interactions mediated by Notch pathway but with other essential components, like a positive feedback loop in *Atonal*. Their model also dealt with a wavefront that was self-regulated through a diffusible morphogen. They showed that their system exhibited a high sensitivity on the initial conditions, and proposed that there was a pattern formation mechanism of switch-and-template in which the propagating pattern used the initial conditions as a template to reproduce.

Our theoretical study focuses on the Notch signaling pathway and a morphogen. Our particular goal is to dechiper how the wavefront progression depends on the state that is being invaded, *i.e.* on the Delta levels in the non-neurogenic tissue. We take the developing chick retina as a model system for studying this issue. Moreover, we test our model in the context of MF progression in the *Drosophila* eye.

3.2 Inspection of the invaded tissue state in the embryonic chick retina

Herein we study the spatiotemporal pattern expression of the *Delta* gene (*Dll1* in the chick retina), the *Notch* gene (*Notch1*), *Lunatic Fringe* (*lFng*), which is a modulator of Notch-Delta trans-interactions being crucial for Notch signaling [162], and other related genes involved in neurogenesis. We use the housekeeping *Gapdh* gene as a control, since it is constantly expressed for basic cellular functions in all cells. The experiments presented in this section have been performed by our collaborator Dr. José María Frade (Cajal Institut, CSIC, Madrid, Spain).

In RT-PCR experiments for mRNA detection, *Dll1* is already found at Hamburger-Hamilton[1] (HH) stage HH15 (Fig. 3.2), a stage in which neurogenesis is about to start [141]. At HH15, both *Notch1*, *lFng*, and the proneural genes *Neurog2*, *NeuroD1*, *NeuroD4*, and *Atoh7* can hardly be detected (Fig. 3.2). Together, it indicates that elevated *Dll1* expression in the chick retina is already present at a stage when neurogenesis has not started yet. Indeed, *Dll1* expression is maintained throughout development following a pattern similar to that of the housekeeping gene Gapdh. In contrast, both *Notch1* and the mentioned proneural genes steadily increase their expression levels at subsequent temporal stages, in accordance with the spreading of the neurogenic region towards the peripheral retina (Fig. 3.2). Just the proneural gene *Acsl1* is first detected at HH20 (Fig. 3.2), which is a relatively late stage of chick retinal development. High levels of RGC-specific marker *Pou4f3* are first observed at HH24 (Fig. 3.2), as expected from its late expression in a subpopulation of differentiated RGCs [164].

The distinctive expression mRNA pattern of *Dll1* is confirmed by *in situ* hybridization. As shown in Fig. 3.3, the *in situ* hybridization technique allows us to see the different mRNA expression patterns through dark blue staining in the tissue, providing spatial information of the gene expression that we can not have through RT-PCR. At stage HH19, *Dll1* expression is detected throughout most of the retinal neuroepithelium, reaching the peripheral retina (Fig. 3.3 (A)). In contrast, *Notch1* expression is restricted to the central retina (3.3 (B)), where neurogenesis takes place as evidenced by the expression of the RGC-specific

[1] See [163] for an explanation of the nomenclature for these early embryonic stages in chick.

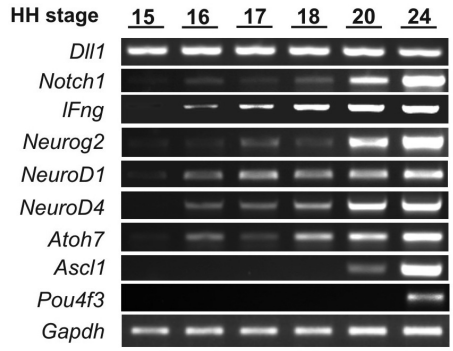

Figure 3.2: mRNA temporal expression pattern of genes involved in retinal neurogenesis through RT-PCR analysis from chick retinas at the indicated Hamburger-Hamilton developmental stages.

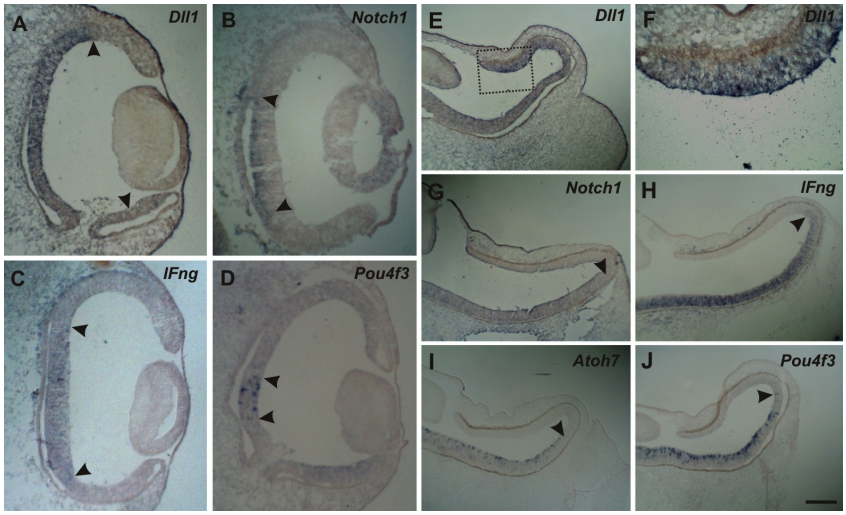

Figure 3.3: Spatial expression pattern of genes involved in retinal neurogenesis. Sections from HH19 (A-D) or HH25 (E-J) chick retinas are shown. Panels illustrate representative *in situ* hybridizations indicating the different mRNA transcripts (labeling in dark blue). Box included in (E) is shown at high magnification in (F). Arrowheads indicate boundaries of expression. Bar: 60 μm (A-D), 150 μm (E-J).

marker *Pou4f3* in just a few cells (Fig. 3.3 (D)). These observations are further confirmed at a later developmental stage (HH25) (Fig. 3.3 (E-H)), as previously shown by [152]. Moreover, the expression of *Notch1* is correlated with lFng (Fig. 3.3 (C,H)), indicating that in such region Notch is probably signal-productive when trans-interacts with Delta.

This data indicates that Delta is expressed before neurogenesis starts in the embryonic chick retina. Moreover, the fact that the proneural genes are not activated and these genes mediate the Delta inhibition due to Notch, this indicates that *Delta* expression ahead of the neurogenic wavefront is Notch-independent, and therefore in such regions lateral inhibition is not taking place yet.

3.3 A model for self-regulated neurogenic wavefront progression

3.3.1 Model equations

To dechiper the role played by the state of the undifferentiated tissue ahead of the neurogenic wavefront, we use a mathematical model of the lateral inhibition process that is dependent on a diffusible morphogen. We model the developing retina as a two dimensional tissue of irregularly shaped cells (Figs. 3.4, 3.5 and 3.7), where for simplicity interkinetic nuclear movement [52,53,65], cell death, or cell division are not considered (in Sec. 3.5 we discuss these aspects). Developmental events occurring after the advance of the initial neurogenic wave are out of the scope of this work.

The core of lateral inhibition dynamics acting in the neurogenic domain is provided by the Collier model [10] (Sec. 1.5). We take into account two additional variables, namely, a readout of differentiation species and a morphogen[2]. The readout of differentiation can be identified with Neurog2 and controls how close a cell is to start differentiating. Since Notch inhibitory activity is downregulated just prior to RGC differentiation [165–167], the Delta-Notch lateral inhibition dynamics is stopped and the cell differentiates when its level of readout reaches

[2]Note Dl1 is not a good readout since positive Dl1 cells (in which Dl1 is independent of Notch) that are entering into lateral inhibition dynamics could straightforwardly differentiate.

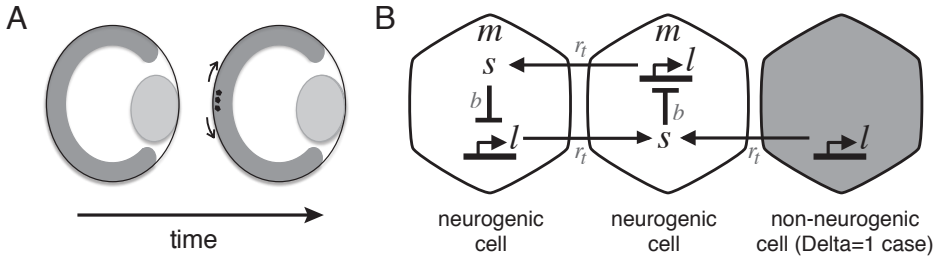

Figure 3.4: A model for lateral inhibition in the chick retina. (A) Cartoon of neurogenic wavefront on the vertebrate retina (see a more detailed cartoon in Fig. 3.1) (B) Diagram illustrating the mathematical model. The presence of sufficient amount of morphogen ($m_i > m_c$) makes cells neurogenic (left, center). These neurogenic cells are able to express proneural genes. Notch activation in these cells by Delta in neighboring cells triggers a Notch signal (s) inhibiting proneural gene expression and Delta ligand (l) expression. During neurogenic wavefront progression, neurogenic cells at the wavefront (center) are in direct contact with non-neurogenic cells ahead of it (right). In the wild type, non-neurogenic cells (right) are able to constitutively express Delta (Delta=1 case). This expression is lacking in the Delta=0 case discussed in the main text.

an established threshold. We model the readout regulation by replicating the ligand regulation.

The morphogen is set to diffuse from differentiated neurons and can be identified with Sonic hedgehog (Shh) or any other putative morphogen released from newly differentiated RGCs [168]. In the model, the non-neurogenic cells ahead of the neurogenic wavefront that become exposed to high enough morphogen concentrations initiate lateral inhibition dynamics (Figs. 3.4, 3.7).

Neurogenesis in the embryonic retina is characterized by a single differentiation front extending from the center of the tissue [141, 142]. Though, lateral inhibition patterning can spontaneously start nucleating from different points if no subject to extra-regulation [109] (Sec. 2.10). For this reason, we model our tissue as an initial non-neurogenic cellular array with several localized morphogen sources at the center of the tissue as an extra regulatory element. Indeed, this *in silico* extraregulatory element is consistent with pattern initiation observations in the zebrafish [51, 144, 169] and chick retinas [169].

The deterministic temporal dynamics for the concentrations of the l_i (ligand),

s_i (signal), r_i (readout) and m_i (morphogen) species in each cell i are described by the following dimensionless equations:

$$\frac{\mathrm{d}s_i}{\mathrm{d}t} = \left\{ \frac{r_t \langle l_i \rangle}{1 + r_t \langle l_i \rangle} - s_i \right\} \Theta(m_i - m_c)\Theta(y_c - y_i) \tag{3.1a}$$

$$\frac{\mathrm{d}l_i}{\mathrm{d}t} = v \left\{ \frac{1}{1 + b s_i^h} - l_i \right\} \Theta(m_i - m_c)\Theta(y_c - y_i) \tag{3.1b}$$

$$\frac{\mathrm{d}y_i}{\mathrm{d}t} = v \left\{ \frac{1}{1 + b s_i^h} - y_i \right\} \Theta(m_i - m_c)\Theta(y_c - y_i) \tag{3.1c}$$

$$\frac{\mathrm{d}m_i}{\mathrm{d}t} = u \left\{ D\nabla_i^2 m_i - m_i + \Theta(y_i - y_m) \right\} \quad , \tag{3.1d}$$

where the new parameters are u, being the ratio of morphogen degradation with respect to the signal degradation, m_c is the morphogen concentration threshold over which a cell has lateral inhibition dynamics, and y_c is the readout threshold over which a cell is committed for differentiation, freezes its lateral inhibition and readout dynamics, and becomes a source of morphogen. Θ denotes the Heaviside step function, which is 1 when its argument is positive and 0 otherwise. The parameters r_t and b are the same as in the Collier model (Sec. 2.1), the trans-interaction strength and the ligand inhibition strength respectively. This model accounts for two spatial coupling mechanisms: the cell-to-cell coupling on an irregular array, $\langle l_i \rangle$ (Eq. 2.10, [131]) and the diffusion term due to the morphogen, $D\nabla_i^2 m_i$, where ∇_i^2 is the discrete Laplacian on a Voronoi lattice [170]:

$$\nabla_i^2 m_i = \frac{1}{A_i} \sum_{j \in nn(i)} \frac{e_{ij}}{\gamma_{ij}} (m_j - m_i) \quad , \tag{3.2}$$

being D the non-dimensional diffusion rate of morphogen, A_i the non-dimensional the area of cell i, e_{ij} is the length of the boundary shared between cells i and j, and γ_{ij} the distance between cell nodes i and j (Fig. 3.5 and Sec. 2.9.2). In a regular hexagonal array, by setting $\gamma_{ij} = 1$, we get $A_i = \sqrt{3}/2$ and $e_{ij} = \sqrt{3}/3$ so we obtain the non-dimensional expression of the discrete Laplacian in a hexagonal lattice, which reads $\nabla_i^2 m_i = \frac{2}{3} \sum_{j \in nn(i)} (m_j - m_i)$ (App. A).

The initial cells acting as morphogen sources have the same dynamics than the rest of the cells (Eqs. 3.1b-3.1c), except for the morphogen concentration,

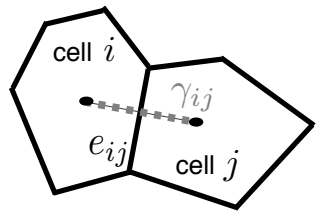

Figure 3.5: Scheme of two interacting irregular cells. e_{ij} and γ_{ij} are the length of the boundary shared between adjacent cells i and j and the distance between the two adjacent cell nodes respectively. Both quantities are necessary for the computation of the discrete Laplacian (Eq. 3.2). A dashed gray line is drawn between the two adjacent cell nodes.

which reads

$$\frac{\mathrm{d}m_i}{\mathrm{d}t} = \left\{1 + D\nabla_i^2 m_i - m_i\right\} \quad . \tag{3.3}$$

Note that for high enough morphogen ($m_i > m_c$) and high threshold for cell differentiation ($y_i > y_c$) the model equations (Eqs. 3.1b-3.1d) can be reduced to the Collier model (Eqs. 1.1a-1.1b).

We include dynamical noise for ligand (l_i), signal (s_i) and readout (r_i) (Eqs. 3.1b-3.1c) in the way we described in Sec. 2.3.

We perform stochastic simulations with parameter values: $r_t = 10$, $b = 10000$, $v = 1$, $u = 0.1$, $h = 4$, $D = 0.5625$, $m_c = 0.001$, $y_c = 0.5$, $V = 2000$ in non-dimensional units unless otherwise stated. We choose the exponent $h = 4$ to take into account in an effective way the nonlinearity introduced by intermediate processes not explicitly included in our phenomenological model. The value $D = 0.5625$ corresponds to an effective range of morphogen influence of approximately 2-3 cells from the morphogen source cell. The ligand inhibition strength b and the trans-interaction strength r_t are the control parameters of our study. We model the spatial arrangement and shape of cells in the developing chick retina building an irregular lattice of cells based on a Voronoi tesselation (see Sec. 2.9.2 for details). Unless otherwise stated, in this work we use lattices of 49×49 irregular cells with $\Delta = 1$ and $\gamma = 1.6$ (Sec. 2.9.2).

To avoid boundary effects, we stop the simulations when the first cells at a distance of five cells from the simulation boundary enter into lateral inhibition

dynamics. To avoid unnecessary long simulation runs, we also set a rule to stop simulations with extremely slow dynamics. The boundary condition for the morphogen m_i at the boundary of the simulated field of cells is set to zero morphogen concentration.

3.3.2 Formal characterization of the growing neurogenic domain

We define three different observables to characterize pattern emergence: the neural density ρ, the front morphology parameter Γ, and the effective velocity of the moving front, v_f. This quantification will enable a systematic exploration of the pattern formation capabilities of the model across the parameter space.

Neural density

We define the neural density parameter ρ as $\rho = n_{n*}/n_n$, with n_{n*} being the number of neural cells (*i.e.* number of cells fulfilling $y_i \geq y_c$) and n_n the total number of cells within the neurogenic domain (*i.e.* number of cells fulfilling $m_i \geq m_c$). $\rho \approx 0$ denotes no neural differentiation; $\rho \approx 1/3$, the regular lateral inhibition pattern; and $\rho \approx 1$ implies massive neural differentiation.

Front morphology parameter

We define the front morphology parameter for the circular growing wavefront[3] Γ as $\Gamma = cn_b^2/(n_n)$, where n_b is the number of neurogenic cells in the border of the neurogenic domain. The prefactor c is defined such that $\Gamma \approx 1$ for a regular circular front morphology, as described as follows.

For obtaining c we can study the value of Γ on what corresponds a regular growing neurogenic domain in a hexagonal array of cells. Let´s consider a neurogenic domain starting with a single neurogenic cell (stage named $i = 0$), and then growing by successive rings of neurogenic cells, what we refer as stages $i = 1, 2, ..., n$ when we find $1, 2, ...n$ rings of cells surrounding the central cell.

[3]We refer to circular growing wavefront when the neurogenic region grows in the radial direction.

The front morphology parameter at the stage n will read

$$\Gamma_n = \frac{c(p_n)^2}{\sum_{i=0}^{n} p_i} \quad , \tag{3.4}$$

where p_i is the number of cells in the boundary at the stage i, and it reads

$$p_i = \begin{cases} 1 & \text{for } i = 0 \\ 6i & \text{for } i \neq 0 \end{cases} \quad . \tag{3.5}$$

Taking into account that $\sum_{i=1}^{n} i = n(n+1)/2$ it can be seen that

$$\lim_{n\to\infty} \Gamma_n = \lim_{n\to\infty} \frac{c(p_n)^2}{1+\sum_{i=1}^{n} p_i} = \lim_{n\to\infty} \frac{c(6n)^2}{1+6n(n+1)/2} = 12c \quad . \tag{3.6}$$

We put $c = 1/12$, so we will have $\Gamma \approx 1$ when we have a large neurogenic domain with a regular shape[4,5]. $\Gamma \geq 1.5$ denotes fronts with a strong irregular morphology. Note that this parameter is related to the roundness shape descriptor [171].

Front velocity

The effective radial velocity of the circular front v_f has been measured by fitting the time-evolution of the non-dimensional area of the neurogenic growing domain $A(t)$ to the expression

$$A(t) \equiv \pi v_f^2 t^2 \tag{3.7}$$

(see an example in Fig. 3.6). More formally, let $u(t,\theta)$ be the radius of the neurogenic region in a particular time t for an angle θ, so that the differential area portion to be integrated can be chosen as the triangle $\mathrm{d}A = u^2(\tau,\theta)d\theta/2$. By assuming that the radius grows linearly with time, $u(t,\theta) \approx v(\theta)\tau$ being $v(\theta)$ a radial velocity, we can say that

$$A(t) = \int \mathrm{d}A(t) = \frac{1}{2}\int_0^{2\pi} u^2(t,\theta)\mathrm{d}\theta \approx \frac{t^2}{2}\int_0^{2\pi} v(\theta)^2\mathrm{d}\theta = \pi\langle v(\theta)^2\rangle t^2 \quad . \tag{3.8}$$

[4]In the perfect hexagonal array of cells the shape of the neurogenic tissue that grows regularly in the radial direction has a hexagonal or circular form, and in irregular arrays of cells this shape is circular. Small regular domains will have $\Gamma \lesssim 1$ values, tending to 1 when they become larger regular domains since Γ_n is an increasing sequence in n.

[5]In the continuum limit, for a circular growing neurogenic domain of radius $u(t)$ we would have $\Gamma = c\frac{(2\pi u(t))^2}{\pi u(t)^2} = 4\pi c$.

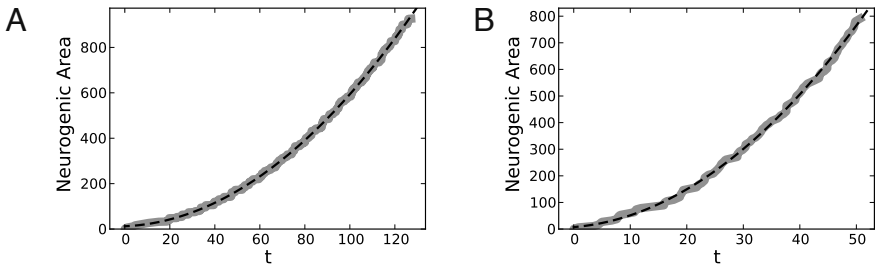

Figure 3.6: Studying the dynamics of the moving front. Area of the neurogenic region along time t for (A) the Delta=1 and (B) the Delta=0 cases. Gray thicker lines indicates the simulation results, and the thin dashed lines are fitting curves. Deterministic simulation results for a system of 49×49 regular hexagonal cells with one central morphogen source. Other parameters and details as indicated in Sec. 3.3.1. The snapshots corresponding to these simulation results are shown in Fig. 3.22 (C).

According to Eq. 3.8, if the velocity does not change a lot in time for a certain direction, the area of the neurogenic domain increases quadratically with respect to the time (Fig. 3.6). Following Eq. 3.8 and comparing it with the definition of $A(t)$ (Eq. 3.7), $v_f = \sqrt{\langle v(\theta)^2 \rangle}$. Hence, for a growing circular domain v_f is the front (radial) velocity v given that $u(t, \theta) = u(t)$ so

$$A(t) = \pi u(t, \theta)^2 = \pi v^2 t^2 \quad . \tag{3.9}$$

For a growing domain with irregular morphology v_f is an effective velocity of growth (Fig. 3.6).

For the case of the planar growing domain, we compute the effective growing velocity v_f by fitting the expression $A(t) = L v_f t$ with the simulated results, where L is the length of the bottom boundary of the simulated tissue, which is 49 cells in all simulations.

3.4 Results

3.4.1 A feedback-regulated wavefront that enables regular neurogenesis

The presented model (Eqs. 3.1-3.3) has a feedback between the morphogen and the lateral inhibition module, leading to a self-regulated wavefront. This model can drive the following sequence of events (Fig. 3.7). An initial morphogen source (cells with green layout in the first snapshot of Fig. 3.7) enables cells exposed to high levels of morphogen to enter into lateral inhibition dynamics (white cells in second snapshot of Fig. 3.7). Driven by lateral inhibition, these cells may reach high levels of readout ($y_i > y_c$) and become differentiating RGCs (black cells in third snapshot of Fig. 3.7). These differentiating cells then freeze the ligand, signal and readout dynamics, and in turn become new sources of morphogen, which diffuses across the tissue. As a result, an expanding domain of active neurogenesis, where lateral inhibition takes place, can spread through non-neurogenic regions giving rise to neurogenic wavefronts (fourth and fifth snapshots of Fig. 3.7). When initial morphogen sources are all closely located at the center of the retina, this model is able to account for a single neurogenic domain that grows regularly and homogeneously and leaves behind a lateral inhibition pattern of differentiated neurons, as occurs in wild-type chick retinas, as shown in Fig. 3.7 [141]. A full characterization of the lateral inhibition pattern formed in terms of all model variables is shown in Fig. 3.8 (see initial conditions in the next section).

This feedback between lateral inhibition and the morphogen sources robustly enables a single growing patterned domain invading the non-neurogenic tissue.

3.4.2 Notch-independent ligand expression ahead of the neurogenic wavefront is crucial for the neurogenic process in the chick retina

To decipher the influence of Dll1 expression ahead of the neurogenic wavefront, we computationally evaluate two different situations. A first wild-type scenario (hereafter Delta=1) which consists of generalized expression of Delta ligand in

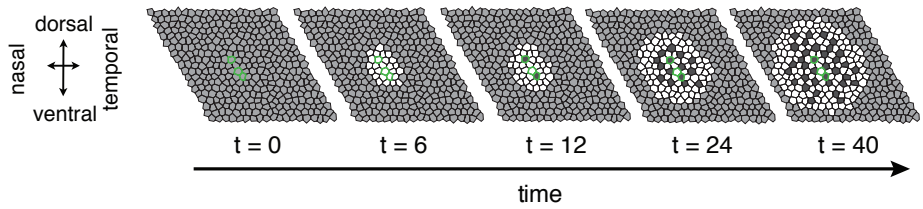

Figure 3.7: Snapshots of sequential time points of a wild-type simulation (Delta=1 case) of wavefront propagation, showing only the central part of the simulated tissue. Grey: non-neurogenic cells; white: neurogenic cells not committed to neural fate; black: neurogenic cells committed to neural fate. The three cells with green contour in all panels denote the initial sources of morphogen. Other parameters and details as indicated in Sec. 3.3.1.

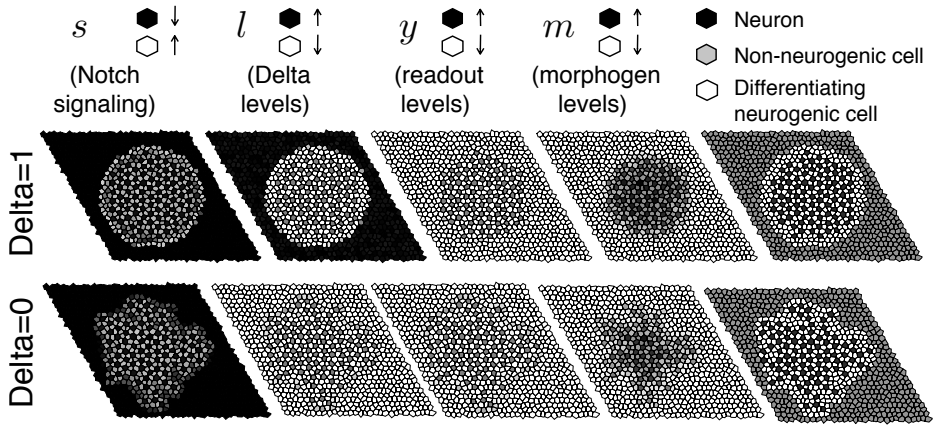

Figure 3.8: Full single-cell state characterization of a neurogenic growing domain for Delta=1 (up) and Delta=0 (bottom) conditions. All panels correspond to the same neurogenic domain. Each row depicts the level of a different state variable (which is indicated next to the snapshot). Grayscale codes for each variable are indicated in the figure. Notice that Notch has opposite grayscale code. The right panel corresponds to the type of snapshot shown in Fig. 3.4 (B), depicting the differentiation state of cells. To facilitate single-cell resolution, it is shown only the central part of the overall tissue. We set a single central cell acting as first source of Shh morphogen. Other parameters and details as indicated in Sec. 3.3.1.

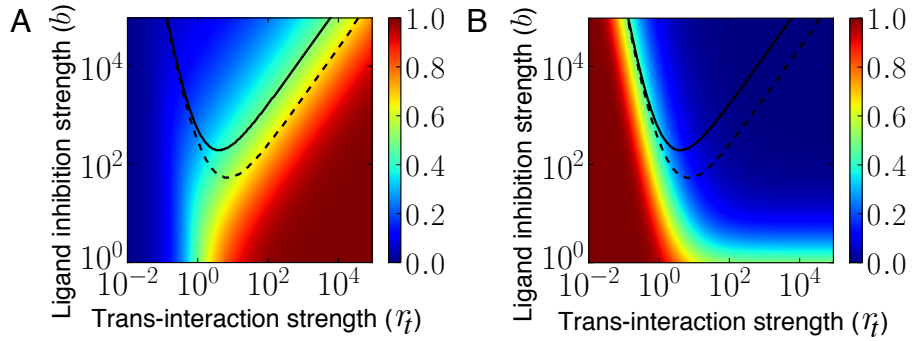

Figure 3.9: Theoretical estimation of the pattern formation region for the model of wavefront progression (lines), and density plot of the homogeneous steady states for the Collier model in the r_t-b parameter space of (A) Notch signal and (B) Delta levels. We find the homogeneous solutions by solving Eq. 2.49. Lines stand for theoretical estimations of the pattern forming region (Sec. 2.10.1 and Fig. 2.6).

non-neurogenic regions (Figs 3.7, 3.8 up), and a second mutant-like scenario (hereafter Delta=0) in which non-neurogenic regions have no Delta expression (Fig. 3.8 bottom). Specifically, we used the following initial conditions:

- Wild type like or Delta=1 case (Fig. 3.8 up): high initial ligand concentration in all cells ($l_i(t=0) = 1 - 0.1U_i$, where U_i is a uniform random number between 0 and 1).
- Delta=0 case (Fig. 3.8 bottom): null initial ligand concentration in all cells ($l_i(t=0) = 0$).

In both cases, there is an initial low concentration of all the other species in all cells ($s_i = 0$, $r_i = 0$, $m_i = 0$ at $t = 0$). One or few initial morphogen sources are located at the center of the tissue.

Since quantitative values of all model parameters are unknown, we perform a study of wavefront progression across the model parameters controlling lateral inhibition dynamics (r_t and b).

As a first estimation of where patterning should be expected, we make use of our theoretical analysis of the Collier model (Sec. 2.10.1). Such analysis is based on a model in which lateral inhibition equally affects a whole tissue with periodic boundary conditions. For this reason, these theoretical results are independent

of Delta=1 and Delta =0 conditions. These results are repeatedly depicted with lines for instance in Figs. 3.9 and 3.10 (we use the same lines found in Fig. 2.6). As we saw in Sec. 2.10.1, this analysis indicates that the patterned state ($\rho = 1/3$) exists and is stable to small perturbations above the dashed line, whereas the homogeneous state with no pattern ($\rho = 0$ or $\rho = 1$) is stable to small perturbations below the solid line. The dashed line is computed through the reduced model of Collier equations (Eq. 2.56), and the continuous line is computed through LSA (Sec. 2.10.1). The steady state of Collier equations indicate that low trans-interaction strengths ($r_t << 1$) will drive a homogeneous neural phenotype, since $s_i \approx r_t \langle l_i \rangle \approx 0$ and therefore $l_i \approx 1$ in the steady state, while high trans-interaction strengths ($r_t >> 1$) will completely inhibit neurogenesis, since $s_i \approx 1$ and therefore $l_i \approx 0$ (Sec. 2.10.1 and Fig. 3.9).

We then analyze our model numerically by performing extensive numerical integration of the dynamics across the r_t–b parameter space. We discretized such parameter space in a logarithmic spaced grid of 35×25 points such that there is a resolution of 5 points in between every order of magnitude along each parameter. The results are described below.

Delta=1 case

In the Delta=1 situation (Figs. 3.10-3.12), a domain of active neurogenesis grows creating a lateral inhibition pattern ($\rho \approx 1/3$), mostly above the dashed line. In this region the neurogenic front advances with a regular circular shape as measured by the front morphology parameter ($\Gamma \approx 1$, Fig. 3.11) and with a moderate average front velocity ($v_f \approx 0.13$ in non-dimensional units, Fig. 3.12). Outside this region, two opposed situations are found (Figs. 3.10 (A) and 3.12 (A)): massive neurogenesis ($\rho \approx 1$) with fast wavefront progression ($v_f \approx 0.75$), and totally inhibited neural differentiation ($\rho \approx 0$) with no wavefront progression ($v_f \approx 0$). Examples of the neurogenic domains that are formed for different parameter values, represented by points A, B, C and D in Figs. 3.10-3.12, are shown in Fig. 3.13 (left panels).

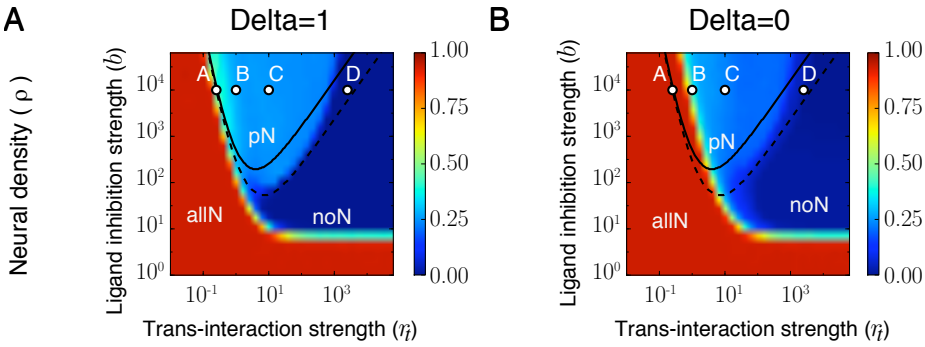

Figure 3.10: Delta expression by non-neurogenic precursors promotes the typical lateral inhibition pattern in a larger region of the parameter space than when Delta is not expressed in the non-neurogenic precursors. Parameter space characterization of the density of neurons ρ for Delta=1 (wild type like, (A)) and Delta=0 (B) conditions. Color bands denotes the non-dimensional values of ρ. These values result from averages over 10 different simulations of the stochastic model at final simulation times. Lines stand for theoretical estimations of the pattern forming region (Sec. 2.10 and Fig. 2.6). Letters A-D inside the diagrams denote different chosen representative points of the parameter space (patterns depicted in Fig. 3.13). The following abbreviations have been used to indicate different kinds of patterns: noN: no neurogenesis, allN: massive neurogenesis, pN: common lateral inhibition pattern of neurogenesis. Parameter values are indicated in Sec. 3.3.1.

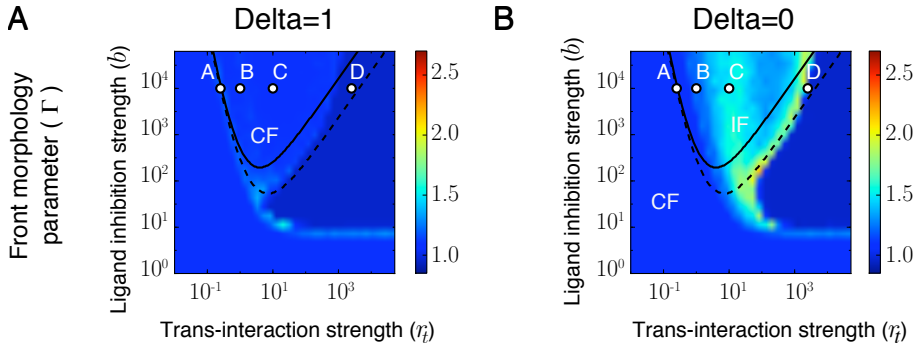

Figure 3.11: Delta expression by non-neurogenic precursors promotes neurogenic wavefronts with more circular wavefront morphology, while in its absence, irregular wavefronts take place. Parameter space characterization of the front morphology Γ for Delta=1 (wild type like, (A)) and Delta=0 (B) conditions. Color bands denotes the non-dimensional values of Γ. The following abbreviations have been used to indicate different kinds of patterns: CF: circular front, IF: irregular front. Other panel details as in Fig. 3.10.

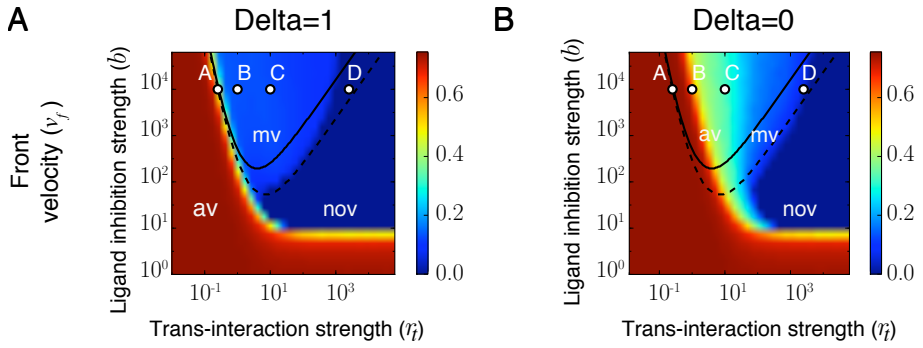

Figure 3.12: Delta expression by non-neurogenic precursors slows down the wavefront progression and conferes a robust velocity across the parameter space, while in its absence, wavefront progression is accelerated and it changes with r_t. Parameter space characterization of the velocity of the front v_f for Delta=1 (wild type like, (A)) and Delta=0 (B) conditions. Color bands denotes the non-dimensional values of v_f. The following abbreviations have been used to indicate different kinds of patterns: av: accelerated front velocity, mv: intermediate front velocity, nov: no front propagation. Other panel details as in Fig. 3.10.

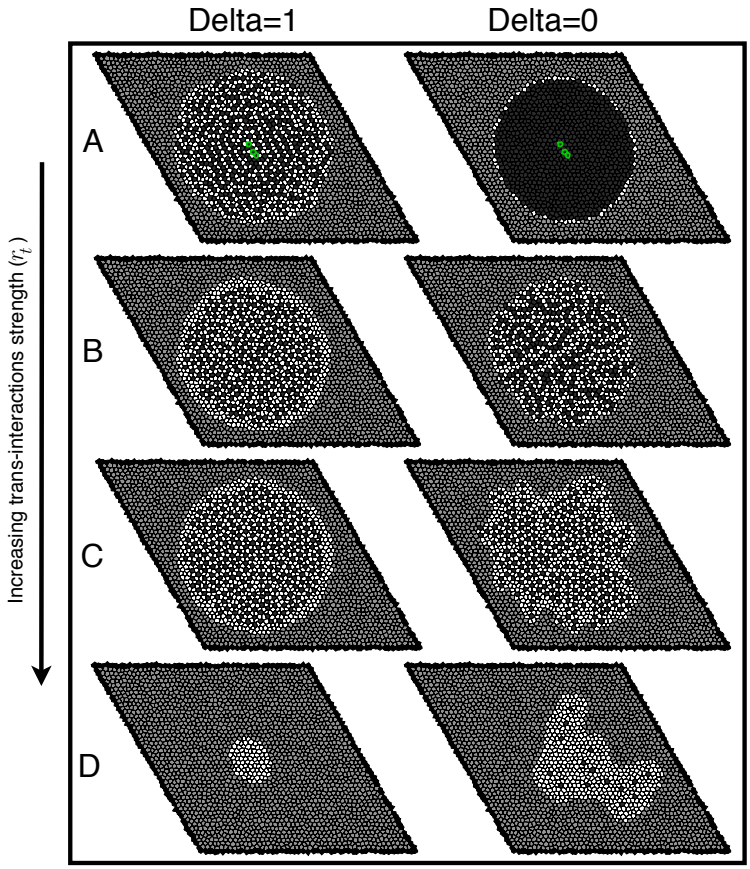

Figure 3.13: Delta expression by non-neurogenic precursors promotes regular lateral inhibition patterning. Snapshots of simulations of the neurogenic domain for Delta=1 (wild type like, left column) and Delta=0 (right column) conditions. Different panels correspond to letters depicted in Figs. 3.10-3.12 with trans-interaction strength values (A) $r_t = 0.2511$, (B) $r_t = 1$, (C) $r_t = 10$, (D) $r_t = 2511$, other parameters as specified in Sec. 3.3.1. Color code for cells and contours as in Fig. 3.7. Patterns similar to (C) are typical for a wide region of parameter space. The same initial cell sources of morphogen where used in all panels and are only shown in (A). Tissue boundary cells are depicted in black. Each snapshot corresponds to the final simulation time (see whole dynamics in Supp. Movies 1-4 in [54]).

Delta=0 case

In the Delta=0 case (Figs. 3.10 (B)), massive neurogenesis (*i.e.* $\rho \approx 1$) persisted for stronger trans-interaction strength (r_t) as compared with the Delta=1 situation (Figs 3.10 (A) and 3.13 (A)). Therefore, stronger trans-interaction strength (r_t) is required in the absence of Delta in the non-neurogenic region to drive lateral inhibition patterning, which as a result arises in a reduced parameter space area (Figs. 3.10 and 3.13). At high r_t values sparse patterns appear whose wavelength is set by the diffusing morphogen (Fig. 3.13 (D) right). Interestingly, our analysis also shows that the neurogenic front acquires an irregular shape when Delta expression is absent from the non-neurogenic region (Fig. 3.13 (C)). The irregular shape of the wavefront is characterized by high values of the front morphology parameter ($\Gamma \geq 1.5$, Fig. 3.11 (B)). Front deformation occurs throughout most of the region where the lateral inhibition pattern (neural density $\rho \approx 1/3$) arises. This result indicates that the presence of Delta throughout the non-neurogenic region can prevent the irregular spreading of neurons across the tissue as the neurogenic wavefront moves forward. Our results also show that the wavefront speeds up when Delta is absent from the non-neurogenic region, as compared with the Delta=1 situation, especially for parameter values that enable the emergence of lateral inhibition fine-grained patterns with moderate densities of neurons (Fig. 3.12 (B) and Supp. Movies 1-4 in [54]).

Overall, our *in silico* experiments suggest a scenario in which Dll1 expression ahead of the neurogenic wavefront prevents neuronal overproduction and alterations in the morphology of the neurogenic wavefront, while controlling the correct timing of the neurogenic events.

3.4.3 Robustness of the results

In this section we show that the presented results are very robust to the model parameters and to model variations.

The front instability is accentuated if cell shape variability and stochasticity are reduced

The irregularity level of the lattice does not affect the qualitative results we found (Figs. 3.14-3.16).

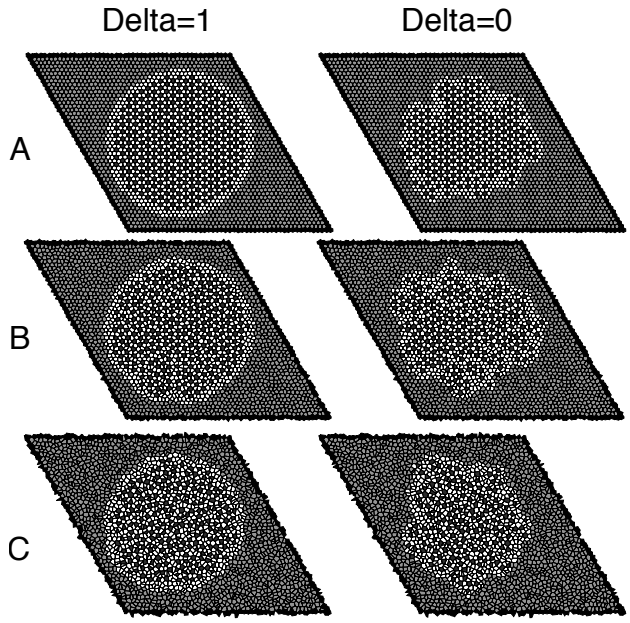

Figure 3.14: The irregularity of the lattice does not alter the qualitative features of patterns. Simulation snapshots for Delta=1 (left column) and Delta=0 (right column) conditions for lattice irregularity parameter (A) $\gamma = 0.67$, (B) $\gamma = 1.6$ and (C) $\gamma = 2.67$. Although for $\gamma = 0.67$ all cells have six neighbors (Fig. 2.2), cell side lengths (and, accordingly, the strength of the ligand-receptor interaction) are not regular. Hence, the hexagonal symmetry is lost and the instability of the front does not follow the appearing hexagonal symmetry that one can observe in perfect hexagonal lattices (Figs. 3.16, 3.22, 3.24-3.26). Grayscale code as in last column of Fig. 3.8. Patterns correspond to a stochastic simulation for $r_t = 10$ with a single central morphogen source. All remaining parameters and conditions are as in 3.3.1.

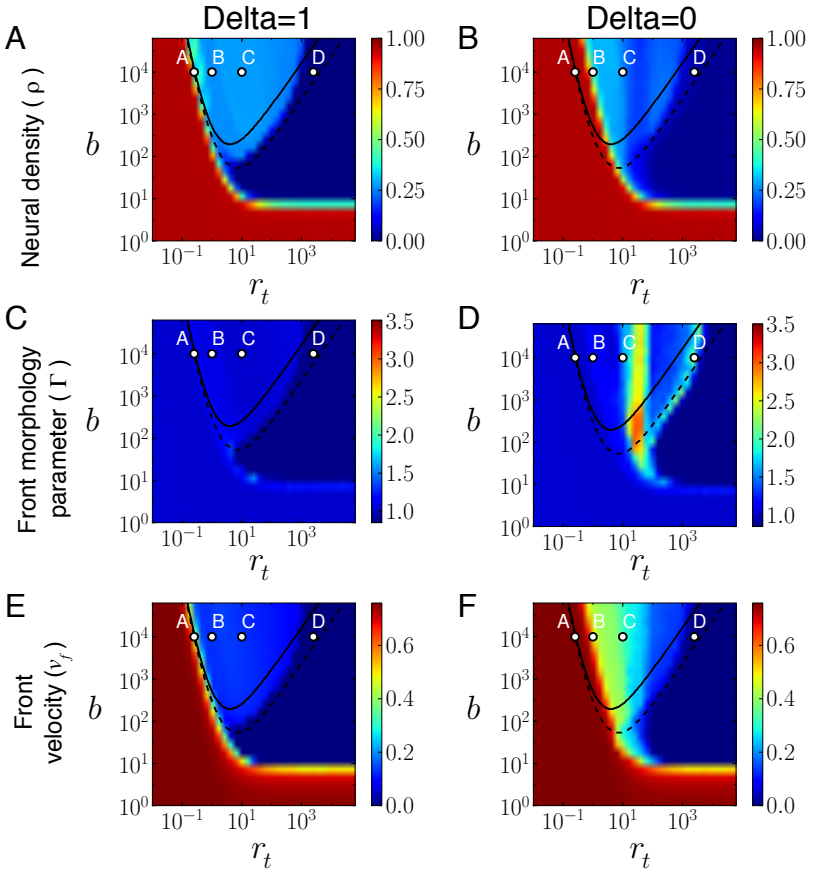

Figure 3.15: Dynamics on hexagonal regular lattices show similar qualitative results. Parameter space characterization of ρ (A,B), Γ (C,D) and v_f (E,F) for Delta=1 conditions (A,C,E) and Delta=0 conditions (B,D,F) as in Fig. 3.10 but on a regular hexagonal lattice and with a single initial morphogen source. Results are averages over 10 stochastic simulations. Letters inside the diagrams denote different chosen representative points of the parameter space (Fig. 3.16). All remaining parameters and conditions are as in Fig. 3.10. Results are very similar to those in Fig. 3.10, but differences in the front morphology parameter between the Delta=1 and the Delta=0 scenario are accentuated here.

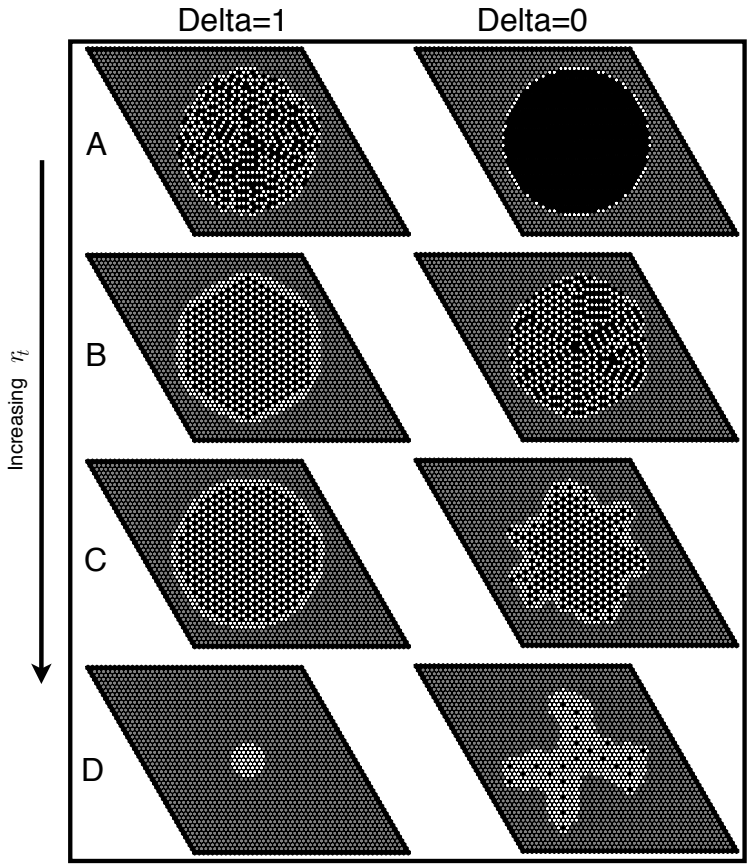

Figure 3.16: Neurogenic patterns for hexagonal regular lattices display equivalent features to those on irregular lattices. Snapshots of the stochastic neurogenic domain on a regular hexagonal lattice with a single initial morphogen source for the parameter values indicated by circles (labelled A-D) inside the diagrams in Fig. 3.15 for Delta=1 (left column) and Delta=0 (right column) conditions. From top to bottom, (A) $r_t = 0.2551$, (B) $r_t = 1$, (C) $r_t = 10$, (D) $r_t = 2511$. In all cases, $b = 10000$. Front instabilities are clearly observed in the Delta=0 case and reflect the hexagonal symmetry of the lattice. Notice this symmetry is only observed in regular lattices (compare to first row in Fig. 3.14). Grayscale code as in last column of Fig. 3.8. Each snapshot corresponds to the corresponding final simulation time (Sec. 3.3.1).

To change the level of stochastic fluctuations, we repeat the parameter space characterization using values of the effective volume V between 100 and 5000 as well. Our conclusions are robust to changes in the level of stochastic fluctuations (Figs. 3.17, 3.18). Interestingly, higher noise intensities inhibit patterning at high r_t's, decreasing the region where the pattern is formed (Fig. 3.17). Additionally, higher noise intensities make the transition between the massive neurogenic to the normal patterned state more graded in terms of the neural density.

All the qualitative results also arise in deterministic (*i.e.* non-stochastic) dynamics as well (Figs. 3.19-3.22).

Our simulation results support that the more regular is the cell lattice and the less stochastic is the dynamics, the more pronounced is the front instability (compare Figs. 3.17 (D), 3.11 (B), 3.15 (D) and 3.21 (D) from less accentuated to more accentuated front instability). In the regular hexagonal lattice it can be observed 6-fold symmetric shapes of the wavefront (Figs. 3.22 (C,D)).

Robustness to source location

Our results do not depend on the exact number or location of the initial morphogen source cells (Fig. 3.13 and data not shown). Though, in more regular lattices, when the front is unstabilized, the initial positioning of the sources are reflected in the shape of the unstable front. A clear example of that appears when we observe the front instability in a perfect hexagonal array (Fig. 3.23). The same source distribution lead to more isotropic front morphologies in irregular cell lattices (Fig. 3.13 (F)).

Limits of temporal and spatial scales

We checked that our results hold for a broad range of timescales of morphogen and lateral inhibition dynamics (Figs. 3.24-3.26).

Specifically, we varied the non-dimensional u and D parameters. The parameter u compares the timescale of the morphogen dynamics with that of lateral inhibition signal. The lower is u, the faster is the Notch signal compared to the morphogen dynamics. $u = 1$ corresponds to equivalent timescale dynamics of morphogen and signal. On the other side, the parameter D controls the size of the initial neurogenic domain and the spatial range over which the morphogen

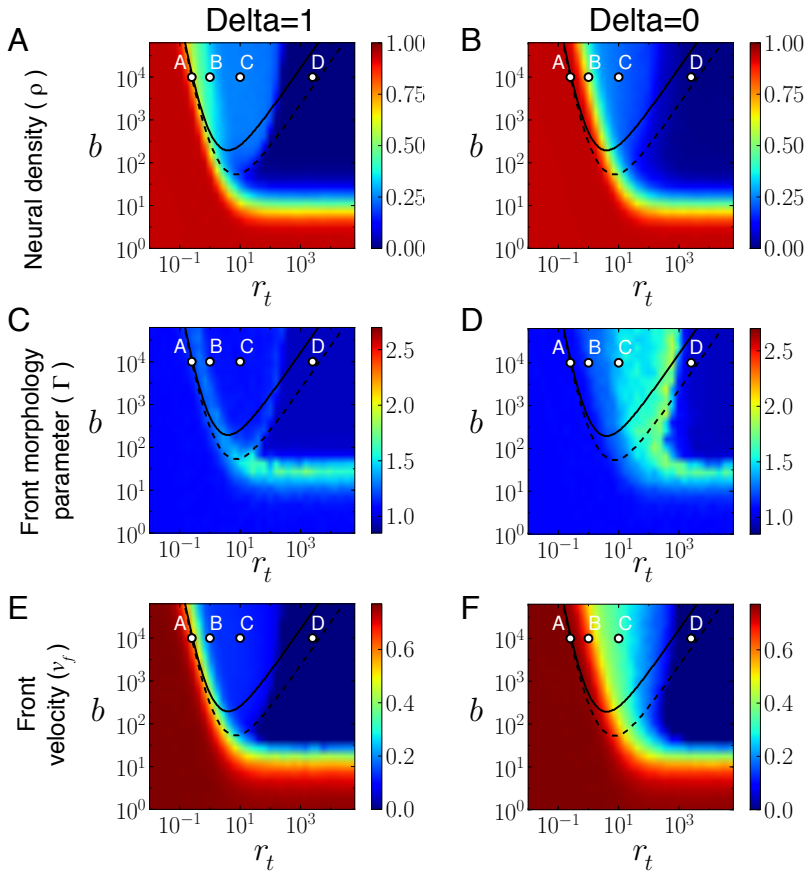

Figure 3.17: Noisier dynamics show the same qualitative results across the parameter space ($V = 100$). Parameter space characterization of the density of neurons ρ (A,B), the front morphology Γ (C,D) and the velocity of the front v_f (E,F) for Delta=1 (A,C,E) and Delta=0 (B,D,F) conditions. Other parameter values are indicated in Sec. 3.3.1.

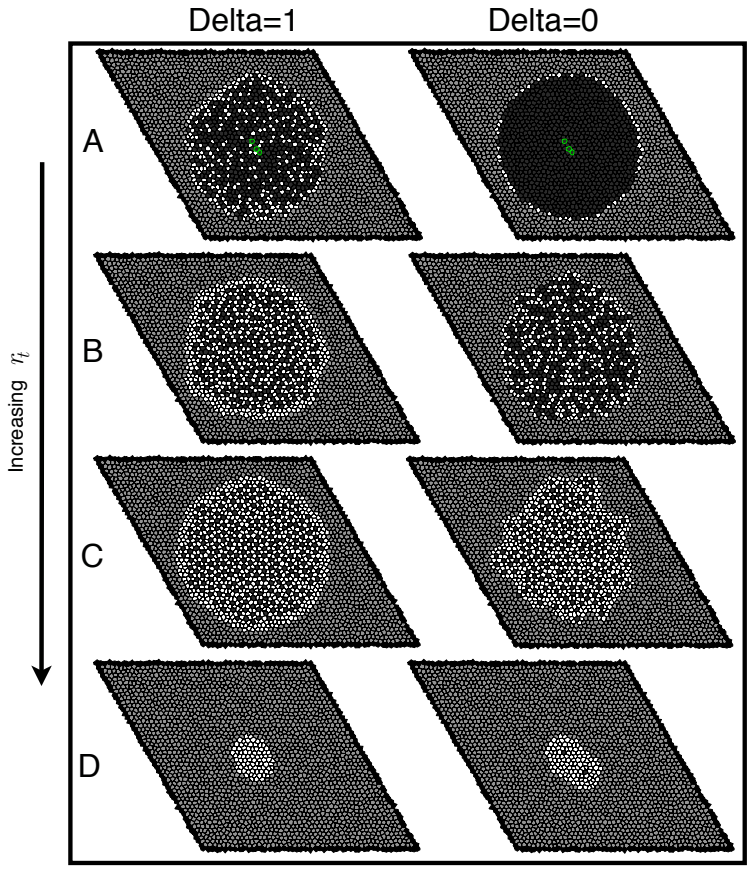

Figure 3.18: Noisier dynamics show the same qualitative results across the parameter space ($V = 100$). Snapshots of simulations of the neurogenic domain for Delta=1 (wild type like, left column) and Delta=0 (right column) conditions. Different panels correspond to letters depicted in Fig. 3.17 with trans-interaction strength values (A) $r_t = 0.2511$, (B) $r_t = 1$, (C) $r_t = 10$, (D) $r_t = 2511$, other parameters as specified in Sec. 3.3.1. Color code for cells and contours as in Fig. 3.7.

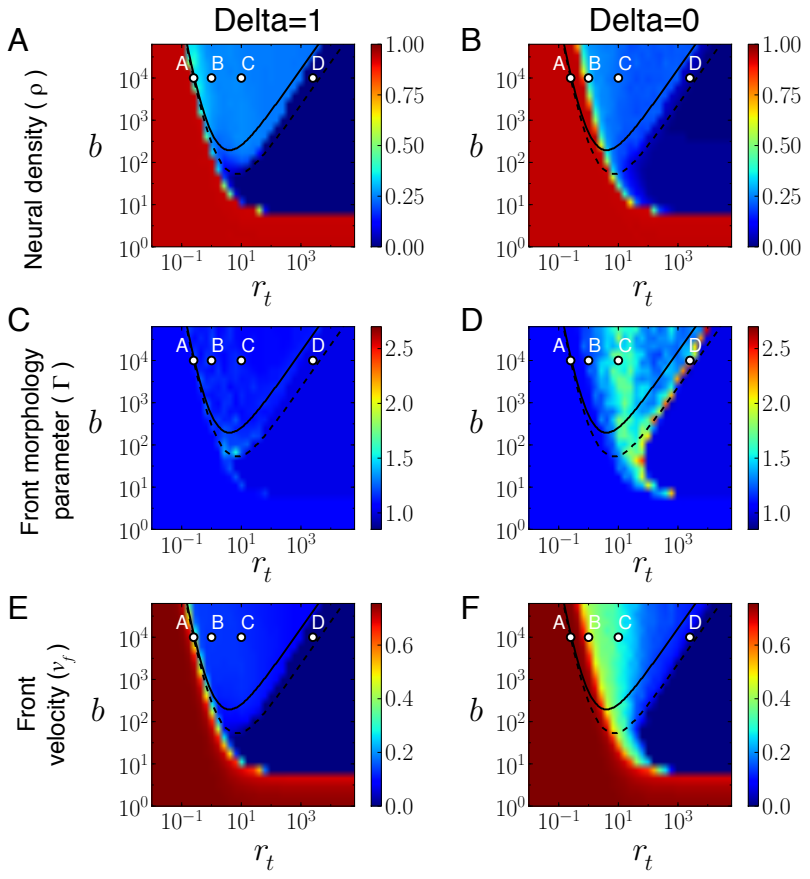

Figure 3.19: Deterministic dynamics show the same qualitative results as stochastic dynamics across the parameter space. Parameter space characterization of ρ (A,B), Γ (C,D) and v_f (E,F) for Delta=1 (A,C,E) and Delta=0 conditions (B,D,F) as in Fig. 3.10 of the main text but for deterministic dynamics on an irregular lattice and with a single initial morphogen source. Letters inside the diagrams denote different chosen representative points of the parameter space (Fig. 3.20). All remaining parameters and conditions are as in Sec. 3.3.1.

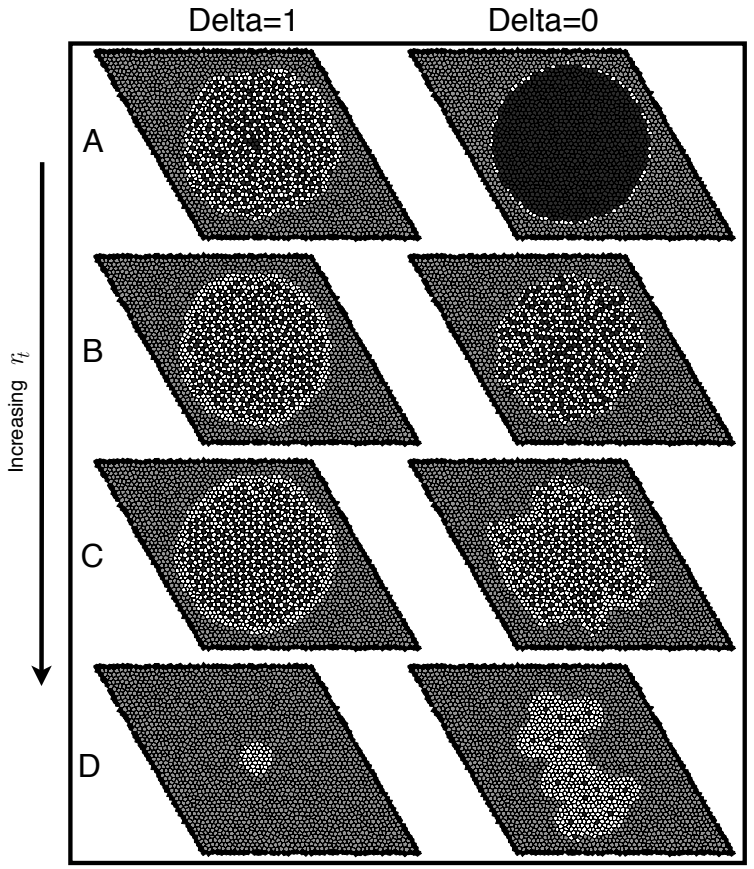

Figure 3.20: Neurogenic patterns for deterministic dynamics are equivalent to those of stochastic dynamics. Snapshots of the deterministic neurogenic domain with a single initial morphogen source for the parameter values indicated by circles (labelled A-D) inside the diagrams in Fig. 3.19 for Delta=1 (left column) and for Delta=0 (right column) conditions. From top to bottom, (A) $r_t = 0.2551$, (B) $r_t = 1$, (C) $r_t = 10$, (D) $r_t = 2511$. In all cases, $b = 10000$. Deterministic (this figure) and stochastic snapshots (Fig. 3.13) are very similar. Grayscale code as in last column of Fig. 3.8. Each snapshot corresponds to the final corresponding simulation time (Sec. 3.3.1).

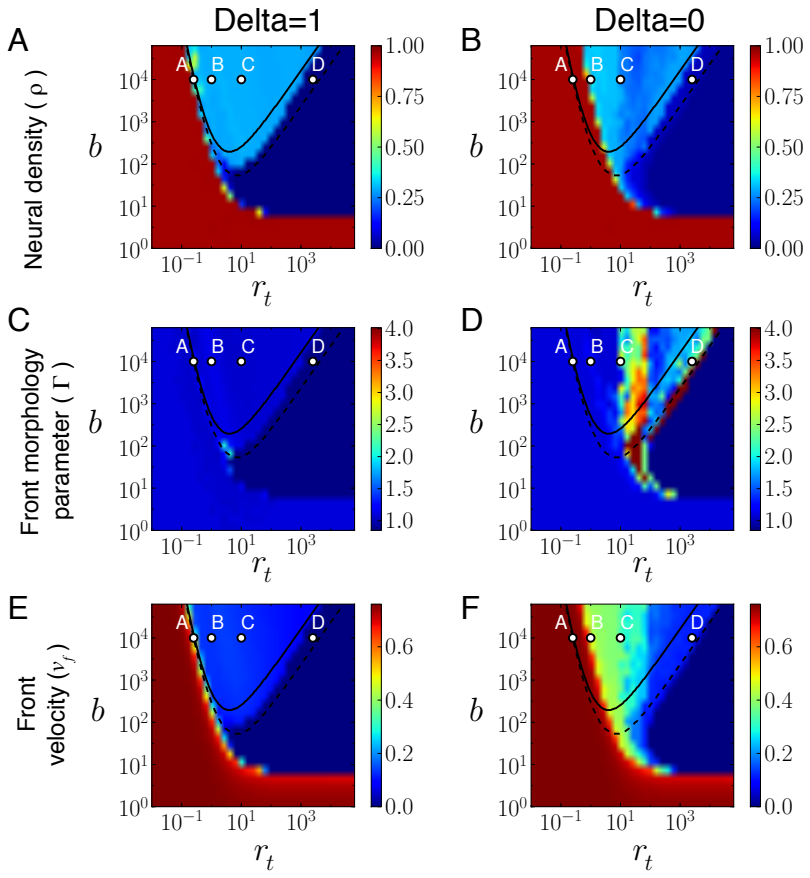

Figure 3.21: Deterministic dynamics in hexagonal regular lattices show the same, but sharper, qualitative results. Parameter space characterization of ρ (A,B), Γ (C,D) and v_f (E,F) for Delta=1 conditions (A,C,E) and Delta=0 (B,D,F) conditions as in Fig. 3.10 but for deterministic dynamics on a regular hexagonal lattice and with a single initial morphogen source. For the Delta=0 case, $\Gamma > 4$ values have been taken as $\Gamma = 4$. Letters inside the diagrams denote different chosen representative points of the parameter space (Fig. 3.22). All remaining parameters and conditions are as in Sec. 3.3.1.

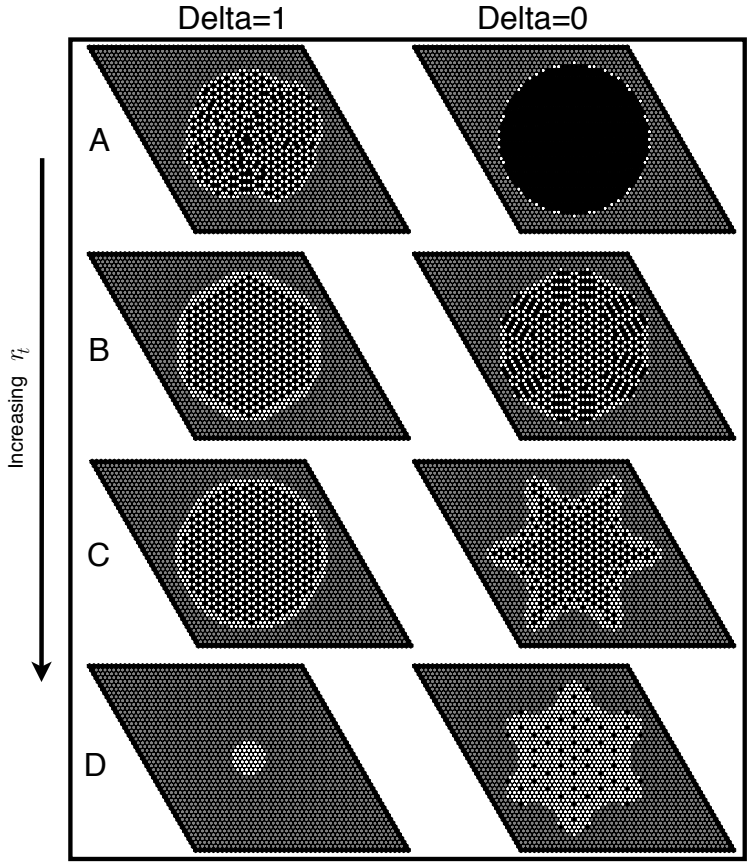

Figure 3.22: Deterministic neurogenic patterns in hexagonal regular lattices display equivalent features to those of stochastic dynamics in irregular lattices. Snapshots of the deterministic neurogenic domain in a regular hexagonal lattice for the parameter values indicated by circles (labelled A-D) inside the diagrams in Fig. 3.21 for Delta=1 (left column) for Delta=0 (right column) conditions. From top to bottom, (A) $r_t = 0.2551$, (B) $r_t = 1$, (C) $r_t = 10$, (D) $r_t = 2511$. In all cases, $b = 10000$. Front instabilities are clearly observed in the Delta=0 case and reflect the hexagonal symmetry of the lattice. Grayscale code as in last column of Fig. 3.8. Each snapshot corresponds to the final corresponding simulation time (Sec. 3.3.1).

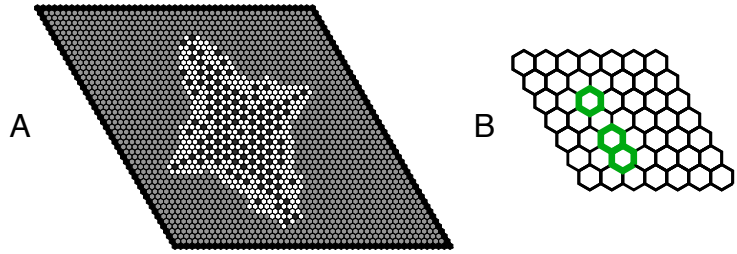

Figure 3.23: Sources distribution has a visible effect on the resulting patterns for the Delta=0 case in just more regular lattices. (A) Deterministic simulation results on a perfect hexagonal lattice. (B) Magnification of the central part of the cellular array, where the sources of morphogen are marked in green. The pattern has been removed for better visualization of the sources distribution. The sources distribution in (B) is reflected in the front morphology in (A). The same sources distribution in more irregular arrays leads to a more isotropic but still irregular front morphology (Fig. 3.20 (F)). All remaining parameters and conditions are as in Sec. 3.3.1.

secreted by each source spans.

Equal or faster timescales ($u \geq 1$) for the morphogen and larger morphogen spreading values (higher D) lead to a wider border of cells having lateral inhibition dynamics but which have not yet differentiated (Figs. 3.24 and 3.25). This softens the shape instability appearing in the Delta=0 situation. The qualitative nature of our results holds for a finite range of morphogen spreading values (finite range of non-dimensional diffusible values for the morphogen, D), as expected (Fig. 3.26). These values are consistent with the fact that the neurogenic pattern starts nucleating in a small patch of cells [142], and ensure that morphogen expression is not observed in front of the neurogenic pattern, in agreement with experimental observations [51,143]. On one side, our numerical study indicates that a minimal value of D is required for pattern expansion (data not shown), since it is necessary that the morphogen reaches new cells in order to start up their lateral inhibition dynamics. On the other side, our model indicates that when the morphogen has too high diffusion rates, bizarre situations arise in which pattern formation starts simultaneously in distant regions of the neurogenic domain, which generate different neurogenic wavefronts inside the tissue. The collision of such wavefronts give rise to patterns exhibiting different kind of defects, *e.g.* spots without any

neurons, or grain boundaries. Such defects are easily observed by increasing the timescale of the morphogen (*i.e.* increasing u, Fig. 3.25 (B)), and is more likely to happen in the Delta=0 scenario.

Differentiable dynamics elicit similar phenomenology

We corroborate that our results do not depend on our simplified modeling based on sharp decision-making switches, implemented through Heaviside functions, by evaluating them more realistically with smoother transitions through Hill functions (Fig. 3.27). The differentiable model reads:

$$\frac{dl_i}{dt} = v\left\{\frac{1}{1+bs_i^h} - l_i\right\}\Psi(m_i, m_c, q_m)\Psi(y_i, y_c, q_y) \tag{3.10a}$$

$$\frac{ds_i}{dt} = \left\{\frac{r_t\langle l_i\rangle}{1+r_t\langle l_i\rangle} - s_i\right\}\Psi(m_i, m_c, q_m)\Psi(y_i, y_c, q_y) \tag{3.10b}$$

$$\frac{dy_i}{dt} = v\left\{\frac{1}{1+bs_i^h} - y_i\right\}\Psi(m_i, m_c, q_m)\Psi(y_i, y_c, q_y) \tag{3.10c}$$

$$\frac{\partial m_i}{\partial t} = u\left\{\Psi(y_i, y_c, q_{ym}) + D\nabla_i^2 m_i - m_i\right\} \quad , \tag{3.10d}$$

with $\Psi(x_i, x_c, q_x) = \frac{x_i^{q_x}}{x_c^{q_x}+x_i^{q_x}}$, $q_m > 0$, $q_{rm} > 0$ and $q_y < 0$.

3.4.4 Similar phenomena can be expected for morphogenetic furrow progression in *Drosophila*

To extend the implications of our model beyond retinal development in vertebrates, we focus on morphogenetic furrow (MF) progression in the developing *Drosophila* eye (Fig. 3.28 (A)). As mentioned in Sec. 3.1, Delta (*Delta*), *hairy* (h) and *extra macrochaetae* (*emc*) are expressed just ahead of the MF [148]. In such region lateral inhibition does not occur since the proneural genes, which are downstream Notch signal and inhibit Delta production, are repressed by h and *emc*; therefore the observed *Delta* expression anteriorly to the MF is Notch-independent.

In this context, we have changed the initial and boundary conditions of our model to produce a straight, planar neurogenic wavefront (as compared with the circular wavefront in the modeling of the chick retina) that mimics neurogenesis

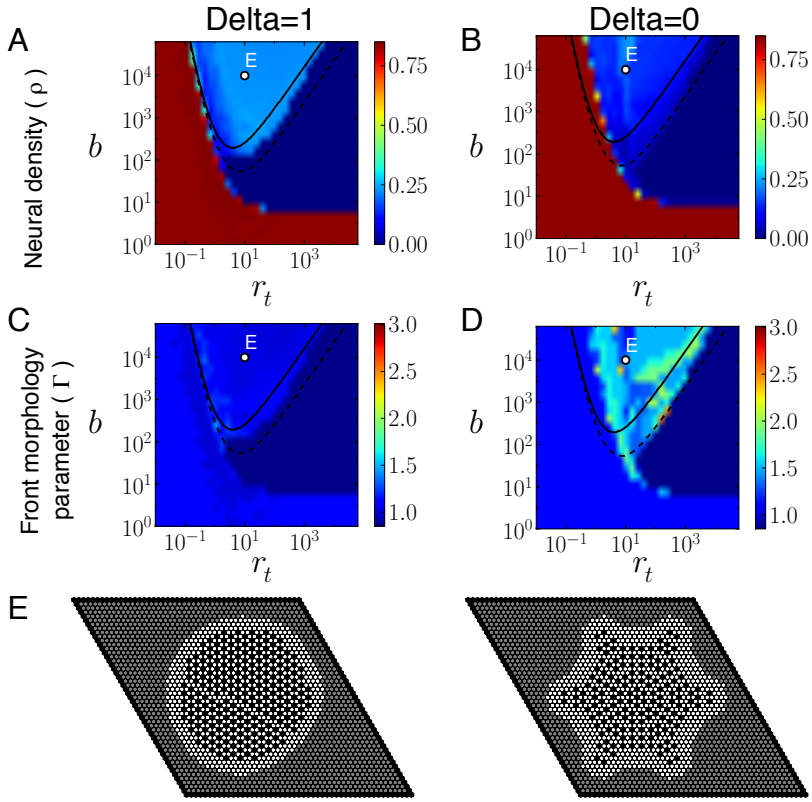

Figure 3.24: Robust results for equivalent timescale dynamics of morphogen and signal ($u = 1$). (A-D) Parameter space characterization of ρ (A,B) and Γ (C,D) for Delta=1 (left column) and Delta=0 (right column) conditions for deterministic dynamics on a regular hexagonal lattice with $u = 1$. (B) Patterns arising at the final time of simulation for the parameter values indicated by the letter E inside the diagrams in (A-D). Grayscale code as in last column of Fig. 3.8. All remaining parameters and conditions are as in Fig. 3.21. Differences between the Delta=1 and the Delta=0 conditions for $u = 1$ are similar to those for $u = 0.1$ (Figs. 3.21 and 3.22).

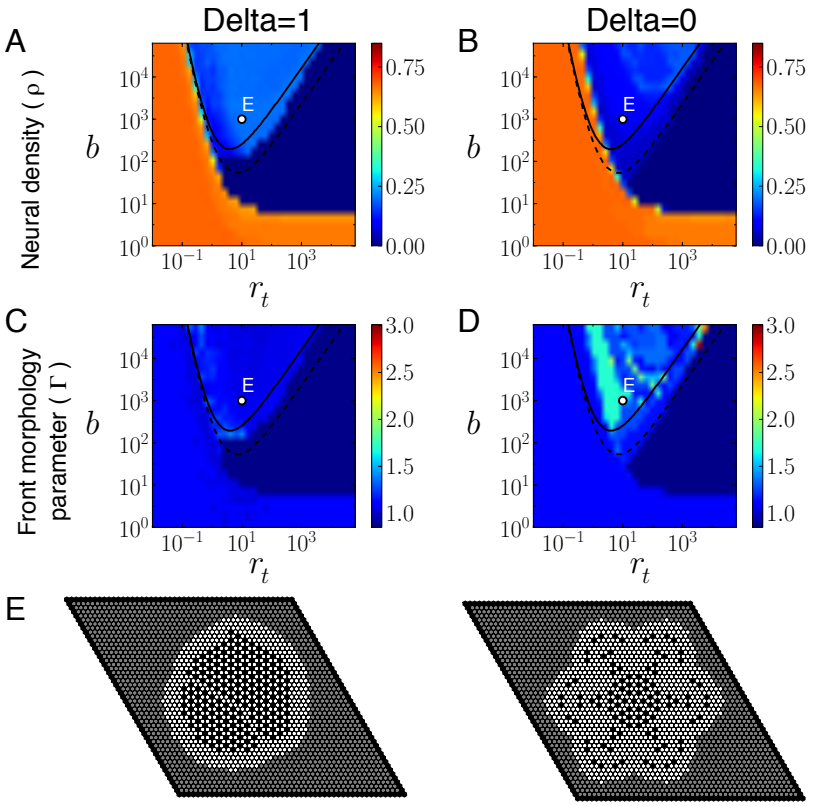

Figure 3.25: Robust results for faster morphogen dynamics than signal ($u = 10$). (A) Parameter space characterization of ρ (A,B) and Γ (C,D) for Delta=1 (left column) and Delta=0 (right column) conditions for deterministic dynamics on a regular hexagonal lattice with $u = 10$. (B) Patterns arising at the final time of simulation for the parameter values indicated by a letter E inside the diagrams in (A). Grayscale code as in last column of Fig. 3.8. All remaining parameters and conditions are as in Fig. 3.21. In the Delta=0 scenario, the front morphology is less altered when the morphogen dynamics become so fast. Moreover, it exemplifies a situation where the pattern spreading is bizarre, and pattern initiation arises simultaneously in different regions of the tissue. In this figure, the faster morphogen dynamics is also reflected in the wider border of cells having lateral inhibition dynamics but which have not yet differentiated. Differences between the Delta=1 and the Delta=0 conditions for $u = 10$ are similar to those for $u = 0.1$ (Figs. 3.21 and 3.22).

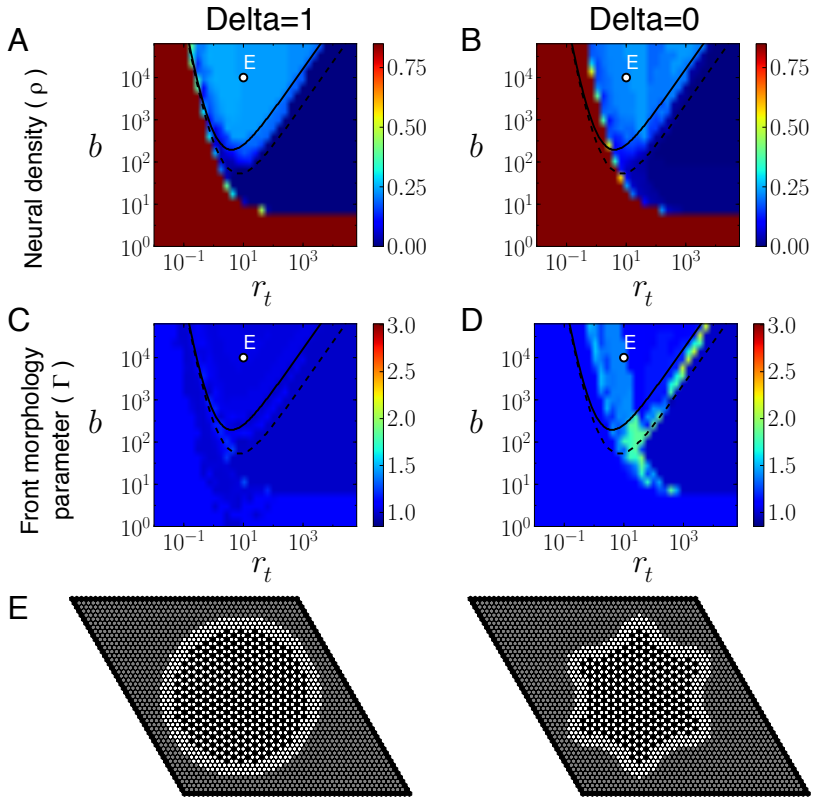

Figure 3.26: Robust results for a longer-range morphogen. (A-D) Parameter space characterization of ρ (A,B) and Γ (C,D) for Delta=1 (left column) and Delta=0 (right column) conditions for deterministic dynamics on a regular hexagonal lattice with $D = 2.25$. All remaining parameters and conditions are as in Fig. 3.21. (E) Patterns arising at the final time of simulation for the parameter values indicated by a letter E inside the diagrams in (A-D). Grayscale code as in last column of Fig. 3.8. In this figure, the longer range of the morphogen is reflected in the wider border of cells having lateral inhibition dynamics but which have not yet differentiated. Results for $D = 2.25$ are qualitatively similar to those for $D = 0.5625$ (Figs. 3.21 and 3.22) with a reduced front morphological deformation across the parameter space.

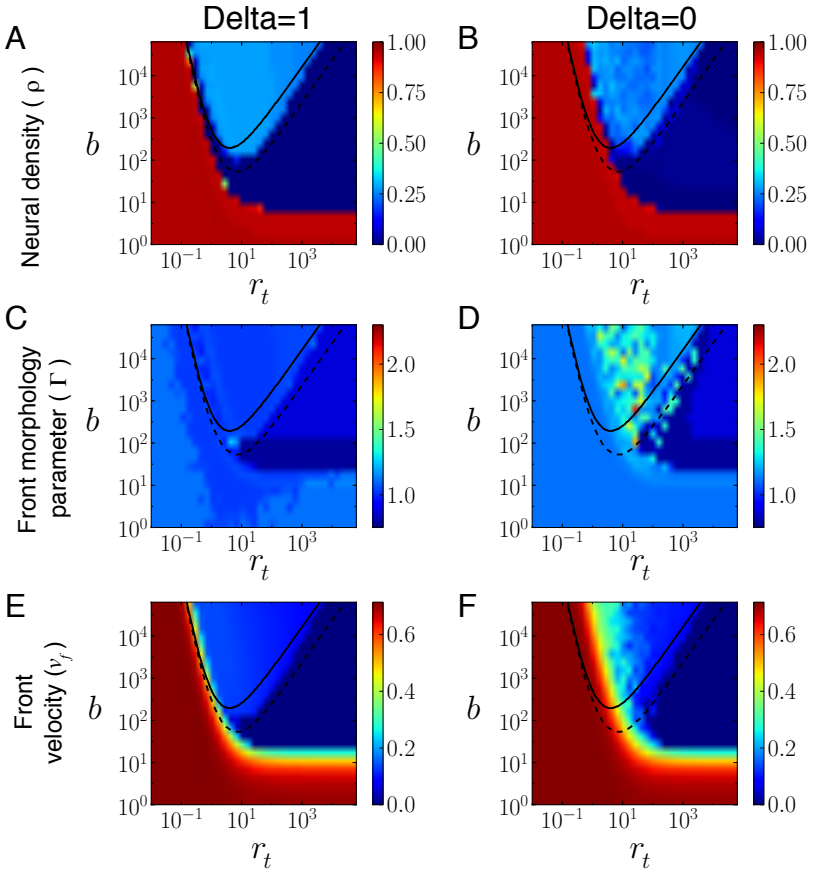

Figure 3.27: Differentiable dynamics yield equivalent results. Parameter space characterization of ρ (A,B), Γ (C,D) and v_f (E,F) for Delta=1 (A,C,E) and Delta=0 (B,D,F) conditions as in Fig. 3.21 but for differentiable deterministic dynamics on a regular hexagonal lattice. Hill exponents have been set to $q_m = q_{ym} = -q_y = 10$. For the Delta=0 case, $\Gamma > 4$ values have been taken as $\Gamma = 4$. All remaining parameters and conditions are as in Fig. 3.21. The qualitative results do not change with respect to the corresponding non-differentiable version of the model with step functions (Fig. 3.21). Pattern snapshots are equivalent as well (data not shown).

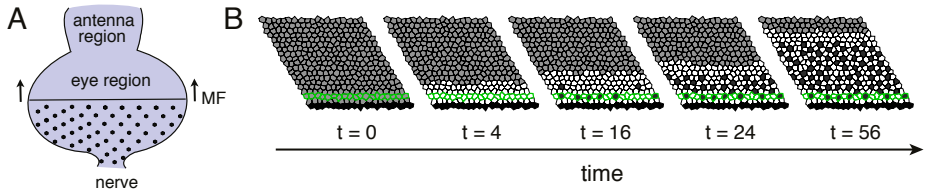

Figure 3.28: Dynamics of wavefront progression in the *Drosophila* eye-antennal disc. (A) Cartoon illustrating morphogenetic furrow progression (MF) in *Drosophila* eye-antennal imaginal disc (see caption in Fig. 3.1). (B) Snapshots of sequential times t of a wild-type simulation of MF progression. Color code for cells and contours as in Fig. 3.7. Black cells on bottom rows denote boundary cells. Parameters and details as indicated in Sec. 3.4.4.

at the MF in the eye imaginal disc of *Drosophila* (Fig. 3.28 (B)). Therefore, the model we are using does not include other relevant regulatory elements for MF progression, like for instance the *Atonal* positive cell-autonomous feedback loop, and the Scarbous factor, which can diffuse in the extracellular space and drives Notch inhibition between non-adjacent cells [97]. These other regulatory elements have been proposed to be important for understanding the precise spacing of the R8 cells, which are the first photoreceptors to get differentiated (Fig. 1.4 (B)) [97]. We expect that our results on how the MF progression depends on Delta state in the invaded tissue will be robust to these other regulatory elements when they are normally expressed in the tissue[6].

For simulating MF progression, we set periodic boundary conditions on the lateral boundaries of the field of cells, while the cells in the top and bottom rows have the morphogen concentration set to zero and no dynamics for the whole simulation. Initially all cells have low readout species y_i and morphogen concentration m_i and just the cells in the third lowest row act as initial sources of morphogen. We stop the simulations when the differentiation front is five cells away from the top boundary of the system. Unless otherwise stated, we use $r_t = 10$. The rest of the parameter values are as in Sec. 3.3.1.

To test whether our model is compatible with empirical observations in *Drosophila*,

[6]However, it is out of our scope to examine the effects on MF progression if the expression patterns of such other regulatory elements are altered in the non-neurogenic tissue.

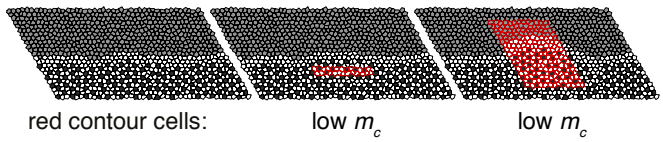

Figure 3.29: Snapshots of simulations of MF progression including cells in clones (red area) with different conditions, as indicated in the figure. Low m_c: 10 times lower morphogen threshold (*i.e.* emc^-h^-). These panels show only the simulated area close to the MF. All snapshots correspond to the same time point, see Supp. Movie 5 in [54] for dynamic progression in the whole simulated tissue. Simulations in these panels are performed by using the same seed for the random number generator, so they share exactly the same initial condition. Parameters and details as indicated in Sec. 3.4.4.

we mimic the experiments by Brown *et al.* [148]. Brown *et al.* showed that in mosaic eyes with large enough double mutant clones of cells lacking both *emc* and *h* expression, what we will refer as emc^-h^- clones, the MF advances in a faster way over the clone. This happened because null mutation of *h* and *emc* would derepress the proneural genes, facilitating lateral inhibition ahead of the MF [148]. In small clones, no alterations were found.

We model emc^-h^- clones with cells that have an increased sensitivity to Hedgehog (Hh) morphogen, triggering Delta/Notch lateral inhibition dynamics at a lower concentration of morphogen. For doing so, we set a patch of cells of variable size (*i.e.* the clone) being ten times more sensitive to the morphogen to reflect easier onset of Delta-Notch dynamics in emc^-h^- clones (Fig. 3.28 (C) and Supp. Movie 5 in [54]). We use $m_c = 0.001$ for all normal cells, and $m_c = 0.0001$ for the emc^-h^- clones. Initial conditions consist on initial high ligand and low signal concentration in all cells ($l_i = 1 - 0.1U_i$, $s_i = 0$, being U_i a uniform random number between 0 and 1).

The left panel of Fig. 3.29 shows a snapshot of a simulation of our model for normal progression of the MF in the absence of an emc^-h^- clone. In the second panel we see that a small clone has no effect on the progression of the furrow, in agreement with Brown *et al.* [148]. The third panel shows a snapshot of the faster advance of the differentiation front over a large emc^-h^- clone, in striking resemblance to Fig. 3 (C,D) in Brown *et al.* [148]. This shows that our model can correctly reproduce perturbations of the conditions ahead of neurogenic fronts in

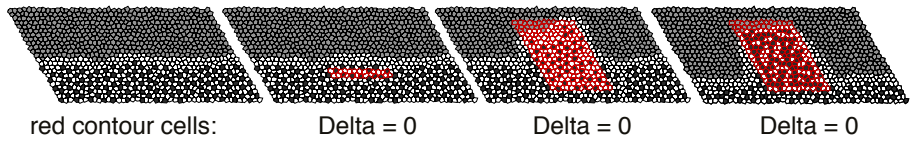

Figure 3.30: Snapshots of simulations of MF progression including cells in clones (red area) with different conditions, as indicated in the figure. Delta=0: non-neurogenic cells lack constitutive Delta expression. The three first snapshots are at $r_t = 10$ and correspond to the same time point, while the fourth is at lower trans-interaction strength, $r_t = 0.75$. Simulations are run using the same seed for the random number generator.

situations beyond our initial study of neuronal differentiation in the vertebrate retina.

To compare with the simulations for the chick retina, we perform simulations where this patch of cells has normal sensitivity to the morphogen ($m_c = 0.001$) but null initial ligand and signal expression ($l_i = 0$, $s_i = 0$). Our simulated clones of null Delta ligand (what we also name as Delta=0 condition, Fig. 3.30 second and third panels) result in a qualitatively similar effect to the case of increased neurogenic potential ahead of the MF (compare with second and third panel in Fig. 3.29). An irregular wavefront seems to additionally arise in the Delta=0 large clone (third panel in Fig. 3.30). Moreover, at weaker trans-interaction strengths (fourth panel in Fig. 3.30) there is an increase of neurogenesis within the Delta=0 clone with respect to the normal tissue, what is consistent with the neural overproduction in the Delta=0 scenario for the simulations in the chick retina.

To confirm wavefront acceleration and morphological instability we perform simulations where all cells ahead of the MF are either emc^-h^- or have absence of Delta ligand (Fig. 3.31 and Supp. Movie 6 in [54]). In comparison with the wild-type simulation (Fig. 3.31 first panel), a faster progression occurs in each case (Fig. 3.31 second and third panel) but irregular progression of the MF arises only in the absence of Delta ligand (Fig. 3.31 third panel). When cells ahead the MF are emc^-h^- and, in addition, have no Delta ligand expression, MF progression is irregular too and slightly faster (Fig. 3.31 fourth panel).

Despite the change in geometry (a linear wavefront in *Drosophila versus* a

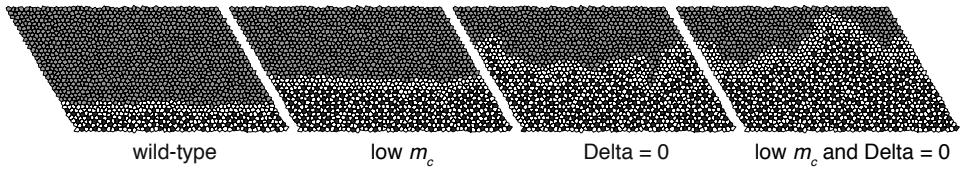

Figure 3.31: Snapshots corresponding to the same time point of simulations of MF progression with different wavefront conditions, as indicated in the figure. These panels show only the simulated area close to the MF. The non-dimensional front velocity (from left to right) is $v_f = 0.18, 0.26, 0.34, 0.39$. See Supp. Movie 6 in [54] for dynamic progression in the whole simulated tissue. Parameters and details as indicated in Sec. 3.4.4.

circular wavefront in the chick retina), these results are fully comparable to our study in the context of the chick retina. These results predict that *Delta* expression ahead of the neurogenic boundary is also essential for regular MF progression in the *Drosophila* eye.

3.5 Discussion

In this chapter we showed experimental evidences in the embryonic chick retina of *Dll1* expression in non-neurogenic regions ahead of the neurogenic wavefront in the absence of Delta/Notch dynamics. Our *in silico* experiments suggest that this *Dll1* makes the neurogenic process more robust.

In our theoretical study we have omitted different aspects of the developing tissues. In particular, for instance, it is known that cell proliferation and cell movement takes place in the embryonic retina [53]. A key point is to check that the timescales of these different events are not close to the timescales governing the studied phenomenon. Our goal was focused on wavefront progression. We argue it is sufficient to focus just on the very early pattern the wavefront leaves on its wake, *i.e.* the emerging pattern in the few rows next to the neurogenic border, inside the neurogenic domain. If such former patterning process is disrupted, this effect will propagate or have a negative impact to subsequent patterning processes. In the retina of chick embryos, cell nuclei travel from the apical to the basal side back and forth, in a synchronized way with its cell cycle (interkinetic

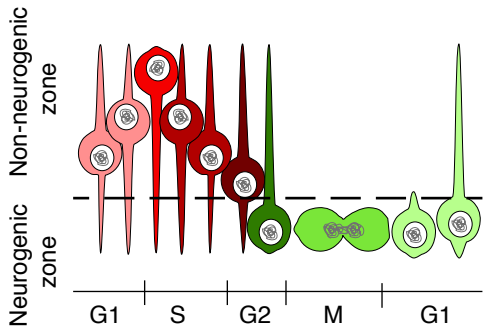

Figure 3.32: Interkinetic nuclear movement (INM) takes place in the vertebrate pseudostratified neuroepithelium, allowing lateral inhibition between apically located precursors (green cells, located in the neurogenic zone) that are undergoing G2/M/early G1 phase, while maintaining a pool of cells in the G1/S/early G2 phases without neurogenic potential (red cells, located in the non-neurogenic zone) in the basal part of the epithelium. This figure is a cartoon inspired by Fig. 1 in [65].

nuclear movement, INM, see Fig. 3.32) [50, 53, 65]. This synchronization makes that just cells situated in the apical side of the tissue are competent for lateral inhibition. INM (and hence cell cycle) occurs on average in 12 hours [53]. On the other side, wavefront progression velocity can be roughly estimated advancing 12.5 cells per INM time[7]. Hence, we consider that patterning at the neurogenic border will be faster enough to neglect INM and cell proliferation.

Our simple model together with our *in silico* experiments show that the presence of Delta ahead of neurogenic wavefronts has three important roles in relation to proper pattern emergence. First of all, Delta protein reduces the possibility to have either neural overproduction or sparse patterns, facilitating proper lateral inhibition patterning. Second, the expression of Delta slows down the velocity of the differentiation wave front. Third, such expression promotes wavefront morphological stability.

Noteworthy, the estimated theoretical region indicating where the pattern solution would exist is quite similar to the patterned regions for the wavefront model for both Delta=1 and Delta=0 scenarios, being the Delta=0 patterned

[7]This estimation can be obtained if we assume that the wavefront advances about 100 cells in 4 days (personal communication by Dr. José María Frade).

region smaller.

Our simulation results indicate that a morphological instability appears for the Delta=0 case. From the presented phase diagrams it can also be pointed out that in the Delta=0 scenario, the velocity decreases with r_t when there is lateral inhibition patterning. In contrast, for the Delta=1 case, the velocity is constant across the whole patterned region, exhibiting a more robust behavior, being potentially more appropriate for developmental patterning.

Some of our predictions could explain observations made by Rocha *et al.* [153] in the retina of mice where Dll1 is conditionally mutated, while Dll4-dependent lateral inhibition remains within the neurogenic region. Rocha *et al.* reported that in such mutants neural overproduction and alteration in the neurogenesis pattern could be found.

Our results raise the question about the mechanism directing Dll1 expression ahead of the neurogenic wavefront. The uncovering of such a mechanism will facilitate to design experiments to further test the predictions of our model. One possible experiment would be the creation of knock-in mice in which Dll1 promoter elements specific for Notch-independent Dll1 expression are mutated. This genetic approach would inhibit Dll1 expression in the non-neurogenic region but not in neurogenic precursors undergoing lateral inhibition.

Our results simulating MF furrow progression in *Drosophila* also support the notion that Notch-independent *Delta* expression is crucial for proper neurogenic wavefront progression. Unfortunately, the analysis of the influence of generalized Delta expression ahead of the MF in preventing neurogenic wavefront disturbances is hampered by its function as a proneural enhancer in this region, which results in the absence of retinal neurogenesis when mutated [172, 173]. Although the absence of retinal neurogenesis in these mutated patches, extra photoreceptors at the edges of such mutant patches in the adult eyes have been found [172], being consistent with our prediction on neural overproduction.

3.5.1 Preliminary results of how the wavefront is unstabilized

Is this section we present some preliminary unpublished results on wavefront progression that provide some arguments for understanding the wavefront instability.

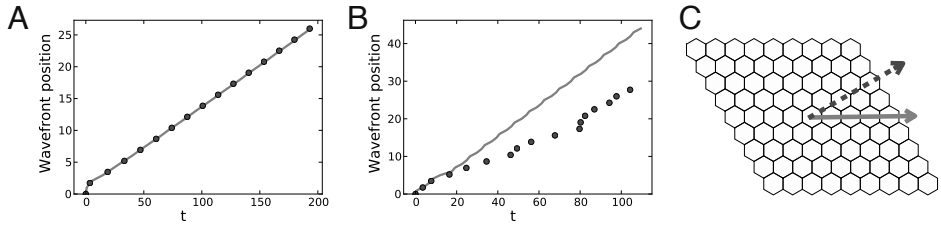

Figure 3.33: Studying the dynamics of the moving front. Front position in cell units *versus* time for two different directions for (A) the Delta=1 and (B) the Delta=0 cases. Dots and gray lines in panels (A) and (B) correspond to the directions drawn in (C) with the black dashed and gray solid arrows, respectively. The slopes of the different front positions are more or less constant, so the linear velocity is constant in each direction. In (B) we can see the footprint of the front instability since two different slopes are found, corresponding to two different directions. These results correspond to simulations performed as in Figs. 3.6 (E,F) and 3.22 (C), but herein are in larger array of cells.

The morphological instability arises as a direct consequence that the velocity of the moving front varies between different directions in the Delta=0 case. A good illustration of this phenomenon is shown when we compute the velocity along two different directions in a perfect hexagonal array (Fig. 3.33). But, which is the origin for the variability of the velocity? In the Delta=1 case, cells at the wavefront becoming neurogenic — *i.e.* entering into lateral inhibition dynamics — undergo strong inhibition from the high-Delta state of their neighbors. After such inhibition with the corresponding Delta depletion, they can rise their ligand and readout concentrations and adopt the neural fate. In the Delta=1 scenario, the first cells to be competent for lateral inhibition will be the first to differentiate into the neural fate (Fig. 3.34). For the Delta=0 scenario, cells entering into lateral inhibition dynamics undergo a much weaker inhibition or even no inhibition from its neighbors, which are non-neurogenic neighbors without any Delta and new neurogenic cells. Such new neurogenic cells transiently start raising its Delta concentration, but lateral inhibition dynamics make them to quickly relax into a state with practically null Delta. As a consequence, depending on when a cell starts being neurogenic and the average Delta level of its neighbors, such cell

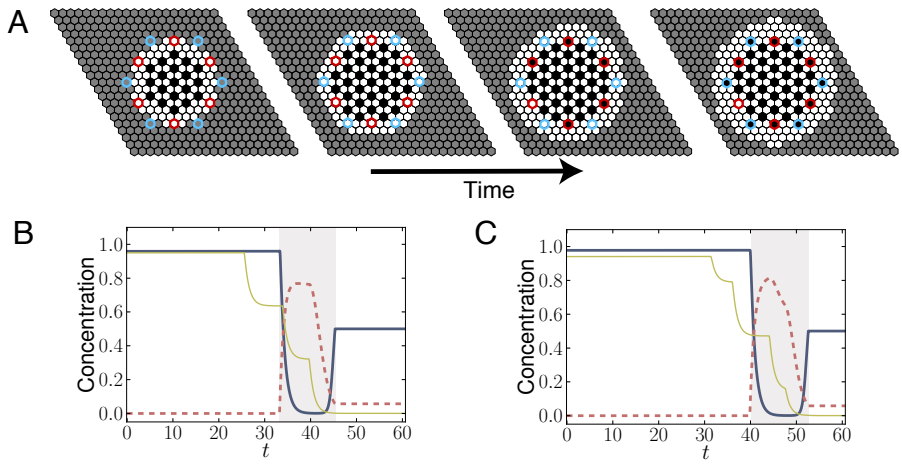

Figure 3.34: Studying regular wavefront progression. (A) Different snapshots from a deterministic simulation performed on a lattice of 29×29 perfect hexagonal cells with a single Shh morphogen source for the Delta=1 scenario. We focus on cells with a red and light blue contour. Red cells enter into lateral inhibition dynamics before light blue cells. Afterwards, differentiation into neural fate occurs in the same sequential order. Just a part of the simulated tissue is shown. (B,C) Dynamics for (B) a light blue cell and (C) a red cell. Blue solid lines denote the ligand concentration for the cells under study, l_i, red dashed lines its Notch signal levels, s_i, and thin dark yellow lines the averaged Delta concentration in neighboring cells of the cells under study, $\langle l_i \rangle$. Grey region represents the time window in which the studied cell undergoes lateral inhibition dynamics. When cells enter into lateral inhibition dynamics, they start receiving the signaling due to Delta in its neighborhood. In this scenario, the averaged Delta concentration in neighboring cells $\langle l_i \rangle$ is much higher than the required ligand for half-inhibition l^*, which for $r_t = 10$ and $b = 10^4$ is $l^* \approx 0.01$ according to Eq. 3.11); for this reason, when cells start being neurogenic, they are all inhibited. After the inhibitory process, cells can adopt the neural fate. Simulation results are the same as presented in Figs. 3.6 (A) and 3.22 (E), but herein are in smaller array of cells.

will initially receive more or less inhibition and therefore will take more or less time for differentiating into a neural fate. Because of that, the first cells to be competent for lateral inhibition in the Delta=0 case can end up differentiating into the neural fate after a new younger neurogenic cell does it, what we call anomalous (wavefront) progression (Fig. 3.35).

For a better understanding of this phenomenon we have to define the concept of half-inhibition of ligand production in a cell, and the critical amount of average trans-interacting ligand in neighboring cells for acquiring such ligand half-inhibition. A ligand in a cell will be half-inhibited if its regulatory production function is reduced to its half value. Mathematically, from the regulatory Hill functions in the Collier model (Eqs. 2.48) we can say that the critical signal level driving ligand half-inhibition s^* is defined by $g(s^*) = 0.5$, so using Eqs 2.48 we get $s^* = b^{-1/h}$. The critical amount of trans-interacting ligand in neighboring cells sufficient for eliciting a signal s^* in the steady state, what we name as l^*, can be found by solving $s^* = \frac{r_t l^*}{1+r_t l^*}$. From these two expressions, we obtain that

$$l^* = \frac{1}{r_t} \frac{1}{b^{\frac{1}{h}} - 1} \quad . \tag{3.11}$$

Then, if $\langle l_i \rangle >> l^*$, the ligand in the i-cell will be highly inhibited, while if $\langle l_i \rangle << l^*$, such ligand will not be inhibited. By representing Eq. 3.11 *versus* r_t we can see that this quantity varies along r_t but is not very dependent on b. For the case presented in Figs. 3.34 and 3.35, *i.e.* for $r_t = 10$ and $b = 10^4$, we have that half-inhibition of ligand production will be achieved if a cell receives $\langle l_i \rangle \approx l^* = 0.01$. In the Delta=1 case, all new neurogenic cells heading for the neural fate will be inhibited, since when entering into the neurogenic state for such cells $\langle l_i \rangle >> l^*$. From Fig. 3.36 we propose that this argument will be mostly fulfilled in the pattern formation region for the Delta=1 case. For the Delta=0 case, we will have some new neurogenic cells that will fulfill $\langle l_i \rangle \lesssim l^*$, as the case presented in Fig. 3.35 (C). In this case, such cells will escape from an initial inhibition, and will even differentiate into the neural fate before older neurogenic cells that later on will end up differentiating into the neural fate, leading to anomalous progression. We have checked that this anomalous progression happens for the Delta=0 scenario even when there is no morphological instability (data not shown). Our proposal is that for certain range of r_t the anomalous progression can be amplified and leads to the morphological instability. Lower r_t leads to a not so accentuated

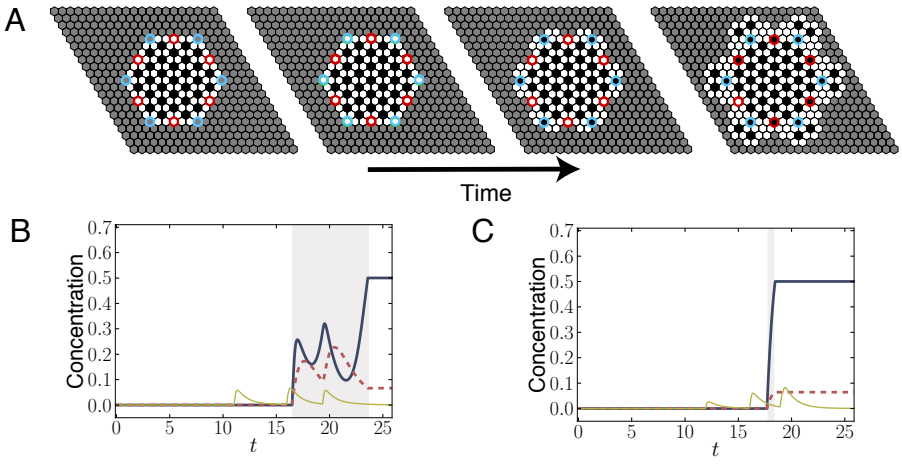

Figure 3.35: Unveiling the wavefront instability. (A) Different snapshots from a deterministic simulation performed on a lattice of 29×29 perfect hexagonal cells with a single Shh morphogen source for the D=0 scenario. We focus on cells with a red and light blue contour. (B,C) Dynamics for (B) a light blue cell and (C) a red cell. Color codes and simulation details as in Fig. 3.34. The red cell (C) enter into lateral inhibition dynamics before the blue cell (C), but the red cell (C) differentiates later into the neural fate than the blue cell (B). We call this phenomena anomalous progression. When both cells start undergoing lateral inhibition (*i.e.* being neurogenic), they both have a neighborhood with low Delta levels (thin dark yellow lines). However slight differences become amplified. The blue cell (C) is less inhibited when it starts lateral inhibition than the red cell (B), since $\langle l_i \rangle \lesssim l^*$ for the blue cell and $\langle l_i \rangle >> l^*$ for the red cell (where $l^* \approx 0.01$ according to Eq. 3.11) at the moment they start being neurogenic. This drives early differentiation of the blue cell, and late differentiation of the red cell. In this case, anomalous progression is amplified and result into a morphological instability. Simulation results are the same as presented in Figs. 3.6 (B) and 3.22 (F) in a larger array of cells.

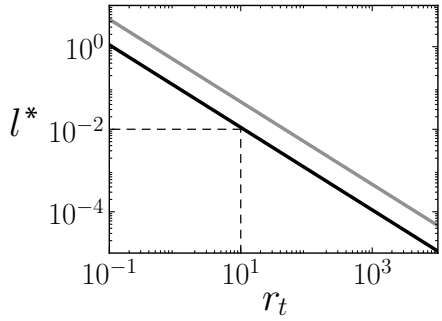

Figure 3.36: Threshold of ligand l^* in a cell required to half-inhibit ligand expression in its neighboring cell for $b = 10^4$ (black line) and $b = 10^3$ (gray line). Dashed thin lines indicate the l^* required for $r_t = 10$ when $b = 10^4$.

anomalous progression (data not shown), what could be not sufficient for the front instability. Too strong r_t leads to very accentuated anomalous progression (data not shown), but we expect that the high cell-to-cell coupling due to high r_t will hamper neural differentiation, what stabilizes the front morphology. In perfect hexagonal arrays our simulation results show the instability is restricted to a certain ranges of $r_t = 10 - 100$ and that this is weakly dependent on b (Figs. 3.15 and 3.21). This weak dependence in b could probably be connected to the weak dependence of l^* with respect to b (Fig. 3.36). Further theoretical efforts will be necessary to determine the nature of the morphological instability.

Chapter 4

Diffusible ligand in lateral inhibition dynamics

4.1 Introduction

Canonical Notch signaling pathway is based on cell-to-cell contact mediated by the Notch receptors and its transmembrane ligands. Nowadays there is experimental evidence pointing out that canonical ligands and non-canonical ligands can diffuse in the extracellular matrix in a soluble form or through small vesicles, activating or inhibiting the pathway [74, 116–120]. For instance, soluble ligands have been found in *C. elegans* which turn Notch into an activated form, being relevant in vulval development [119]. Another example is the case of Dll4 in human cells, which is found in vesicles that diffuse in the extracellular space and inhibit the Notch pathway. However, it is still unknown how this diffusible ligand participates in lateral inhibition dynamics [174, 175].

In this chapter we address the question of how this diffusible extracellular transport, which can involve longer wavelengths than the direct cell-to-cell trans-interactions, affects lateral inhibition patterning. First, we propose an equivalent Collier model in which cell-to-cell coupling is just mediated through an extracellular diffusible ligand, what we call for simplicity a diffusible ligand (Fig. 4.1 (A)). Then, we propose a model for lateral inhibition dynamics with feedback that

takes into account both cell-to-cell trans-interaction (Secs. 2.1 and 2.10) and an diffusible cell-to-cell coupling through a diffusible ligand (Fig. 4.1 (B)). Through these two models, we analyze which are the pattern formation capabilities of a diffusible ligand that can activate the Notch receptor, eliciting a signal[1].

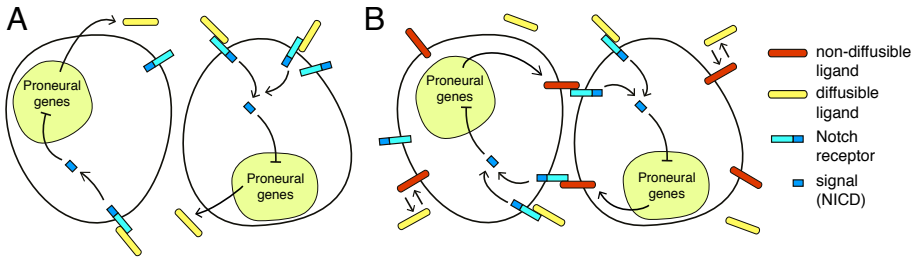

Figure 4.1: Diagrams of the models for diffusible ligand. (A) Model of Notch signaling mediated by a diffusible ligand that binds to Notch receptor and elicits a signal towards the cell harboring the receptor. The signal inhibits the proneural genes, inhibiting the production of further diffusible ligand. (B) Model for Notch signaling mediated by the transmembrane non-diffusible ligand and a diffusible ligand. In this model, the non-diffusible ligand can be reversibly converted into a diffusible ligand. Both non-diffusible and diffusible ligands can interact with Notch, eliciting a signal that inhibit the proneural genes, which inhibit now just the production of non-diffusible ligand.

4.2 Modeling diffusible ligand

First, we can directly reformulate Collier model by modifying the cell-to-cell coupling through trans-interactions with the use of a diffusible transport mediated by a ligand l' (Fig. 4.1 (A)), what reads

$$\frac{\mathrm{d}s_i}{\mathrm{d}t} = f(l'_i) - s_i \tag{4.1a}$$

$$\frac{\mathrm{d}l'_i}{\mathrm{d}t} = v\left\{g(s_i) - l'_i + D\nabla_i^2 l'_i\right\} \quad , \tag{4.1b}$$

where D is a non-dimensional diffusion coefficient, v accounts for the ratio of the degradations of the diffusible ligand and the Notch signal, ∇_i^2 is an non-

[1]These models do not pretend to capture a realistic process of how the diffusible ligand is produced, but just to incorporate this new kind of transport.

dimensional discrete Laplacian in an hexagonal lattice that we define as[2] $\nabla_i^2 l'_i = \frac{1}{6}\sum_{j\in nn(i)}\left(l'_j - l'_i\right)$, and being f and g functions defined by

$$g(s_i) = \frac{1}{1+bs_i^h}, \qquad f(l'_i) = \frac{r_s l'_i}{1+r_s l'_i} \quad , \tag{4.2}$$

where b, h are the same as in Collier model and r_s is proportional to the affinity of the diffusible ligand interaction with the Notch receptor, being herein equivalent to the r_t parameter in Collier model (Sec. 2.1). A scheme of the modeled variables can be found in Fig. 4.2 (A).

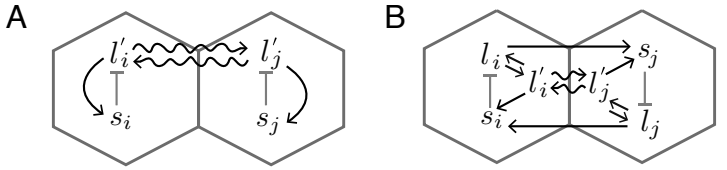

Figure 4.2: Schemes of the models for diffusible ligand. (A) Scheme for the model Eqs. 4.1, and of the cartoon depicted in 4.1 (A). (B) Scheme for the model Eqs. 4.11 and of the cartoon depicted in 4.1 (B). Hexagons denote each cell and its surrounding extracellular space. Straight black arrows denote activation, gray blunt arrows denote inhibition, and black curvy arrows denote diffusible transport. In these schemes, we omit linear degradations all variables have.

Moreover, it might be instructive studying a model in which both direct cell-to-cell coupling (trans-interactions) and diffusible coupling take place. For this reason, we propose the following model (Fig. 4.1 (B)). We consider that the non-diffusible ligand can reversible turn into a diffusible ligand L'_i, so

$$L_i \underset{\widetilde{k}_{-d}}{\overset{\widetilde{k}_d}{\rightleftharpoons}} L'_i \quad , \tag{4.3}$$

being $\widetilde{k}_d$ and $\widetilde{k}_{-d}$ the rates of conversion from non-diffusible to diffusible ligands and vice versa. The new diffusible transport is implemented through the discrete Laplacian $\widetilde{\nabla}_i^2$, which in an hexagonal array it reads

$$\widetilde{\nabla}_i^2 L'_i = \frac{1}{\Delta^2}\frac{2}{3}\sum_{j\in nn(i)}\left(L'_j - L'_i\right) \quad , \tag{4.4}$$

[2]See details below.

where Δ is the distance between two nodes of the hexagonal array (App. A). Now, we assume that the signal production is the normal linear degradation with a production term that is proportional to the sum of the equilibrium concentrations of the trans complex C_i and the new complex B_i formed by the interaction of the diffusible ligand when bound with the Notch receptor.

For computing the equilibrium concentration of both complexes we assume the following reactions:

$$N_i + L_j \underset{k_{-b}}{\overset{k_b}{\rightleftharpoons}} C_i \xrightarrow{k_s} S_i + C_i \tag{4.5a}$$

$$N_i + L'_i \underset{k'_{-b}}{\overset{k'_b}{\rightleftharpoons}} B_i \xrightarrow{k_s} S_i + B_i \quad , \tag{4.5b}$$

where we impose that the B_i complex elicits the Notch signal at the same rate k_s as the complex formed by cell-to-cell trans-interactions. We omit once more proteolytic cleavage, so the Notch receptor is conserved and its conservation equation now reads

$$N \equiv N_T = N_i + C_i + B_i \quad , \tag{4.6}$$

where the total Notch concentration is the same in each cell. By imposing homogeneity in each cell, the equilibrium complex concentrations will read

$$C_i = K_b N_i \langle L_i \rangle \tag{4.7a}$$

$$B_i = K'_b N_i L'_i \quad , \tag{4.7b}$$

where K_b and K'_b are the affinities for the C_i and B_i complexes formations, respectively, *i.e.* $K_b = k_b/k_{-b}$ and $K'_b = k'_b/k'_{-b}$. By using Eqs. 4.6 and 4.7 we obtain

$$C_i = \frac{N K_b \langle L_i \rangle}{1 + K_b \langle L_i \rangle + K'_b L'_i} \tag{4.8a}$$

$$B_i = \frac{N K'_b L'_i}{1 + K_b \langle L_i \rangle + K'_b L'_i} \quad . \tag{4.8b}$$

The equation for the signal now reads

$$\frac{\mathrm{d}S_i}{\mathrm{d}\tau} = \frac{k_s N K_b \langle L_i \rangle}{1 + K_b \langle L_i \rangle + K'_b L'_i} + \frac{k_s N K'_b L'_i}{1 + K_b \langle L_i \rangle + K'_b L'_i} - \nu_s S_i \quad . \tag{4.9}$$

We consider the phenomenological Collier equation for the ligand (Sec. 2.1) with the reversible transition into the diffusible ligand (Eq. 4.3). We also set

a dynamical equation for the diffusible ligand L'_i with the transition into the transmembrane non-diffusible ligand (Eq. 4.3), its diffusible transport (Eq. 4.4) and linear degradation. Then, the dimensional equations for both ligands read

$$\frac{\mathrm{d}L_i}{\mathrm{d}\tau} = \widetilde{k}_{-d}L'_i - \widetilde{k}_d L_i + \frac{\beta_l}{1+K_p S_i^h} - \nu_l L_i \tag{4.10a}$$

$$\frac{\mathrm{d}L'_i}{\mathrm{d}\tau} = -\widetilde{k}_{-d}L'_i + \widetilde{k}_d L_i + \widetilde{D}\widetilde{\nabla}_i^2 L'_i - \nu'_l L'_i \quad , \tag{4.10b}$$

where ν'_l and $\widetilde{D}$ are the linear degradation rate and the diffusion coefficient for the diffusible ligand, and the rest of parameters have been defined in Sec. 2.1.

We adimensionalize Eqs. 4.9- 4.10 by doing $S_i = S_0 s_i$, $L_i = L_0 l_i$, $L'_i = L'_0 l_i$, $\tau = T_0 t$ with S_0, L_0 and T_0 as $S_0 = \frac{k_s N}{\nu_s}$, $L_0 = \beta_l/\nu_l$, $L_0 = L'_0$ and $T_0 = 1/\nu_s$ where s_i, l_i and l'_i are the new non-dimensional variables for the signal, the ligand and the diffusible ligand, and t is the non-dimensional time. Hence, the adimensionalized dynamics now reads

$$\frac{\mathrm{d}s_i}{\mathrm{d}t} = \frac{r_t\langle l_i\rangle + r_s l'_i}{1+r_t\langle l_i\rangle + r_s l'_i} - s_i \tag{4.11a}$$

$$\frac{\mathrm{d}l_i}{\mathrm{d}t} = k_{-d}l'_i - k_d l_i + v\left\{\frac{1}{1+bs_i^h} - l_i\right\} \tag{4.11b}$$

$$\frac{\mathrm{d}l'_i}{\mathrm{d}t} = -k_{-d}l'_i + k_d l_i - \nu l'_i + D\nabla_i^2 l'_i \quad , \tag{4.11c}$$

where $r_t = K_b L_0$, $r_s = K'_b L_0$, $k_d = \widetilde{k}_d/\nu_s$, $k_{-d} = \widetilde{k}_{-d}/\nu_s$, $v = \nu_l/\nu_s$, $\nu = \nu_{l'}/\nu_s$ and $b = K_p S_0^h$. We set the non-dimensional diffusion coefficient $D = 4\widetilde{D}/(\nu_s\Delta^2)$ so that the non-dimensional discrete Laplacian now reads $\nabla_i^2 l'_i = \frac{1}{6}\sum_{j\in nn(i)}\left(l'_j - l'_i\right) = \langle l'_i\rangle - l_i$. We rewrite the model as

$$\frac{\mathrm{d}s_i}{\mathrm{d}t} = f(\langle l_i\rangle + \epsilon_r l'_i) - s_i \tag{4.12a}$$

$$\frac{\mathrm{d}l_i}{\mathrm{d}t} = k_{-d}l'_i - k_d l_i + v\left\{g(s_i) - l_i\right\} \tag{4.12b}$$

$$\frac{\mathrm{d}l'_i}{\mathrm{d}t} = -k_{-d}l'_i + k_d l_i - \nu l'_i + D\nabla_i^2 l'_i \quad , \tag{4.12c}$$

being f and g functions defined by

$$g(s_i) = \frac{1}{1+bs_i^h}, \qquad f(\langle l_i\rangle + \epsilon_r l'_i) = \frac{\langle l_i\rangle + \epsilon_r l'_i}{a + \langle l_i\rangle + \epsilon_r l'_i} \quad , \tag{4.13}$$

where $a = 1/r_t$, and $\epsilon_r = r_s/r_t$. ϵ_r measures the differential affinities between the receptor and the two ligands. A scheme of the modeled variables can be found in Fig. 4.2 (B).

For $\epsilon_r >> 1$ the receptor binds highly preferentially to the diffusible ligand and accordingly this ligand mediates all production of the signal. In contrast, for $\epsilon_r << 1$ the receptor mostly binds to the membrane-bound ligand and only trans-interactions are responsible for the signal. It can be readily shown that if no diffusible ligand is created ($k_d = 0$) then Collier model is recovered (Eqs. 1.1), as desired. We will use $h = 4$ in the following sections.

We will focus on studying when patterning occurs in the a–b parameter space, being a and b related to the threshold for signal activation and the strength of ligand repression, respectively. Also, we will study what happens when both diffusion coefficient D and the differential affinity parameter ϵ_r are varied.

4.3 Results

4.3.1 Lateral inhibition mediated by a diffusible ligand is not sufficient to generate a pattern

We now consider the pattern formation capabilities when cell-to-cell coupling is mediated by a diffusible ligand, what can be defined by the model Eqs. 4.12-4.13 (Fig. 4.1 (A)). In this case, the matrix $\mathscr{M}$ (Eq. 2.27), which is obtained from doing LSA (Sec. 2.4), is

$$\begin{pmatrix} -1 & \mathscr{C} \\ v\mathscr{B} & D\Omega - (D+v) \end{pmatrix} \quad , \tag{4.14}$$

where

$$\mathscr{B} = \left.\frac{\partial g(s_i)}{\partial s_i}\right|_{s_0} , \qquad \mathscr{C} = \left.\frac{\partial f(l_i')}{\partial l_i'}\right|_{l_0'} \quad , \tag{4.15}$$

and its eigenvalues read

$$\begin{aligned} \alpha_\Omega^\pm \quad &= \quad \frac{1}{2}\left\{-\left(1+v+D\left(1-\Omega\right)\right) \pm \right. \\ \left. \pm\sqrt{\left(1+v+D\left(1-\Omega\right)\right)^2 - 4\left(v(1-\mathscr{B}\mathscr{C}) + D\left(1-\Omega\right)\right)}\right\} \quad . \end{aligned} \tag{4.16}$$

Taking into account that $\Omega \in [-0.5, 1]$, then $(1 + v + D(1 - \Omega)) > 0$ is always fulfilled. Accordingly, α_Ω^+ is positive when $4(v(1 - \mathscr{B}\mathscr{C}) + D(1 - \Omega)) < 0$. However, since $\mathscr{B} < 0$ and $\mathscr{C} > 0$, this condition is never satisfied. Hence, for this model $Re(\alpha_\Omega) < 0$ is always satisfied and the homogeneous state is linearly stable. Indeed, no local bistable dynamics can be defined in this limit case which could yield, at least, transient patterns, such as those arising during phase transitions [176].

In summary, this analysis indicates that the diffusible ligand is not able to drive on its own pattern formation. Accordingly, we expect that when the overall ligand activity is distributed among the soluble and membrane-bound ligands, diffusion will tend to inhibit lateral inhibition pattern formation.

4.3.2 Diffusible ligand competing with transmembrane non-diffusible ligand inhibits patterning

Now we turn into the full model with diffusible and non-diffusible ligand (Eqs. 4.12a-4.12c)(Fig. 4.1 (B)) By doing LSA to this model, we end up with the $\mathscr{M}$ matrix (Eq. 2.27) as

$$\begin{pmatrix} -1 & \mathscr{A}\Omega & \mathscr{C} \\ v\mathscr{B} & -(v + k_d) & k_{-d} \\ 0 & k_d & D\Omega - (D + \nu + k_{-d}) \end{pmatrix} \quad , \tag{4.17}$$

where $\mathscr{B}$ is the same as in Sec. 4.3.1 and

$$\mathscr{C} = \left.\frac{\partial f(\langle l_i \rangle + \epsilon_r l_i')}{\partial l_i'}\right|_{l_0, l_0'} , \qquad \mathscr{A} = \omega \left.\frac{\partial f(\langle l_i \rangle + \epsilon_r l_i')}{\partial l_{i'}}\right|_{l_0, l_0'} , \tag{4.18}$$

where i' refers to the first neighbor cells to cell i. The diagonalization matrix 4.17 leads to the following third-order characteristic polynomial (Sec. 2.4):

$$P(\alpha_\Omega, \Omega) = \alpha_\Omega^3 + a_1\alpha_\Omega^2 + a_2\alpha_\Omega + a_3 \quad , \tag{4.19}$$

being a_1, a_2 and a_3 coefficients given by

$$\begin{aligned} a_1 &= (1 + D + k_d + k_{-d} + v + \nu) - D\Omega & (4.20a)\\ a_2 &= k_d + v + k_{-d}(1 + v) + (\nu + D)(1 + k_d + v) - \\ &\quad -(D(1 + k_d + v) + v\mathscr{A}\mathscr{B})\Omega & (4.20b)\\ a_3 &= k_{-d}v + (D + \nu)(k_d + v) - k_d v\mathscr{B}\mathscr{C} - (D(k_d + v) \\ &\quad +v(D + k_{-d} + \nu)\mathscr{A}\mathscr{B})\Omega + vD\mathscr{A}\mathscr{B}\Omega^2 \quad . & (4.20c) \end{aligned}$$

Notice that these coefficients depend on the homogeneous state (through the functions defined by $\mathscr{A}, \mathscr{B}$ and $\mathscr{C}$) and on the wavelength of the perturbation (Ω).

To address the stability of the homogeneous state, the Routh-Hurwitz stability criterion is used [3] (Sec. 2.4). This criterion establishes that the homogeneous solution is linearly unstable if any of the following conditions is not fulfilled:

$$a_1 > 0, \quad a_1 a_2 - a_3 > 0, \quad a_3 > 0 \quad . \tag{4.21}$$

In such a case, the Ω value within the interval $[-0.5, 1]$ that stronger violates such conditions will provide the fastest growing mode. Since all the parameters take positive values and $\Omega \in [-0.5, 1]$, the first condition is always fulfilled. Our numerical study shows that the third condition is first broken (Figs 4.3 and 4.4) and a_3 is minimum for $\Omega = -0.5$, which corresponds to the two modes of the lateral inhibition pattern ($\bar{q} = 1/3, \bar{p} = 2/3$) and ($\bar{q} = 2/3, \bar{p} = 1/3$). Hence, the fastest growing modes correspond to the periodicity of the lateral inhibition pattern, like in the Collier model with typical trans-interactions.

We analyze across the parameter space a–b the region where the homogeneous state becomes linearly unstable to inhomogeneous perturbations, *i.e.* the spontaneous pattern formation region. In agreement with the model with just trans-interactions (Sec. 2.10), intermediate a parameter values and high enough b parameter values leads to spontaneous patterning (Fig. 4.3). We compute this region for different values of the diffusion coefficient. As shown in Fig. 4.3, the spontaneous pattern formation region decreases in size as the diffusion coefficient increases. Hence, these results point out that diffusion promotes the stability of the homogeneous state, in agreement with results in previous section.

Taking into account our LSA results, we now evaluate along the parameter space whether the lateral inhibition pattern can arise in our full model 4.12a-4.12b. To this end, we apply the reduced model methodology explained in Sec. 2.5 and exemplified in Sec. 2.10 in Eqs. 4.12a-4.12b. Note that the spatial coupling now is mediated by both $\langle l_i \rangle$ and $\langle l'_i \rangle$, so pattern symmetries will be introduced in these two terms. The resulting reduced model reads

$$
\begin{aligned}
l_A &= \frac{k_{-d}}{k_d + v} l'_A + \frac{v}{k_d + v} g(s_A) && \text{(4.22a)} \\
l'_A &= \frac{k_d}{k_{-d} + \nu + D} l_A + \frac{D}{k_{-d} + \nu + D} l'_B && \text{(4.22b)} \\
s_A &= f(l_B + \epsilon_r l'_A) && \text{(4.22c)} \\
l_B &= \frac{k_{-d}}{k_d + v} l'_B + \frac{v}{k_d + v} g(s_B) && \text{(4.22d)} \\
l'_B &= \frac{k_d}{k_{-d} + \nu + D/2} l_B + \frac{D}{2(k_{-d} + \nu + D/2)} l'_A && \text{(4.22e)} \\
s_B &= f\left(\frac{1}{2}(l_A + l_B) + \epsilon_r l'_B \right) \quad . && \text{(4.22f)}
\end{aligned}
$$

By numerically solving it with Mathematica (Sec. 2.6) we obtain the exact activities corresponding to the homogeneous solution and to the lateral inhibition pattern. We evaluate the region in the a–b parameter space where the lateral inhibition pattern solution appears (region above the dashed lines in Fig. 4.3). As presented in Sec. 2.10.1 for the purely lateral inhibition model mediated by trans-interactions, we find that the lateral inhibition pattern solution exists as well in parameter regions where the homogeneous state is linearly stable. Therein we expect that small perturbations of the homogeneous state will decay in this region, but large enough perturbations may drive the appearance of the lateral inhibition pattern. Notice that this region of coexistence enlarges as the diffusion coefficient D increases (Fig. 4.3). Conversely, the region where the lateral inhibition pattern solution exists diminishes for soluble ligands with higher diffusion coefficients.

Another way to evaluate the role of the diffusible ligand in patterning is to study the effect of the differential affinity of the diffusible ligand with the receptor with respect to the trans-affinity (the ϵ_r parameter) in spontaneous patterning (Fig. 4.5). As expected, when ϵ_r decreases and thus the signal is

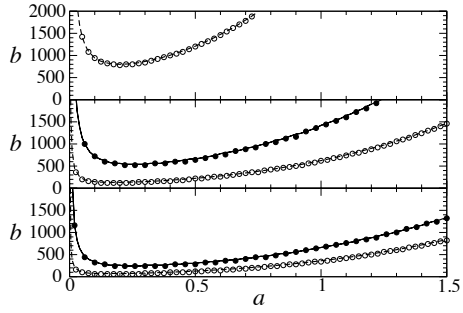

Figure 4.3: Diffusible ligand promotes the stability of the homogeneous state. Phase diagram of the model Eqs. 4.12a-4.12c across the a–b parameter space for diffusion coefficients $D = 0.01$ (bottom), $D = 0.1$ (middle) and $D = 0.5$ (top). Continuous lines and filled circles denote the boundary region above which the homogeneous solution is unstable to inhomogeneous perturbations. Discontinuous lines and empty circles denote the boundary region above which the lateral inhibition pattern solution exists. The regions in between continuous and dashed lines are the coexistence regions. Solid lines are numerical linear stability results for $a_3(\Omega = -0.5) = 0$, limiting an upper region where $a_3(\Omega = -0.5) < 0$. For $D = 0.5$ the homogeneous solution is linearly stable on the whole parameter space being shown. Dashed lines are computed as the boundary region above which Eqs. 4.22a-4.22f have a pattern solution. Symbols denote the boundary region above which $\eta_s \geq 0.01$ (Eq. 2.35). η_s is computed from data on the numerical integration of the full model with initial conditions corresponding to small uniformly distributed random perturbations of amplitude $\delta = 0.1$ added to the homogeneous solution (filled circles) or to the lateral inhibition pattern solution (empty circles). Perfect agreement between lines and symbols is found. Parameter values are $\epsilon_r = 0.01$, $k_d = k_{-d} = 1$, $v = 1$, $\nu = 0$.

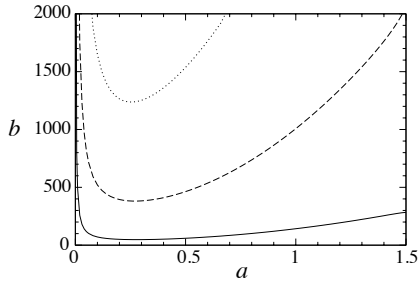

Figure 4.4: The second Routh-Hurwitz condition $a_1 a_2 - a_3 > 0$ is not violated in the a–b parameter space for Eqs. 4.12a-4.12c. Numerical LSA results for $D = 0.1$ showing the curves where function $F(\Omega) \equiv a_1 a_2 - a_3$ at its minimum ($\Omega = -0.5$) takes the values $F = 13.355$ (dotted), 13.845 (dashed) and 14.83 (solid). Parameter values as in Fig. 4.3.

increasingly mediated by trans-interactions, the region where the pattern solution exists enlarges. Therefore, decreasing ϵ_r favors pattern formation.

By solving Eqs. 4.22a-4.22f for different diffusion coefficients D and by checking the stability of the different solutions with Xpp-Aut software in a system of three cells on a line with periodic boundary conditions (Fig. 2.5 (B)), we find a bifurcation diagram along the D parameter, so we can analyze how the stable activity levels of each cell type change with diffusion. These bifurcation diagrams exhibit a region in a parameter space where both homogeneous and the lateral inhibition pattern state are linearly stable, being consistent with the bistable regions presented in Sec. 2.10. As shown in Fig. 4.6, the difference between the activities associated with the two cell types becomes smaller as D increases (s_A and s_B become more similar, and equivalently for $l_{A,B}$ and $l'_{A,B}$). In agreement with the presence of bistable regions where both the homogeneous state and the lateral inhibition pattern are stable, we find that the two cell states of the lateral inhibition pattern solution do not become arbitrarily similar and a discontinuous transition between the pattern and homogeneous solutions is observed as D increases. As expected from our previous results, for large enough diffusion coefficients, the homogeneous state is the only solution found.

We also compute the stationary activities that satisfy Eqs. 4.22a-4.22f together with its stability when the ligand inhibition strength b increases (Fig.

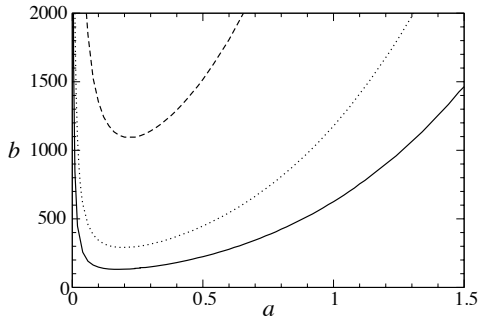

Figure 4.5: Pattern formation is inhibited when signaling mediated by the diffusible ligand dominates. Regions in the a–b parameter space where the lateral inhibition pattern solution is found for different contributions of diffusible ligand to the signal as measured by parameter ϵ_r: $\epsilon_r = 0.01$ (solid), $\epsilon_r = 0.05$ (dotted) and $\epsilon_r = 0.1$ (dashed). In the region above the line Eqs. 4.22a-4.22f have a pattern solution. Spontaneous patterning regions by LSA are omitted in this diagram for simplicity. Parameter values are $D = 0.1$, $k_d = k_{-d} = 1$, $v = 1$, $\nu = 0$.

4.7). As for the bifurcation diagram found for D, there is a region of bistability where both the homogeneous and the pattern solutions are stable. In contrast, the homogeneous state strongly depends on the value of b, and the pattern solution arises when the signal inhibits the ligand strongly enough, creating two distinct cell types whose activities do not significantly change for a broad range of the parameter values (Fig. 4.7).

Altogether these results show that the existence of a diffusible ligand destroys pattern formation in three ways: first, the parameter region where the homogeneous solution becomes linearly unstable is reduced; second, the parameter region where the pattern can emerge is also reduced, albeit less significantly; and third, the pattern softens since the two different cell types become less distinct.

In order to check the results above and further characterize the effects of a diffusible ligand, we turn to the numerical integration of the dynamics of the full model 4.12b-4.12a. In this chapter, integration is done with a Runge-Kutta fourth-order algorithm with time step $dt = 0.1$ on a two-dimensional hexagonal lattice of 30×30 cells with periodic boundary conditions. To compare these data with the results of the previous sections we use the order parameter defined in

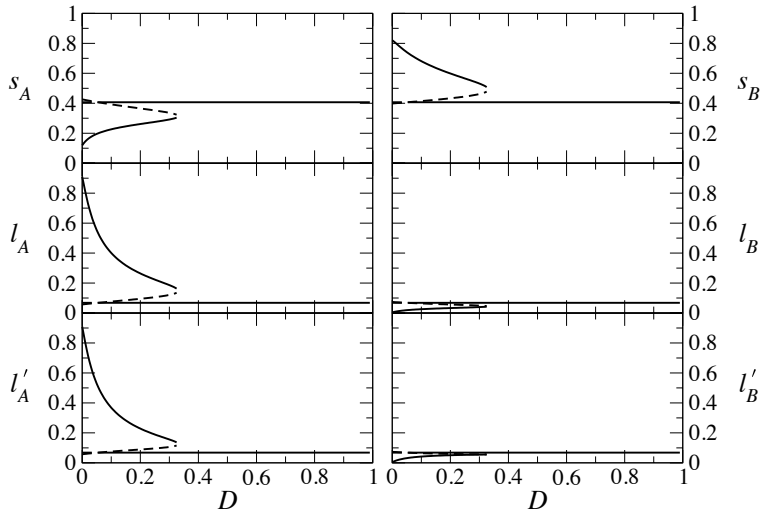

Figure 4.6: Diffusion softens the pattern. Bifurcation diagrams showing the stationary signal and ligand activities as a function of the diffusion coefficient D. These activities are solutions of Eqs. 4.22a-4.22f. Solid and dashed lines correspond to stable and unstable solutions, respectively. We determine the stability of the solutions with Xpp-Aut software. Parameter values are $a = 0.1$, $\epsilon_r = 0.01$, $k_d = k_{-d} = 1$, $v = 1$, $\nu = 0$ and $b = 500$.

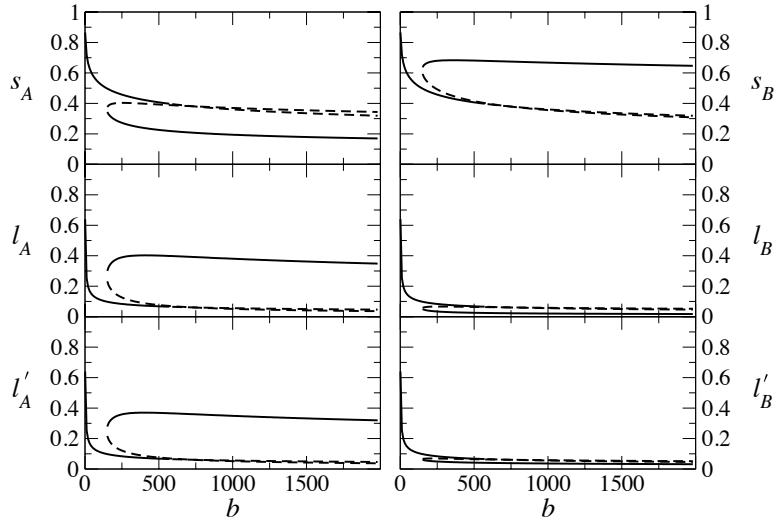

Figure 4.7: The homogeneous solution is dependent on ligand inhibition strength b, while the patterned states are not dependent on that. Bifurcation diagrams showing the stationary signal and ligand activities as in Fig. 4.6 as a function of the parameter b. Parameter values are $a = 0.1$, $\epsilon_r = 0.01$, $k_d = k_{-d} = 1$, $v = 1$, $\nu = 0$ and $D = 0.1$.

Sec. 2.8.1 for the Notch signal η_s.

We first confirm through numerical integration of the full model dynamics the LSA results. To this end, we use as initial condition the homogeneous solution with small uniformly distributed random perturbations. Small perturbations (Sec. 2.9.1) are expected to yield $\eta_s = 0$ exactly in those parameter regions where the homogeneous state is linearly stable. We explore the a–b parameter space for different values of the diffusion coefficient by discretizing it into a mesh of sizes $\Delta b = 40$ and $\Delta a = 0.04$. Our numerical results for η_s (filled circles in Fig. 4.3) are in perfect agreement with the LSA (solid lines in Fig. 4.3), as expected.

We also confirm by numerical integration of the full dynamics the parameter region where the lateral inhibition pattern solution exists. To this end, we apply an initial perturbation on the perfect lateral inhibition pattern and integrate the dynamics until the stationary state for the order parameter is reached (Sec. 2.9.1). Our numerical integration results (empty circles in Fig. 4.3) are in perfect agreement with the parameter region obtained in the previous section (dashed lines in Fig. 4.3).

To evaluate whether the lateral inhibition pattern is a stable solution of the full model dynamics, we numerically integrate the dynamics for a set of 50 different initial random perturbations of the lateral inhibition pattern introduced as described above. Notice that we can obtain theoretically which is the order parameter for the lateral inhibition pattern $\eta_s^{th,P}$ (Sec. 2.8.1 for details), and, hence, we can compare it to the average order parameter $< \eta_s >_E$ coming from simulation results. When necessary, averages are computed separately for data on ensembles with $\eta_s < 0.01$ and with $\eta_s \geq 0.01$. The order parameter for the lateral inhibition pattern is:

$$\eta_s^{th,P} = \frac{1}{3}\eta_{s_A}^{th,P} + \frac{2}{3}\eta_{s_B}^{th,P} \quad , \tag{4.23}$$

being $\eta_{s_1}^{th,P}$ and $\eta_{s_2}^{th,P}$ the local theoretical parameters evaluated with respect to cell type A and B respectively (right panels in Fig. 2.5). Given that $\eta_{s_A}^{th} = |s_A - s_B|$ and $\eta_{s_B}^{th} = \frac{1}{2}|s_A - s_B|$ we have

$$\eta_s^{th,P} = \frac{2}{3}|s_A - s_B| \quad . \tag{4.24}$$

This theoretical order parameter is plotted as lines in Figs. 4.8 and 4.9 as a

function of D and b respectively, by using the stable stationary solutions of Figs. 4.6 and 4.7. Our results for the numerical integration of the dynamics show that random initial perturbations of the lateral inhibition pattern always decay over time yielding $\eta_s = \eta_s^{th,P}$ (Fig. 4.9, top). Therefore, the lateral inhibition pattern is large hexagonal arrays (30×30) is a stable solution in the parameter region where the lateral inhibition pattern solution exists (positive-valued lines in Figs. 4.8 and 4.9).

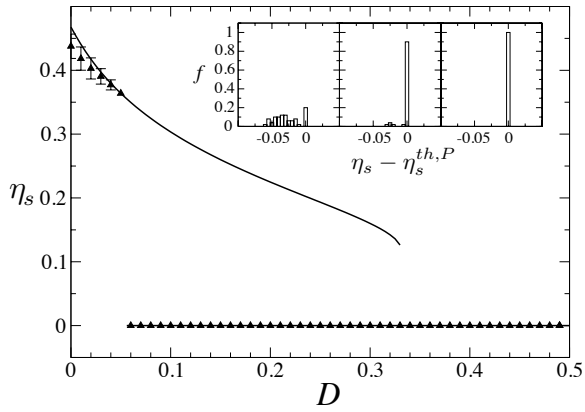

Figure 4.8: Order parameters from simulation results along D parameters confirming our LSA results. Lines stand for $\eta_s^{th,P}$ and for the order parameter of the homogeneous state ($\eta_s = 0$). $\eta_s = 0$ is plotted only for those parameter values where the homogeneous state is linearly stable. Symbols correspond to $< \eta_s >_E$ averaged over an ensemble of steady states reached by 50 different initial uniformly distributed random perturbations of amplitude size $\delta = 0.1$ applied to the homogeneous solution. Whiskers denote the standard deviation. Inset: Frequency of cases f reaching the perfect lateral inhibition pattern ($\eta_s - \eta_s^{th,P} = 0$) and the lateral inhibition pattern with defects ($\eta - \eta_s^{th,P} < 0$) for (left panel) $D = 0$, (middle) $D = 0.04$ and (right panel) $D = 0.05$. Parameter values are $a = 0.1$, $b = 500$ $\epsilon_r = 0.01$, $k_d = k_{-d} = 1$, $\nu = 0$ and $v = 1$.

To analyze whether the expected perfect lateral inhibition pattern solution arises spontaneously, we average the stationary order parameter reached by 50 different initial perturbations of the homogeneous state for different values of D and b. Our results show that perturbations decay over time when the homogeneous solution is linearly stable, further confirming our linear stability results

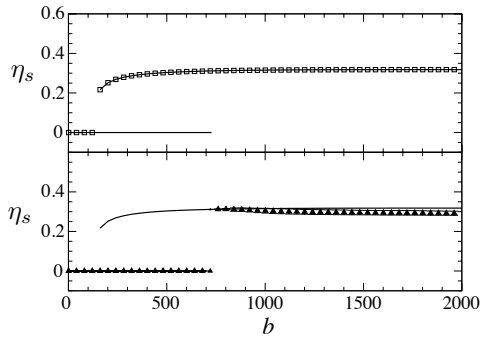

Figure 4.9: Order parameters from simulation results along b parameter confirming the exact pattern solutions (top) and our LSA (bottom) results for $D = 0.1$. Lines stand for $\eta_s^{th,P}$ and for the order parameter of the homogeneous state ($\eta_s = 0$). $\eta_s = 0$ is plotted only for those parameter values where the homogeneous state is linearly stable. Symbols correspond to $< \eta_s >_E$ averaged over an ensemble of steady states reached by 50 different initial uniformly distributed random perturbations of amplitude size $\delta = 0.1$ applied to the lateral inhibition pattern (top, empty symbols) and to the homogeneous solution (bottom, filled symbols). Whiskers denote the standard deviation. Other parameter values as in Fig. 4.8.

(Figs. 4.8 and 4.9). In contrast, when the homogeneous state is linearly unstable according to the LSA, these small perturbations grow and a pattern ($\eta_s > 0$) arises, as expected. Close to the transition point and still within the region of stability of the homogeneous state, an increase in the amplitude of perturbations favors nonlinear effects and the chance of reaching the pattern state (not shown), being consistent with Fig. 2.15 (B). Snapshots of the stationary pattern of the diffusible ligand are depicted in Fig. 4.10 for different values of the diffusion coefficient D, confirming that the normal lateral inhibition pattern spontaneously emerges, and hence, that the diffusible ligand is not able to change the characteristic length of the pattern.

Altogether, these results confirm the stability of the homogeneous and the lateral inhibition pattern states as well as the coexistence of these two states presented in the previous sections.

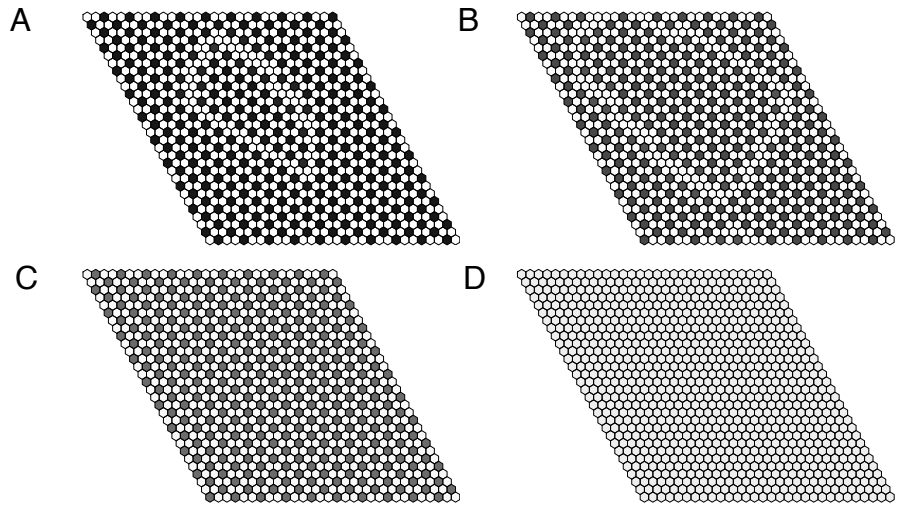

Figure 4.10: Intermediate diffusion coefficients help to create perfect patterns, while higher diffusion coefficients destroy patterning. Simulation snapshots of the activity of the diffusible ligand l'_i across a lattice of cells for different values of the diffusion coefficient D: (A) $D = 0$, (B) $D = 0.02$, (C) $D = 0.04$ and (D) $D = 0.06$. Black stands for high ligand activities (black is for $l'_i = 1$ and white for $l'_i = 0$). In all panels, data correspond to steady states reached by initial perturbations applied to the homogeneous state for a lattice of 30×30 cells. Other parameter values as in Fig. 4.8.

4.3.3 Diffusible ligand can help to create perfect patterns

As shown in Fig. 4.10 and as indicated by the small differences between the values of η_s and $\eta_s^{th,P}$ in Fig. 4.8 , the pattern that is spontaneously formed can have small imperfections that consist in additional white cells being present between domains with the perfect lateral inhibition pattern. These imperfections correspond to longer-range modes, as evidenced by an analysis of the structure function of the stationary patterns (Fig. 4.11 (A)). The structure function has been computed as (Sec. 2.8.2)

$$\mathbb{S}(\Omega) = \frac{1}{C(\Omega)} \sum_{(\bar{q},\bar{p})\in\Omega} \mathbb{S}(\bar{q},\bar{p}) \quad , \tag{4.25}$$

with $C(\Omega)$ being the number of $\bar{q}$,$\bar{p}$ modes that yield the same Ω value (Eq. 2.24), and

$$\mathbb{S}(\bar{q},\bar{p}) = \frac{1}{MN}\langle \sigma'_{\bar{q},\bar{p}}\sigma'_{-\bar{q},-\bar{p}}\rangle_E \tag{4.26a}$$

$$\sigma'_{\bar{q},\bar{p}} = \sum_{k=1}^{M}\sum_{j=1}^{N}(s_{j,k}-s_b)e^{-2\pi \mathrm{i}(\bar{q}j+\bar{p}k)} \quad , \tag{4.26b}$$

where $s_{j,k}$ is the signal in the cell located at site j,k (Fig. 2.1 for the cell labeling scheme) and $s_b \equiv (s_A + 2s_B)/3$ with s_A and s_B being the stationary signal state values for the lateral inhibition pattern obtained from Eqs. 4.22a-4.22f. This value of s_b has been chosen such that no contribution arises for the homogeneous solution $\Omega = 1$ ($\bar{q} = 1$, $\bar{p} = 1$) (Sec. 2.8.2 and App. B). Brackets with subindex E stand for averages over the whole ensemble of numerically steady states reached by the set of initial random perturbations.

Interestingly, our results show that diffusion can erase these imperfections and allow the emergence of the perfect periodic pattern (Figs. 4.10). In the inset of Fig. 4.8 we can see that $\eta_s \leq \eta_s^{th}$, and also that the frequency of cases that reach the perfect lateral inhibition increases as the transition point where the homogeneous state loses its linear stability is approached by diffusion.

We evaluate through LSA described in Sec. 4.3.2 the growth rate $Re(\alpha)$ of different modes across the parameter space (Fig. 4.12 and 4.13 (A)). As we move far away from the transition point, we expect additional modes apart from the fastest growing mode to grow as well and become significant in the full nonlinear

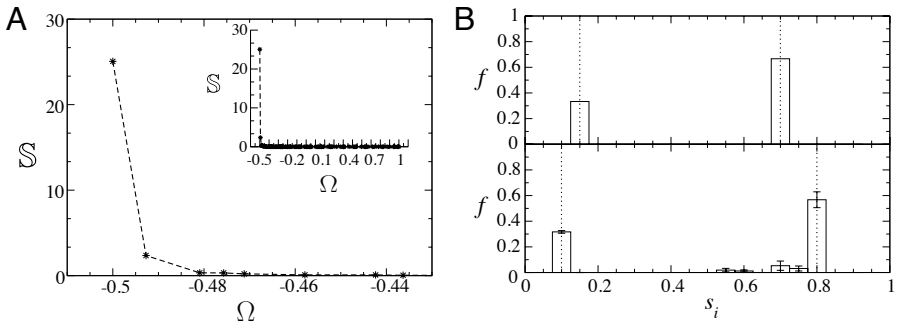

Figure 4.11: Characterization of the pattern defects. (A) Structure function averaged over the ensemble of data of Fig. 4.8 for $D = 0$. Stars denote the structure function at the discrete values of Ω. Lines are a guide to the eye. The inset shows the same structure function for the whole range of Ω values. (B) Frequency of cells f with signal activity s_i evaluated for the ensemble of patterns of Fig. 4.8 (A) for (bottom) $D = 0$ and (top) $D = 0.05$. Whiskers denote the standard deviation. Vertical dotted lines stand at the signal activity values that characterize the two cell states of the lateral inhibition pattern, obtained as solutions of Eqs. 4.22a-4.22f. In all panels, data correspond to steady states reached by initial perturbations applied to the homogeneous state for a lattice of 30×30 cells. Other parameter values as in Fig. 4.8.

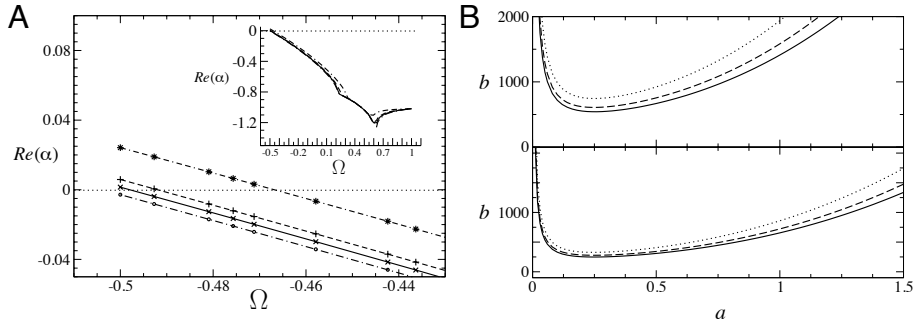

Figure 4.12: LSA results show where a single mode can grow, being consistent with simulation results leading to perfect regular lateral inhibition patterns. (A) Growth rate $Re(\alpha)$ of discrete modes characterized by Ω computed through the LSA in section 3.3 for $D = 0$ (stars), $D = 0.04$ (+ symbol), $D = 0.05$ ($\times$ symbol) and $D = 0.06$ (circles) for a lattice of 30×30 cells. Lines are a guide to the eye. The inset shows the same dispersion relation for the whole range of Ω values in lines. (B) Lines denote the a–b parameter region above which the group of modes being analyzed grow. Results are shown for the third (dotted, $\Omega \approx -0.481$) and second (dashed, $\Omega \approx -0.492$) group of fastest growing modes as well as for the fastest growing mode (solid line, $\Omega = -0.5$) for a lattice of 30×30 cells. The bottom panel is for $D = 0$ and the top panel corresponds to $D = 0.1$. Other parameter values as in Fig. 4.8.

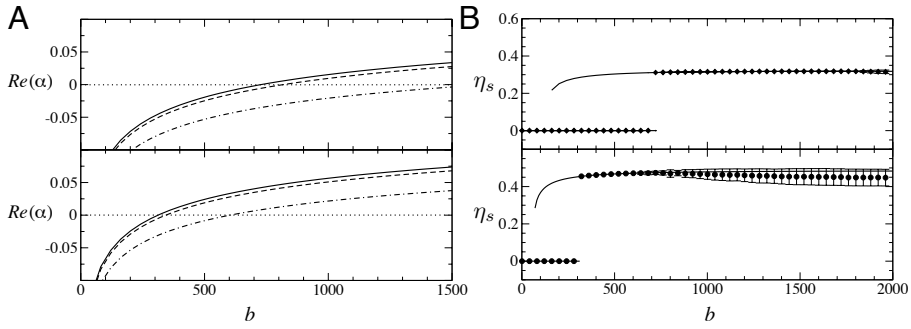

Figure 4.13: Diffusion strongly promotes perfect lateral inhibition patterns in smaller systems. (A) Growth rate as a function of b for the fastest growing mode (continuous line, $\Omega = -0.5$) and for the subsequent group of fastest modes for a lattice of 30×30 cells (dashed line, $\Omega \approx -0.492$) and a lattice of 12×12 cells (point-dashed line, $\Omega \approx -0.455$). The bottom panel is for $D = 0$ and the top panel corresponds to $D = 0.1$. The horizontal dotted lines indicate null growth. (B) Order parameter versus b as in Fig. 4.9 (bottom) for a lattice of 12×12 cells for (bottom) $D = 0$ and (top) $D = 0.1$. The remaining parameter values are as in Fig. 4.8.

dynamic regime. These modes can yield spatial domains similar to the domains that we observe with characteristic wavelengths that differ from those of the fastest growing mode [5]. Figs. 4.12 and 4.13 (A) show parameter regions obtained from the numerical LSA where a single mode can grow. In agreement, our simulations (Figs. 4.8 and 4.9) always reach the perfect lateral inhibition pattern just within those parameter regions that have a single, the fastest, growing mode. Outside these parameter regions, the dynamics yield patterns with defects, although the perfect lateral inhibition pattern may still be reached (inset in Fig. 4.8). Moreover, our analysis of the structure function (Fig. 4.11 (A)) shows that the spatial modes that arise on patterns with these imperfections correspond to modes that linearly destabilize the homogeneous state (*i.e.* these modes have a positive growth rate $Re(\alpha)$ as shown in Fig. 4.12 (A)).

In Fig. 4.12 (B), we show the boundary region within the a–b parameter space where each of the three groups of fastest growing modes (Ω) start to grow. Our numerical LSA analysis reveals that these modes start to grow for larger distances across the parameter space as D increases. Notice also that these distances

increase strongly for modes that have more distant values of Ω. Hence, diffusion promotes a larger separation of modes within the parameter space and a larger parameter region where the fastest growing mode is the single one destabilizing the homogeneous solution. Consequently, diffusion promotes the appearance of the perfect lateral inhibition pattern.

Taking into account these results and the inherent discrete nature of the characteristic modes (Ω), we analyze the dynamics on a system with fewer cells (12×12). For such a system, the two groups of fastest growing modes have quite distant values of function Ω. Hence, our stability analysis indicates that large parameter regions separate the boundaries where these modes start to grow (Fig. 4.13 (A)). Accordingly, the diffusion coefficient is expected to strongly promote the perfect lateral inhibition pattern in this small system. We numerically integrate the dynamics on this small system for a set of 50 different well-defined random perturbations of the homogeneous state. As expected, our results show that diffusion strongly enlarges the parameter region where the perfect lateral inhibition pattern is reached (Fig. 4.13 (B)) and which corresponds to the region where a single mode can grow.

4.4 Discussion

In this chapter we investigated numerically and analytically the effect of a diffusible ligand on the lateral inhibition dynamics of pattern formation. Our study shows that the existence of a molecular ligand species that diffuses in the extracellular space and activates the Notch pathway is not able to induce patterning *per se* (without the canonical transmembrane non-diffusible ligand). Also our study shows that combined with the canonical trans-interactions, the diffusible ligand does not introduce any new characteristic wavelength on the pattern being formed. In this case, diffusion of this ligand extends the region where the homogeneous solution is stable and homogenizes the cell states reached by cells, which become less distinct. For large enough diffusion coefficients or when the signal is controled just by the diffusible ligand, no pattern can emerge. Our results predict that by increasing the diffusion coefficient of the diffusible ligand or by increasing its affinity for Notch, the pattern should be destroyed. These results are consistent with the fact that diffusible ligands activating Nocth introduce a

negative feedback within the cell (Fig. 4.2), leading to homeostasis[3].

Our results show that lateral inhibition *per se* (without diffusible ligand) drives patterning with imperfections. We have proved that these imperfections correspond to other modes that can also linearly unstabilize the homogeneous steady state. It is worth mentioning that we do not observe any dynamical evolution of the spatial imperfections that arise across the pattern over long time intervals (100 times longer than the time required to achieving stationary cell states within domains with the periodicity of the fastest growing mode). However, since these dynamics can be expected to be extremely slow, we cannot totally discard a dynamical evolution. In any case, a dynamical evolution will be promoted if dynamical fluctuations — noise — are introduced. At low noise intensities, these defects will not move (Sec. 2.10.2). It will be worth analyzing in future studies in a quantitative way the effect of noise on the evolution of these domains or imperfections characterized by modes that do not correspond to the fastest growing mode. Interestingly, our results predict that when we consider lateral inhibition through trans-interactions, the addition of a diffusible ligand facilitates the emergence of the perfect periodic lateral inhibition pattern and this effect becomes more relevant for small cell arrays composed of few cells.

Experimental observations have shown that in some contexts, lateral inhibition patterns exhibit a very precise order, while in other contexts pattern imperfections can appear. Hence, in tissues where the order is required, mechanisms for the control of pattern regularity should exist. Different mechanisms have been proposed to reduce pattern imperfections. For instance, Cohen *et al.* (2012) recently showed with a combined theoretical and experimental approach that dynamic filopodia has an important role for pattern refinement, and that it helps to create regular patterns [114]. Also, it has been proposed from a theoretical ground that programmed cell death and cellular rearrangements due to differential adhesion can also help to reduce patterning errors [131]. Indeed, it has recently observed that in the auditory epithelia of mice cell adhesion molecules called nectins interact between them, and they are essential for the proper cell rearrangement, driving very well ordered lateral inhibition patterns [177, 178]. Togashi *et al.* [177] show that different nectins knock outs in mice embryos alter

[3]Negative feedbacks are rather associated with homeostasis, and contrarily, positive feedbacks are associated to multistability [32].

the perfect salt-and-pepper pattern of hair cells and supporting cells found in the wild type tissues. Barad *et al.* (2010) have also proposed that a reduction of the delay of the performance in the lateral inhibition process would reduce errors in patterning, and they propose that cis-interactions, *i.e.* receptor-ligand binding within the same cell, would contribute on that [49]. Our work predicts that in the canonical Notch signaling pathway mediated by trans-interactions, a diffusible ligand that activates Notch signaling can enhance pattern regularity.

Nowadays there are multiple evidences from experimental data that diffusible canonical and non-canonical ligands can present different effects in Notch signaling in vertebrates and non-vertebrates [74, 117–120]. Our work does not focus on any particular diffusible molecule, but introduces a diffusible cell-to-cell coupling that activates Notch signaling. Diffusible canonical and non-canonical ligands have been reported to have both inhibitory and activatory effects to the Notch signal [117]. The next step then would be to explore different signaling rates from the receptor-diffusible ligand interactions. In particular, if diffusible ligand just blocks the Notch receptor, it could create an additional positive feedback loop that linked with the diffusion and the normal trans-interactions will possibly modify the characteristic wavelength of the pattern.

On the other side, more experimental efforts will have to be done to determine whether diffusible ligands have an active role on lateral inhibition patterning. The application of soluble ligand concentration in developing tissues could be used to test our model predictions. The systematic variation of the control parameters used in this study (the threshold for signal activation a, the ligand inhibition strength b, the differential affinities of the two ligands with the receptor ϵ_r, and the diffusion coefficient of the diffusible ligand D) will lead to different results when diffusible ligand is present and when it is not. Some predictions, like the pattern softening and the pattern inhibition will be easily to test, while the effect of pattern regularity will be probably more difficult to figure out. Hence, we will probably have to wait several more years to achieve this experimental control to test our predictions.

Chapter 5

Competition in Notch signaling dynamics with cis enriches cellular decision making

5.1 Introduction

Recent experimental evidences have shown that the Notch receptor and its ligands can interact in *cis*, by binding within the same cell [72, 122, 127, 179]. These cis-interactions compete with trans-interactions since both need the Notch receptor, and result in cis-inhibition, *i.e.* in a reduction of Notch signaling [47, 121–129]. Computational studies have revealed that cis-inhibition facilitates patterning, by promoting faster responses, enhancing robustness and precision and relaxing the constraints required for patterning [47, 49, 90, 105, 130].

The complexity of the Notch signaling pathway at the post-translational level and its interplay with endocytic routes has been recently started to be uncovered. On this basis, Notch signaling activity coming from cis-interactions has been proposed for specific developmental scenarios [81,180]. But, is a cis-driven Notch

signal compatible with cis-inhibition? Commonly, cis-inhibition arises from the absence of cis-signaling.

Apart from cis-interactions, which set a cell-autonomous component in Notch pathway, recently it has been shown that Notch activity that is ligand-independent can arise. This has been observed in situations in which endocytosis was impaired and also in wild-type situations [63, 81, 181–188, 188, 189]. For instance, a recent study in *Drosophila* blood cells has detected a ligand-independent Notch signal that has significant role in development [188, 189]. This sets an additional potential cell-autonomous element of Notch signaling. What is the role of such cell-autonomous dynamics? This ligand-independent signaling mechanism will also compete with cis-interactions for the receptor, as trans-interactions do.

In this chapter we address these issues and evaluate the role of cis-interactions in cellular decision making both in single (autonomous) cells and in a coordinated manner during patterning. We will often refer to the Delta ligand, but it could be extended to the other ligands of the Notch pathway.

5.2 Modeling ligand-receptor cis-interactions

5.2.1 Multicellular system

We have constructed a mathematical model that takes into account cis and trans-interactions between the Notch receptor and the ligand in a multicellular system (Fig. 5.1 (A)). As what we did when a diffusible ligand was considered (Chap. 4), we set canonical Notch signaling activity proportional to the trans-interactions complex in equilibrium C_i and add a signal coming from cis-interactions from the cis-complex concentration B_i. We assume trans and cis-signals have the same genetic targets but can have different signaling rates, whose ratio is given by parameter ϵ[1]. For $\epsilon = 0$ the well-known cis-inhibition that sequesters the ligand and drives no signal is recovered. For $\epsilon = 1$, both trans and cis signals are elicited at the same rate.

Now, following a similar procedure as in Sec. 4.2 we obtain the equation for

[1] We will also refer to signaling strengths as a synonym of signaling rates.

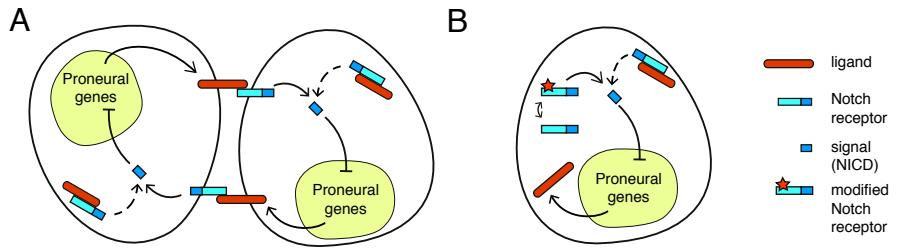

Figure 5.1: Cartoons of the Notch signaling pathway with cis-interactions. We study its implications at the multicellular (A) and cell-autonomous (B) levels. In the multicellular case (A) the ligand (red) in a cell trans-interacts with the Notch receptor (blue) in a neighboring cell, eliciting a signal (NICD) towards the cell harboring the receptor that inhibits ligand production. In the single cell case (B) we assume a free Notch receptor that can be reversively modified, eliciting a signal (NICD) that inhibits ligand production. In both schemes, cis-interactions between the ligand and the Notch receptor within the same cell can trap the receptor and elicit no signal ($\epsilon = 0$), or elicit an inhibitory signal on ligand production with relative signaling rate ϵ compared to the other existing signaling source (dashed arrow).

the signal, which reads

$$\frac{\mathrm{d}S_i}{\mathrm{d}\tau} = \frac{k_s N K_b \langle L_i \rangle}{1 + K_b \langle L_i \rangle + K_b' L_i} + \frac{\epsilon k_s N K_b' L_i}{1 + K_b \langle L_i \rangle + K_b' L_i} - \nu_s S_i \quad , \tag{5.1}$$

where K_b and K_b' are the affinities for the trans and cis complexes formations, respectively. By using the Collier dimensional equation for the ligand (Eq. 2.7) and doing the usual adimensionalization, the dynamics in cell i of the Notch signal s_i and the ligand l_i read

$$\frac{\mathrm{d}s_i}{\mathrm{d}t} = f(\mu, l_i) - s_i \tag{5.2a}$$

$$\frac{\mathrm{d}l_i}{\mathrm{d}t} = \nu \left\{ g(s_i) - l_i \right\} \quad , \tag{5.2b}$$

where

$$g(s_i) = \frac{1}{1 + b s_i^h} \quad , \quad f(\mu, l_i) = P_{1i} + P_{2i} \quad . \tag{5.3}$$

P_{1i} and P_{2i} are the Notch signal production terms due to trans and cis-interactions,

respectively, which read

$$P_{1i} = \frac{\mu}{1+\mu+r_c l_i} \tag{5.4a}$$

$$P_{2i} = \frac{\epsilon r_c l_i}{1+\mu+r_c l_i} \quad , \tag{5.4b}$$

where $\mu = r_t \langle l_i \rangle$. $r_{t,c}$ are proportional to the trans and cis-affinities respectively, and read $r_t = K_b L_0$ and $r_c = K'_b L_0$. Herein we will refer to them as the trans and cis-interactions strengths. $g(s_i)$ function and b, v and h parameters are defined as in Collier model. The competing effect between trans and cis-interactions becomes evident in the denominator of P_{1i} and P_{2i} terms, both depending on r_c and μ. If cis-interactions are not taken into account (*i.e.* $r_c = 0$) we recover the Collier model (see Eqs. 1.1).

5.2.2 Single cell system

Our model enables to easily evaluate as well the cell-autonomous role of Notch dynamics if cis-interactions and ligand-independent signaling occur together (Fig. 5.1 (B)). In this case, we suppose that the Notch signal has a ligand independent signaling source coming from a modified form of Notch C_i, and the cis-signaling source. For computing the equilibrium concentration of the Notch modified term, we take into account the following chemical reaction:

$$N_i \underset{k_{-b}}{\overset{k_b}{\rightleftharpoons}} C_i \xrightarrow{k_s} S_i + C_i \quad . \tag{5.5}$$

By a similar procedure as in Sec. 4.2 we obtain the equilibrium concentration of the Notch modified species:

$$C_i = \frac{N\mu_0}{1+\mu_0+K'_b L_i} \quad , \tag{5.6}$$

where now μ_0 is the equilibrium constant $\mu_0 = k_b/k_{-b}$. Then, by the usual procedure we obtain the dynamical equations for this system which are the same as for the multicellular system (Eqs. 5.2-5.4) but with μ being set as a constant, *i.e.* $\mu = \mu_0$.

Our mathematical approach allows the study of cis-interactions competing with trans-interactions or with ligand-independent signaling by using a single

theoretical framework[2]. Note that this formalism can be extended to two different ligands that are acting cell-autonomously with different signaling rates (see next chapter).

In Sec. 5.3.7 we will study the single cell system in a more general model.

5.3 Results

5.3.1 Competition for Notch signaling can result in cis-inhibition

The above model takes into account two potential sources of Notch signaling: one that is either driven by trans-interactions or is ligand-independent P_{1i}, that for simplicity will be referred as the primary signal source, and an additional one driven by cis-interactions P_{2i}. At $\epsilon = 0$ cis-interactions just trap the receptor, which is then unable to signal (Fig. 5.1). Accordingly, at $\epsilon = 0$ cis-interactions act as an effective inhibitor of Notch signal production, driving cis-inhibition. However, if cis-interactions can elicit and additional extra Notch signal ($\epsilon > 0$), will these interactions drive cis-activation or could still cis-inhibition be taking place? In this case, there are two competing signaling sources that share the same substrate — the Notch receptor — and drive signaling at different rates.

Mathematically, cis-inhibition can be identified as a reduction of Notch signal production within a cell when the amount of Delta ligand increases in the cell ($\mathscr{R}_{s_i,l_i} = \frac{\partial f(\mu,l_i)}{\partial l_i} < 0$) (Sec. 2.2)[3]. Conversely, cis-activation occurs when Notch signal production increases with ligand accumulation within the cell ($\mathscr{R}_{s_i,l_i} = \frac{\partial f(\mu,l_i)}{\partial l_i} > 0$). By using

$$\mathscr{R}_{s_i,l_i} = \frac{r_c(\epsilon + \mu(\epsilon - 1))}{(1 + \mu + r_c l_i)^2} \quad , \tag{5.7}$$

and taking into account these definitions, it can be readily obtained that cis-inhibition occurs for

$$\epsilon + \mu\,(\epsilon - 1) < 0 \quad . \tag{5.8}$$

[2]For simplicity, we will keep the subindex i even if we refer to the single cell system.

[3]We remind that in Sec. 2.2 we defined $\mathscr{R}_{x_i,y_i} = \frac{\partial}{\partial y_i}\frac{\mathrm{d}x_i}{\mathrm{d}t}$.

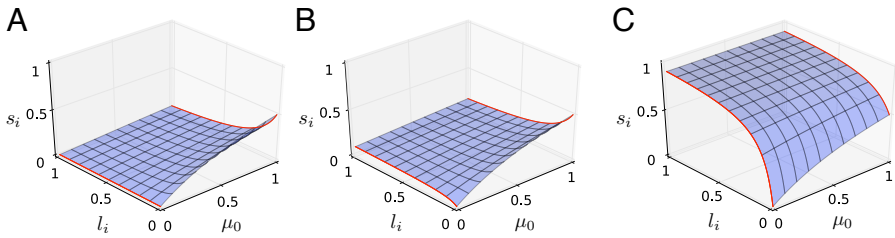

Figure 5.2: Cis-interactions role depends on the relative cis/trans-signaling rates ϵ and the ligand independent rate μ_0 at the cell-autonomous scenario. Notch signal *versus* l_i and μ_0 for (A) null $\epsilon = 0$, (B) weak $\epsilon = 0.1$ and (C) strong ($\epsilon = 1$) cis signaling. Red lines indicate that s_i increases or decreases as a function of l_i, indicating cis-activation or cis-inhibition respectively. Other parameter values: $r_c = 10$.

Otherwise, cis-activation is taking place. Four different aspects of this relation are worth mentioning. First, as indicated above, $\epsilon = 0$ always drives cis-inhibition. Second, $\epsilon \geq 1$ (*i.e.* cis-interactions elicit at least as much Notch signal as the primary signal source does) always drives cis-activation [4]. Third, when cis-interactions elicit a signal weaker than the primary signal source ($\epsilon < 1$), cis-inhibition can still be occurring. This can be understood as follows: when the ligand within a cell increases, it can bind the receptor in cis, reducing the amount of receptors that would otherwise contribute to the primary signal source (through trans-binding, for instance). Since the signal generated from cis is weaker than otherwise, a reduction of Notch signaling (cis-inhibition) happens. Therefore, cis-inhibition when cis-interactions are signal-productive involves competition between signaling sources for the receptor. Fourth, whether cis-inhibition or cis-activation is taking place for $0 < \epsilon < 1$ depends on ϵ and μ (see Figs. 5.2-5.3).

We have evaluated Eq. 5.8 for different values of ϵ and μ for the cell-autonomous system ($\mu = \mu_0$, Figs. 5.2 and 5.4 (A)) and for different values of ϵ and r_t for the multicellular system ($\mu = r_t\langle l_i \rangle$ for trans-interactions, being $\langle l_i \rangle$ the cell-to-cell coupling term, Figs. 5.3 and 5.4 (B)) when $\langle l_i \rangle$ takes the value of the homogeneous steady state of the system. In the multicellular context, this evaluation indicates whether cis-activation or cis-inhibition is taking

[4] In the non-conserved model it can be shown that such condition is fulfilled for ϵ_c which not necessarily is $\epsilon_c = 1$ (see Sec. 5.3.7).

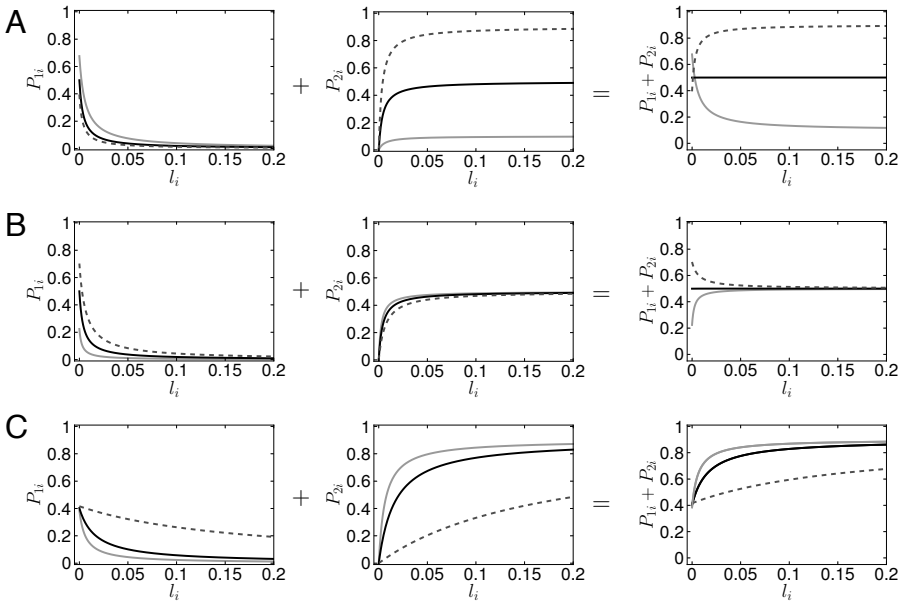

Figure 5.3: Cis-interactions role depends on the relative cis/trans signaling rates ϵ and the trans-interactions strength r_t in the multicellular scenario. Diagrams showing how the signal production rate due to trans (P_{1i}), cis (P_{2i}) and the total signal production ($P_{1i}+P_{2i}$) change by varying the quantity of Delta within the cell, for (A) different relative cis/trans signaling rates, (B) trans-interactions strengths r_t and (C) cis-interactions strengths r_c. The Delta trans contribution $\langle l_i \rangle$ is set to the homogeneous fixed point. In (A) we have $\epsilon = 0.1$ (gray solid line), $\epsilon = 0.5$ (black solid line) and $\epsilon = 0.9$ (dashed line); $r_t = 250$ and $r_c = 500$ is used for all lines. In (B) $r_t = 50$ (gray solid line), $r_t = 100$ (black solid line) and $r_t = 1000$ (dashed line); $\epsilon = 0.5$ and $r_c = 500$ for all lines. In (C) we have $r_c = 10$ (dashed line), $r_c = 100$ (black solid line) and $r_c = 250$ (gray solid line) ; $\epsilon = 0.9$ and $r_t = 250$ for all lines. P_{2i} always increases with the Delta ligand in a cell, while P_{1i} decreases because of the sequestering effect of the receptors due to cis. Other parameter values: $h = 2$, $b = 1000$. Cis-inhibition acts for null cis-signaling and for high trans-interactions strengths when the cis-signaling rate is weak. Cis-activation acts for strong cis-signaling. Cis-interactions strength does not change the nature of cis-interactions.

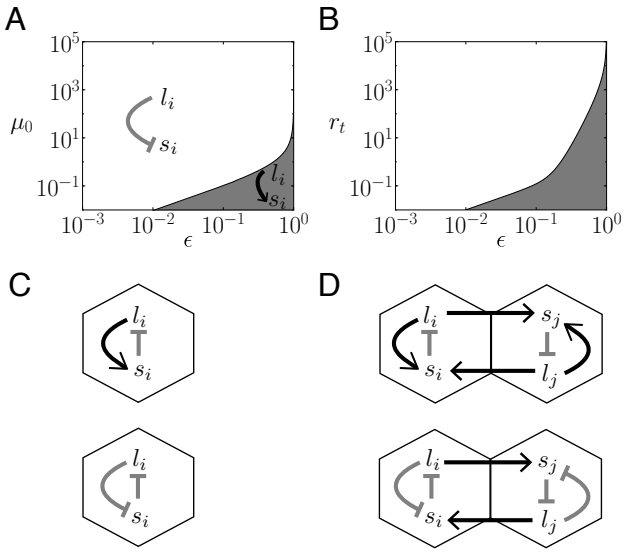

Figure 5.4: Cis-interactions can lead to cis-activation or cis-inhibition. Implications at the cell-autonomous (left) and multicellular (right) scenarios. (A,B) Parameter space showing where cis-activation (grey region) and cis-inhibition (white region) occurs. The activating or inhibiting role of cis-interactions depends on the rate of cis-signaling (ϵ) and the primary signal production rate μ, which is in the multicellular case proportional to the trans-interactions strength (r_t). Cis-inhibition acts for null or weak cis-signaling. Cis-activation acts for strong cis-signaling. (C,D) Cis-interactions set an intracellular feedback, leading to two possible effective transcriptional regulatory circuit designs. Cis-activation drives a negative feedback loop on ligand production within the cell. Cis-inhibition drives a positive feedback loop on ligand production. Parameter values for panels (A,B): $h = 4$, $r_c = 1$, $v = 1$.

place in a field of equivalent precursor cells, all in the same state. Our results show that weak cis-signaling (small ϵ) and strong trans-interactions (r_t) or ligand-independent signaling (μ_0) facilitate cis-inhibition. Taken together, these results exemplify that a reduction of Notch signaling when ligand Delta is increased within a cell (cis-inhibition) is not necessarily due to the absence of cis-signaling and can result from weak enough cis-driven Notch signaling.

5.3.2 Cis-inhibition can facilitate cell-autonomous bistability

Notch signaling inhibits Delta ligand expression. In turn, we have shown that the Delta ligand can either inhibit (cis-inhibition) or activate (cis-activation) Notch signaling within the cell. Taken together, cis-inhibition drives a transcriptional positive feedback loop within the cell, whereas cis-activation drives a transcriptional negative feedback loop (Fig. 5.4 (C,D)).

It is well known that positive feedback loops enable bistability, while negative feedback loops yield monostable states (see for instance review [32]). Then, is the positive feedback generated by cis-inhibition sufficient to drive bistability? From the precedent section, we can state that cis-inhibition requires a competing primary signaling source to happen, so the existence of the positive intracellular feedback also relies on that. Herein we focus on cell-autonomous dynamics and take into account ligand-independent Notch signaling $P_{1i} = \frac{\mu_0}{1+\mu_0+r_c l_i}$.

We compute the steady state solutions for the Eqs. 5.2-5.4 when $\mu = \mu_0$ by solving

$$l_i = \frac{s_i(1+\mu_0)-\mu_0}{r_c(\epsilon - s_i)} \tag{5.9a}$$

$$l_i = \frac{1}{1+bs_i^h} \quad . \tag{5.9b}$$

We can evaluate the stability of such solutions with simulations (Fig. 5.5) and LSA. Specifically, the Jacobian matrix $\mathscr{M}$ (Eq. 2.27) for a single cell system reads

$$\begin{pmatrix} -1 & \mathscr{C} \\ v\mathscr{B} & -v \end{pmatrix} \quad ,$$

where $\mathscr{B}$ and $\mathscr{C}$ are related to the partial derivatives of the ligand and signal production with respect to its variables evaluated at stationary states s_0 and l_0

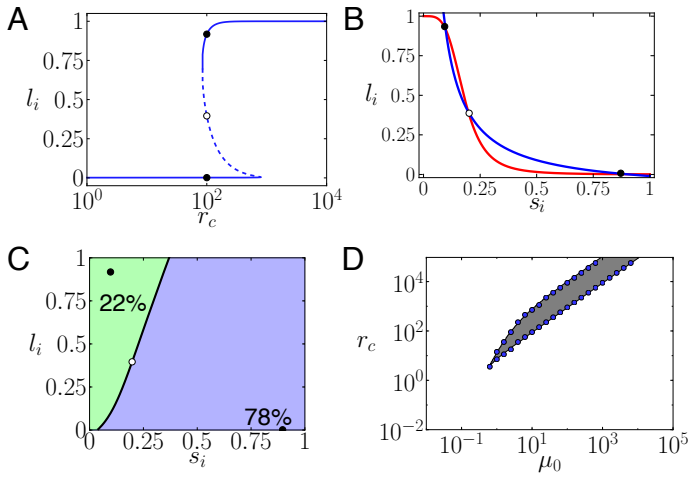

Figure 5.5: Cis-inhibition with a basal Notch signal source creates a bistable cell-autonomous switch. For strong enough cis-interactions and weak or null cis-signaling, cells will be able to end up in two different cell populations. Theoretical and simulation results for a population of isolated cells with a basal Notch production. (A) Bifurcation diagram of Delta ligand for $\mu_0 = 10$. Black dots refer to the attained solutions in simulations performed on an ensemble of 4×10^4 cells, the empty dot is the unstable solution. (B) Nullclines showing the three possible solutions found in (A) at $r_c = 100$. Blue and red lines represents the curves set by Eqs. 5.9a and 5.9b respectively. (C) Basins of attraction for $r_c = 100$. The continuous black line is a separatrice, which divides the parameter space into two basins of attraction of the two stable solutions. The separatrice was determined by doing simulations with negative time steps from the unstable solution. Simulations in a population of 4×10^4 cells in an heterogeneous initial state provide the ratios of cell types adopting the two possible stable solutions. These ratios can also be computed from the relative areas of the two basins. In a more general case, the ratio of the two cell populations will be determined by the initial precursor state of the cells and the basins of attractions of the final states. (D) Phase diagram showing the cell-autonomous switch region zone where two states are linearly stable. The gray area is the theoretically computed region, and the blue circles correspond to simulation results. LSA analysis was used for stability evaluations in all panels. Parameter values: $h = 4$, $\epsilon = 0$ and $\nu = 1$ for all panels.

of Eq. 5.9:

$$\mathscr{B} = \frac{1}{v}\frac{\partial \dot{l}_i}{\partial s_i}\bigg|_{s_0,l_0} = -\frac{h s_0^{h-1} b}{(1+b s_0^h)^2}\ , \quad \mathscr{C} = \frac{\partial \dot{s}_i}{\partial l_i}\bigg|_{s_0,l_0} = \frac{r_c(\epsilon+\mu_0(\epsilon-1))}{(1+\mu_0+r_c l_0)^2} \quad . \tag{5.10}$$

Using the methodology found in Sec. 2.4 we find that a solution is linearly stable to small perturbations if the following criterion is fulfilled:

$$1 < \mathscr{B}\mathscr{C}\ . \tag{5.11}$$

Our nullcline analysis shows that the cis-inhibition-driven intracellular and transcriptional positive feedback loop dynamics can generate bistability (Fig. 5.5). Low values of cis-interactions strength (r_c) drive a cell state with no Delta ligand, while high cis-interactions strengths r_c drive a state with very strong Delta expression. At intermediate equilibrium constant values, both states are possible and bistability occurs. Accordingly, non-interacting cells endowed with a basal ligand-independent Notch signal and cis-inhibition can end up in two very different cellular states (Fig. 5.5 (C)). By solving Eq. 5.9 in the r_c–r_t parameter space, applying LSA and corroborating it with numerical simulations we find that bistability requires a minimal amount of cis-interactions and ligand-independent Notch signal (Fig. 5.5 (A,D)).

A necessary condition to have more than one fixed point is that the two nullclines are both increasing or decreasing functions, what can be formulated as $\mathscr{R}_{l_i,s_i}/\mathscr{R}_{s_i,l_i} > 0$. Given that we always have $\mathscr{R}_{l_i,s_i} < 0$ for the Eq. 5.2b, we need $\mathscr{R}_{l_i,s_i} < 0$ (*i.e.* cis-inhibition). Eq. 5.7 tells us that this can not be fulfilled if $\mu_0 = 0$ when $\epsilon > 0$, what provides an analytic prove that we need this alternative source of signal production μ_0 for bistability. Moreover, cooperativity and null or low cis-signaling enhances the possibility to have the switch. Indeed, without cooperativities we could not find any bistable solution [5].

In the cis-activation regime we have $\mathscr{R}_{s_i,l_i} > 0$, what will always lead to a monostable solution. Hence, cis-activation generates a negative intracellular feedback loop, which will reinforce monostability in a cell-autonomous way.

[5] In a more realistic model where Notch is not conserved, we will show that bistability can be also reached without the need of cooperativity (Sec. 5.3.7).

Therefore, cis-interactions might be responsible of novel cell-autonomous functions in the Notch signaling pathway without the need of cell-to-cell interactions; either a cell-autonomous bistable switch when cis-inhibition takes place, or a cell-autonomous homeostat when cis-activation occurs.

5.3.3 Cis-activation inhibits fine grained pattern formation, while optimal values of cis-inhibition promotes it

In this section we study how cis-activation and cis-inhibition affect lateral-inhibition patterning in the multicellular scenario. Specifically, we study whether cis-interactions enlarge or reduce the parameter region where spontaneous pattern formation occurs. Also, we will study the region in the parameter space where the pattern solution exist, what we call the nonlinear pattern region. This region includes the spontaneous pattern region and the bistable region we presented in Sec. 2.10 in which both homogeneous and pattern states are linearly stable.

We may expect that cis-inhibition will promote patterning as it enhances cell bistability by driving an additional positive feedback loop within cells. In contrast, we may propose that cis-activation will inhibit pattern formation since it drives a negative feedback loop within cells which tends to reduce the bistability created from intercellular trans-interactions (see Fig. 5.4 (C,D)). To check it, we compute both theoretically and computationally the parameter region enclosing spontaneous and nonlinear pattern formation to our model in the multicellular case, including trans and cis-interactions.

For the evaluation of spontaneous patterning we perform the usual LSA to the model equations 5.2-5.4 (see Secs. 2.4 and 2.10). The $\mathscr{M}$ matrix (Eq. 2.27) reads

$$\begin{pmatrix} -1 & (\mathscr{C} + \mathscr{A}\Omega) \\ v\mathscr{B} & -v \end{pmatrix} \quad ,$$

where $\mathscr{A}$, $\mathscr{B}$ and $\mathscr{C}$ are related to the partial derivatives of the ligand and signal

production with respect to its variables evaluated at the homogeneous fixed point,

$$\mathscr{A} = \omega \frac{\partial \dot{s}_i}{\partial l_{i'}}\bigg|_{s_0,l_0}, \quad \mathscr{B} = \frac{1}{v}\frac{\partial \dot{l}_i}{\partial s_i}\bigg|_{s_0,l_0}, \mathscr{C} = \frac{\partial \dot{s}_i}{\partial l_i}\bigg|_{s_0,l_0} \tag{5.12}$$

where now (s_0, l_0) refers to the steady homogeneous solution for the studied system, and the subindex i' refers to the cells that are first neighbors to cell i. Such expressions read

$$\mathscr{B} = -\frac{h s_0^{h-1} b}{(1+b s_0^h)^2}, \quad \mathscr{C} = \frac{r_c(\epsilon + r_t l_0(\epsilon - 1))}{(1 + l_0(r_t + r_c))^2}, \quad \mathscr{A} = \frac{r_t(1 + r_c l_0(1-\epsilon))}{(1 + l_0(r_t + r_c))^2} \tag{5.13}$$

Hence, the dispersion relation of the system reads

$$\alpha(\Omega)^{\pm} = \frac{1}{2}\left\{-(1+v) \pm \left((1+v)^2 - 4v(1 - \mathscr{B}(\mathscr{C} + \mathscr{A}\Omega))\right)^{1/2}\right\}. \tag{5.14}$$

The homogeneous steady state will be linearly unstabilized when Eq. 5.14 is positive, *i.e.* if the following relation is fulfilled:

$$1 < \mathscr{B}(\mathscr{C} + \mathscr{A}\Omega) \quad . \tag{5.15}$$

Given that $\mathscr{B} < 0$ in all the parameter space and $\mathscr{A} > 0$ for $\epsilon \leq 1$, which is the case we are studying, the fastest growing modes are those ones giving rise to the typical lateral inhibition pattern, *i.e.* $\Omega = -0.5$ (see Sec. 2.10). Hence, LSA indicates that cis-interactions do not change the characteristic wavelength of the emerging pattern, at least in the regions of the parameter space where the model behaves linearly. The critical line enclosing the spontaneous pattern formation region will be determined by $1 = \mathscr{B}(\mathscr{C} - 0.5\mathscr{A})$.

Note that cis-inhibition occurs when $\mathscr{C} < 0$, while cis-activation happens when $\mathscr{C} > 0$. Then, condition set by Eq. 5.15 tells us cis-inhibition facilitates spontaneous patterning while cis-activation prevents it.

To evaluate nonlinear patterning, we apply the method presented in Secs. 2.5 and 2.10 to our system of equations for obtaining the exact solutions of the typical three-period pattern in a perfect hexagonal lattice. We write Eqs. 5.2a-5.2b for the two cell types A and B in the steady state, *i.e.*

$$l_A = g(s_A), \quad s_A = f(r_t\langle l_A\rangle, l_A) \tag{5.16a}$$

$$l_B = g(s_B), \quad s_B = f\left(r_t\langle l_B\rangle, l_B\right) \tag{5.16b}$$

with

$$\langle l_A \rangle = c_A l_A + (1 - c_A) l_B \tag{5.17a}$$

$$\langle l_B \rangle = c_B l_B + (1 - c_B) l_A \quad , \tag{5.17b}$$

where for the typical lateral inhibition pattern $c_A = 0$ and $c_B = 1/2$.

We evaluated the simplest case of cis-activation, *i.e.* when cis-interactions elicit the same amount of signal as trans-interactions do ($\epsilon = 1$). In the absence of cis-interactions ($r_c = 0$), the pattern spontaneously emerges and exists in a wide range of values of the trans-interactions strength r_t (Fig. 5.6). As cis-interactions increase ($r_c > 0$), the range of r_t values enabling pattern formation becomes strongly reduced. Indeed, by slightly increasing the cis-interactions strength r_c, we fall into a region where no pattern can emerge, specially from small variability between cells (Fig. 5.6). These results show that cis-activation inhibits the emergence of patterning.

We have checked the limits of the spontaneous pattern formation region through simulations on a system of 30 hexagonal cells with a time step $\mathrm{d}t = 0.1$. We have set homogeneous initial conditions with small noise (see Sec. 2.9.1 for details). A systematic exploration in the parameter space has shown a perfect agreement with the critical line determined by LSA (data not shown).

Following the same procedures, we evaluated whether pattern formation is promoted by cis-inhibition. To this end, we analyzed the simplest case of cis-inhibition, which corresponds to the absence of cis-signaling ($\epsilon = 0$, see Fig.5.7). Sprinzak *et al.* (2010) [47, 130] showed that cis-inhibition can enable pattern formation on a case where trans-interactions are unable to create a pattern *per se* which corresponds to no cooperativity in Notch-mediated inhibition ($h = 1$) [10, 47, 130]. Our study confirms it and shows that both spontaneous pattern formation from small variability between cells and nonlinear pattern formation require a minimal cis-interactions strength (see Fig.5.7 (A)). Moreover, note that nonlinear pattern formation regions are enhanced due to cis at low and higher cooperativities (see Fig. 5.7 (B,C)). Our results also show that cis-inhibition promotes spontaneous and nonlinear patterning at higher cooperativities ($h > 1$) [105] at weak inhibition of Delta (low b values) as well (Fig. 5.7 (D)). In this case, a minimal amount of cis-inhibition is also required for spontaneous and/or non-linear pattern formation (Fig. 5.7 (A,B,D)). Overall, our results show that the

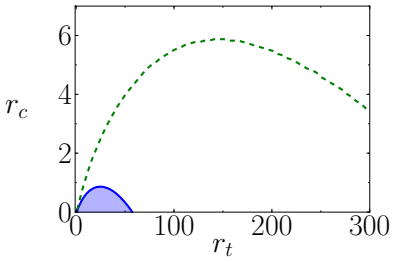

Figure 5.6: Cis-activation in lateral inhibition patterning. Phase diagram for high cis-signaling rates ($\epsilon = 1$), leading to the cis-activation scenario. By increasing the cis-interactions strength r_c we destroy the pattern. Blue region enclosed by the blue continuous line represents where the pattern grows spontaneously. Green dashed line encloses the nonlinear pattern formation regions. The blue line has been checked with computer simulations (data not shown, see text for details).

positive intracellular feedback loop due to cis-inhibition promotes the homogeneous state unstabilization, providing to the multicellular system more capacity to amplify perturbations, and thus, facilitating patterning. A systematic exploration through numerical simulations in the parameter space for panels (A,C) in Fig. 5.7 has shown a perfect agreement with the critical lines determined by LSA (data not shown, simulation details as explained above for the $\epsilon = 1$ case).

Now we evaluate a more complex scenario in which either cis-activation or cis-inhibition can be taking place, depending on the trans-interactions strengths. Specifically, we consider the case in which cis-interactions drive a weak Notch signal, such that $\epsilon = 0.4$. At low trans-interactions (low r_t values), cis-activation is taking place (Fig. 5.8), while at high trans-interactions (high r_t values) cis-inhibition is participating. Our results show than in the cis-activation regime, pattern formation is inhibited, since an increase in cis-interactions impedes spontaneous pattern formation (Fig. 5.8). In contrast, in the cis-inhibition regime, pattern formation is facilitated since a minimal amount of cis-interactions strength is required for spontaneous patterning (Fig. 5.8). Numerical simulations across the parameter space agree with the critical line shown in Fig. 5.8 (data not shown, simulation details as explained above for the $\epsilon = 1$ case). These results confirm the existence of distinct regimes (cis-activation/cis-inhibition) as well as

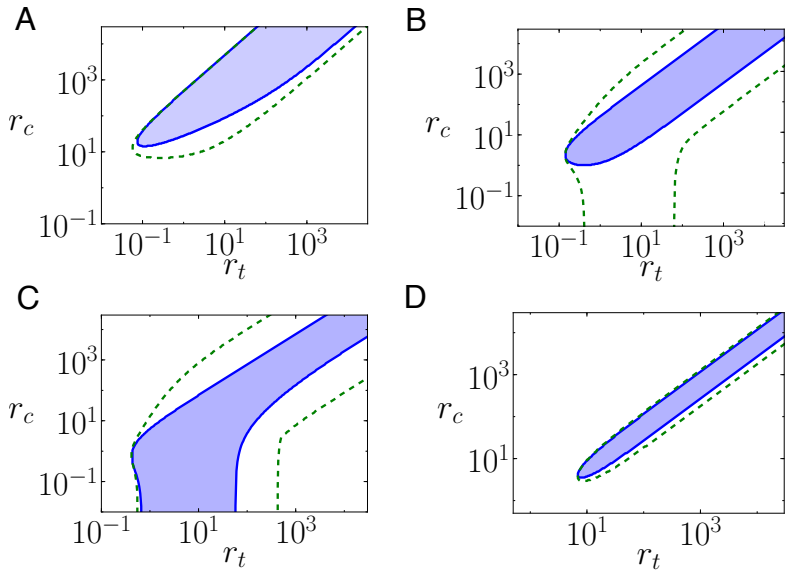

Figure 5.7: Cis-inhibition promotes lateral inhibition patterning. Phase diagram for null signaling rates ($\epsilon = 0$) at (A) null ($h = 1$), (B) low ($h = 2$) and (C,D) higher ($h = 4$) cooperativities h of ligand inhibition. We obtain patterning in the cis-inhibition scenario at optimal cis-interactions *versus* trans-interactions rations. (A) When there is no cooperativity ($h = 1$) we need a minimal amount of cis-interactions to be in the patterned region, whatever it is the Notch signal inhibition power (*i.e.* parameter b, data not shown) being consistent with Sprinzak *et al.* (2010) [47]. (B) At low ($h = 2$) cooperativities, cis-interactions promote patterning, and specially spontaneous patterning. (C,D) At higher cooperativities ($h = 4$) nonlinear patterning is facilitated due to cis-interactions, and spontaneous patterning is facilitated at weaker ligand inhibition (D). Other parameter values: $b = 1000$ for (A-C) and $b = 10$ for (D). In all panels the shape of the pattern formation region when cis-interactions become relevant $r_c \gtrsim 1$ indicate that the ratio r_c/r_t becomes relevant for patterning. The blue lines in panels (A,C) have been checked with computer simulations (data not shown, see text for details). Color codes as in Fig. 5.6.

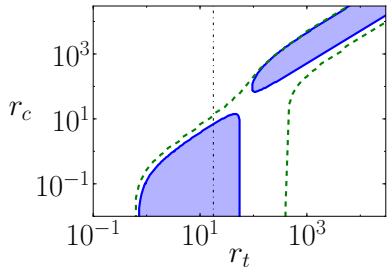

Figure 5.8: Lateral inhibition patterning at intermediate cis-signaling rates. Phase diagram for intermediate relative cis to trans signaling rates ($\epsilon = 0.4$). The black dotted-dashed line divides the parameter space into the cis-activation region, on its left, and the cis-inhibition region, on its right (Fig. 5.9). Color codes as in Fig. 5.6. The blue lines have been checked with computer simulations (data not shown, see text for details). Other parameter values as in Fig. 5.6.

the different roles each of them has on lateral inhibition pattern emergence.

Our study also reveals that optimal values of cis-interactions strengths are required for pattern emergence. If cis-interactions strengths are high, pattern formation can only occur for high enough trans-interactions too (Fig. 5.7). Actually, in these phase diagrams for cis-inhibition we observe that for relevant cis-interactions strengths ($r_c \gtrsim 1$) the ratio r_c/r_t becomes relevant. When cis-interactions strengths are too high compared to trans-interactions ($r_c >> r_t$ or r_c increases), the pattern can not arise and the homogeneous solution becomes stable. In this regime, the coupling between cells becomes less relevant, impeding the spatial organization that creates an ordered pattern. In addition, since in this scenario the signal is very weak, the homogeneous state is high in Delta ligand levels (Fig. 5.10 (A)).

5.3.4 Cis-inhibition promotes the high Delta fate by reducing the lateral inhibition effect

In the precedent section we saw that cis-inhibition promotes fine-grained patterning, but actually how does the emerging patterns look like in this scenario?

Computer simulations reveal that the emerging patterns contain a large num-

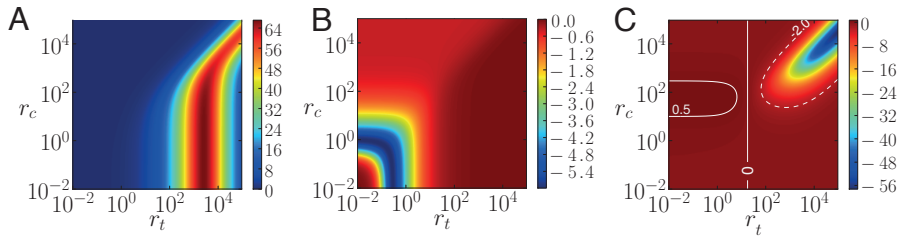

Figure 5.9: Trans-interactions strengths are crucial for determining the cis-role at intermediate cis-signaling rates. LSA terms showing (A) the trans-interactions contribution $\mathscr{A}$, (B) the ligand inhibition contribution $\mathscr{B}$ and (C) the cis-interactions contribution $\mathscr{C}$. At low trans-interactions strengths there is cis-activation ($\mathscr{C} > 0$). At higher trans-interactions strengths there is cis-inhibition ($\mathscr{C} < 0$). Parameter values as in Fig. 5.8.

ber of high Delta cells in a large region of the parameter space when cis-interactions are considered (see Figs. 5.10 and 5.11). A prove of that is that if cis-interactions are present, the inverted lateral inhibition pattern, in which 2/3 of the cells have high ligand, spontaneously emerges in the tissue (Fig. 5.11).

Plahte (2001) showed through a lateral inhibition model in which the regulatory functions were step-like functions, that that this exchange of cell type numbers (between the normal inhibition pattern and its inverted version) is a straightforward consequence of the rising of the threshold of Delta needed to trans-activate the Notch signal [102]. For this reason, we focused on how a similar threshold was affected in the context of cis-interactions. From our modeling equations (Eqs. 5.2-5.4) it can be shown that cis-inhibition effectively increases the threshold of the Delta quantity a cell should feel from neighboring cells in order to be inhibited from being a high Delta cell. In particular, we can compute the level of averaged ligand concentration due to trans-interactions $\langle l_i \rangle$ that will enable half-inhibition of the ligand production, what we termed l^* in Sec. 3.5.1). By using the same method as in Sec. 3.5.1 we find that such critical ligand concentration value reads

$$l^* = \frac{1 + l_i(r_c - b^{\frac{1}{h}}\epsilon r_c)}{(b^{\frac{1}{h}} - 1)r_t} \quad . \tag{5.18}$$

By representing Eq. 5.18, we can confirm that cis-interactions are worse receivers for being inhibited (Fig. 5.12). This effect is due to the sequestering

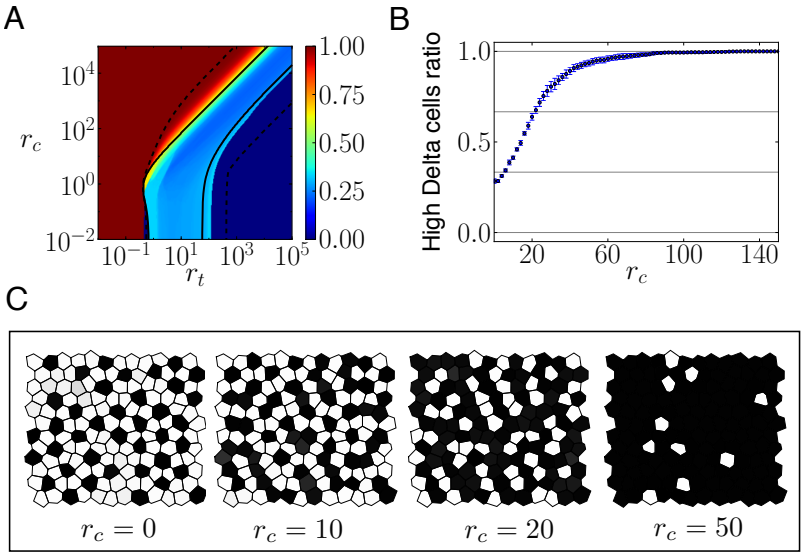

Figure 5.10: Cis-inhibition promotes high Delta fated cells from a very heterogeneous precursor state (noisy initial conditions). (A) Density plot representing the ratio of high Delta cells in a tissue from simulations performed over a lattice of 30×30 perfect hexagonal cells. Random initial conditions in Notch signal and Delta has been used, generated from a uniform distribution from 0 to 1. Solid lines are enclosing the region where the pattern emerges spontaneously, the thick dashed lines enclose the nonlinear pattern formation region. (B) Ratio of high Delta cells when the cis-interactions strengths are changed. Simulations performed on an irregular array of cells. Each point comes from the average of 10 simulations starting at different initial conditions. (C) Snapshots corresponding to simulations in (B). Darker colors represent high Delta levels. By increasing the cis-interactions we disrupt the lateral inhibition pattern and it appears a more high Delta fated phenotype. In (A) and (B) cells are considered high Delta fated cells when its Delta level is over the threshold of 0.5. Simulations have been performed on arrays with irregularity parameter $\gamma = 1.33$. Parameter values: $r_t = 3$ for panels (B) and (C), $\epsilon = 0$, $h = 4$, $b = 1000$ and $v = 1$ for all panels.

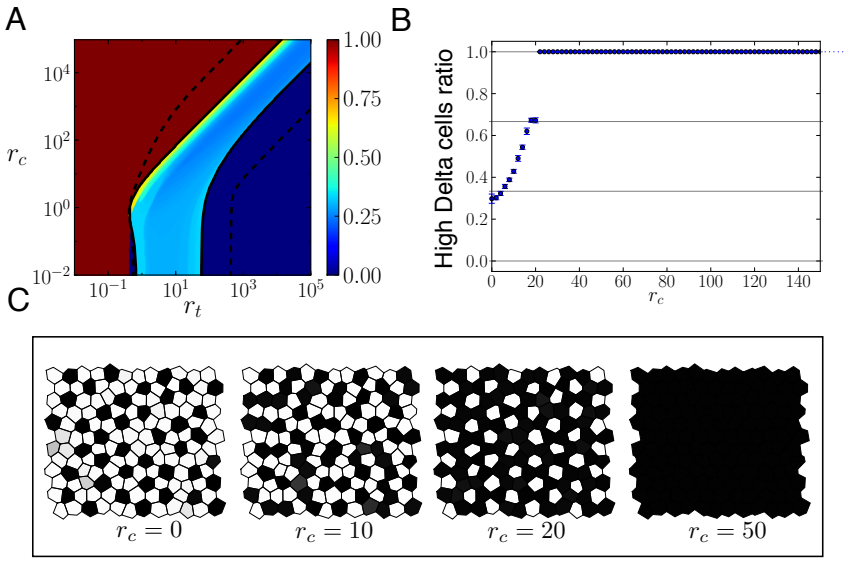

Figure 5.11: Cis-inhibition also promotes high Delta fated cells from a more homogeneous precursor state (low noisy initial conditions). (A) Density plot representing the ratio of high Delta cells in a tissue from simulations performed over a lattice of 30×30 perfect hexagonal cells. Small random variations around the homogeneous fixed point for Notch signal and Delta has been used as initial conditions (See Sec. 2.9.1). (B) Ratio of high Delta cells when the cis-interactions strengths are changed. Simulations performed on an irregular array of cells. Each point comes from the average of 10 simulations starting at different initial conditions. (C) Snapshots corresponding to simulations in (B). By increasing the cis-interactions we disrupt the lateral inhibition pattern and it appears a more high Delta fated phenotype. Note that by increasing cis-interactions we obtain an inverted lateral inhibition pattern. Parameter values as in Fig. 5.10.

of receptors from the cell membrane when they cis-interact with ligands within the cell, which effectively lowers the signal within the cell for the same level of ligand in the neighboring cell (Fig. 5.12). In our simulated precursor state, all cells are initially expressing a certain quantity of Delta, so they are all worse receivers of inhibitory signal than if they would have just trans-interactions. As a consequence of that, new kind of patterns show up, where high Delta cells are not that likely to appear isolated, and adjacent high Delta cells may appear together, what is consistent with the theoretical results found by Sprinzak *et al.* (2010) [47]. On the other side, the appearance of low-Delta cells will require to be surrounded by more high Delta cells to keep its inhibited state.

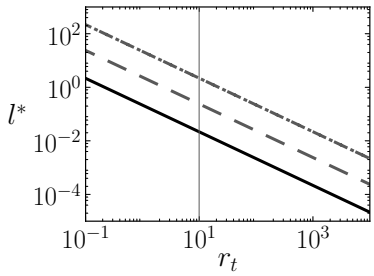

Figure 5.12: Cis-interactions in the cis-inhibition scenario make cells worse receivers, and therefore enhance the amount of trans-interactions a cell needs in order to inhibit ligand production. Threshold of ligand l^* in a cell required to half-inhibit ligand expression in its neighboring cell (Eq. 5.18). Results for different amounts of cis-interactions: null amount of cis-interactions ($r_c l_i = 0$, black solid line), moderate amount ($r_c l_i = 10$, gray dashed line) and a higher amount ($r_c l_i = 100$ dotted-dashed gray line). Vertical line is a guide to the eye for a certain trans-interactions strength r_t to better appreciate the rise of l^* due to cis-interactions. Other parameter values: $\epsilon = 0$, $b = 1000$ and $h = 4$.

5.3.5 Cis-inhibition allows localized patterning highly sensible to the precursor state

Fig. 5.10 confirms that in the cis-inhibition scenario there is a large region in which the homogeneous state is nonlinearly unstable, where patterning can emerge and the number of high-Delta cells can be gradually increased when r_c is

increased. Also, in Sec. 5.3.3 it was shown shown that cis-inhibition enables the positive feedback loop in the multicellular system and we have studied it independently as a cell-autonomous switch as well. Now we go step further and try to understand how the intra and the intercellular positive feedbacks are integrated. Herein we will see that cells in a tissue in the cis-inhibition scenario are not totally governed by the intracellular positive feedback, nor by the intercellular feedback, but by a mixed mode of both.

We start exploring the bistability region — where the homogeneous can be nonlinearly unstabilized — where cis-interactions are more important $r_c/r_t > 1$. In this region, we observe that the emerging patterns are very sensible to the precursor state (see Figs. 5.13, and data not shown) . Thus, a noisy initial condition ends up in a very disordered pattern, while a prepattern can be very influential for the final result (Figs. 5.13) [6]. We perform simulations in other regions of the parameter space with noisy initial conditions to study whether the noise from the initial conditions persists and is still present at the final simulation time. For the sake of simplicity these simulations are performed on hexagonal arrays, and then we can make use of the structure function (Fig. 5.14). We find that in the final simulation time, the noise is more evident in the bistability region at high cis-interaction strengths (Fig. 5.14 (A)). In such case, the simulation result contains a very noisy outcome, but the structure function presents a certain degree of correlation due to the cell-to-cell interaction. The noise in the final state is less evident in spontaneous patterning regions (Fig. 5.14 (B)) and it totally disappears in bistable regions at low cis-interactions strengths (Fig. 5.14 (C)).

Which is the effect of the bistable switch in a tissue of cells undergoing trans-interactions? For this purpose, we studied where the intracellular positive feedback enables bistability in the phase diagram of the multicellular system when it is in the homogeneous steady state. We have found that such region falls inside the pattern formation region (see Fig. 5.15 (A)) of the multicellular system.

Strikingly, simulation results indicate that in such region where the intracellular positive feedback can drive cell-autonomous bistability, patterns can keep localized without spreading to the rest of the tissue (see Figs. 5.15 (A,B)). Pattern localization effects should be the cause of sensibility to initial conditions.

[6] Prepatterns with low density of high-Delta cells will not tend to persist on such region of the parameter space.

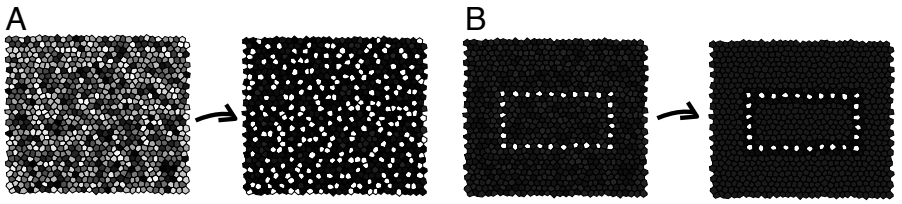

Figure 5.13: Cis-inhibition makes the system sensible to initial conditions at the bistable zone with higher cis-interactions $r_c/r_t > 1$. Snapshots from simulation results showing Delta levels of initial (left column) and final (right column) conditions. (A) Simulations with noisy initial conditions. (B) Simulations around the homogeneous state with small noise, and a rectangular prepattern in the Delta levels. The final result strongly depends on the initial conditions. Parameter values are $r_t = 3$ and $r_c = 25$. The rest of the parameters are as in Fig. 5.10.

5.3.6 Cis-inhibition promotes pattern multistability, allowing other periodic patterns to emerge

When cis-inhibition is acting, the growth rate for the fastest growing mode is larger according to Eq. 5.14, what has already been found by Sprinzak *et al.* [130]. Consequently, cis-inhibition confers nonlinearity to the system [130]. Because of that, other periodic patterns can be expected to be formed (Fig. 5.16). Indeed, at high r_c/r_t values, the system of Eqs. 5.16-5.17 with $c_A = 0$ and $c_B = 1/2$ leads to additional fixed points which corresponds a periodic pattern like the lateral inhibition pattern but with exchanged numbers of cells with high Delta levels and low Delta levels (2/3 and 1/3 *versus* 1/3 and 2/3 in the common lateral inhibition pattern). Hereafter we name this pattern the inverted lateral inhibition pattern or pattern I (Fig. 5.16 (A)), in contraposition to the normal lateral inhibition pattern P. Numerical simulations confirm this pattern spontaneously arises in the system (Fig. 5.11 (C)).

Herein we study whether other periodic patterns can appear in this system. Specifically, we focus on two new patterns, corresponding to the second fastest growing mode in a lattice of 6×6 cells, those corresponding to $\Omega = -1/3$ (see Figs. 2.8 (A) and 5.16. Specifically, we focus on a spotted pattern in which 1/4 of the cells presented high Delta expression (Fig. 5.16 (B) top), what we will refer as P2, and on its inverted version, I2. Also, we focus on a pattern of stripes

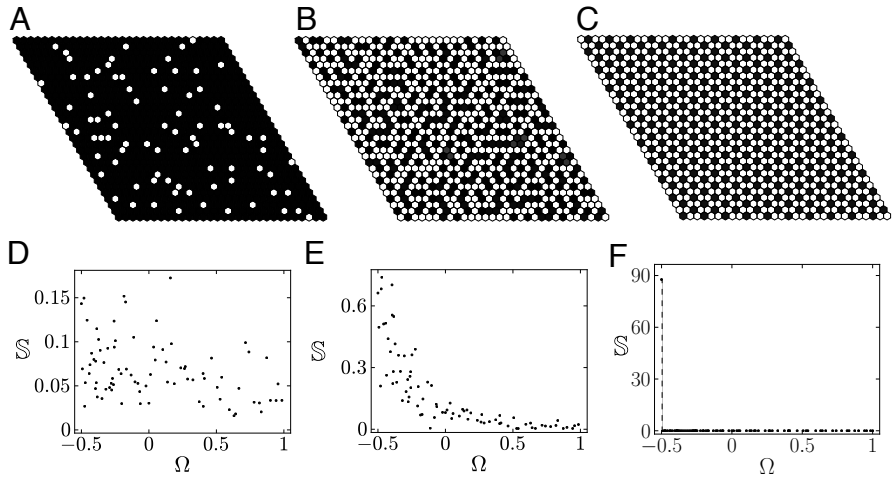

Figure 5.14: Simulation results with noisy initial conditions indicates that disorder persist in the bistable zone at higher cis-interactions with respect to trans-interactions. Final simulation results showing (A-C) three patterns of Delta levels with (D-F) its structure functions for the Delta patterns. (A,C) Emergent patterns in the bistability region for (A) high and (C) low cis-interactions strengths, and (B) in the spontaneous region. Structure functions are computed as explained in Sec. 2.8.2, but we set $x_b = 0$ and we omit the homogeneous mode contribution. In (D) we draw a vertical line for a better visualization of the amplitude for $\Omega = -0.5$, which is in perfect agreement with the theoretical value predicted for a regular lateral inhibition pattern (see App. B). Parameter values: in (A,D), $r_t = 50$ and $r_c = 1000$ is used; in (B,E), $r_t = 50$ and $r_c = 200$ is used; in (C,F), $r_t = 100$ and $r_c = 0.1$. Other parameter values as in Fig. 5.10.

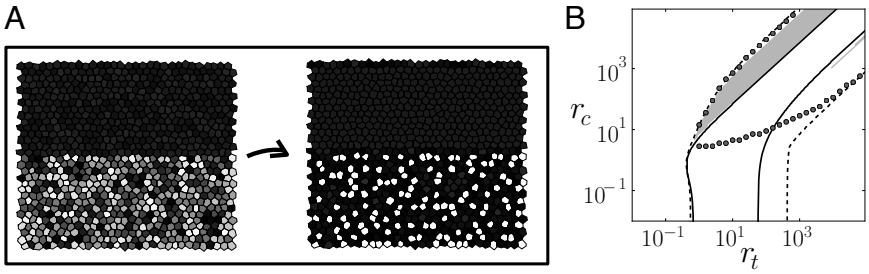

Figure 5.15: Cis-inhibition allows pattern localization. (A) Simulation results in an irregular array of cells showing a localized and quite disordered pattern of two cell types. On the left there is the initial configuration, and on the right there is the final configuration. Half of the cellular array is prepared with a more heterogeneous initial condition, which will give rise to the localized pattern. The other half is prepared with smaller variability around the homogeneous state. (B) Phase diagram for high cooperativity ($h = 4$) showing through simulation results the region where localized patterns are found. Simulation results were done for the same type of initial conditions as in (A) but in a regular array of cells. The upper region enclosed by the gray dots is the bistable region for the switch, where two states are linearly stable (see Fig. 5.5). The black solid and dashed lines denote the same as in Fig. 5.7. The grey colored region denotes where pattern localization occurs. Other parameter values: $b = 1000$, $\epsilon = 0$ and $v = 1$ for all panels and $r_t = 3$ and $r_c = 25$ for (A).

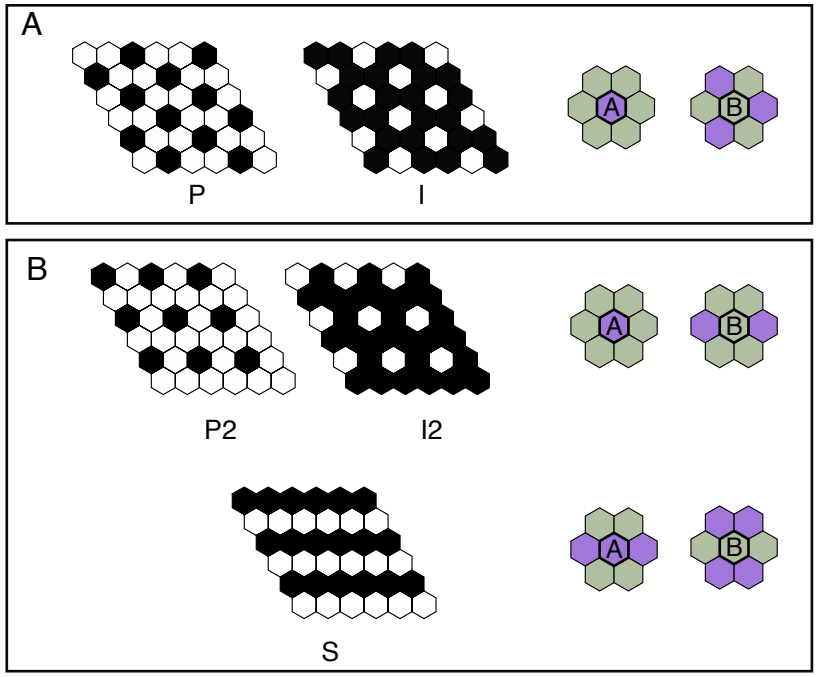

Figure 5.16: Exact solutions for periodic patterns. (A) Patterns with the periodicity of the fastest growing mode ($\Omega = -1/2$). (B) Patterns with the periodicity of the secondary fastest growing mode ($\Omega = -1/3$) in a perfect hexagonal lattice. (A) The normal lateral inhibition pattern (P) with 1/3 of high Delta cells and its inverted pattern (I). (B) A variant of the lateral inhibition pattern (P2) with 1/4 of high Delta cells, its inverted pattern (I2) and a stripped pattern (S). On the right of each row of patterns, two groups of 7 cells illustrate the neighborhood for cell type A (violet) and cell type B (green) with respect to the central cell type. Note that P and I share the same symmetry (*i.e.* they have the same c_A and c_B values), and also P2 and I2. This sets the values of c_A and c_B for finding the exact solution of these patterns according to the method described in Sec. 2.5 (Eqs. 2.34). Patterns P and P2 are present in the absence of cis-interactions, while I, I2 and S appear when cis-interactions are present.

(Fig. 5.16 (B) bottom) or pattern S. We find the exact solutions for the spotted pattern by solving Eqs. 5.16-5.17 with $c_A = 0$ and $c_B = 2/3$, while for the stripes we use $c_A = c_B = 1/3$ (Fig. 5.16).

We find the exact solutions numerically with Mathematica and custom made programs following the procedure described in Sec. 2.6. For determining the stability of the patterns we perform simulations on a perfect hexagonal array of 3×3 cells for the P and I patterns, and on arrays of 6×6 cells for P2, I2 and S patterns. Patterned solutions are used as initial conditions with a small noise (Sec. 2.9.1). Ten simulations are performed for each chosen parameter value with different initial conditions. We define a distance of the patterned solution with respect to the final result, η^c:

$$\Delta\eta \equiv \left|\eta_l^{th} + \eta_s^{th} - (\eta_l + \eta_s)\right| < \Delta\eta^c \quad , \tag{5.19}$$

being η_s^{th} and η_l^{th} the theoretical order parameters of the ligand and the signal for the periodic patterned solution respectively, and η_l and η_s the computed order parameters of the simulation. By using Eq. 2.37 one can see that $\eta_x^{th} = \frac{2}{3}|x_A - x_B|$ for patterns P,I and S, and $\eta_x^{th} = \frac{1}{2}|x_A - x_B|$ for P2 and I2 with x_A and x_B being the corresponding patterned state solutions (see Sec. 2.8.1). A solution is considered to be closed to the patterned solution if for all ten simulations it is fulfilled $\Delta\eta < \Delta\eta^c$, being $\eta^c = 10^{-5}$. We perform simulations for different parameter values defined on a logarithmic mesh across the r_c–r_t parameter space. All simulations are performed with a time step of $\mathrm{d}t = 0.1$ and are stopped when the steady state is achieved ($\Delta t = 5$ and $\Delta\eta^* = 10^{-7}$ for the criterion presented in Sec. 2.9.1).

Additionally, we determine the stability of pattern solutions P, I and S through LSA over the pattern solutions (see the method in Sec. 2.7 and its application to Collier model in Sec. 2.10). This analysis and the associated results can be found in App. C. Our stability analysis is in perfect agreement with simulations for P and I patterns, and provides a very reasonable approximation for the stability region of the S pattern.

The parameter region in the r_t and r_c space where these stable patterns arise and the bifurcation diagrams are shown in Figs. 5.17-5.19. At intermediate ($h = 2$, not shown) and high cooperativities ($h = 4$) (see Figs. 5.17-5.19) patterns P and P2 were already present in the trans-limit ($r_c = 0$) while patterns I, I2

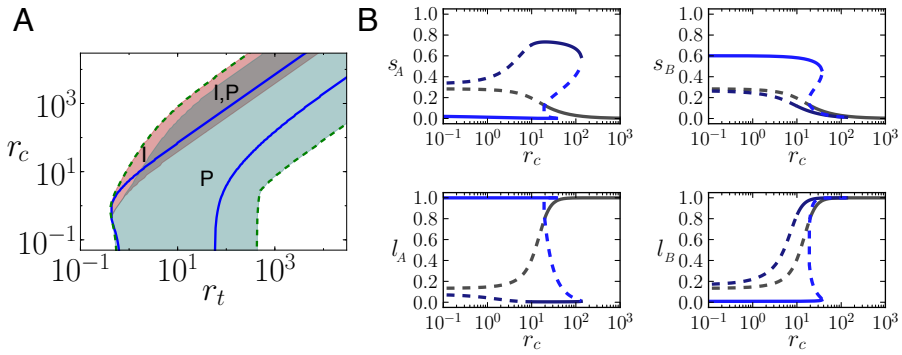

Figure 5.17: Phase and bifurcation diagrams for patterns with the lateral inhibition periodicity ($\Omega = -1/2$; P, I). (A) Phase diagram as in Fig. 5.7 (C) showing the region in which the normal lateral inhibition pattern (P) and the inverted pattern (I) are stable to small perturbations. (B) Bifurcation diagrams for $r_t = 3$. Blue lines correspond to the patterned states, gray branch correspond to the homogeneous state. Solid lines correspond to linearly stable states, dashed lines correspond to linearly unstable states. At low cis-interactions, the stable branches correspond to P and at higher cis-interactions to I. Note that there is a coexistence region in which both patterns are stable. Stability in (A) and (B) corresponds to simulation results performed on 3×3 hexagonal lattices. Parameter values: $h = 4$, $\epsilon = 0$, $v = 1$, $b = 1000$.

and S appeared just when cis-interactions were present ($r_c > 0$). In the non-cooperative case, just the normal P pattern was present (data not shown). These phase diagrams show that more than one stable pattern can be found at the same region of the space. These patterns are also stable on more irregular lattices (see Fig. 5.20)

5.3.7 A more realistic model leads to the same conclusions

In this section we will use a more realistic model in which we take into account the proteolytic cleavage of the ligand-receptor forming complex that gives rise to the Notch signal, to verify that our main conclusions are not dependent on this approximation. Herein the Notch receptor is not conserved, so we call this

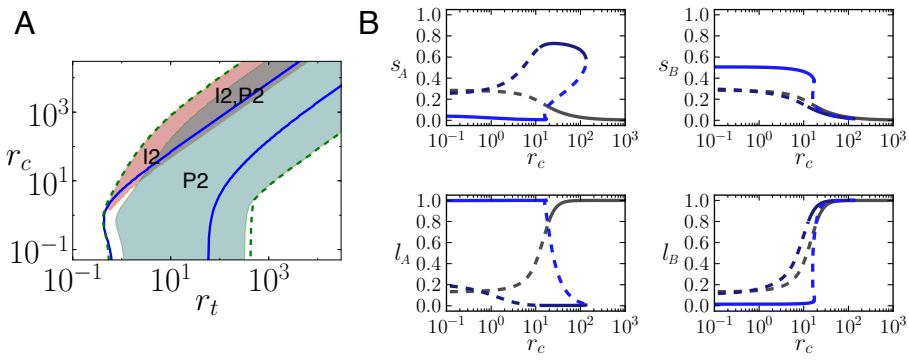

Figure 5.18: Phase and bifurcation diagrams for spotted patterns with the periodicity $\Omega = -1/3$ (P2, I2). (A) Phase diagram as in Fig. 5.7 (C) showing the region in which the lateral inhibition pattern of 1/4 high Delta cells (P2) and its inverted pattern (I2) are stable to small perturbations. (B) Bifurcation diagrams for $r_t = 3$. At low cis-interactions, the stable branches correspond to P2 and at higher cis-interactions to I2. Note that there is a coexistence region in which both patterns are stable. Stability in (A) and (B) corresponds to simulation results performed on 6×6 hexagonal lattices. Parameter values and other figure details as in Fig. 5.17.

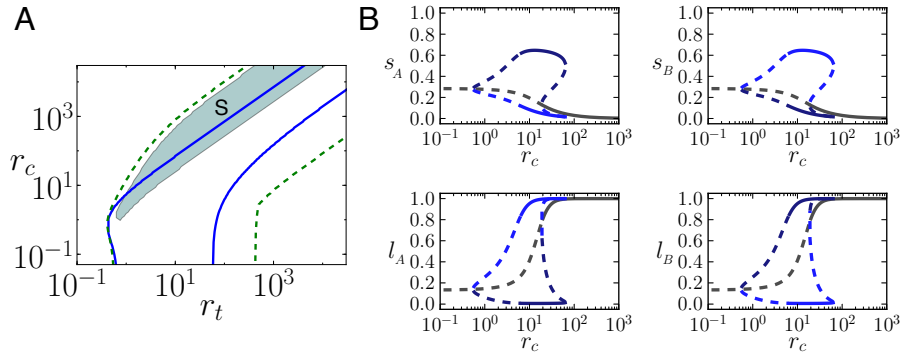

Figure 5.19: Phase and bifurcation diagrams for pattern of stripes (S) corresponding to the secondary growing mode ($\Omega = -1/3$). (A) Phase diagram as in Fig. 5.7 (C) showing the region in which the stripes are stable to small perturbations. (B) Bifurcation diagrams for $r_t = 3$. At low cis-interactions, the stable branches correspond to P2 and at higher cis-interactions to I2. Stability in (A) and (B) corresponds to simulation results performed on 6×6 hexagonal lattices. Parameter values and other figure details as in Fig. 5.17.

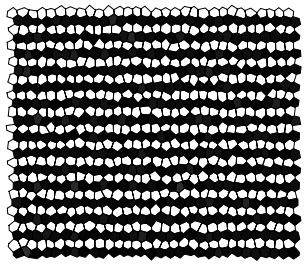

Figure 5.20: Stripes are also stable on more irregular lattices. Parameter values: $h = 2$, $\epsilon = 0$, $v = 1$, $r_t = 50$ and $r_c = 200$.

approach the non-conserved model[7].

Multicellular system

Suppose that both cis and trans-complexes C_i and B_i get cleaved, giving rise to the Notch signal :

$$N_i + L_j \quad \underset{k_{-b}}{\overset{k_b}{\rightleftharpoons}} C_i \xrightarrow{k_s} \quad S_i \tag{5.20a}$$

$$N_i + L_i \quad \underset{k'_{-b}}{\overset{k'_b}{\rightleftharpoons}} B_i \xrightarrow{\epsilon k_s} \quad S_i \quad . \tag{5.20b}$$

Besides, we consider complex degradations, *i.e*

$$C_i \xrightarrow{\nu_c} \phi, \quad B_i \xrightarrow{\nu_b} \phi \quad . \tag{5.21}$$

In this approach, we include basal production and linear degradation for the Notch receptor:

$$\phi \xrightarrow{\beta_n} N_i, \quad N_i \quad \xrightarrow{\nu_n} \quad \phi \quad . \tag{5.22}$$

Once considered fast mRNA, assuming that ligand production is down-regulated by the signal through the usual Hill function, the dimensional system of equations

[7]The conclusions we present in this section are robust to parameter values. Because of that, the dimensional values we use for the parameters are not based on experimental works, but are representative for the conclusions we are presenting.

for all the existing variables will take the following form:

$$\frac{\mathrm{d}L_i}{\mathrm{d}\tau} = -k_b\langle N_i\rangle L_i + k_{-b}\langle C_i\rangle - k'_b N_i L_i + k'_{-b}B_i + \frac{\beta_l}{1+bS_i^h} - \nu_l L_i \quad (5.23a)$$

$$\frac{\mathrm{d}N_i}{\mathrm{d}\tau} = -k_b N_i\langle L_i\rangle - k'_b N_i L_i + k_{-b}C_i + k'_{-b}B_i + \beta_n - \nu_n N_i \quad (5.23b)$$

$$\frac{\mathrm{d}C_i}{\mathrm{d}\tau} = k_b N_i\langle L_i\rangle - k_{-b}C_i - k_s C_i - \nu_c C_i \quad (5.23c)$$

$$\frac{\mathrm{d}B_i}{\mathrm{d}\tau} = k'_b N_i L_i - k'_{-b}B_i - \epsilon k_s B_i - \nu_b B_i \quad (5.23d)$$

$$\frac{\mathrm{d}S_i}{\mathrm{d}\tau} = k_s C_i + \epsilon k_s B_i - \nu_s S_i \quad , \quad (5.23e)$$

where now we consider the binding and unbinding reactions in the equation for the ligand. We will not perform any additional adiabatic approximation nor adimensionalization, since our intention is just to prove that our main conclusions are also found in a more realistic modeling of the Notch signaling pathway.

Single cell system

We can write an equivalent model for the single cell system by assuming that Notch receptor turns into a modified form C_i in a ligand-independent way, and its cleavage drives signaling:

$$N_i \underset{\mu_{-0}}{\overset{\mu_0}{\rightleftharpoons}} C_i \xrightarrow{k_s} S_i \quad . \quad (5.24)$$

The corresponding system would read[8]

$$\frac{\mathrm{d}L_i}{\mathrm{d}\tau} = -k'_b N_i L_i + k'_{-b}B_i + \frac{\beta_l}{1+bS_i^h} - \nu_l L_i \quad (5.25a)$$

$$\frac{\mathrm{d}N_i}{\mathrm{d}\tau} = -\mu_0 N_i - k'_b N_i L_i + \mu_{-0}C_i + k'_{-b}B_i + \beta_n - \nu_n N_i \quad (5.25b)$$

$$\frac{\mathrm{d}C_i}{\mathrm{d}\tau} = \mu_0 N_i - \mu_{-0}C_i - k_s C_i - \nu_c C_i \quad (5.25c)$$

$$\frac{\mathrm{d}B_i}{\mathrm{d}\tau} = k'_b N_i L_i - k'_{-b}B_i - \epsilon k_s B_i - \nu_b B_i \quad (5.25d)$$

$$\frac{\mathrm{d}S_i}{\mathrm{d}\tau} = k_s C_i + \epsilon k_s B_i - \nu_s S_i \quad . \quad (5.25e)$$

Note that this model we do not consider trans-interactions between cells, so even if we have the same number of equations per cell, the equations for the

[8] We keep the subindex for coherence with the single cell model in which Notch is conserved (Sec. 5.2.2), but it can be omitted.

ligand and receptor (Eqs. 5.25a-5.25b) are simpler than in the multicellular non-conserved case (Eqs. 5.23a-5.23b).

In this section, we will show that some of the already presented results for the model in which Notch is conserved (Eqs. 5.2-5.4) hold for this modeling approach in which Notch receptor is non-conserved. Moreover, in this section our simulations will also deal with the kinetics of receptor-ligand binding and unbinding and also with the complexes kinetics.

Competition of the Notch signaling sources leads to the same results.

Herein we study the role of cis-interactions for both multicellular (see Eqs. 5.23) and single cell (see Eqs. 5.25) frameworks. $\mathscr{R}_{S_i,L_i} = \frac{\partial}{\partial L_i}\frac{dS_i}{d\tau} = \frac{\partial S_i^{st}}{\partial L_i}$ where S_i^{st} refers to the steady state of S_i. Once more, the sign of $\mathscr{R}_{S_i,L_i}$ will determine the activatory/inhibitory role of cis interactions. Applying the chain rule to $\mathscr{R}_{S_i,L_i}$ we obtain $\frac{\partial S_i}{\partial L_i} = \frac{\partial S_i}{\partial C_i}\frac{\partial C_i}{\partial L_i} + \frac{\partial S_i}{\partial B_i}\frac{\partial B_i}{\partial L_i}$ where the derivatives are performed over the steady state of the variables, but we do not write it for simplicity.

We find that cis-inhibition occurs when

$$\epsilon < \frac{\nu_b k_b \langle L_i \rangle}{\nu_n(k_{-b} + k_s + \nu_c) + \nu_c k_b \langle L_i \rangle} \tag{5.26}$$

for the multicellular case and

$$\epsilon < \frac{\nu_b \mu_0}{\nu_n(\mu_{-0} + k_s + \nu_c) + \nu_c \mu_0} \tag{5.27}$$

for the single cell case. Cis-inhibition always occurs when $\epsilon = 0$, and cis-activation happens if $\epsilon > \frac{\nu_b}{\nu_c}$. In this approach we still have a regime of weak cis-signaling rates $0 < \epsilon < \frac{\nu_b}{\nu_c}$ where competition can still lead to cis-inhibition if Eqs. 5.26 and 5.27 are fullfiled for the multicellular and single cell cases respectively (Fig. 5.21).

It is worth noting that these criterions do not depend on the Notch receptor production β_n, so competition does not relay on the saturation of the receptors.

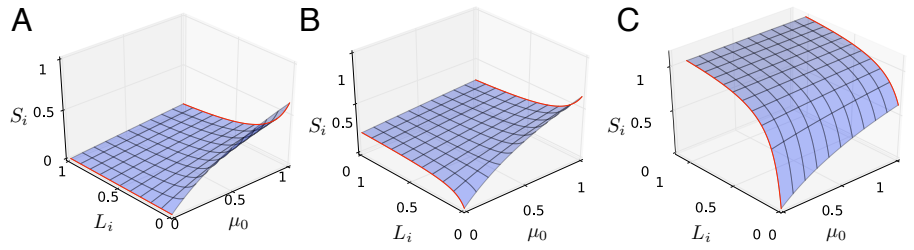

Figure 5.21: Cis-interactions role depends on the relative cis/trans-signal rates ϵ and the ligand independent rate μ_0 at the cell-autonomous scenario. Notch signal *versus* L_i and μ_0 for (A) null $\epsilon = 0$, (B) weak $\epsilon = 0.1$ and (C) strong ($\epsilon = 1$) cis-signaling. Red lines indicate that S_i increases or decreases as a function of L_i, indicating cis-activation or cis-inhibition respectively. Other parameter values: $\beta_n = 2.5$ au hr^{-1}, $\nu_c = \nu_b = \nu_n = \nu_s = 1$ hr^{-1}, $k_{-0} = 0$ hr^{-1}, $k_s = 1$ hr^{-1}. hr refer to hours and au refer to arbitrary concentration units.

The cell-autonomous bistable switch is also found in the non-conserved model

To evaluate the existence of a cell-autonomous bistable switch, we focus once more on the steady states of the system 5.25. These can be found by solving

$$S_i = \frac{1}{\nu_s}(A_1 L_i + A_2 \mu_0) N_i \tag{5.28a}$$

$$S_i = \left(\frac{\beta_d - L_i(\nu_l + (A_1 + \widetilde{A}_1)N_i)}{b(L_i(\nu_l + (A_1 + \widetilde{A}_1)N_i)} \right)^{1/h} , \tag{5.28b}$$

where

$$A_1 = \frac{\epsilon k_s k'_b}{k'_{-b} + \epsilon k_s + \nu_b}, \quad A_2 = \frac{k_s}{\mu_{-0} + k_s + \nu_c} \tag{5.29a}$$

$$\widetilde{A}_1 = \frac{\nu_b k'_b}{k'_{-b} + \epsilon k_s + \nu_b}, \quad \widetilde{A}_2 = \frac{\nu_c}{\mu_{-0} + k_s + \nu_c} , \tag{5.29b}$$

and

$$N_i = \frac{\beta_n}{\nu_n + (A_1 + \widetilde{A}_1)L_i + (A_2 + \widetilde{A}_2)\mu_0} . \tag{5.30}$$

Nullclines analysis and numerical simulations confirm that more than one stable solution arises (Fig. 5.22). Notably, in this case we find bistability can be achieved in the case where there is no cooperativity.

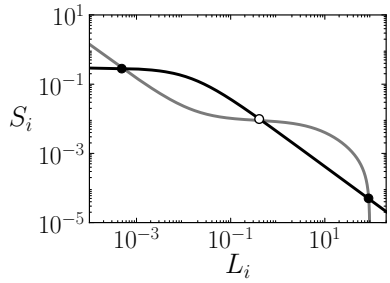

Figure 5.22: In the non-conserved model, cis-inhibition with a basal Notch signal source creates a bistable cell-autonomous switch. For strong enough cis-interactions and weak or null cis-signaling, cells are able to end up in two different cell populations. In the non-conserved model no cooperativity is needed for having bistability. Black line corresponds to Eq. 5.28a and gray line to Eq. 5.28b. Empty dots are unstable solutions, while filled dots are stable solutions. Stability has been evaluated through numerical simulations. Parameter values: $k_b' = 150$ au^{-1} hr^{-1}, $\epsilon = 0$, $h = 1$, $\beta_n = 10$ au hr^{-1}, $\beta_l = 100$ au hr^{-1}, $\nu_c = \nu_b = \nu_l = \nu_s = 1$ hr^{-1}, $k'_{-b} = 1$ hr^{-1}, $\mu_{-0} = 30$ hr^{-1}, $b = 1000$ au^{-h}, $k_s = 1$ hr^{-1}, $\mu_0 = 1$ hr^{-1}. hr refer to hours and au refer to arbitrary concentration units.

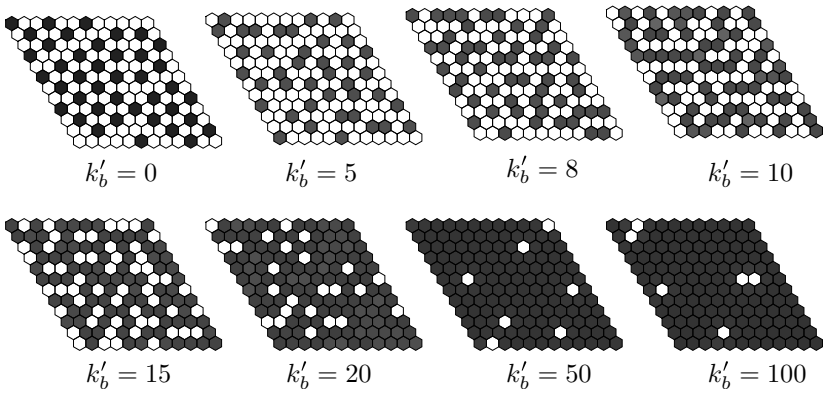

Figure 5.23: In the non-conserved model, cis-inhibition also promote high Delta fated cells. Simulation results of Eqs. 5.23 for different cis-binding rates k_b' indicated below the panels (we omit unities for simplicity, which are in hr^-1 (hr means hours). Delta-levels are represented in gray scale, being black $\beta_l/\nu_l = 10$ and white 0. We use random initial conditions for ligand and receptor variables of the form $L_i(t = 0) = U_i^l \beta_l$ and $N_i(t = 0) = U_i^n \beta_n$ where U_i^x is a uniform random number between 0 and 1. The rest of the variables have zero initial conditions. Low cis binding affinities ($k_b' = 5$) allows high-Delta cell pairs being next to each other, being consistent with results by Sprinzak *et al.* (2010) [47]. Higher cis-affinities leads to a gradual increase of Delta-positive cells in the tissue. This phenomenology is recovered for other parameter sets. Parameter values: $\beta_l = 10$ au hr^-1,$\beta_n = 2$ au hr^{-1}, $k_s = 50$ hr^{-1}, $k_b = 0.1$ au^{-1} hr^{-1}, $\nu_c = \nu_b = \nu_l = \nu_n = 1$ hr^{-1}, $\nu_s = 5$ hr^{-1}, $k_{-b} = k'_{-b} = 0.01$ hr^{-1}, $b = 1000$ au^{-h}, $h = 4$. hr refer to hours and au refer to arbitrary concentration units.

Cis-inhibition promotes the high Delta fate by reducing the lateral inhibition effect

We simulate the whole dimensional model for addressing this issue (see Eqs. 5.23). For avoiding numerical instabilities (stiffness), we use the NDSolve function of Mathematica 8.0).

We find that the non-conserved model also yield high Delta cells worse receivers, and the increase of cis-inhibition gradually lead to more cells achieving the high Delta fate (see Fig. 5.23).

5.4 Discussion

Nowadays there is empirical evidence pointing at a signal elicited by cis-interactions [81, 180, 183]. Thus far, theoretically approaches focused on cis-inhibition with null cis-signaling [47, 49, 66, 105, 130, 190–192]. In this work we have theoretically characterized the effect of the cis-interactions for different cis-signaling production rates in a cell-autonomous and multicellular contexts. Null or weak cis-signaling competing with an alternative Notch signal source - what we called the primary signaling source - leads to cis-inhibition, while strong cis-signaling to cis-activation. Our analysis shows that these two scenarios correspond to different effective transcriptional regulatory circuit designs and accordingly drive different capabilities at both cell-autonomous and multicellular levels [193].

Our analysis exemplifies a case of competition leading to a complex counterintuitive dynamical output: two signaling sources — the trans and the cis-sources in the multicellular case — competing for the same substrate — the Notch receptor — can lead to a unexpected behavior: cis-productive signaling is still mediating cis-inhibition [193]. Such competition is reminiscent to what has been reported in pharmacology when a full and a partial agonists are both interacting with a receptor [194]; in this case the partial agonist can act as a competitive antagonist of a full agonist.

Our model reveals the potential existence of a cell-autonomous switch that is bistable and driven by cis-interactions when a basal cell-autonomous activity of Notch is present [193]. This could lead to a cell-fate decision switch that is cell-autonomous. Indeed, the resulting network architecture can be under-

stood as what has been called mixed-feedback look [195]. On the other side, cis-interactions could also enable a cell-autonomous homeostat, what for instance would make the cell more resistant to perturbations. Finding out the existence of such a switch or homeostat in real cells could unveil unknown functions of the Notch signaling pathway. The search for the existence of such bistable switch could be addressed in different experimental setups, *e.g* either in cell cultures on a plate covered with different amount of ligands (see for instance [47]) or by eliciting in a controlled way ligand independent Notch signaling, for instance by EDTA treatment (see [127]).

We have seen that the two aforementioned scenarios drive different capabilities to the patterning process: on one side, cis-activation creates a negative intracellular feedback loop that inhibits pattern formation, and on the other side, cis-inhibition creates a positive intracellular loop facilitating patterning. Our model also predicts that optimal cis-inhibition is needed to have fine grained patterning, since too high cis-interactions strengths would lead the system to a massive high-ligand fated phenotype.

Previous theoretical studies have already shown that cis-inhibition promotes lateral inhibition patterning from different perspectives [47, 105, 130, 191]. Meir *et al.* [105] proposed a computational detailed model where the cis-inhibition module constitutes an explicit phenomenological transcriptional positive feedback loop embedded in a much more complex gene regulatory network. They showed that cis-inhibition could facilitate patterning in small groups of equivalent cells where the lateral inhibition effect operates. On the other side, Sprinzak *et al.* (2010) [47,130,191] showed with a simple but still very realistic model that cis-inhibition with Delta inactivation drives a positive post-transcriptional feedback loop, creating an ultrasensitive switch where cells adopt a signal sending fate or a receiving fate, but not both. In their model they show that lateral inhibition patterning could be achieved even without cooperativity in a large field of initially equivalent cells with periodic boundary conditions. Interestingly, they also obtained that cis-inhibition speeds the lateral inhibition patterning process [130]. In our modeling approach, such post-transcriptional feedback loop does not appear since we consider the conservation of the full amount of receptor. Though, our results are robust and are not dependent on this approximation. Instead, we focus on the transcriptional feedback introduced by cis-interactions in a model

that can be derived from a more detailed chemical reaction scheme.

Our model on cis-interactions allows an easy exploration in the parameter space. Indeed, it facilitates the study the region in the parameter space where the lateral inhibition solution do exist [135,193], what we called nonlinear pattern formation region.

Our simulation results have revealed that in the cis-inhibition scenario the ratio of the two different cell types can be quite gradually changed [193]. Indeed, when cis-interactions amount increases in relation of the trans-interactions in a cell population without any prepatterning bias, there is a graded increase of the ratio of the high-ligand cell type in the tissue, giving rise to more disordered and even random patterns. This effect is a direct consequence of the fact that cis-inhibition makes all ligand expressing cells being worse receivers by increasing the threshold of trans-activation, what has been already pointed from experimental grounds [122, 123, 128, 196] and also can be derived from our equations. Indeed, Delta ligand leading to cis-inhibition can be understood as a dominant-negative form of the ligand that is antagonizing the receptor activity [123]. Then, unless no-ligand is reported in the precursor state, cis-inhibition should clearly disrupt the lateral inhibition effect, giving rise to a much richer variety of patterns [47]. These new emerging patterns are consistent with the fact that cis-inhibition introduces nonlinearity to the system, as reported by Sprinzak *et al.* (2011) [130].

Recently it has been reported that *Lunatic Fringe* knockdown produces an increase in the neurogenesis ratio in the neural tube of zebrafish embryos [197]. This could be a possible experimental evidence of the predicted cell-type ratio modulation, since Fringe potentiates Delta-Notch trans-interactions [83] and also could inhibit the cell-autonomous association of Dl/N [123, 198]. Graded cell ratios in a lateral inhibition framework have also been theoretically obtained in other contexts. Specifically, it has also been shown that by increasing the inhibitory threshold in a cellular automata framework for a purely lateral inhibition model, one can gradually obtain different patterns with higher density of high Delta cells [199], which is consistent with our results. In our case, this threshold is changed due to cis-inhibition.

The increase of Delta production in a more detailed lateral inhibition model without cis-inhibition has shown a graded increase of high Delta cells and was validated experimentally [60]. It would be interesting to study whether this

phenomenon in such a different context where no cis-interactions are taken into account has something to do with our findings in the framework of cis-inhibition.

We have also shown that cis-interactions can enable the emergence of other periodic patterns high higher ratio of high-Delta cells [193]. For instance, the inverted version of the lateral inhibition pattern and a pattern of stripes. Spontaneously, just the normal lateral inhibition pattern and its inverted version were possible to identify in our simulations. Prepatterned initial conditions and additional mechanisms (paper in preparation, [200]) are required for the emergence of the other patterns.

Last, we have seen that cis-inhibition allows the existence of localized patterned states [193]. This was not the case when cis-interactions were not present, since a nucleating pattern would spread out to the rest of the system through a traveling wave [10, 104, 109]. Our results indicate that high cis *versus* trans-interaction strengths makes the associated traveling wave of the pattern having null propagating velocity, what presumably corresponds to a wave-pinning phenomenon [104]. Typically, wave-pinning arises in discrete dynamical systems when the cell-cell coupling is below a critical strength [201], that in our case would correspond to high r_c/r_t ratios. Moreover, the most disordered patterns appear in the regions where localized patterning occurs. In such regions of the parameter space, the final pattern was very sensible to the precursor state. This new kind of patterning exhibits the trans and cis-interactions in its most entangled mode; if the homogeneous initial conditions are perturbed, then the positive intracellular feedback conferes different choices to cells. In this regime, trans-interactions just bias the cell fate choice, and will not be able to trigger a propagating wave of cell-fate decisions. In such a novel situation, external signals will have a high impact in the final pattern.

The fact that cis-inhibition promotes multistability and drives pattern localization is also a footprint of the nonlinear effects due to cis-inhibition [130].

This work can be generalized for a better understanding of how Notch receptor is shared between different components. One example is how different types of Notch ligands are orchestrated. Another example is the Dlk1/2 non-canonical ligands, which are present with Notch in very different contexts. Indeed, it has been proposed that these non-canonical ligands cis-inhibit Notch while not being able to perform trans-activation [79], but its function during development and

diseases still remains obscure [202].

Chapter 6

Competition in Notch signaling matters: lateral induction and lateral inhibition in the embryonic inner ear.

6.1 Introduction

The developing inner ear in vertebrates is another example where lateral inhibition takes place and drives a regular mosaic of hair cells (HC) surrounded by supporting cells (SC) [56]. This developmental process is preceded by another Notch-mediated phenomenon called prosensory specification (Fig. 6.1). In this previous step, the Notch ligand Jag1 establishes the domain of cells that will be competent for differentiate into hair cells. At this stage, Notch has been proposed to act through Jag1 in a lateral induction mode (see Fig. 1.3 (A)) by which all cells end up exhibiting a coherent state of sensory competence[1] [56, 57, 203, 204].

[1] In this chapter we use the term coherent as a synonym of homogeneous.

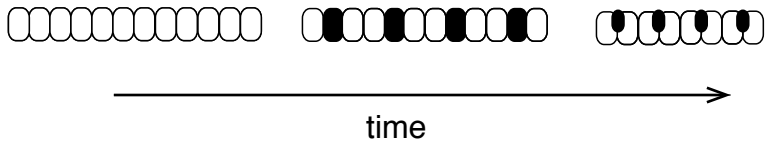

Figure 6.1: Cartoon of the hair cell development in the embryonic inner ear. First, a prosensory patch is established exhibiting a coherent state of Jag1 in which cells are competent for adopting the sensory fate (left). Next (middle, right) a lateral inhibition pattern emerges, giving rise to a salt-and-pepper patter of hair cells (HC, black) surrounded by supporting cells (SC, orange).

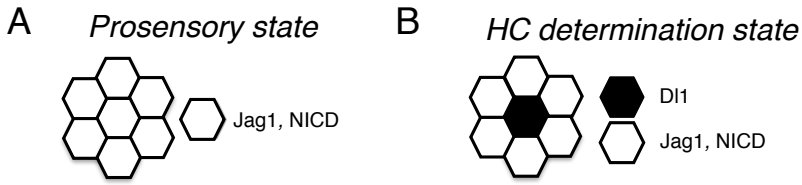

Figure 6.2: Characterization of the cellular states. Wild-type tissue states in the (A) prosensory and (B) sensory domains. White cells represent cells with Notch activity (NICD) and Jag1 expression while the black cell represents a cell expressing Dl1.

Jag1 and NICD (Notch intracellular domain or active Notch) are expressed together in the sensory epithelium, and restricted to the sensory patches. Thereafter, the proneural gene *Atoh1* is expressed and drives Dl1 expression, which, in turn, gives rise to lateral inhibition (see Fig. 1.3 (B)). Hair cells differentiate and the salt-and-pepper pattern shows up with Dl1-positive cells in HC-precursors and Jag1 and NICD in the surrounding SCs (Fig. 6.2).

Experimental evidences have shown that Dl1 is inhibited by Notch, while Jag1 is activated by Notch [57, 204, 205]. Such ligand regulation, in combination with Notch trans-activation by both ligands, it creates a lateral inhibition circuit for Dl1 [10] and a lateral induction circuit for Jag1 [48] (see Fig. 6.3).

In this chapter we assume that these two opposite operating modes occur sequentially. Our goal is to study how such two different circuits are combined during the development of the embryonic inner ear. By using a simple model, we

try to generate first the homogeneous state due to lateral induction where both Jag1 and NICD are found. Then, we introduce Dl1 and we try to obtain the wild-type salt-and-pepper pattern driven by lateral inhibition.

6.2 A model for two ligands

In this section we extend the Collier model for two ligands. We propose a model in which the two ligands are acting in opposite modes when they are not expressed together (*i.e.* when they act separately). In particular, we set that Dl1 (d) is inhibited by the Notch signal (s) while Jag1 (z) is up-regulated by that (s) (see Fig. 6.3). Following the procedure presented in the precedent chapters, we propose the system of equations

$$\frac{\mathrm{d}s_i}{\mathrm{d}t} = \frac{r_d\langle d_i\rangle + \epsilon r_z\langle z_i\rangle}{1 + r_d\langle d_i\rangle + r_z\langle z_i\rangle} - s_i \tag{6.1a}$$

$$\frac{\mathrm{d}d_i}{\mathrm{d}t} = v_d\left\{\frac{1}{1+b_d s_i^{h_d}} - d_i\right\} \tag{6.1b}$$

$$\frac{\mathrm{d}z_i}{\mathrm{d}t} = v_z\left\{\frac{s_i^{h_z}}{a_z^{h_z} + s_i^{h_z}} - z_i\right\} \quad , \tag{6.1c}$$

where r_x is proportional to the affinity K_x between the x-ligand and Notch and to a characteristic x-ligand concentration X_0, h_x is the cooperativity in the regulatory Hill function for the x-ligand, ϵ is the relation of the signaling rates (or intensities) due to Jag1-Notch complex in relation to Dl1-Notch complex, b_d is the strength of the Delta-ligand inhibition, a_z is the Notch signal threshold at

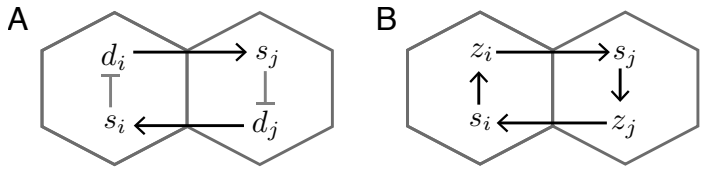

Figure 6.3: Two different modes of action for Notch signaling. (A) Cartoon of the lateral inhibition circuit due to Dl1 (d). (B) Cartoon of the lateral induction circuit due to Jag1 (z). These two circuits can appear together in the same cells (see Fig 6.4 (A)).

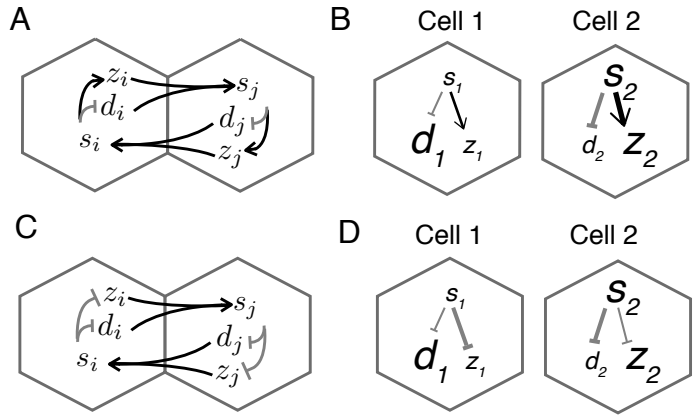

Figure 6.4: Our model with two ligands acting in opposite modes does enable the wild-type pattern. (A,C) Two scenarios for Notch signaling with the two ligands. (B,D) Schematic representation of ligand regulation by the Notch signal for achieving the two cell fates found in sensory organs. Large (small) letter size refers to a certain chemical species that is found at high (low) concentration. Blunt arrows denote inhibition. Arrows' width qualitatively indicates the required inhibition strength consistent with the cell fate. Cell fate A and B corresponds to the HC and SC fates, respectively. (A,B) Scenario in which Notch activated Jag1 and inhibits Dl1. (B) This scenario allows the wild-type pattern (see Fig. 6.2). (C,D) Scenario in which both ligands are inhibited by Notch (B) With this scenario, cell 1 and cell 2 fates lead to the inconsistence that low signal can not provide a stronger inhibition to Jag1 than a strong Notch signal.

which Jag1 is half-activated, v_x set the time scale of the x-ligand in relation to the signal and $\langle x_i \rangle$ is the cell-to-cell coupling term by the x-ligand (see Eq. 2.9).

We define an additional parameter ϵ_r as $\epsilon_r = r_z/r_d$. This parameter compares the amount of trans-interactions due to Jag1 with respect to the amount of trans-interactions due to Dl1. We term ϵ_r as the Jag1/Dl1 relative interaction strength. We can redefine Eq. 6.1a in terms of ϵ_r instead of r_z . This enables to increase the r_d value and to reflect it in terms of the differences between Jag1 and Dl1 (a decrease in ϵ_r). An increase (decrease) on r_d (ϵ_r) will mimic the transition between the two operating modes driven by *Atoh1* in the chick inner ear. In particular, this parameter change will mimic the inclusion of Dl1 into the tissue.

Our model with two ligands regulated by Notch in opposite ways is expected to result in the generation of the wild-type pattern (see Figs. 6.2 and 6.4). Other scenarios, like the one in which the two ligands are downregulated by Notch, do also allow a salt-and-pepper pattern. However, in this alternative case both ligands concentrate in the same cells and this does not occur in the real sensory organs (Fig. 6.4).

The numerical integration of the model is carried out as as explained in Sec. 2.9.1 on regular and irregular two-dimensional arrays of cells with periodic boundary conditions. The time step of the simulations is $\mathrm{d}t = 0.1$. Simulations are stopped when the steady state is reached. The irregular array of cells has an irregularity parameter $\gamma = 0.67$.

6.3 Results

6.3.1 Jag1 activation drives lateral induction

The model, when only Jag1 ligand is present ($r_d \approx 0$ in Eqs. 6.1), generates a positive intercellular loop composed of two mutual activations mediated by Jag1 (Fig. 6.3 (B)). This architecture has been proposed in a synthetic biology context for studying signal propagation between cells [48]. *A priori*, this type of loop could also generate ligand propagation, which would emulate the formation of the prosensory state. A necessary condition for ligand propagation is that the dynamical system has two homogeneous stable states (one with low levels of ligand and another one with higher levels of ligand). Therefore, we search across the parameter space homogeneous solutions of the above model by means of our bisection method (Sec. 2.6). We find that Jag1 on its own can drive several homogeneous coherent states (Fig. 6.5 (A)). It is possible to provide a constraint on some parameters for which more than one homogeneous solution appears, enabling lateral induction. Such relationship can be extracted from computing the intersection of the nullclines defined by Eq. 6.1a for $r_d = 0$ and Eq. 6.1c and by imposing that both nullclines are tangent at the intersection point. This condition reads

$$\epsilon \geq \frac{a_z(h_z(1+r_z)^{(h_z-1)/h_z})}{r_z(h_z-1)^{(h_z-1)/h_z}} \quad . \tag{6.2}$$

Then, for a particular a_z such relation establishes a minimal amount of ϵ above which different homogeneous solutions can arise.

To evaluate the stability of the homogeneous solutions, we make use of LSA in a perfect hexagonal array of cells. Following the procedure described in sections 2.4 and 2.10 for the above model, we obtain that the $\mathscr{M}$ matrix (Eq. 2.27) reads

$$\begin{pmatrix} -1 & \mathscr{A}_d\Omega_{\overline{q},\overline{p}} & \mathscr{A}_z\Omega_{\overline{q},\overline{p}} \\ v\mathscr{B}_d & -v & 0 \\ v\mathscr{B}_z & 0 & -v \end{pmatrix} \quad ,$$

where

$$\mathscr{B}_x = \frac{1}{v}\frac{\partial}{\partial s_i}\frac{\mathrm{d}x_i}{\mathrm{d}t}\bigg|_{s_0,d_0,z_0} \quad , \quad \mathscr{A}_x = \omega \left.\frac{\partial}{\partial x_k}\frac{\mathrm{d}s_i}{\mathrm{d}t}\right|_{s_0,d_0,z_0} \quad , \tag{6.3}$$

being x and y the two ligand species, and the index j refers to a cell that is a nearest neighbor of cell i. These expressions read

$$\mathscr{A}_z = \frac{r_z(r_d d_0(\epsilon-1)+\epsilon)}{(1+r_d d_0+r_z z_0)^2} \, , \quad \mathscr{A}_d = \frac{r_d(r_z z_0(1-\epsilon)+1)}{(1+r_d d_0+r_z z_0)^2} \tag{6.4a}$$

$$\mathscr{B}_d = -\frac{h_d b_d s_0^{h_d-1}}{(1+b_d s_0^{h_d})^2} \, , \quad \mathscr{B}_z = \frac{h_z a_z^{h_z} s_0^{h_z-1}}{(a_z^{h_z}+s_0^{h_z})^2} \, . \tag{6.4b}$$

One eigenvalue of the above $\mathscr{M}$ matrix has the form $\alpha = -v$ and the other two are

$$\alpha^{\pm} = \frac{1}{2}\left\{-(1+v) \pm \left((1+v)^2 - 4v(1-\Omega(\mathscr{A}_d\mathscr{B}_d+\mathscr{A}_z\mathscr{B}_z))\right)^{1/2}\right\} \tag{6.5}$$

According to it, a homogeneous solution is stable to homogeneous and inhomogeneous perturbations if the following conditions are satisfied

$$1 > \mathscr{A}_d\mathscr{B}_d + \mathscr{A}_z\mathscr{B}_z \tag{6.6a}$$

$$-2 < \mathscr{A}_d\mathscr{B}_d + \mathscr{A}_z\mathscr{B}_z \quad . \tag{6.6b}$$

By using the above stability conditions into the homogeneous solutions we find that Jag1 on its own drives bistability of homogeneous coherent states (Fig. 6.5 (A)). In this coherent bistable regime, two homogeneous states are stable to small perturbations, both at low and high levels of ligand expression (Fig. 6.5

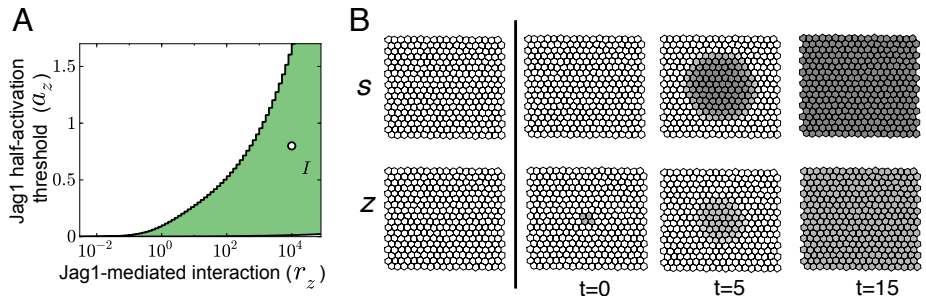

Figure 6.5: Jag1 robustly generates homogeneous bistability, enabling on its own cell-to-cell mediated ligand propagation. (A) Phase diagram for the model of two ligands (Eqs. 6.1) showing the region where two homogeneous fixed points are linearly stable (green region) when only Jag1 acts ($r_d = 10^{-4}$). This enables ligand propagating dynamics from a low Jag1 to a high Jag1 state (see panel (B) corresponding to point I in the phase diagram). (B) Snapshots corresponding to simulation results for the signal and ligand tissue states. Signal and ligand levels in gray scale from low (white) to high (black). The dimensional levels of signal and ligand from low (white) to high (black) are shown with logarithmic gray scales. The chosen dimensional concentrations $S_0 s_i$, $D_0 d_i$ and $Z_0 z_i$ are set to $S_0 = 1$, $D_0 = r_d$ and $Z_0 = r_z$. The gray scale is set for the Notch signal from 0.1 to 1 and for Jag1 from 50 to 5000. Increasing locally Jag1 at time $t = 0$ in the low-ligand tissue state induces ligand propagation and switch to the high-ligand tissue state. This corresponds to point I in panel (A). Parameter values: $\epsilon = 0.3$, $h_z = h_d = 4$, $b_d = 10^4$ and $v = 1$.

(B)). Under this regime, after a local transient overexpression of Jag1 in the low-ligand homogeneous state, a propagating wave is formed such that Jag1 is induced laterally and all cells ultimately express higher levels of Jag1 (Fig. 6.5 (B)). In terms of dynamics, the system "switches" from the stable state with low Jag1 and Notch signal to the stable state with higher levels of Jag1 and Notch signal. This mimics the results of the gain of function of Jag1 or Notch in the inner ear [57, 203], suggesting that this model appropriately simulates the prosensory state in which lateral induction takes place.

6.3.2 Signaling intensities ratio by the two ligands is essential for the proper lateral induction to lateral inhibition transition

In the model, the transition from the prosensory to the differentiation state corresponds to an increase in the amount of Dl1-mediated interaction (increased r_d, see Sec. 6.2), which drives a decrease in the Jag1/Dl1 relative interaction ($\epsilon_r = r_z/r_d$). The ratio of Jag1 to Dl1-induced signaling rates become crucial for this transition to happen properly (Fig. 6.6 (A)). For $\epsilon = 0.3$ the transition (from I to II in Fig. 6.6 (A,C)) drives the change from a coherent state with lateral induction to a salt-and-pepper lateral inhibition pattern state. This pattern is like the one in the sensory organs of wild-type embryos, *i.e.* high-Dl1 expressing cells with no Jag1 nor Notch signal, surrounded by cells expressing high levels of both Notch signal and Jag1 (see Figs. 6.2, 6.6 (B)). The results in Fig. 6.6 (A) show that this change in Notch operation modes from lateral induction to lateral inhibition requires Jag1 signaling rate to be weaker than Dl1 signaling rate (*i.e.* $\epsilon < 1$). Jag1 needs to signal less than Dl1 to enable salt-and-pepper lateral inhibition patterning when both ligands are present. Additionally, Jag1 has to signal strong enough to drive ligand propagation by lateral induction when it is acting on its own (*i.e.* without Dl1) (Fig. 6.6 (A)).

We numerically evaluate in a perfect hexagonal array whether the emerging pattern has the wild-type properties across a significant region of the phase diagram. To this end we define a control parameter, which is zero only when the proper wild-type pattern is formed. This control parameter is defined as follows:

$$\xi = (\rho_s - 2/3)^2 + (\rho_d - 1/3)^2 + (\rho_z - 2/3)^2 \quad , \tag{6.7}$$

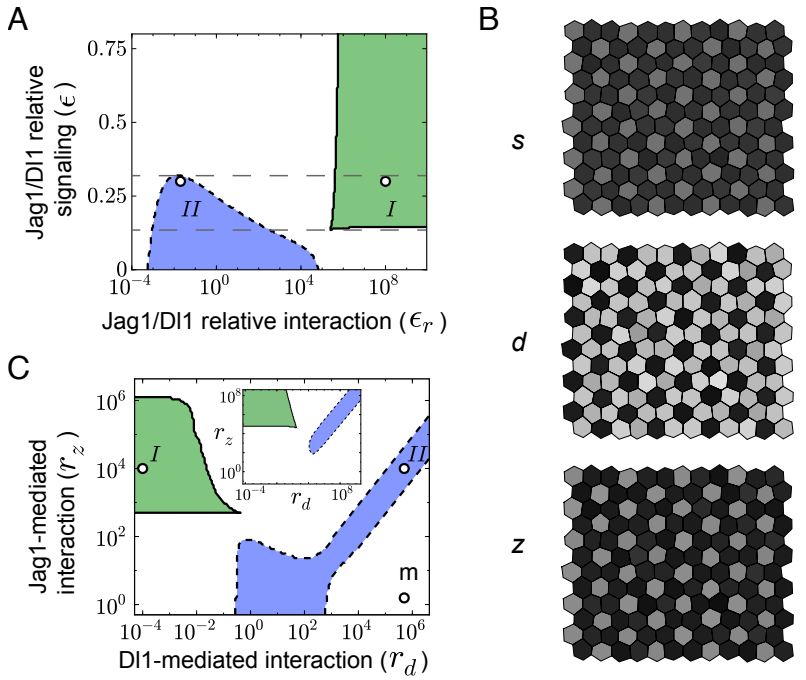

Figure 6.6: Transition form lateral induction to lateral inhibition. (A) Phase diagram when both Jag1 and Dl1 act for $a_z = 0.8$, $r_z = 10^4$, $h_d = h_z = 4$. The blue region indicates where the homogeneous state is linearly unstable to inhomogeneous perturbations, leading to lateral inhibition patterning. The green region indicates where two homogeneous states are linearly stable due to the lateral induction effect. Thin dashed lines as guide to the eye for ϵ values at which the transition from lateral induction to lateral inhibition would be possible. The lower horizontal line is obtained by setting the equality in Eq. 6.2. (B) Tissue state for point II in (A). This corresponds to the wild-type salt-and-pepper pattern, in which Jag1 and Dl1 are found in different cells. Color code as in Fig. 6.5 (B). (C) Phase diagram when both Jag1 and Dl1 act for $\epsilon = 0.3$ and $a_z = 0.8$, $h_d = h_z = 4$. Color code as in (A). Inset: as (C) for $h_z = 8$ and $h_d = 1$. Point I in (A, C) and in Fig. 6.5 (A) is the same as well as II in (A,C).

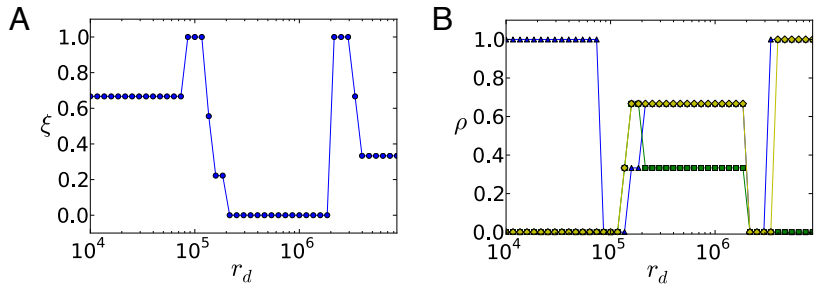

Figure 6.7: Characterization of tissue state patterns. Simulation results of the model for two ligands for different r_d values in a perfect hexagonal lattice of 9×9 cells. (A) ξ control parameter. $\xi = 0$ indicates that the wild-type pattern found in sensory organs is reproduced. (B) Cell ratios of high Notch signal, Dl1 and Jag1 levels, represented by the blue triangles, green squares and yellow rhombus, respectively. Lines in both panels are a guide to the eye. Other parameter values as in Fig. 6.6 (C).

where ρ_s, ρ_d and ρ_z are the ratios of cells in a tissue with high Notch signal, high Dl1 and high Jag1 respectively. A cell is considered to have a high concentration of a particular molecular species in a patterned situation when its concentration value is at least 1.3 higher than its minimal value in the tissue for the final simulation time. If the studied species does not present any pattern, we consider it has a high concentration value if it exceeds 0.2. A patterned situation for the x-molecular species is considered if $\eta_x > 10^{-6}$ and a homogeneous situation if $\eta_x \leq 10^{-6}$ (see Eq. 2.35 in Sec. 2.8.1). Our numerical simulations results confirm that such pattern is robust in the phase diagram (Fig. 6.7).

6.3.3 Jag1 promotes lateral inhibition through signal competition while enabling lateral induction on its own

To unveil the role of Jag1 in lateral inhibition, we investigate the tissue states as a function of Dl1- and Jag1-mediated interactions (r_d and r_z) for $\epsilon = 0.3$ (Fig. 6.6 (C)). Point II in Fig. 6.6 (C) exemplifies the lateral inhibition mode when both Jag1 and Dl1 act together (hair cell determination state).

When the two ligands act simultaneously but with different signaling rates, the actual function of the ligands may change. In our case, the result is that Jag1, contrarily to its role in isolation, effectively performs lateral inhibition when it

acts together with Dl1. This is reminiscent to what was described in Chap. 5 for two interacting modes of Notch with a ligand acting in cis and trans. In the present case, the ligand inducing a weaker signal can effectively inhibit signal production. This effective inhibition can be evaluated from the partial derivative of the signal dynamics with respect to the ligand (see Sec. 2.2). This results in

(A) Jag1 activates the signal in neighboring cells ($\mathscr{R}_{s_i,z_k} = \frac{\partial}{\partial z_k}\frac{\mathrm{d}s_i}{\mathrm{d}t}\Big|_{s_0,d_0,z_0} > 0$) for $\epsilon > (r_d d_0)/(r_d d_0 + 1)$.

(B) Jag1 effectively inhibits the signal in adjacent cells ($\mathscr{R}_{s_i,z_k} < 0$) for $\epsilon < (r_d d_0)/(r_d d_0 + 1)$.

According to (A), Jag1 always activates the signal in neighboring cells (provided that $\epsilon > 0$) when Dl1 is absent (*i.e.* for $r_d = 0$). According to (B), Jag1 must signal less than Dl1 (*i.e.* $\epsilon < 1$) for effective inhibition to happen in the presence of Dl1. If condition (B) holds, then Jag1 is effectively performing lateral inhibition, by inhibiting the signal in neighboring cells.

If Dl1 is absent (prosensory state, point I in Fig. 6.6 (C)), Notch signal operates in a lateral induction mode. However, if Jag1 is absent in the presence of Dl1 (point m in Fig. 6.6 (C)), lateral inhibition patterning can not occur. Therefore, under such conditions, Jag1 effectively facilitates lateral inhibition pattern formation. But how can Jag1 promote lateral inhibition if it drives lateral induction on its own? As with the cis/trans interactions mentioned above, the ratio of Jag1 to Dl1 -induced signaling rates (ϵ) becomes crucial. The results show that Jag1 can facilitate lateral inhibition patterning if it signals less than Dl1 (*i.e.* $\epsilon < 1$). In this case, Jag1 effectively inhibits signal production by sequestering the Notch receptor that otherwise would bind to Dl1 (see Fig. 6.8). As a result, in the presence of Dl1, Jag1 actually performs lateral inhibition and not lateral induction, promoting salt-and-pepper patterning (see Fig. 6.8 (C-F) and Sec. 6.4). In summary, the results from the model show that in the sensory organs of the inner ear, Dl1 requires stronger signaling rates when it binds to Notch to drive high enough levels of Notch signal to promote patterning, while Jag1 facilitates this patterning by driving lower levels of active Notch. In addition, weak Jag1 signaling has to be strong enough to drive lateral induction on its own.

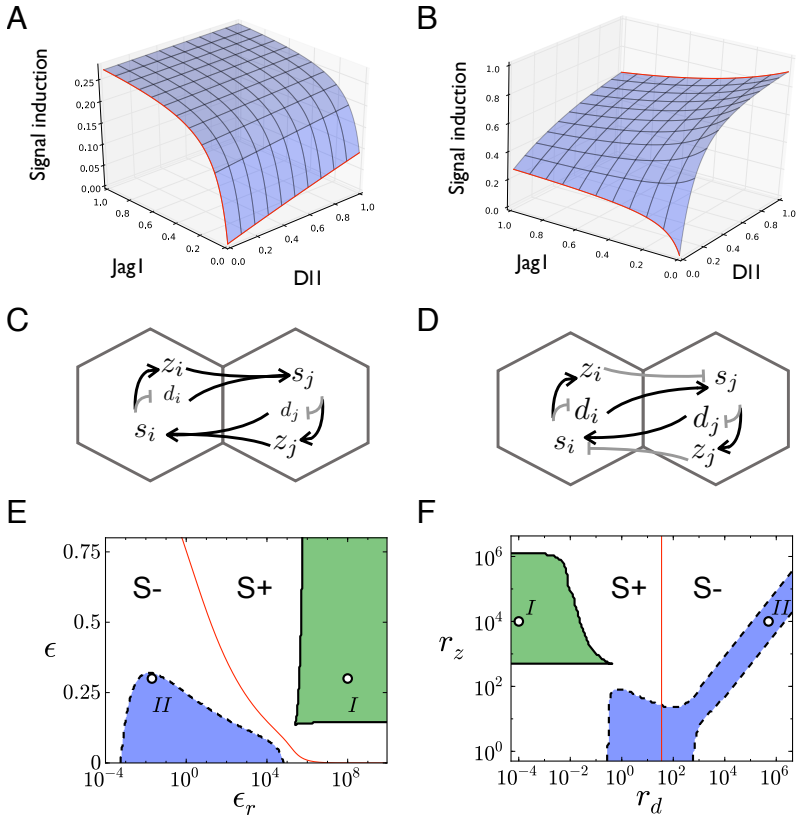

Figure 6.8: Jag1 switches from lateral induction to lateral inhibition when Dl1 arises. (A,B) Signal induction by each ligand as a function of ligand levels for $\epsilon = 0.3$. in a non-competitive (A) and competitive (B) regimes for $r_z = 10$. In (A), the Dl1 mediated interaction is weak ($r_d = 0.1$). Red lines emphasize that both ligands enhance signal production. In (B) Dl1 interaction is stronger ($r_d = 10$). Red lines denote that Jag1 can either enhance or deplete signal production, depending on Dl1 quantities. These scenarios lead to two effective network topologies (C,D), in which Jag1 either trans-activates (C) or trans-inhibits (D) the Notch signal. (E,F) Phase diagrams as in Fig. 6.6 (A) and 6.6 (C) with an additional thin red line indicating the switch in Jag1 behavior. Jag1 performs lateral inhibition at high r_d (S- regions), while lateral induction at low r_d (S+ regions).

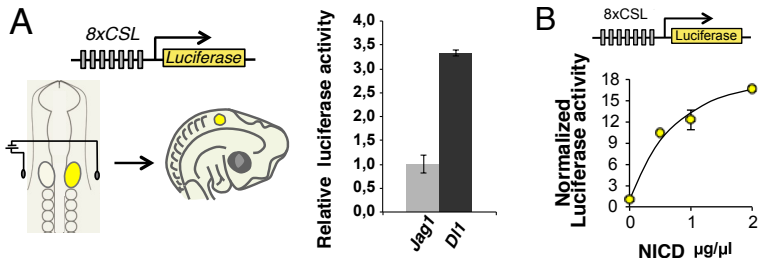

Figure 6.9: Jag1 and Dl1 induce different levels of Notch. (A) Left: Cartoon in which otic vesicles, which is a region of the inner ear, are co-electroporated with the 8xCSL-Luc Notch reporter construct and with Dl1 or Jag1. Right: bar diagram representing the relative levels of normalized Luciferase activity in the different experimental for Jag1 and Dl1 electroporation conditions. Values are mean ± SD of triplicate analysis of two representative experiments. (B) Quantification of the Luciferase activity at different NICD concentrations. We will use these points for calibrating the Luciferase. The solid line is a guide to the eye.

6.3.4 Experimental results confirms a lower signaling rate of Jag1 with respect to Dl1

In this section we present some experimental results performed by our collaborators, the group of Prof. Fernando Giraldez (UPF-PRBB, Barcelona, Spain), in order to quantify the signaling rate of Jag1 and Dl1 when they trans-interact with the Notch receptor.

Electroporation experiments allow the overexpression of Jag1 and Dl1 at very high cellular concentrations in the cells of the otic vesicle, the region we study in the inner ear. Under this regime, one can hypothesize that the receptors are saturated due to the trans-interactions with the electroporated ligand. NICD elicited by the trans-interactions is quantified with a Luciferase Notch reporter 8xCSL-Luc that is co-electroporated with the corresponding ligand.

The data show that the signaling rate of Jag1 trans-interaction with Notch is lower than when the ligand trans-interacting with Notch is Dl1 (Fig. 6.9 (A)). These data, together with a calibration of the Luciferase reporter with respect of the NICD concentration (Fig. 6.9 (B)) allow a first estimation of ϵ.

According to Fig. 6.9 (B) we suppose the Luciferase Notch reporter output

depends in a Michaelis-Menten form with respect to NICD concentration, so if the dimensional Luciferase and NICD concentrations in every cell are variables Y_i and S_i respectively, we have

$$Y_i = \frac{CS_i}{\theta + S_i} \quad , \tag{6.8}$$

being C and θ the saturation and activation threshold levels. According to Eq. 6.1a, the steady state for the NICD concentration can be written as

$$S = sS_0 = S_0 \frac{K_d\langle D_i\rangle + \epsilon K_z\langle Z_i\rangle}{1 + K_d\langle D_i\rangle + K_z\langle Z_i\rangle} \quad . \tag{6.9}$$

where K_x is the trans-affinity of the x-ligand with the receptor, and D and Z are the dimensional variables for Dl1 and Jag1. In a Jag1 electroporation experiment we set every cell with Jag1 electroporated concentration Z_{EP} so that $1 + K_d\langle D_i\rangle << K_z\langle Z_{EP}\rangle$. Then, by using Eq. 6.9 we obtain that electroporated Jag1 elicits ϵS_0 signal. By following a similar argument we obtain that Dl1 electroporation elicits a signal S_0.

Applying it to Eq. 6.9 we find that ϵ is

$$\epsilon = \frac{Y_Z}{Y_D}\frac{C - Y_D}{C - Y_Z} \quad , \tag{6.10}$$

where Y_Z and Y_D are the Luciferase levels in Jag1 and Dl1 electroporation experiments, respectively. By using the data presented in Fig. 6.9 and the above equation, we obtain that $\epsilon \approx 0.285$.

6.4 Discussion

Our model predicts the opposed expression pattern of Jag1 and Dl1 in the sensory organs [206] can be expected when Notch inhibits Dl1 but activates Jag1. When modeled, this situation shows that Jag1 on its own can drive bistability of homogeneous coherent states and mimic local transient overexpression of Jag1 [57]. Interestingly, if Dl1 is expressed in this Jag1-mediated lateral induction background, differences in ligand-driven signaling rates become crucial for the final pattern. Our study shows that the transition from lateral induction to lateral inhibition, as it occurs during inner ear development, requires Jag1 signaling rate to be weaker than Dl1 [204]. Reporter experiments have confirmed that this is the case in the otic vesicle, giving a signaling rates ratio $\epsilon \approx 0.3$ [204].

This situation is reminiscent to what has recently found in the context of angiogenesis by Benedito *et al.* [64]. In that context it was found that Jag1 elicited a weaker signal than the other ligand participating in the process, Dll4.

Our model also yields a non-trivial behavior in which Jag1 actually facilitates lateral inhibition patterning [204]. It predicts that the salt-and-pepper pattern is disrupted if Jag1 is removed or overexpressed in the hair cell determination state, and that Dl1 is not sufficient to drive pattern formation in the inner ear, as suggested by Chrysostomou et al. (2012) [207]. This role of Jag1 results from the competition between strong signaling ligands and weak signaling ligands when they interact with Notch. When Jag1 signals less than Dl1, Jag1 may act as a dominant negative or a partial agonist [208]. Benedito *et al.* proposed a similar competitive effect between Jag1 and Dll4 during angiogenesis [64]. This situation also resembles the one we presented above when cis-inhibition occurs in Notch signaling (Sec. 5). In the context of inner ear development cis-inhibition does not occur [207]. However, the competition between Dl1 and Jag1 ligands results in a switch of Jag1 performance from lateral induction to lateral inhibition in the presence of Dl1 (Fig. 6.8). Cells then interact through two (coupled) lateral inhibitions, one mediated by Dl1 and an additional one mediated by Jag1. This additional mode mediated by Jag1 consists in a new topology for lateral inhibition (see Fig. 6.8 (C)). While the Dl1 circuit yields a trans-activation of Notch signal followed by an inhibition of the ligand, the Jag1 circuit consists of an effective trans-inhibition, followed by an activation of the ligand. This new circuitry enables a new type of salt-and-pepper lateral inhibition pattern in which cells choose between two exclusive states: one with low levels of both signal and Jag1 and the other one with high levels of both signal and Jag1.

The inhibition of Dl1 by Notch has been associated to the repressor effect of Hes/Hey genes on bHLH proneural genes, which in turn drive Dl1 expression [77]. The regulation of Jag1 is less well understood. Besides Notch, other signals like Wnt are able to modulate Jag1 expression. How the activation of Hes and Hey factors, which are transcriptional repressors, may activate Jag1 is an open question. We are currently working in different scenarios in which competition between different factors could drive Jag1 upregulation due to Notch activation.

Lateral induction can be also achieved through a different circuit architecture (see Fig. 6.10). For instance, in a model with two ligands inhibited by Notch,

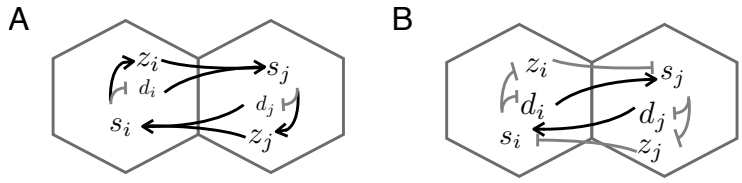

Figure 6.10: Lateral induction can be achieved by different circuit topologies. Two scenarios lead to two a positive feedback loop where lateral induction takes place (A) In the model presented in this section, in which Dl1 is inhibited but Jag1 activated, low Dl1 levels enables lateral induction through a double activation (see Fig. 6.10 (A)). (B) In the model where the two ligands are inhibited by Notch though, high Dl1 levels enable lateral induction through a double inhibition. Note that herein Jag1 has a competitive effect (see Fig. 6.10 (B)).

it is possible to obtain an effective intercellular mutual activatory circuit. This can be obtained once more through a competitive effect between the two ligands binding with the receptor in which Jag1 effectively inhibits the Notch signal in the neighboring cell (Fig. 6.10 (B)). Indeed, it can be shown that such scenario generates homogenous bistability, enabling a wave of ligand propagation (data not shown). However, competition arises only when Delta is present and we discarded this scenario in this study because it is well established that Delta is not expressed at the prosensory stage.

Chapter 7

Conclusions

This Thesis has focused on pattern formation through lateral inhibition mediated by the Notch signaling pathway. We have used a modeling approach based on the model presented by Collier and colleagues [10] to evaluate the effects of different elements on patterning.

In Sec. 7.1 we summarize the original results presented in this Thesis. Then, in Sec. 7.2 we discuss about new perspectives that arise from our results. Finally, we provide a list of our publications, preprints and manuscripts in preparation.

7.1 Summary of original results

First, we start providing the methodological contributions that we have in this Thesis (Sec. 7.1.1). Afterwards, we summarize the presented original scientific results (Secs. 7.1.2-7.1.5). All of them are motivated by experimental evidences and address the effect that different regulatory circuit elements have on patterning.

7.1.1 Methodological contributions

In this Thesis we have used some standard and new methodological tools applied to our models. Herein we present our most important methodological contributions and some of their implications.

In Chap. 2 we proposed a new method that provided the exact solutions of pattern states in discrete cellular lattices **[I,II,IV,V]**. By using this method we found that lateral inhibition patterning in hexagonal lattices occurred in a wider region of the parameter space than what was predicted by linear stability analysis (LSA). This extra region exhibited bistability, so two spatially extended solutions were both linearly stable: the homogeneous state and at least the pattern solution corresponding to the lateral inhibition pattern. In different occasions we showed that, in such bistable region in which the homogeneous state was linearly stable, it was still possible to unstabilize the homogeneous state in different ways, leading to patterning (see for instance Sec. 2.10.2). This new methodology has enabled us a systematic and effective search in the parameter space of bistable regions, and has facilitated the obtention of different bifurcation diagrams. We applied this methodology in Chaps. 3-5 and we found that our different models also presented the aforementioned bistable regions. These bistable regions were important for a better understanding of the pattern formation capabilities of our systems.

Thanks to the knowledge of the exact pattern solutions, we could provide theoretical estimations of an order parameter (see for instance Sec. 5.3.6) or the structure function in periodic patterns (App. B). This has facilitated different tasks when we performed the numerical simulations **[I,V,VII]**. The evaluation of a theoretical order parameter in a patterned situation was used for instance to determine whether the achieved pattern had imperfections **[I]**.

This methodology enabled the search of different exact periodic pattern solutions. This was specially useful in Chap. 5.

In Chap. 2 we have developed a technique for studying the stability of different pattern solutions. In this methodology we used LSA over pattern solutions. The evaluation of pattern solutions is not so standard in the framework of spatially extended discrete systems. Our methodology has facilitated this study. Our method has helped us to provide the stability regions of different patterns (Sec. 2.10 and App. C) revealing results like a coexistence region where different stable patterns could be found (see App. C,**[V,VII]**).

In different occasions we had to deal with effective single and multiple-root finding algorithms, and numerical integration of the model dynamics across the parameter space. For doing that efficiently, we made our own custom-made software. Our software enabled us to perform extensive searches in the parameter

space along different orders of magnitude for different parameters. We applied our numerical integration for deterministic and stochastic dynamics in regular hexagonal and more irregular bidimensional cellular lattices.

7.1.2 Progression of differentiation wavefronts

Chap. 3 focused on pattern propagation and its interplay with the state of the invaded tissue. In particular, we focused on neurogenesis in the embryonic vertebrate retina. In this case, patterning occurred as a single circular growing differentiation wavefront in which the capability of the tissue for lateral inhibition dynamics was established progressively, leaving on its wake the fine-grained pattern.

We proposed a model for self-regulated pattern propagation, which robustly exhibited single growing pattern domains **[II]**. Two different tissue domains were established. An inner growing domain in which lateral inhibition and patterning occurred, and an outer domain, the invaded tissue, which initially had no lateral inhibition dynamics. A morphogen could turn it into a neurogenic tissue that would start having lateral inhibition dynamics. This morphogen was secreted from the inner domain, specifically by the cells that had differentiated within the inner domain. This wavefront was self-regulated since (i) neurogenic differentiation released a morphogen and (ii) such morphogen invaded non-neurogenic tissue and turned it into competent for lateral inhibition dynamics.

Experimental evidences motivated the study of what happened if the invaded tissue had no inhibition capabilities to the differentiating neurogenic tissue, *i.e.* if there was no ligand in the invaded tissue inhibiting differentiation at the neurogenic wavefront. We performed a systematic exploration of the parameter space through numerical simulations. Our results showed that the properties (pattern formed, shape and velocity) of progressing fronts of lateral inhibition, in our case neuronal differentiation, depended crucially on the presence of ligand ahead of the differentiation front. In particular, such ligand expression made more robust the normal salt-and-pepper pattern in the parameter space (*e.g.* preventing neural overproduction at low trans-interactions strengths), it impeded the morphological instability of the wavefront, and slowed down wavefront progression into the invaded tissue. These results could be used to explain previous

observations in mouse embryonic retina, being in agreement with different experimental evidences [153]. We found similar results in a planar growing wavefront that would mimic morphogenetic furrow progression in embryonic *Drosophila* eye [148]. Hence, our results point to a mechanism for neurogenic front regulation **[II,III]**, and to a new design principle of a more general developmental mechanism.

7.1.3 Pattern formation capabilities of a diffusible ligand that activates Notch signal

In Chap. 4 we have analyzed the effect of a ligand that is able to diffuse in the extracellular space and activates Notch. Through LSA we found that such diffusible ligand combined with its own downregulation by Notch signal was not able to generate patterns.

We proposed a second model in which a diffusible ligand that activates Notch was combined with the classical lateral inhibition circuit. Our analytical and numerical tools helped us to unravel the pattern formation capabilities of this new system. We found that the diffusible ligand softened the patterns, and ultimately destroyed patterning (*e.g.* for high diffusion rates). Our results also showed that ligand diffusion could also have a constructive effect on patterning: intermediate diffusion rates for the ligand could suppress pattern imperfections that normally arise when patterning is just mediated by trans-interactions. This effect was even more visible in small systems. All these results can be found in **[I]**.

7.1.4 Cis-interactions in lateral inhibition patterning and single-cell dynamics

In Chap. 5 we have examined the effect of signal-productive cis-interactions in combination with another signaling source in two different situations: (i) in a multicellular scenario, where the other signaling source would be provided by the trans-interactions, and (ii) in a single-cell scenario in which a basal ligand-independent signaling source would be provided. We proposed a simple Collier-like model that captured both multicellular and single-cell scenarios with this

new phenomenology. We used our analytical and numerical tools to study it.

In both situations, we predicted that cis-interactions could lead to cis-inhibition — *i.e.* an effective depletion of the signal production rate — at weak cis-signaling rates when acting together with a stronger signaling source, *e.g.* trans-interactions or with a ligand-independent signaling source. This is a case in which the molecular mechanism does not determine the emerging dynamical behavior, but the interplay of different components of the network is important to unveil it [208]**[V]** . We found that such counterintuitive phenomenon was due to the existence of a competitive effect. This competition between the signaling sources arose because the two signaling sources required the same kind of receptor to signal, and because there was a difference of signaling rates between the cis-signaling source and the other source.

Our work also showed that cis-inhibition in the single-cell system together with a basal signal production could drive bistability.

In the multicellular case, we observed that by increasing the amount of cis-interactions in the cis-inhibition scenario the proportion of high-Delta fated cells in a tissue gradually increased. We justified this effect with an analytical proof by showing that cells undergoing cis-inhibition were worse receivers, what disrupts the lateral inhibition effect. This was a nonlinear effect, since LSA over the homogeneous state predicted that cis-interactions in both cis-inhibition and cis-activation scenarios would not change the pattern characteristic wavelength. With the help of simulations and analytical work we found that cis-inhibition promoted multistability, and therefore other regular stable patterns could be formed when cis-inhibition was considered. Also, in the parameter region where the intracellular positive feedback was able to induce cell-autonomous bistability, we observed the effect of pattern localization for the multicellular system. In such region, the emerging patterns were more sensible to the initial precursor state, what was consistent with a high performance of the intracellular positive feedback loop there.

We have also shown that some key results we found in our more phenomenological model were also present in a more realistic model.

These original results can be found in **[V]**.

7.1.5 Pattern formation in the chick inner ear with two different ligands acting in opposite modes

We studied the case of hair cell differentiation in the chick inner ear. In this context, Notch pathway operated in two opposite modes: lateral induction and lateral inhibition. Both situations occurred during vertebrate inner ear development where the former was characteristic of the prosensory patches and the latter of neurogenesis and hair cell determination [18].

In Chap. 6 we addressed the question of how the system transits from a lateral induction regime to a lateral inhibition regime. Experimental evidences point that first, in the prosensory stage, Jag1 ligand (Jagged1) acts in lateral induction mode and afterwards, in the hair cell determination stage, Dl1 (Delta1) expression in the tissue drives the system into a lateral inhibition operating mode. For modeling this situation we proposed a model of two ligands, Jag1 and Dl1, in which we imposed that, when they were acting on its own, Jag1 performed lateral induction and Dl1 performed lateral inhibition. When acting together, this regulatory circuitry could lead to the wild-type pattern. We predicted that relative signaling rates (or strengths) by Jag1 and Dl1 were critical for the transit of operating modes. On one side, a minimal signaling amount due to Jag1 was necessary for generating a traveling wave of ligand propagation (lateral induction regime). On the other side, too high signaling rates due to Jag1 with respect to Dl1 would not enable lateral inhibition patterning at the cell determination stage. The prediction of different signaling rates by Jag1 and Dl1 has been corroborated experimentally by our collaborators, the group of Prof. Fernando Giraldez (UPF-PRBB, Barcelona).

We also predicted that in the hair cell determination stage, competition between Dl1 and Jag1 ligands arose because (i) the two ligands wanted to bind to the same kind of receptor Notch and (ii) Jag1 signaling rate was lower that Dl1 signaling rate when bound to Notch. This competition makes that an increase of Jag1 in a cell drives additional Jag1 trans-interactions with Notch receptors in neighboring cells that otherwise would bind to Dl1, and this effectively depletes the amount of signal in neighboring cells. For this reason, Jag1 is effectively introducing an intercellular mutual inhibitory feedback loop, contributing to lateral inhibition.

Last, we predicted that Jag1 loss of function mutants at the cell determination stage would destroy the pattern.

These original results could be obtained through analytical and numerical analysis and can be found in **[IV]**.

Our predictions are currently being tested experimentally by the group of Prof. Fernando Giraldez (UPF-PRBB, Barcelona, Spain).

7.2 Perspectives

The results presented in this Thesis have opened a series of new questions. We have started investigating some of them. Herein we briefly summarize some of these open fronts.

The precise factor triggering the front instability when there is no ligand ahead of neurogenic wavefronts remains elusive. In Chap. 3 we proposed the existence of anomalous front progression as a possible mechanism to trigger this phenomenon. The study and proper quantification of this anomalous front progression across the parameter space will give new insights for understanding this instability. Also, the instability in planar growing fronts could behave differently, so it will require a more systematic characterization.

It is known that diffusible ligands and other diffusing molecules can bind to the Notch receptor, resulting into Notch signaling or a blockage of the Notch receptor [117]. From our results in cis-interactions, it would also be very instructive to study what happens if we consider a relative signaling rate ϵ of the diffusible species when it binds to the receptor with respect to the signaling rate due to trans-interactions. Probably, at weak or null signaling rates new interesting effects will appear, since it will create a local positive feedback loop acting together with the diffusible transport and the positive intercellular loop due to lateral inhibition.

We have seen that low cis-signaling rates could lead to effective cis-inhibition phenomenology. It would be interesting to study in more detail which is the effect of having cis-signaling ability in this cis-inhibitory regime.

The cell-autonomous switch due to cis-inhibition with a basal Notch signaling source provides a new mechanism for cellular fate choice. Finding out the cell-autonomous bistable switch in real cells could reveal other unknown functions of

the Notch pathway. Also, further theoretical work is required to fully understand the effect of such bistable switch in lateral inhibition patterning. It would be interesting to study such bistable switch in combination with other elements of the Notch pathway; for instance, what would happen if the basal Notch signal required for the bistable switch is provided by diffusible ligands that activate Notch.

Cis-inhibition leads to the existence of new regular patterns, as the formation of stripes. This poses the theoretical question of how regular patterns are selected in a case of multistability. Spatiotemporal signals might be a way to control it **[VII]**.

The way in which Jag1 is activated by Notch still remains elusive. Recent data on Notch targets in the context of the chick inner ear could help to unveil this puzzle **[IV]**. Different scenarios of competition between different downstream Notch targets could be a mechanism to achieve it.

In Chaps. 5 and 6 we have seen two cases in which competition of two signaling sources with different signaling rates sharing the same substrate can change the effective roles of its components 7.1. This could be a generic mechanism of competition in gene regulatory networks. It would be interesting to test these effects experimentally. Also, there are very different situations in the Notch signaling pathway in which this basic ingredients for competition could lead to different effective behaviors. For instance, competition could arise in other situations in which more than one ligand is acting together, or when different non-canonical molecules act cell-autonomously or non-cell autonomously as alternative signaling sources together with the canonical Notch signaling pathway [117]. Competition effects could be a way to explain the well-known context-dependent effects observed in the Notch signaling pathway, in which the same regulatory element exhibits antagonistic roles in different situations.

Our competition effects did not rely on receptor saturation. Further theoretical work will have to be done to better understand this phenomenon. One open question is to study our proposed competition in a more dynamic framework, *i.e.* , to study how our competence effects can be dynamically reflected.

Also, more generally, it would be interesting to theoretically study which competitive phenomena can occur in small genetic circuits at both transcriptional and post-transcriptional levels. The design of simple competing elements

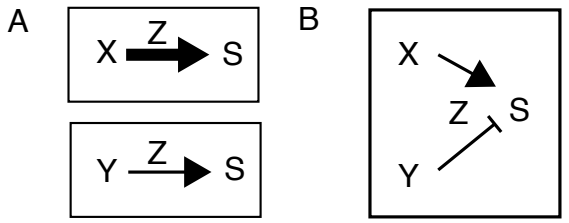

Figure 7.1: A possible generic mechanism for competition in a genetic regulatory network. X and Y are two different signaling sources that by means of a mediator Z elicit a signal S with different rates acting (A) separately or (B) together. Competition can arise if X and Y share a substrate Z (in our case the receptor). For instance, X represents the ligand concentration that will be used for trans-interactions, and Y represents the ligand concentration that will be used for cis-interactions. Alternatively X could represent the Delta ligand concentration that will trans-activate Notch in the neighboring cell, and Y could be the Jag1 ligand concentration that would trans-activate Notch. In the first case, when cis-interactions elicit a weak Notch signal with respect to trans-interactions, they can have a cis-inhibitory effect. In the second case, if Jag1 elicits a weaker Notch signal when it trans-activates Notch with respect to Delta-mediated trans-interactions, then Jag1 can effectively be performing trans-inhibition. The identification and characterization of such competition motif in the Notch signaling pathway could help to unveil context-dependent phenomena.

could provide new ways to obtain multifunctional regulatory genetic circuits with a reduced number of elements that could be used for instance in Synthetic Biology. Also, the effect of competition could help to solve other paradoxical effects observed in different genetic circuits.

Our phenomenological models can not be obtained from rigorous adiabatic reductions of more chemical-based models. Therefore, some dynamical aspects could be missing in our approach. It would be instructive to better understand more realistic models to determine the limitations of our phenomenological modeling approach. We expect that these models will have qualitative similar results at the steady state, but they will present a richer dynamics in some regimes.

The methodology developed for the computation of exact pattern solutions and the LSA applied to these solutions could be used for evaluating other short wavelength patterning phenomena in completely different contexts, like for in-

stance in the study of stomata and trichome development in plants [15].

There is a great list of additional interesting phenomena to study in the Notch signaling pathway. To mention one of them, the effect of cell cycle has been reported to affect cellular neurogenic potential, and therefore, the capacity to participate in a lateral inhibition process **[III]**. It would be interesting to study in more detail how this affects cellular patterning.

7.3 List of publications

I. Pau Formosa-Jordan and Marta Ibañes (2009) Diffusible ligand and lateral inhibition dynamics for pattern formation. J. Stat. Mech. P03019

II. Pau Formosa-Jordan, Marta Ibañes, Saúl Ares, and José María Frade (2012) Regulation of neuronal differentiation at the neurogenic wavefront. Development, 139, 2321-2329 doi:10.1242/dev.076406

III. Pau Formosa-Jordan, Marta Ibañes, Saúl Ares, and José María Frade. Lateral inhibition and neurogenesis: novel aspects in motion. The International Journal of Developmental Biology, in press.

IV. Jelena Petrovic *, Pau Formosa-Jordan*, Juan Camilo Luna, Marta Ibañes, Joana Neves and Fernando Giraldez. Lateral induction and lateral inhibition depend on Notch signal strength in the developing inner ear (Manuscript under revision in Development)

V. Pau Formosa-Jordan and Marta Ibañes. Competition in Notch signaling dynamics with cis enriches cellular decision making (Preprint)

VI. Pau Formosa-Jordan*, Norma Fàbregas*, Ana Confraria*, Ana I. Caño-Delgado and Marta Ibañes. Auxin influx carriers control vascular differentiation in *Arabidopsis* (In preparation)

VII. David Palau, Pau Formosa-Jordan, José María Sancho and Marta Ibañes. Dynamical selection of coexisting patterns (In preparation)

*Equal contributors

References

[1] Gilbert S (2006) Developmental Biology. Sunderland: Sinauer Associates.

[2] Alberts B, Johnson A, Lewis J, Raff M, Roberts K, et al. (2008) Molecular biology of the cell. New York: Garland Science.

[3] Murray J (2002) Mathematical biology. New York: Springer.

[4] Cross M, Hohenberg P (1993) Pattern formation outside of equilibrium. Rev Mod Phys 65: 851–1112.

[5] Cross M, Greenside H (2009) Pattern formation and dynamics in nonequilibrium systems. Cambridge University Press New York.

[6] Strogatz S (2000) Nonlinear dynamics and chaos : with applications to physics, biology, chemistry, and engineering. Cambridge, MA: Westview Press.

[7] García-Ojalvo J, Sancho JM (1999) Noise in spatially extended systems. New York: Springer.

[8] Morelli LG, Uriu K, Ares S, Oates AC (2012) Computational approaches to developmental patterning. Science 336: 187–91.

[9] Alon U (2007) An Introduction to Systems Biology: Design Principles of Biological Circuits. Chapman &Hall/CRS Mathematical and Computational Biology Series. Chapman & Hall. URL `http://books.google.es/books?id=pAUdPQlCZ54C`.

[10] Collier JR, Monk NA, Maini PK, Lewis JH (1996) J Theor Biol 183: 429–46.

[11] Davidson EH (2010) Emerging properties of animal gene regulatory networks. Nature 468: 911–20.

[12] Salazar-Ciudad I, Jernvall J, Newman SA (2003) Mechanisms of pattern formation in development and evolution. Development 130: 2027–37.

[13] Reinhardt D, Pesce ER, Stieger P, Mandel T, Baltensperger K, et al. (2003) Regulation of phyllotaxis by polar auxin transport. Nature 426: 255–60.

[14] Oates A, Morelli L, Ares S (2012) Patterning embryos with oscillations: structure, function and dynamics of the vertebrate segmentation clock. Development 139: 625–639.

[15] Torii KU (2012) Two-dimensional spatial patterning in developmental systems. Trends Cell Biol 22: 438–46.

[16] Sugano SS, Shimada T, Imai Y, Okawa K, Tamai A, et al. (2010) Stomagen positively regulates stomatal density in arabidopsis. Nature 463: 241–4.

[17] Frankfort BJ, Mardon G (2002) R8 development in the drosophila eye: a paradigm for neural selection and differentiation. Development 129: 1295–306.

[18] Neves J, Abelló G, Petrovic J, Giraldez F (2012) Patterning and cell fate in the inner ear: a case for notch in the chicken embryo. Dev Growth Differ .

[19] Crowe R, Henrique D, Ish-Horowicz D, Niswander L (1998) A new role for notch and delta in cell fate decisions: patterning the feather array. Development 125: 767–75.

[20] Goodyear R, Richardson G (1997) Pattern formation in the basilar papilla: evidence for cell rearrangement. J Neurosci 17: 6289.

[21] Hudspeth A (2008) Making an effort to listen: mechanical amplification in the ear. Neuron 59: 530–545.

[22] Waddington C (1940) Organisers & genes. Cambridge biological studies. The University Press.

[23] Waddington C (1957) The strategy of the genes: a discussion of some aspects of theoretical biology. Allen & Unwin. URL http://books.google.com/books?id=PdU9AAAAIAAJ.

[24] Ferrell JE (2012) Bistability, bifurcations, and waddington's epigenetic landscape. Curr Biol 22: R458–66.

[25] Turing A (1952) The chemical basis of morphogenesis. B Math Biol 52: 153–197.

[26] Gierer A, Meinhardt H (1972) A theory of biological pattern formation. Biol Cybern 12: 30–39.

[27] Meinhardt H (1982) Models of biological pattern formation. Academic Press. URL http://books.google.es/books?id=sLMTAQAAIAAJ.

[28] Kauffman SA (1969) Metabolic stability and epigenesis in randomly constructed genetic nets. J Theor Biol 22: 437–67.

[29] Kauffman S (1969) Homeostasis and differentiation in random genetic control networks. Nature 224: 177–8.

[30] Milo R, Shen-Orr S, Itzkovitz S, Kashtan N, Chklovskii D, et al. (2002) Network motifs: simple building blocks of complex networks. Sci Signal 298: 824.

[31] Alon U (2007) Network motifs: theory and experimental approaches. Nat Rev Genet 8: 450–61.

[32] Tyson J, Chen K, Novak B (2003) Sniffers, buzzers, toggles and blinkers: dynamics of regulatory and signaling pathways in the cell. Curr Opin Cell Biol 15: 221–231.

[33] Nakamasu A, Takahashi G, Kanbe A, Kondo S (2009) Interactions between zebrafish pigment cells responsible for the generation of turing patterns. Proc Natl Acad Sci USA 106: 8429–34.

[34] Goehring NW, Trong PK, Bois JS, Chowdhury D, Nicola EM, et al. (2011) Polarization of par proteins by advective triggering of a pattern-forming system. Science 334: 1137–41.

[35] Economou AD, Ohazama A, Porntaveetus T, Sharpe PT, Kondo S, et al. (2012) Periodic stripe formation by a turing mechanism operating at growth zones in the mammalian palate. Nat Genet 44: 348–51.

[36] Sheth R, Marcon L, Bastida MF, Junco M, Quintana L, et al. (2012) Hox genes regulate digit patterning by controlling the wavelength of a turing-type mechanism. Science 338: 1476–80.

[37] Jönsson H, Heisler M, Shapiro B, Meyerowitz E, Mjolsness E (2006) An auxin-driven polarized transport model for phyllotaxis. P Natl Acad Sci USA 103: 1633.

[38] Smith RS, Guyomarc'h S, Mandel T, Reinhardt D, Kuhlemeier C, et al. (2006) A plausible model of phyllotaxis. Proc Natl Acad Sci USA 103: 1301–6.

[39] Ibañes M, Fàbregas N, Chory J, Caño-Delgado A (2009) Brassinosteroid signaling and auxin transport are required to establish the periodic pattern of arabidopsis shoot vascular bundles. P Natl Acad Sci USA 106: 13630.

[40] Fàbregas N, Ibañes M, Caño-Delgado A (2010) A systems biology approach to dissect the contribution of brassinosteroid and auxin hormones to vascular patterning in the shoot of arabidopsis thaliana. Plant signal behav 5: 903.

[41] Howard J, Grill SW, Bois JS (2011) Turing's next steps: the mechanochemical basis of morphogenesis. Nat Rev Mol Cell Biol 12: 392–8.

[42] Salazar-Ciudad I, Jernvall J (2010) A computational model of teeth and the developmental origins of morphological variation. Nature 464: 583–586.

[43] Heisler MG, Hamant O, Krupinski P, Uyttewaal M, Ohno C, et al. (2010) Alignment between pin1 polarity and microtubule orientation in the shoot apical meristem reveals a tight coupling between morphogenesis and auxin transport. Plos Biol 8: e1000516.

[44] Sprinzak D, Elowitz MB (2005) Reconstruction of genetic circuits. Nature 438: 443–8.

[45] Lim WA, Lee CM, Tang C (2013) Design principles of regulatory networks: searching for the molecular algorithms of the cell. Mol Cell 49: 202–12.

[46] Elowitz MB, Leibler S (2000) A synthetic oscillatory network of transcriptional regulators. Nature 403: 335–8.

[47] Sprinzak D, Lakhanpal A, Lebon L, Santat LA, Fontes ME, et al. (2010) Cis-interactions between notch and delta generate mutually exclusive signalling states. Nature 465: 86–90.

[48] Matsuda M, Koga M, Nishida E, Ebisuya M (2012) Synthetic signal propagation through direct cell-cell interaction. Sci Signal 5: ra31–ra31.

[49] Barad O, Rosin D, Hornstein E, Barkai N (2010) Error minimization in lateral inhibition circuits. Sci Signal 3: ra51–ra51.

[50] Formosa-Jordan P, Ibañes M, Ares S, Frade JM (in press) Lateral inhibition and neurogenesis: novel aspects in motion. Int J Dev Biol .

[51] Neumann C, Nuesslein-Volhard C (2000) Patterning of the zebrafish retina by a wave of sonic hedgehog activity. Science 289: 2137–2139.

[52] Frade J (2002) Interkinetic nuclear movement in the vertebrate neuroepithelium: encounters with an old acquaintance. Prog Brain Res 136: 67–72.

[53] Murciano A, Zamora J, Lopezsanchez J, Frade J (2002) Interkinetic nuclear movement may provide spatial clues to the regulation of neurogenesis. Mol Cell Neurosci 21: 285–300.

[54] Formosa-Jordan P, Ibañes M, Ares S, Frade JM (2012) Regulation of neuronal differentiation at the neurogenic wavefront. Development 139: 2321–9.

[55] Zine A, Water TRVD, de Ribaupierre F (2000) Notch signaling regulates the pattern of auditory hair cell differentiation in mammals. Development 127: 3373–83.

[56] Daudet N, Lewis J (2005) Two contrasting roles for notch activity in chick inner ear development: specification of prosensory patches and lateral inhibition of hair-cell differentiation. Development 132: 541.

[57] Neves J, Parada C, Chamizo M, Giraldez F (2011) Jagged 1 regulates the restriction of sox2 expression in the developing chicken inner ear: a mechanism for sensory organ specification. Development 138: 735–744.

[58] Chang W, Hwang P (2011) Development of zebrafish epidermis. Birth Defects Research Part C: Embryo Today: Reviews 93: 205–214.

[59] Crosnier C, Vargesson N, Gschmeissner S, Ariza-McNaughton L, Morrison A, et al. (2005) Delta-notch signalling controls commitment to a secretory fate in the zebrafish intestine. Development 132: 1093–104.

[60] Stamataki D, Holder M, Hodgetts C, Jeffery R, Nye E, et al. (2011) Delta1 expression, cell cycle exit, and commitment to a specific secretory fate coincide within a few hours in the mouse intestinal stem cell system. PLoS One 6: e24484.

[61] Hayward P, Kalmar T, Arias AM (2008) Wnt/notch signalling and information processing during development. Development 135: 411.

[62] Artavanis-Tsakonas S, Rand M, Lake R (1999) Notch signaling: cell fate control and signal integration in development. Science 284: 770.

[63] Guruharsha KG, Kankel MW, Artavanis-Tsakonas S (2012) The notch signalling system: recent insights into the complexity of a conserved pathway. Nat Rev Genet 13: 654–66.

[64] Benedito R, Roca C, Sörensen I, Adams S, Gossler A, et al. (2009) The notch ligands dll4 and jagged1 have opposing effects on angiogenesis. Cell 137: 1124–1135.

[65] Latasa MJ, Cisneros E, Frade JM (2009) Cell cycle control of notch signaling and the functional regionalization of the neuroepithelium during vertebrate neurogenesis. Int J Dev Biol 53: 895–908.

[66] Buceta J, Herranz H, Canela-Xandri O, Reigada R, Sagués F, et al. (2007) Robustness and stability of the gene regulatory network involved in dv boundary formation in the drosophila wing. PLoS One 2: e602.

[67] Domingo-Domenech J, Vidal S, Rodriguez-Bravo V, Castillo-Martin M, Quinn S, et al. (2012) Suppression of acquired docetaxel resistance in prostate cancer through depletion of notch-and hedgehog-dependent tumor-initiating cells. Cancer Cell 22: 373–388.

[68] Bridges C, Morgan T (1800) Sex-linked inheritance in Drosophila.

[69] Dexter J (1914) The analysis of a case of continuous variation in drosophila by a study of its linkage relations. Am Nat : 712–758.

[70] Morgan T (1917) The theory of the gene. Am Nat 51: 513–544.

[71] Poulson D (1937) Chromosomal deficiencies and the embryonic development of drosophila melanogaster. Proc Natl Acad Sci USA 23: 133.

[72] Fehon RG, Kooh PJ, Rebay I, Regan CL, Xu T, et al. (1990) Molecular interactions between the protein products of the neurogenic loci notch and delta, two egf-homologous genes in drosophila. Cell 61: 523–34.

[73] Bray SJ (2006) Notch signalling: a simple pathway becomes complex. Nat Rev Mol Cell Biol 7: 678–89.

[74] Kopan R, Ilagan MXG (2009) The canonical notch signaling pathway: unfolding the activation mechanism. Cell 137: 216–33.

[75] Fischer A, Gessler M (2007) Delta-notch–and then? protein interactions and proposed modes of repression by hes and hey bhlh factors. Nucleic Acids Res 35: 4583–96.

[76] Kageyama R, Ohtsuka T, Kobayashi T (2007) The hes gene family: repressors and oscillators that orchestrate embryogenesis. Development 134: 1243–51.

[77] Kageyama R, Ohtsuka T, Shimojo H, Imayoshi I (2009) Dynamic regulation of notch signaling in neural progenitor cells. Curr Opin Cell Biol 21: 733–40.

[78] Wang MM (2011) Notch signaling and notch signaling modifiers. Int J Biochem Cell B 43: 1550–62.

[79] Andersson ER, Sandberg R, Lendahl U (2011) Notch signaling: simplicity in design, versatility in function. Development 138: 3593–612.

[80] Schweisguth F (2004) Regulation of notch signaling activity. Curr Biol 14: R129–38.

[81] Fürthauer M, González-Gaitán M (2009) Endocytic regulation of notch signalling during development. Traffic 10: 792–802.

[82] Weinmaster G, Fischer JA (2011) Notch ligand ubiquitylation: what is it good for? Dev Cell 21: 134–44.

[83] Panin V, Papayannopoulos V, Wilson R, Irvine K (1997) Fringe modulates notch-ligand interactions. Nature 387: 908–912.

[84] Haines N, Irvine K (2003) Glycosylation regulates notch signalling. Nat Rev Mol Cell Biol 4: 786–797.

[85] Shimojo H, Ohtsuka T, Kageyama R (2008) Oscillations in notch signaling regulate maintenance of neural progenitors. Neuron 58: 52–64.

[86] Morelli LG, Ares S, Herrgen L, Schröter C, Jülicher F, et al. (2009) Delayed coupling theory of vertebrate segmentation. HFSP J 3: 55.

[87] Herrgen L, Ares S, Morelli LG, Schröter C, Jülicher F, et al. (2010) Intercellular coupling regulates the period of the segmentation clock. Curr Biol : 1–10.

[88] Schröter C, Ares S, Morelli LG, Isakova A, Hens K, et al. (2012) Topology and dynamics of the zebrafish segmentation clock core circuit. Plos Biol 10: e1001364.

[89] Wigglesworth V (1940) Local and general factors in the development of" pattern" in rhodnius prolixus (hemiptera). J Exp Biol 17: 180–201.

[90] Shaya O, Sprinzak D (2011) From notch signaling to fine-grained patterning: Modeling meets experiments. Curr Opin Genet Dev : 1–8.

[91] Schoute JC (1913) Beiträge zur blattstellunggslehre. Rec Trav Bot Néerland 10: 153-324.

[92] Thimann K (1937) On the nature of inhibitions caused by auxin. Am J Bot : 407–412.

[93] Lehmann R, Jiménez F, Dietrich U, Campos-Ortega J (1983) On the phenotype and development of mutants of early neurogenesis indrosophila melanogaster. Dev Genes Evol 192: 62–74.

[94] Simpson P, Carteret C (1990) Proneural clusters: equivalence groups in the epithelium of drosophila. Development 110: 927–32.

[95] Heitzler P, Simpson P (1991) The choice of cell fate in the epidermis of drosophila. Cell 64: 1083–1092.

[96] Reed R (2004) Evidence for notch-mediated lateral inhibition in organizing butterfly wing scales. Dev Genes Evol 214: 43–46.

[97] Lubensky DK, Pennington MW, Shraiman BI, Baker NE (2011) A dynamical model of ommatidial crystal formation. Proc Natl Acad Sci USA 108: 11145–50.

[98] Honda H, Tanemura M, Yoshida A (1990) Estimation of neuroblast numbers in insect neurogenesis using the lateral inhibition hypothesis of cell differentiation. Development 110: 1349–1352.

[99] Tanemura M, Honda H, Yoshida A (1991) Distribution of differentiated cells in a cell sheet under the lateral inhibition rule of differentiation. J Theor Biol 153: 287–300.

[100] Owen M, Sherratt J (1998) Mathematical modelling of juxtacrine cell signalling. Math Biosci 153: 125–150.

[101] Owen M (2000) Lateral induction by juxtacrine signaling is a new mechanism for pattern formation. Dev Biol 217: 54–61.

[102] Plahte E (2001) Pattern formation in discrete cell lattices. J Math Biol 43: 411–445.

[103] Wearing H, Sherratt J (2001) Nonlinear analysis of juxtacrine patterns. SIAM J Appl Math : 283–309.

[104] Owen MR (2002) Waves and propagation failure in discrete space models with nonlinear coupling and feedback. Physica D 173: 59.

[105] Meir E, von Dassow G, Munro E, Odell GM (2002) Robustness, flexibility, and the role of lateral inhibition in the neurogenic network. Curr Biol 12: 778–86.

[106] Webb SD, Owen MR (2004) Oscillations and patterns in spatially discrete models for developmental intercellular signalling. J Math Biol 48: 444–76.

[107] Webb S, Owen M (2004) Intra-membrane ligand diffusion and cell shape modulate juxtacrine patterning. J Theor Biol 230: 99–117.

[108] Veflingstad S, Plahte E, Monk N (2005) Effect of time delay on pattern formation: Competition between homogenisation and patterning. Physica D 207: 254–271.

[109] Plahte E, Øyehaug L (2007) Pattern-generating travelling waves in a discrete multicellular system with lateral inhibition. Physica D 226: 117–128.

[110] Rudge T, Burrage K (2008) Effects of intrinsic and extrinsic noise can accelerate juxtacrine pattern formation. B Math Biol 70: 971–991.

[111] O'Dea RD, King JR (2011) Multiscale analysis of pattern formation via intercellular signalling. Math Biosci 231: 172–85.

[112] O'Dea RD, King JR (2012) Continuum limits of pattern formation in hexagonal-cell monolayers. J Math Biol 64: 579–610.

[113] Momiji H, Monk NAM (2009) Oscillatory notch-pathway activity in a delay model of neuronal differentiation. Phys Rev E 80: 21930.

[114] Cohen M, Georgiou M, Stevenson NL, Miodownik M, Baum B (2010) Dynamic filopodia transmit intermittent delta-notch signaling to drive pattern refinement during lateral inhibition. Dev Cell 19: 78–89.

[115] Lewis J (2003) Autoinhibition with transcriptional delay a simple mechanism for the zebrafish somitogenesis oscillator. Curr Biol 13: 1398–1408.

[116] Qi H, Rand MD, Wu X, Sestan N, Wang W, et al. (1999) Processing of the notch ligand delta by the metalloprotease kuzbanian. Science 283: 91–4.

[117] D'Souza B, Meloty-Kapella L, Weinmaster G (2010) Notch Signaling. Chapter Three - Canonical and Non-Canonical Notch Ligands, volume 92 of *Curr Top Dev Biol*. Academic Press, 73 - 129 pp. doi:10.1016/S0070-2153(10)92003-6.

[118] Caolo V, Schulten H, Zhuang Z, Murakami M, Wagenaar A, et al. (2011) Soluble jagged-1 inhibits neointima formation by attenuating notch-herp2 signaling. Arterioscl Throm Vas : ATVBAHA. 110.217935 v1.

[119] Hoyos E, Kim K, Milloz J, Barkoulas M, Pénigault JB, et al. (2011) Quantitative variation in autocrine signaling and pathway crosstalk in the caenorhabditis vulval network. Curr Biol 21: 527–538.

[120] Camelo S, Raoul W, Lavalette S, Calippe B, Cristofaro B, et al. (2012) Delta-like 4 inhibits choroidal neovascularization despite opposing effects on vascular endothelium and macrophages. Angiogenesis : 1–14.

[121] Heitzler P, Simpson P (1993) Altered epidermal growth factor-like sequences provide evidence for a role of notch as a receptor in cell fate decisions. Development 117: 1113–23.

[122] Jacobsen TL, Brennan K, Arias AM, Muskavitch MA (1998) Cis-interactions between delta and notch modulate neurogenic signalling in drosophila. Development 125: 4531–40.

[123] Sakamoto K, Ohara O, Takagi M, Takeda S, Katsube K (2002) Intracellular cell-autonomous association of notch and its ligands: A novel mechanism of notch signal modification. Dev Biol 241: 313–326.

[124] Ladi E, Nichols JT, Ge W, Miyamoto A, Yao C, et al. (2005) The divergent dsl ligand dll3 does not activate notch signaling but cell autonomously attenuates signaling induced by other dsl ligands. J Cell Biol 170: 983–92.

[125] Glittenberg M, Pitsouli C, Garvey C, Delidakis C, Bray S (2006) Role of conserved intracellular motifs in serrate signalling, cis-inhibition and endocytosis. EMBO J 25: 4697–4706.

[126] Matsuda M, Chitnis AB (2008) Interaction with notch determines endocytosis of specific delta ligands in zebrafish neural tissue. Development 136: 197–206.

[127] Fiuza UM, Klein T, Arias AM, Hayward P (2010) Mechanisms of ligand-mediated inhibition in notch signaling activity in drosophila. Dev Dyn 239: 798–805.

[128] Miller AC, Lyons EL, Herman TG (2009) cis-inhibition of notch by endogenous delta biases the outcome of lateral inhibition. Curr Biol 19: 1378–83.

[129] Yamamoto S, Charng WL, Rana NA, Kakuda S, Jaiswal M, et al. (2012) A mutation in egf repeat-8 of notch discriminates between serrate/jagged and delta family ligands. Science 338: 1229–32.

[130] Sprinzak D, Lakhanpal A, Lebon L, Garcia-Ojalvo J, Elowitz MB (2011) Mutual inactivation of notch receptors and ligands facilitates developmental patterning. PLoS Comput Biol 7: e1002069.

[131] Podgorski G, Bansal M, Flann N (2007) Regular mosaic pattern development: A study of the interplay between lateral inhibition, apoptosis and differential adhesion. Theor Biol Med Model 4: 43.

[132] Gillespie D (2000) The chemical langevin equation. J Chem Phys 113: 297.

[133] Gardiner C (2004) Handbook of stochastic methods for physics, chemistry, and the natural sciences. Berlin New York: Springer-Verlag.

[134] Adalsteinsson D, McMillen D, Elston T (2004) Biochemical network stochastic simulator (bionets): software for stochastic modeling of biochemical networks. BMC bioinformatics 5: 24.

[135] Formosa-Jordan P, Ibañes M (2009) Diffusible ligand and lateral inhibition dynamics for pattern formation. J Stat Mech 03: 019.

[136] Press W, Vetterling W, Teukolsky S, Flannery B (1993) Numerical Recipes in FORTRAN; The Art of Scientific Computing. New York, NY, USA: Cambridge University Press, 2nd edition.

[137] Kashima K, Imura J (2010) Local stability analysis of heterogeneous equilibrium patterns observed in delta,Äênotch signalling interaction. J Chin Inst Eng 33: 347–355.

[138] Carrillo O, Ibanes M, Garcia-Ojalvo J, Casademunt J, Sancho J (2003) Intrinsic noise-induced phase transitions: Beyond the noise interpretation. Phys Rev E 67: 46110.

[139] Toral R, Chakrabarti A (1993) Generation of gaussian distributed random numbers by using a numerical inversion method. Comput Phys Commun 74: 327–334.

[140] Honda H (1978) Description of cellular patterns by dirichlet domains: The two-dimensional case. J Theor Biol 72: 523–543.

[141] Prada C, Puga J, Pérez-Méndez L, López R, Ramírez G (1991) Spatial and temporal patterns of neurogenesis in the chick retina. Eur J Neurosci 3: 559–569.

[142] Hu M, Easter SS (1999) Retinal neurogenesis: the formation of the initial central patch of postmitotic cells. Dev Biol 207: 309–21.

[143] Zhang X, Yang X (2001) Regulation of retinal ganglion cell production by sonic hedgehog. Development 128: 943–957.

[144] Stenkamp D, Frey R (2003) Extraretinal and retinal hedgehog signaling sequentially regulate retinal differentiation in zebrafish. Dev Biol 258: 349–363.

[145] Choy S, Cheng C, Lee S, Li V, Hui M, et al. (2010) A cascade of irx1a and irx2a controls shh expression during retinogenesis. Dev Dyn 239: 3204–3214.

[146] Wang Y, Dakubo G, Thurig S, Mazerolle C, Wallace V (2005) Retinal ganglion cell-derived sonic hedgehog locally controls proliferation and the timing of rgc development in the embryonic mouse retina. Development 132: 5103–5113.

[147] Dominguez M, Hafen E (1997) Hedgehog directly controls initiation and propagation of retinal differentiation in the drosophila eye. Gene Dev 11: 3254–3264.

[148] Brown N, Sattler C, Paddock S, Carroll S (1995) Hairy and emc negatively regulate morphogenetic furrow progression in the drosophila eye. Cell 80: 879–887.

[149] Greenwood S, Struhl G (1999) Progression of the morphogenetic furrow in the drosophila eye: the roles of hedgehog, decapentaplegic and the raf pathway. Development 126: 5795–808.

[150] Haddon C, Smithers L, Schneider-Maunoury S, Coche T, Henrique D, et al. (1998) Multiple delta genes and lateral inhibition in zebrafish primary neurogenesis. Development 125: 359.

[151] Kay JN, Link BA, Baier H (2005) Staggered cell-intrinsic timing of ath5 expression underlies the wave of ganglion cell neurogenesis in the zebrafish retina. Development 132: 2573–85.

[152] Nelson B, Reh T (2008) Relationship between delta-like and proneural bhlh genes during chick retinal development. Dev Dyn 237: 1565–1580.

[153] Rocha SF, Lopes SS, Gossler A, Henrique D (2009) Dll1 and dll4 function sequentially in the retina and pv2 domain of the spinal cord to regulate neurogenesis and create cell diversity. Dev Biol 328: 54–65.

[154] Yang HJ, Silva AO, Koyano-Nakagawa N, Mcloon SC (2009) Progenitor cell maturation in the developing vertebrate retina. Dev Dyn 238: 2823–36.

[155] Parks A, Huppert S, Muskavitch M (1997) The dynamics of neurogenic signalling underlying bristle development in drosophila melanogaster. Mech Develop 63: 61–74.

[156] Fehon R, Johansen K, Rebay I, Artavanis-Tsakonas S (1991) Complex cellular and subcellular regulation of notch expression during embryonic and imaginal development of drosophila: implications for notch function. J Cell Biol 113: 657.

[157] Kooh P, Fehon R, Muskavitch M (1993) Implications of dynamic patterns of delta and notch expression for cellular interactions during drosophila development. Development 117: 493.

[158] Baker NE, Zitron AE (1995) Drosophila eye development: Notch and delta amplify a neurogenic pattern conferred on the morphogenetic furrow by scabrous. Mech Develop 49: 173–89.

[159] Parks AL, Turner FR, Muskavitch MA (1995) Relationships between complex delta expression and the specification of retinal cell fates during drosophila eye development. Mech Develop 50: 201–16.

[160] Kunisch M, Haenlin M, Campos-Ortega JA (1994) Lateral inhibition mediated by the drosophila neurogenic gene delta is enhanced by proneural proteins. Proc Natl Acad Sci USA 91: 10139–43.

[161] Pennington MW, Lubensky DK (2010) Switch and template pattern formation in a discrete reaction-diffusion system inspired by the drosophila eye. Eur Phys J E Soft Matter 33: 129–48.

[162] Moloney D, Panin V, Johnston S, Chen J, Shao L, et al. (2000) Fringe is a glycosyltransferase that modifies notch. Nature 406: 369.

[163] Hamburger V, Hamilton HL (1992) A series of normal stages in the development of the chick embryo. 1951. Dev Dyn 195: 231–72.

[164] Xiang M, Zhou L, Macke JP, Yoshioka T, Hendry SH, et al. (1995) The brn-3 family of pou-domain factors: primary structure, binding specificity, and expression in subsets of retinal ganglion cells and somatosensory neurons. J Neurosci 15: 4762–85.

[165] Bellefroid E, Bourguignon C, Hollemann T, Ma Q, Anderson D, et al. (1996) X-myt1, a xenopus c2hc-type zinc finger protein with a regulatory function in neuronal differentiation. Cell 87: 1191–1202.

[166] Nelson BR, Gumuscu B, Hartman BH, Reh TA (2006) Notch activity is downregulated just prior to retinal ganglion cell differentiation. Dev Neurosci 28: 128–41.

[167] Hämmerle B, Ulin E, Guimera J, Becker W, Guillemot F, et al. (2011) Transient expression of mnb/dyrk1a couples cell cycle exit and differentiation of neuronal precursors by inducing p27kip1 expression and suppressing notch signaling. Development 138: 2543–54.

[168] Hufnagel RB, Le TT, Riesenberg AL, Brown NL (2010) Neurog2 controls the leading edge of neurogenesis in the mammalian retina. Dev Biol 340: 490–503.

[169] Martinez-Morales JR, Bene FD, Nica G, Hammerschmidt M, Bovolenta P, et al. (2005) Differentiation of the vertebrate retina is coordinated by an fgf signaling center. Dev Cell 8: 565–74.

[170] Sukumar N, Bolander J (2003) Numerical computation of discrete differential operators on non-uniform grids. Cmes-Comp Model Eng 4: 691–706.

[171] Russ J (2002) The Image Processing Handbook, Fourth Edition. Image Processing Handbook. Taylor & Francis. URL `http://books.google.es/books?id=OZVeoomxxhYC`.

[172] Baker NE, Yu SY (1997) Proneural function of neurogenic genes in the developing drosophila eye. Curr Biol 7: 122–32.

[173] Ligoxygakis P, Yu SY, Delidakis C, Baker NE (1998) A subset of notch functions during drosophila eye development require su(h) and the e(spl) gene complex. Development 125: 2893–900.

[174] Hicks C, Ladi E, Lindsell C, Hsieh JJD, Hayward SD, et al. (2002) A secreted delta1-fc fusion protein functions both as an activator and inhibitor of notch1 signaling. J Neurosci Res 68: 655–667.

[175] Mishra-Gorur K (2002) Down-regulation of delta by proteolytic processing. J Cell Biol 159: 313–324.

[176] Ibanes M, García-Ojalvo J, Toral R, Sancho J (2000) Dynamics and scaling of noise-induced domain growth. Eur Phys J B-Condensed Matter and Complex Systems 18: 663–673.

[177] Togashi H, Kominami K, Waseda M, Komura H, Miyoshi J, et al. (2011) Nectins establish a checkerboard-like cellular pattern in the auditory epithelium. Science 333: 1144–7.

[178] Choi W, Peifer M (2011) Cell biology. arranging a cellular checkerboard. Science 333: 1099–100.

[179] Cordle J, Johnson S, Tay JZY, Roversi P, Wilkin MB, et al. (2008) A conserved face of the jagged/serrate dsl domain is involved in notch trans-activation and cis-inhibition. Nat Struct Mol Biol 15: 849–857.

[180] Ghosh S, Paez-Cortez JR, Boppidi K, Vasconcelos M, Roy M, et al. (2011) Activation dynamics and signaling properties of notch3 receptor in the developing pulmonary artery. J Biol Chem 286: 22678–22687.

[181] Childress J, Acar M, Tao C, Halder G (2006) Lethal giant discs, a novel c2-domain protein, restricts notch activation during endocytosis. Curr Biol 16: 2228–2233.

[182] Wilkin M, Tongngok P, Gensch N, Clemence S, Motoki M, et al. (2008) Drosophila hops and ap-3 complex genes are required for a deltex-regulated activation of notch in the endosomal trafficking pathway. Dev Cell 15: 762–772.

[183] Coumailleau F, Fürthauer M, Knoblich JA, González-Gaitán M (2009) Directional delta and notch trafficking in sara endosomes during asymmetric cell division. Nature 458: 1051–1055.

[184] Fortini M, Bilder D (2009) Endocytic regulation of notch signaling. Curr Opin Genet Dev 19: 323–328.

[185] Fortini M (2009) Notch signaling: the core pathway and its posttranslational regulation. Dev Cell 16: 633–647.

[186] Cho B, Fischer JA (2011) Ral gtpase promotes asymmetric notch activation in the drosophila eye in response to frizzled/pcp signaling by repressing ligand-independent receptor activation. Development 138: 1349–59.

[187] Yamada K, Fuwa TJ, Ayukawa T, Tanaka T, Nakamura A, et al. (2011) Roles of drosophila deltex in notch receptor endocytic trafficking and activation. Genes Cells 16: 261–72.

[188] Mukherjee T, Kim WS, Mandal L, Banerjee U (2011) Interaction between notch and hif-alpha in development and survival of drosophila blood cells. Science 332: 1210–3.

[189] Hori K, Sen A, Kirchhausen T, Artavanis-Tsakonas S (2012) Regulation of ligand-independent notch signal through intracellular trafficking. Commun Integr Biol 5: 374–6.

[190] Hsu CP, Lee PH, Chang CW, Lee CT (2006) Constructing quantitative models from qualitative mutant phenotypes: preferences in selecting sensory organ precursors. Bioinformatics 22: 1375–82.

[191] Lakhanpal A, Sprinzak D, Elowitz MB (2010) Mutual inactivation of notch and delta permits a simple mechanism for lateral inhibition patterning. eprint arXiv 1005: 4301.

[192] Wang R, Liu K, Chen L, Aihara K (2011) Neural fate decisions mediated by trans-activation and cis-inhibition in notch signaling. Bioinformatics 27: 3158–3165.

[193] Formosa-Jordan P, Ibañes M (Preprint) Competition in notch signaling dynamics with cis enriches cellular decision making .

[194] Zhu B (2005) Mechanistic explanation for the unique pharmacologic properties of receptor partial agonists. Biomed Pharmacother 59: 76–89.

[195] Rouault H, Hakim V (2012) Different cell fates from cell-cell interactions: core architectures of two-cell bistable networks. Biophys J 102: 417–26.

[196] Held W, Mariuzza RA (2011) Cis-trans interactions of cell surface receptors: biological roles and structural basis. Cell Mol Life Sci 68: 3469–78.

[197] Nikolaou N, Watanabe-Asaka T, Gerety S, Distel M, Köster RW, et al. (2009) Lunatic fringe promotes the lateral inhibition of neurogenesis. Development 136: 2523–33.

[198] Shao L, Moloney DJ, Haltiwanger R (2003) Fringe modifies o-fucose on mouse notch1 at epidermal growth factor-like repeats within the ligand-binding site and the abruptex region. J Biol Chem 278: 7775–82.

[199] Cohen M, Baum B, Miodownik M (2011) The importance of structured noise in the generation of self-organizing tissue patterns through contact-mediated cell-cell signalling. J R Soc Interface 8: 787–98.

[200] Palau D, Formosa-Jordan P, Sancho J, Ibañes M (In preparation) Dynamical selection of coexisting patterns .

[201] Kladko K, Mitkov I, Bishop A (2000) Universal scaling of wave propagation failure in arrays of coupled nonlinear cells. Phys Rev Lett 84: 4505–4508.

[202] Falix FA, Aronson DC, Lamers WH, Gaemers IC (2012) Possible roles of dlk1 in the notch pathway during development and disease. Biochim Biophys Acta 1822: 988–95.

[203] Hartman BH, Reh TA, Bermingham-Mcdonogh O (2010) Notch signaling specifies prosensory domains via lateral induction in the developing mammalian inner ear. P Natl Acad Sci USA 107: 15792–15797.

[204] Petrovic J, Formosa-Jordan P, Luna JC, Ibañes M, Neves J, et al. (Manuscript under revision in Development) Lateral induction and lateral inhibition depend on notch signal strength in the developing inner ear .

[205] Daudet N, Ariza-McNaughton L, Lewis J (2007) Notch signalling is needed to maintain, but not to initiate, the formation of prosensory patches in the chick inner ear. Development 134: 2369–78.

[206] Morrison A, Hodgetts C, Gossler A, de Angelis MH, Lewis J (1999) Expression of delta1 and serrate1 (jagged1) in the mouse inner ear. Mech Develop 84: 169–72.

[207] Chrysostomou E, Gale JE, Daudet N (2012) Delta-like 1 and lateral inhibition during hair cell formation in the chicken inner ear: evidence against cis-inhibition. Development 139: 3764–74.

[208] Buchler NE, Gerland U, Hwa T (2003) On schemes of combinatorial transcription logic. Proc Natl Acad Sci USA 100: 5136–41.

Appendices

Appendix A

Derivation of the Laplacian in a hexagonal lattice

We consider a continuous function $\varphi(\mathbf{r})$ where $\mathbf{r}$ denotes the spatial variable in a bidimensional array so its coordinates are $\mathbf{r} = (x, y)$. We perform a second order Taylor expansion around $\mathbf{r} = \mathbf{0} = (0, 0)$ and evaluate it at the 6 points drawn in Fig. A.1, named $\mathbf{r_j}$ with $j = 1...6$. The Taylor series at second order read :

$$\begin{aligned}
\varphi(\mathbf{r_1}) &\approx \varphi(\mathbf{0}) - \frac{\partial\varphi}{\partial x}h_1 + \frac{\partial\varphi}{\partial y}h_2 + \frac{\partial^2\varphi}{\partial x^2}\frac{h_1^2}{2} + \frac{\partial^2\varphi}{\partial y^2}\frac{h_2^2}{2} - \frac{\partial^2\varphi}{\partial x\partial y}h_1h_2 \\
\varphi(\mathbf{r_2}) &\approx \varphi(\mathbf{0}) + \frac{\partial\varphi}{\partial x}h_1 + \frac{\partial\varphi}{\partial y}h_2 + \frac{\partial^2\varphi}{\partial x^2}\frac{h_1^2}{2} + \frac{\partial^2\varphi}{\partial y^2}\frac{h_2^2}{2} + \frac{\partial^2\varphi}{\partial x\partial y}h_1h_2 \\
\varphi(\mathbf{r_3}) &\approx \varphi(\mathbf{0}) - \frac{\partial\varphi}{\partial x}\Delta + \frac{\partial^2\varphi}{\partial x^2}\frac{\Delta}{2} \\
\varphi(\mathbf{r_4}) &\approx \varphi(\mathbf{0}) + \frac{\partial\varphi}{\partial x}h_1 - \frac{\partial\varphi}{\partial y}h_2 + \frac{\partial^2\varphi}{\partial x^2}\frac{h_1^2}{2} + \frac{\partial^2\varphi}{\partial y^2}\frac{h_2^2}{2} - \frac{\partial^2\varphi}{\partial x\partial y}h_1h_2 \\
\varphi(\mathbf{r_5}) &\approx \varphi(\mathbf{0}) - \frac{\partial\varphi}{\partial x}h_1 - \frac{\partial\varphi}{\partial y}h_2 + \frac{\partial^2\varphi}{\partial x^2}\frac{h_1^2}{2} + \frac{\partial^2\varphi}{\partial y^2}\frac{h_2^2}{2} - \frac{\partial^2\varphi}{\partial x\partial y}h_1h_2 \\
\varphi(\mathbf{r_6}) &\approx \varphi(\mathbf{0}) + \frac{\partial\varphi}{\partial x}\Delta + \frac{\partial^2\varphi}{\partial x^2}\frac{\Delta}{2} \quad , \qquad \text{(A.1)}
\end{aligned}$$

where $h_1 = \Delta sin(\pi/6) = \Delta/2$ and $h_2 = \Delta cos(\pi/6) = (\sqrt{3}/2)\Delta$. All the derivatives are evaluated at $\mathbf{r} = \mathbf{0} = (0, 0)$ but for simplicity it has not been explicitly indicated. The system of algebraic Eqs. A.1 is linear with its derivatives, so we

can isolate the term $\frac{\partial^2\varphi}{\partial x^2} + \frac{\partial^2\varphi}{\partial y^2}$, what resuls in

$$\nabla^2\varphi(\mathbf{r}) = \frac{\partial^2\varphi}{\partial x^2} + \frac{\partial^2\varphi}{\partial y^2} \approx \frac{2}{3}\left\{\frac{1}{\Delta}\left(\frac{\varphi(\mathbf{r_1}) - \varphi(\mathbf{0})}{\Delta} - \frac{\varphi(\mathbf{0}) - \varphi(\mathbf{r_4})}{\Delta}\right) + \right.$$
$$\left. + \frac{1}{\Delta}\left(\frac{\varphi(\mathbf{r_2}) - \varphi(\mathbf{0})}{\Delta} - \frac{\varphi(\mathbf{0}) - \varphi(\mathbf{r_5})}{\Delta}\right) + \frac{1}{\Delta}\left(\frac{\varphi(\mathbf{r_3}) - \varphi(\mathbf{0})}{\Delta} - \frac{\varphi(\mathbf{0}) - \varphi(\mathbf{r_6})}{\Delta}\right)\right\} \quad \text{(A.2)}$$

By rewriting Eq. A.2 we have

$$\nabla^2\varphi(\mathbf{r}) \approx \frac{1}{\Delta^2}\frac{2}{3}\sum_{j\in nn(i)}(\varphi_j - \varphi_i) \equiv \nabla_i^2\varphi_i \quad , \quad \text{(A.3)}$$

where φ_i is defined as $\varphi(\mathbf{r_i})$ and i is the central node and j refers to its six nearest nodes defined on a hexagonal lattice.

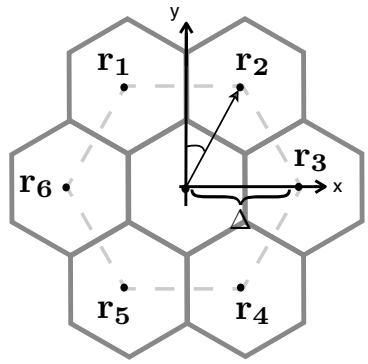

Figure A.1: Diagram of an hexagonal array of cells with its respective centroids. A continuous function in space φ can be evaluated at the nodes $\mathbf{r_j}$ for $j = 1, ..., 6$ by doing a Taylor expansion around the origin (see Eqs. A.1). The hexagon drawn with dashed line is a guide to the eye, joining the nodes that are used for the Taylor expansion.

Appendix B

Structure function of a periodic lateral inhibition pattern

Herein we mathematically derive a theoretical expression for the structure function of a periodic lateral inhibition pattern of two cell types. The pattern we study has a cell type A in proportion $1/3$, and cell type B in proportion B, and cell type A is always surrounded by cell type B (see Fig 5.16 (A)). The exact pattern solutions are provided by using the method presented in Secs. 2.5 and 2.10.

The structure function will have a contribution of the pattern periodicity, what corresponds to the bidimensional wavenumbers $(\bar{q}, \bar{p}) = (2/3, 1/3)$ and $(\bar{q}, \bar{p}) = (1/3, 2/3)$, and another contribution due to the homogeneous mode $(\bar{q}, \bar{p}) = (1, 1)$ (see Sec. 2.10 for details). Eq. 2.24 allows us to refer to the lateral inhibition pattern and the homogeneous modes as $\Omega = -1/2$ and $\Omega = 1$ respectively.

The size of the cell array is $N \times M$ and it has to be compatible with the studied pattern, so both N and M are multiples of three. We rewrite the expression 2.41 of the structure function

$$\mathbb{S}(\bar{p},\bar{q}) = \frac{1}{MN}\sum_{j,k}\sum_{j',k'}(x_{j,k}-x_b)(x_{j',k'}-x_b)e^{-2\pi \mathrm{i}(\bar{q}(j-j')+\bar{p}(k-k'))} \quad , \qquad \text{(B.1)}$$

where x_b is a constant we subtract from the pattern. For this kind of pattern of two cell types, the $(x_{j,k}-x_b)$ terms can be either Δx_A or Δx_B defined by

$$\Delta x_A = x_A - x_b, \quad \Delta x_B = x_B - x_b \quad , \qquad \text{(B.2)}$$

where x_A and x_B are the x-levels of the A cell fate and the B cell fate, respectively, and x_b is a constant. If we apply the structure function $(B.1)$ to our periodic pattern, we will have three different contributions, one coming from the autocorrelation of every pair of A cells ($\mathbb{S}^{AA}_{\bar{q},\bar{p}}$), another coming from every pair of B cells ($\mathbb{S}^{BB}_{\bar{q},\bar{p}}$) and finally the one that comes from every pair of the two different cell types ($\mathbb{S}^{AB}_{\bar{q},\bar{p}}$):

$$\mathbb{S}(\bar{p},\bar{q}) = \frac{1}{MN}(\mathbb{S}^{AA}_{\bar{q},\bar{p}} + \mathbb{S}^{BB}_{\bar{q},\bar{p}} + \mathbb{S}^{AB}_{\bar{q},\bar{p}}) \qquad \text{(B.3)}$$

Each of these three terms contains the number of cell pairs, the amplitude contribution, and the phase contribution, given by the value of the exponential part. In order to compute the phase contribution, we have to think about how are the exponential terms among the studied pairs of cells, taking into account the two possible family modes that we can find in the pattern; the $\Omega = 1$ family, which corresponds to the homogeneous mode, and the $\Omega = -1/2$ family, which is really that one behind the pattern. The phase term for the homogeneous mode $((\bar{q},\bar{p}) = (1,1))$ will be 1 always one. The phase term for the patterned mode is also 1 in the $\mathbb{S}^{AA}_{\bar{q},\bar{p}}$ contribution, but for the $\mathbb{S}^{BB}_{\bar{q},\bar{p}}$ term, half of the cell pairs gives 1 and the other half $-1/2$, while for the $\mathbb{S}^{AB}_{\bar{q},\bar{p}}$ term the phase contribution is always $-1/2$.

In order to introduce such phase constants properly in the structure function we make use of $\delta_{i,j}$, the Kronecker delta functions. Thus, we can define a $\zeta^{patt}_{\bar{q},\bar{p}}$ function, which will be 1 when we compute the structure function of the patterned mode, and a a $\zeta^{homo}_{\bar{q},\bar{p}}$ function, which will be 1 when we are referring to the homogeneous mode:

$$\zeta^{patt}_{\bar{q},\bar{p}} = \delta_{\bar{q},1/3}\delta_{\bar{p},2/3} + \delta_{\bar{q},2/3}\delta_{\bar{p},1/3} \quad \text{(B.4a)}$$

$$\zeta^{homo}_{\bar{q},\bar{p}} = \delta_{\bar{q},1}\delta_{\bar{p},1} \quad \text{(B.4b)}$$

We can check that $\zeta^{patt}_{1,1} = 0$, $\zeta^{patt}_{1/3,2/3} = \zeta^{patt}_{2/3,/3} = 1$ and $\zeta^{homo}_{1,1} = 1$, $\zeta^{homo}_{2/3,1/3} = \zeta^{homo}_{1/3,2/3} = 0$.

Taking into account the phase values for the patterned modes and the homogeneous mode, we can write

$$\mathbb{S}^{AA}_{\bar{q},\bar{p}} = N_{AA}\Delta x_A^2(\zeta^{homo}_{\bar{q},\bar{p}} + \zeta^{patt}_{\bar{q},\bar{p}}) \quad \text{(B.5a)}$$

$$\mathbb{S}^{BB}_{\bar{q},\bar{p}} = N_{BB}\Delta x_A^2(\zeta^{homo}_{\bar{q},\bar{p}} + \frac{1}{2}(1-1/2)\zeta^{patt}_{\bar{q},\bar{p}}) \quad \text{(B.5b)}$$

$$\mathbb{S}^{AB}_{\bar{q},\bar{p}} = N_{AB}\Delta x_A\Delta x_B(\zeta^{homo}_{\bar{q},\bar{p}} - \frac{1}{2}\zeta^{patt}_{\bar{q},\bar{p}}) \quad , \quad \text{(B.5c)}$$

where N_{AA}, N_{BB} and N_{AB} are twice the number of pairs of A-A cells, B-B cells, and A-B cells respectively. In our case, it is

$$N_{AA} = \left(\frac{NM}{3}\right)^2, \quad N_{BB} = \left(\frac{2NM}{3}\right)^2, \quad N_{AB} = 2\frac{2NM}{3}\frac{NM}{3} \quad . \quad \text{(B.6)}$$

The theoretical structure function is

$$\mathbb{S}(\bar{p},\bar{q}) = \frac{MN}{9}(\omega^1_{\bar{q},\bar{p}}\Delta x_A^2 + 4\omega^{1/4}_{\bar{q},\bar{p}}\Delta x_B^2 \quad , +4\omega^{-1/2}_{\bar{q},\bar{p}}\Delta x_A\Delta x_B) \quad \text{(B.7)}$$

where

$$\omega^c_{\bar{q},\bar{p}} = \zeta^{homo}_{\bar{q},\bar{p}} + c\zeta^{patt}_{\bar{q},\bar{p}} \quad , \quad \text{(B.8)}$$

being c a superindex that has being used to simplify the expression of Eq. B.8. Finally, our theoretical structure function for our lateral inhibition pattern reads

$$\mathbb{S}(\bar{p},\bar{q}) = \begin{cases} \frac{MN}{9}(\Delta x_A + 2\Delta x_B)^2 & \text{if } (\bar{q},\bar{p}) = (1,1) \\ \frac{MN}{9}(\Delta x_A - \Delta x_B)^2 & \text{if } (\bar{q},\bar{p}) = (1/3,2/3) \text{ or } (\bar{q},\bar{p}) = (2/3,1/3) \\ 0 & \text{otherwise} \quad . \end{cases}$$

In order to annulate the homogeneous mode herein it should be fulfilled $\Delta x_A + 2\Delta x_B = 0$, so by using Eq. B.2 we obtain the background x_b that we have to subtract to the pattern:

$$x_b = \frac{x_A + 2x_B}{3} \quad . \tag{B.9}$$

Note that the contribution for the patterned mode does not depend on x_b.

Appendix C

Linear stability analysis of pattern solutions

In this section we study the linear stability of different pattern solutions (Sec. 2.7, 2.10.1). We apply this analysis to our model of lateral inhibition with cis-interactions presented in Chap. 5 (Eqs. 5.2-5.4). We focus on the lateral inhibition pattern and on the pattern of stripes.

$$\frac{\mathrm{d}s_i}{\mathrm{d}t} = f\left(l_i, \langle l_i \rangle\right) - s_i \tag{C.1a}$$

$$\frac{\mathrm{d}l_i}{\mathrm{d}t} = v\left\{g(s_i) - l_i\right\} \quad , \tag{C.1b}$$

where

$$f(l_i, \langle l_i \rangle) = \frac{r_t \langle l_i \rangle + \epsilon r_c l_i}{1 + \langle l_i \rangle + r_c l_i} \quad , \quad g(s_i) = \frac{1}{1 + b s_i^h} \quad , \tag{C.2}$$

and $\langle l_i \rangle = \frac{1}{\omega} \sum_{j \in nn(i)} l_j$, being ω the number of first neighbors.

For doing this analysis, we also make use of the reduced model approach presented (Secs. 2.5, 2.10.1 and 5.3.6). We rewrite the reduced model (Eqs. 5.16-5.17) for the two cell types A and B :

$$l_A = g(s_A), \qquad s_A = f(r_t \langle l_A \rangle, l_A) \tag{C.3a}$$

$$l_B = g(s_B), \qquad s_B = f\left(r_t \langle l_B \rangle, l_B\right) \quad , \tag{C.3b}$$

with

$$\langle l_A \rangle = c_A l_A + (1 - c_A) l_B \tag{C.4a}$$

$$\langle l_B \rangle = c_B l_B + (1 - c_B) l_A \quad , \tag{C.4b}$$

where c_A and c_B are determined by the symmetry properties of the pattern. For the lateral inhibition pattern it is fulfilled $c_A = 0$ and $c_B = 1/2$.

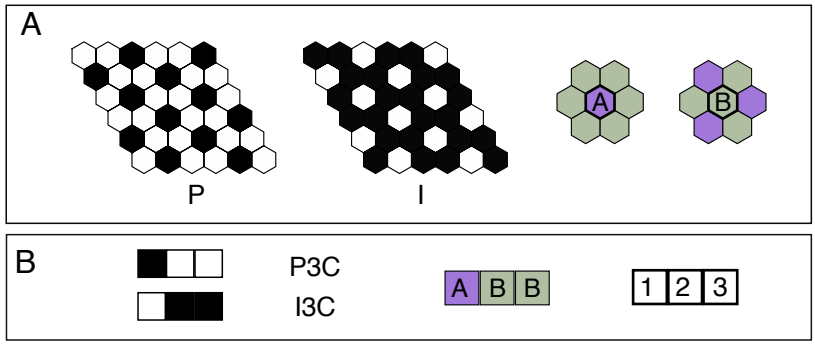

Figure C.1: Patterns with the periodicity of $\Omega = -1/2$ with 1/3 of cell type A *versus* 2/3 of cell type B. (A) Pattern that we want to study. Left: Normal lateral inhibition pattern (P) with 1/3 of high Delta cells and its inverted pattern (I). Right: A group of 7 cells illustrate the symmetry of the pattern of cell type A (violet) and cell type B (green). (B) Equivalent pattern in a line of cells with periodic boundary conditions that we use for studying pattern shown in (A). Left: Normal pattern in three cells (P3C) and its inverted version (I3C). Black represents high ligand concentration, white represents low ligand concentration. Middle: A group of 3 cells illustrating pattern symmetry. Note that P, I, P1D and I1D share the same symmetry. Right: Labeling scheme. The $c_{A,B}$ coefficients determined by the pattern symmetries (right in (A,B)) are $c_A = 0$ and $c_B = 1/2$. This enables us to find the exact solution of these patterns according to the method described in Sec. 2.5 (Eqs. 2.34).

To find the stability of the lateral inhibition pattern (Fig. C.1 (A)), we use the fact that our pattern in a hexagonal array has the same symmetry properties (*i.e.* c_A and c_B values) than the lateral inhibition pattern in the line of cells shown in Fig. C.1 (B). Then, for studying pattern stability in a hexagonal lattice we can also write the following system of equations of three cells in one dimension with periodic boundary conditions (see labeling scheme in the right panel of Fig.

C.1 (B)):

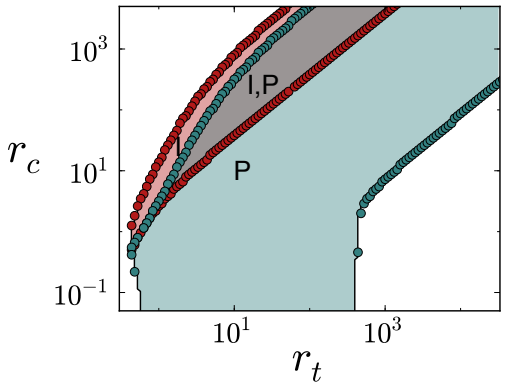

Figure C.2: Phase diagram showing the regions where the normal lateral inhibition pattern (P) and the inverted pattern (I) are stable to small perturbations. (A) Phase diagram as in Fig. 5.17 (A) computed with LSA over the pattern solutions (filled regions in blue for pattern P and in red for pattern I) and with simulation results depicted with dots. Note that there is a coexistence region in which both patterns are stable. Stability through numerical analysis is computed with simulations on 3×3 hexagonal lattices. Parameter values: $h = 4$, $\epsilon = 0$, $v = 1$, $b = 1000$. Simulation details as in Fig. 5.17 (A).

$$\frac{\mathrm{d}s_1}{\mathrm{d}t} = f\left(g(s_1), \frac{g(s_2)+g(s_3)}{2}\right) - s_1 \tag{C.5a}$$

$$\frac{\mathrm{d}s_2}{\mathrm{d}t} = f\left(g(s_2), \frac{g(s_1)+g(s_3)}{2}\right) - s_2 \tag{C.5b}$$

$$\frac{\mathrm{d}s_3}{\mathrm{d}t} = f\left(g(s_3), \frac{g(s_1)+g(s_2)}{2}\right) - s_3 \quad , \tag{C.5c}$$

where we have performed the adiabatic reduction of the ligand equations for simplicity. We compute Jacobian matrix $\mathscr{M}$ for the above system and we impose a pattern shown in the middle panel of Fig. C.1 (B):

$$\mathscr{M} = \left(\begin{array}{ccc} \frac{\partial}{\partial s_1}\frac{\mathrm{d}s_1}{\mathrm{d}t} & \frac{\partial}{\partial s_2}\frac{\mathrm{d}s_1}{\mathrm{d}t} & \frac{\partial}{\partial s_3}\frac{\mathrm{d}s_1}{\mathrm{d}t} \\ \frac{\partial}{\partial s_1}\frac{\mathrm{d}s_2}{\mathrm{d}t} & \frac{\partial}{\partial s_2}\frac{\mathrm{d}s_2}{\mathrm{d}t} & \frac{\partial}{\partial s_3}\frac{\mathrm{d}s_2}{\mathrm{d}t} \\ \frac{\partial}{\partial s_1}\frac{\mathrm{d}s_3}{\mathrm{d}t} & \frac{\partial}{\partial s_2}\frac{\mathrm{d}s_3}{\mathrm{d}t} & \frac{\partial}{\partial s_3}\frac{\mathrm{d}s_3}{\mathrm{d}t} \end{array} \right)\Bigg|_{A,B} =$$

$$= \left(\begin{array}{ccc} -1+\mathscr{C}_A\mathscr{B}_A & \mathscr{A}_A\mathscr{B}_B & \mathscr{A}_A\mathscr{B}_B \\ \mathscr{A}_B\mathscr{B}_A & -1+\mathscr{C}_B\mathscr{B}_B & \mathscr{A}_B\mathscr{B}_B \\ \mathscr{A}_B\mathscr{B}_A & \mathscr{A}_B\mathscr{B}_B & -1+\mathscr{C}_B\mathscr{B}_B \end{array} \right), \tag{C.6}$$

where A and B mean that we evaluate the different terms according to the pattern solutions $l_{A,B}$ and $s_{A,B}$, and

$$\begin{aligned} \mathscr{A}_A &= \frac{\frac{r_t}{2}\left(1+r_c l_A(1-\epsilon)\right)}{(1+r_t l_B + r_c l_A)^2}, \qquad \mathscr{A}_B = \frac{\frac{r_t}{2}\left(1+r_c l_B(1-\epsilon)\right)}{(1+\frac{r_t}{2}(l_B+l_A)+r_c l_B)^2}, \\ \mathscr{C}_A &= \frac{r_c\left(\epsilon + r_t l_B(\epsilon-1)\right)}{(1+r_t l_B + r_c l_A)^2}, \qquad \mathscr{C}_B = \frac{r_c\left(\epsilon + \frac{r_t}{2}(l_A+l_B)(\epsilon-1)\right)}{(1+\frac{r_t}{2}(l_B+l_A)+r_c l_B)^2} \quad , \\ \mathscr{B}_{A,B} &= -\frac{b h s_{A,B}^{h-1}}{(1+b s_{A,B}^h)^2} \quad . \end{aligned} \tag{C.7}$$

We diagonalize matrix $\mathscr{M}$ set by Eq. C.6 and find its three eigenvalues $\alpha_{1,2,3}$:

$$\alpha_1 = -\left(1+(\mathscr{A}_B+\mathscr{C}_B)\mathscr{B}_B\right) \tag{C.8a}$$

$$\begin{aligned} \alpha_{2,3} &= \frac{1}{2}(-2+\mathscr{B}_A\mathscr{C}_A+(\mathscr{A}_B+\mathscr{C}_B)\mathscr{B}_B) \pm \\ &\pm \frac{1}{2}\left(4\mathscr{A}_A\mathscr{A}_B\mathscr{B}_A\mathscr{B}_B + (\mathscr{B}_A\mathscr{C}_A - \mathscr{B}_B(\mathscr{A}_B+\mathscr{C}_B))^2\right)^{1/2} . \end{aligned} \tag{C.8b}$$

We evaluate these eigenvalues on the solutions found with the corresponding reduced model (Eqs. C.3-C.4 with $c_A = 0$ and $c_A = 1/2$). When its real part is negative ($Re(\alpha_i) < 0$ for $i = 1, 2, 3$) then the pattern solution is linearly stable. Our study across the r_c–r_t parameter space is shown in Fig. C.1. We confirm that our theoretical analysis agrees with simulations of the model Eqs. C.1-C.2 in a system of 3×3 cells with patterned initial conditions (see Sec. 5.3.6 for details of the simulations). Note that the criterion for pattern stability assumes adiabacity for the ligand equations, but it still agrees with the simulated model in a parameter regime where both ligand and signal variables have the same time scale (*i.e.* $v = 1$).

Now we evaluate the stability of the stripped pattern (Fig. C.3 (A)) over the solutions found with the reduced model (Eqs. C.3-C.4 with $c_A = 1/3$ and

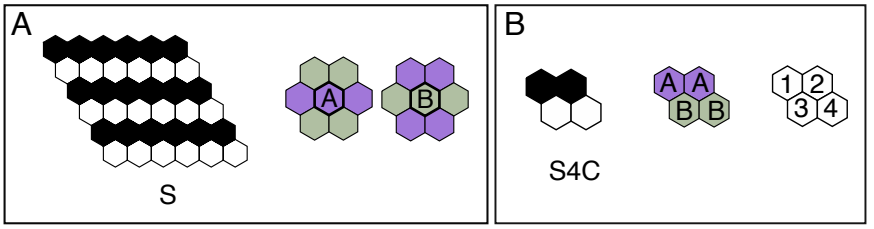

Figure C.3: Stripped patterns with the periodicity of $\Omega = -1/3$, with 1/2 of cell type A *versus* 1/2 of cell type B. (A) Pattern that we want to study. Left: Normal stripped pattern (S) with 1/2 of high Delta cells. Right: two groups of 7 cells illustrate the neighborhood (or symmetry) properties of the pattern of cell type A (violet) and cell type B (green). (B) Equivalent pattern in a group of four cells with periodic boundary conditions that we use for studying pattern shown in (A). Left: Stripped pattern in four cells (S4C). Black represents high ligand concentration, white represents low ligand concentration. Middle: A group of 4 cells illustrating pattern symmetry. Note that P, I, P1D and I1D share the same symmetry. Right: Labeling scheme. The $c_{A,B}$ coefficients determined by the pattern symmetries (right in (A,B)) are $c_A = 1/3$ and $c_B = 1/3$. This enables us to find the exact solution of these patterns according to the method described in Sec. 2.5 (Eqs. 2.34).

$c_B = 1/3$). We use the fact that our pattern can be obtained in a smaller system (Fig. C.1 (B)). Then, we can write the following system of equations for four cells with periodic boundary conditions:

$$\frac{\mathrm{d}s_1}{\mathrm{d}t} = f\left(g(s_1), \frac{g(s_2)+g(s_3)+g(s_4)}{3}\right) - s_1 \tag{C.9a}$$
$$\frac{\mathrm{d}s_2}{\mathrm{d}t} = f\left(g(s_2), \frac{g(s_1)+g(s_3)+g(s_4)}{3}\right) - s_2 \tag{C.9b}$$
$$\frac{\mathrm{d}s_3}{\mathrm{d}t} = f\left(g(s_3), \frac{g(s_1)+g(s_2)+g(s_4)}{2}\right) - s_3 \tag{C.9c}$$
$$\frac{\mathrm{d}s_4}{\mathrm{d}t} = f\left(g(s_3), \frac{g(s_1)+g(s_2)+g(s_3)}{2}\right) - s_4 \quad , \tag{C.9d}$$

where we have used the labeling scheme in the right panel of Fig. C.3 (B)). We compute the Jacobian matrix $\mathscr{M}$ of the above equations and we impose a pattern shown in the middle panel of Fig. C.3 (B):

$$\begin{aligned}\mathscr{M} &= \left.\begin{pmatrix} \frac{\partial}{\partial s_1}\frac{\mathrm{d}s_1}{\mathrm{d}t} & \frac{\partial}{\partial s_2}\frac{\mathrm{d}s_1}{\mathrm{d}t} & \frac{\partial}{\partial s_3}\frac{\mathrm{d}s_1}{\mathrm{d}t} & \frac{\partial}{\partial s_4}\frac{\mathrm{d}s_1}{\mathrm{d}t} \\ \frac{\partial}{\partial s_1}\frac{\mathrm{d}s_2}{\mathrm{d}t} & \frac{\partial}{\partial s_2}\frac{\mathrm{d}s_2}{\mathrm{d}t} & \frac{\partial}{\partial s_3}\frac{\mathrm{d}s_2}{\mathrm{d}t} & \frac{\partial}{\partial s_4}\frac{\mathrm{d}s_2}{\mathrm{d}t} \\ \frac{\partial}{\partial s_1}\frac{\mathrm{d}s_3}{\mathrm{d}t} & \frac{\partial}{\partial s_2}\frac{\mathrm{d}s_3}{\mathrm{d}t} & \frac{\partial}{\partial s_3}\frac{\mathrm{d}s_3}{\mathrm{d}t} & \frac{\partial}{\partial s_4}\frac{\mathrm{d}s_3}{\mathrm{d}t} \\ \frac{\partial}{\partial s_1}\frac{\mathrm{d}s_4}{\mathrm{d}t} & \frac{\partial}{\partial s_2}\frac{\mathrm{d}s_4}{\mathrm{d}t} & \frac{\partial}{\partial s_3}\frac{\mathrm{d}s_4}{\mathrm{d}t} & \frac{\partial}{\partial s_4}\frac{\mathrm{d}s_4}{\mathrm{d}t} \end{pmatrix}\right|_{A,B} = \\ &= \begin{pmatrix} -1+\mathscr{C}_A\mathscr{B}_A & \mathscr{A}_A\mathscr{B}_A & \mathscr{A}_A\mathscr{B}_B & \mathscr{A}_A\mathscr{B}_B \\ \mathscr{A}_A\mathscr{B}_A & -1+\mathscr{C}_A\mathscr{B}_A & \mathscr{A}_A\mathscr{B}_B & \mathscr{A}_A\mathscr{B}_B \\ \mathscr{A}_B\mathscr{B}_A & \mathscr{A}_B\mathscr{B}_A & -1+\mathscr{C}_B\mathscr{B}_B & \mathscr{A}_B\mathscr{B}_B \\ \mathscr{A}_B\mathscr{B}_A & \mathscr{A}_B\mathscr{B}_A & \mathscr{A}_B\mathscr{B}_B & -1+\mathscr{C}_B\mathscr{B}_B \end{pmatrix},\end{aligned} \tag{C.10}$$

where A and B mean that we evaluate the different terms according to the pattern solutions $l_{A,B}$ and $s_{A,B}$, and

$$\begin{aligned}\mathscr{A}_A &= \frac{\frac{r_t}{3}\left(1+r_c l_A(1-\epsilon)\right)}{\left(1+\frac{r_t}{3}(2l_B+l_A)+r_c l_A\right)^2}, \qquad \mathscr{A}_B = \frac{\frac{r_t}{3}\left(1+r_c l_B(1-\epsilon)\right)}{\left(1+\frac{r_t}{3}(l_B+2l_A)+r_c l_B\right)^2}, \\ \mathscr{C}_A &= \frac{r_c\left(\epsilon+\frac{r_t}{3}(2l_B+l_A)(\epsilon-1)\right)}{\left(1+\frac{r_t}{3}(2l_B+l_A)+r_c l_A\right)^2}, \qquad \mathscr{C}_B = \frac{r_c\left(\epsilon+\frac{r_t}{3}(l_B+2l_A)(\epsilon-1)\right)}{\left(1+\frac{r_t}{3}(l_B+2l_A)+r_c l_B\right)^2} \quad ,\end{aligned} \tag{C.11}$$

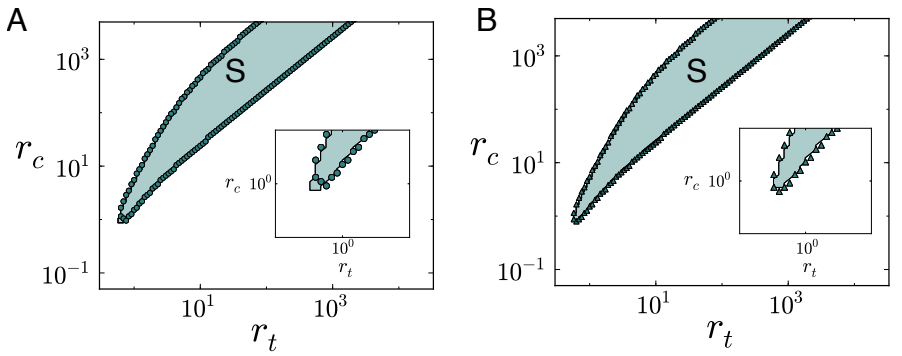

Figure C.4: Phase diagram showing the regions where the stripped pattern (S) is stable to small perturbations. (A,B) Phase diagrams as in Fig. 5.19 (A) computed with LSA over the pattern solutions (blue regions) and with simulations on a system of (A) 6×6 cells and (B) 2×2 cells depicted with (A) dots and (B) triangles. Insets in (A,B) show a small region where theoretical results are (A) in small disagreement with simulations on a system of 6×6 celll while (B) agree with simulations on a system of 2×2 cells. Total agreement is observed in panel (B). A dot or triangle is set in the parameter space between to simulation points along the r_c direction, in which one point the pattern is stable and the other point the pattern is not stable (or the pattern solutions do not exist). Because of that, in the insets one can see the points slightly outside the region that has been determined through the theoretical criterion. Numerical simulations in (A) and (B) correspond to simulation results performed on hexagonal lattices with periodic boundary conditions. Parameter values: $h = 4$, $\epsilon = 0$, $v = 1$, $b = 1000$. Simulation details as in Fig. 5.19 (A).

and $\mathscr{B}_{A,B}$ are defined as in Eqs. C.7. We diagonalize matrix $\mathscr{M}$ set by Eq. C.10 and find its four eigenvalues $\alpha_{1,2,3,4}$:

$$\alpha_1 = -(1 + (\mathscr{A}_A + \mathscr{C}_A)\mathscr{B}_A) \quad \text{(C.12a)}$$

$$\alpha_2 = -(1 + (\mathscr{A}_B + \mathscr{C}_B)\mathscr{B}_B) \quad \text{(C.12b)}$$

$$\alpha_{3,4} = \frac{1}{6}(-6 + 3\mathscr{B}_A(\mathscr{A}_A + \mathscr{C}_A) + 3\mathscr{B}_B(\mathscr{A}_B + \mathscr{C}_B)) \pm \frac{\sqrt{3\chi}}{6} \quad \text{(C.12c)}$$

being $\chi = \mathscr{A}_A^2\mathscr{B}_A^2 + \mathscr{A}_B^2\mathscr{B}_B^2 + 6(\mathscr{A}_A\mathscr{B}_B(\mathscr{B}_A\mathscr{C}_A + \mathscr{B}_B(7\mathscr{A}_B - \mathscr{C}_B))) + 3\left(\mathscr{B}_A\mathscr{C}_A - \mathscr{B}_B\mathscr{C}_B\right)^2 + 6\mathscr{A}_B\mathscr{B}_B\left(\mathscr{B}_B\mathscr{C}_B - \mathscr{B}_A\mathscr{C}_A\right)$.

We evaluate these eigenvalues on the solutions found with the corresponding pattern solutions. When its real part is negative ($Re(\alpha_i) < 0$ for $i = 1, 2, 3, 4$) then the pattern solution is linearly stable. Our study across the r_c–r_t parameter space is shown in Fig. C.3. Our theoretical analysis shows a very good agreement with simulation results in a system of 6×6 cells with patterned initial conditions (Fig. C.3 (A)). Just a small region of disagreement appear (see inset in Fig. C.3 (A)), where an extra-region for the stripes is theoretically linearly stable, while simulations would point that it is not stable. Simulation results in a system of 2×2 hexagonal cells with periodic boundary conditions agree with theoretical results. This probably means that such small region in the parameter space is linearly unstable to the mode $\Omega = -1/2$.

By applying this method at lower cooperativities ($h = 2$) for patterns P, I and S we obtain equivalent results (data not shown).

The method we propose to determine the linear stability of pattern states has shown a very good agreement with simulation results. This method can be easily extended to other fine-grained patterns.

Apèndix D

Resum (Catalan summary)

A continuació, farem un resum de la Tesi en català, titulada Formació de patrons mitjançant la inhibició lateral mediada per la senyalització de Notch. Primerament, en la secció D.1 fem una breu introducció. Tot seguit, en la secció D.2 es resumeixen els resultats originals de la Tesi. A continuació, en la secció D.3 presentarem les perspectives que sorgeixen a partir dels nostres resultats. Finalment, en la secció D.4 donarem una llista de les nostres contribucions, manuscrits enviats i manuscrits en preparació.

D.1 Introducció

Els organismes multicel·lulars estan constituïts per diferents tipus cel·lulars ordenats d'una certa manera, formant teixits amb funcions específiques. L'organització de cèl·lules de tipus diferents pot donar lloc a patrons espacio-temporals [1,8].

Aquesta Tesi es basa en l'estudi de com a partir d'un teixit de cèl·lules equivalents — estat homogeni precursor — s'estableixen patrons ordenats de tipus cel·lulars diferents. En particular, ens hem centrat en l'estudi d'un tipus de patrons que sorgeixen en teixits animals que tenen dos tipus cel·lulars i que presenten un ordre fi en el teixit, *i.e.* de longitud d'ona de poques cèl·lules. Aquest tipus de patrons són formats degut al efecte de la inhibició lateral. La inhibició lateral és un fenomen en el qual cèl·lules precursores equivalents intenten adoptar un cert estat o destí cel·lular per a diferenciar-se en un tipus cel·lular en particular, i al

mateix temps inhibeixen a les seves cèl·lules veïnes que adquireixin aquest mateix estat. Aquest procés dinàmic dóna lloc a un patró fi, on les cèl·lules que han finalment adoptat l'estat desitjat vénen rodejades per cèl·lules que són inhibides, i que acabaran diferenciant-se en un tipus cel·lular diferent. Aquest tipus de patró es troba en una àmplia varietat de teixits animals, com ara en la retina (veure **[II,III]** en el llistat de publicacions, secció D.4) i en l'oïda interna **[IV]** [18] de vertebrats, i en l'ull de la mosca *Drosophila* [97].

El procés d'inhibició lateral està mediat per l'anomenada via de senyalització de Notch [62]. Aquesta via de senyalització està involucrada en diferents etapes del desenvolupament animal en una gran varietat de processos. Dos dels seus elements més importants són dos tipus de proteïna transmembrana: els lligands, entre ells la proteïna Delta i Jagged en vertebrats, i els receptors, l'anomenada proteïna Notch. Lligands i receptors interaccionen: quan un lligand es troba en la membrana d'una cèl·lula, aquest interacciona amb un receptor localitzat en la membrana d'una cèl·lula adjacent. Aquest procés s'anomena interacció trans, i dóna lloc a la formació d'un complex que passa a alliberar el que anomenem el senyal de Notch cap a la cèl·lula que conté el receptor. Aquest senyal passa al nucli de tal cèl·lula, on finalment inhibeix la producció de lligand. Per tant, una cèl·lula que té lligand, mitjançant la interacció trans, inhibeix a les seves cèl·lules veïnes que produeixen lligand. El fet que totes les cèl·lules tinguin lligands i receptors fa que s'estableixin retroalimentacions (*feedbacks*) positius intercel·lulars. Aquests *feedbacks* amplifiquen les diferències inicials entre cèl·lules que es volen començar a diferenciar, i resulta en l'esmentat patró fi d'inhibició lateral, on cèl·lules amb alt lligand acaben essent rodejades per cèl·lules amb baix lligand.

En aquesta Tesi avaluem des d'una perspectiva teòrica els efectes de diferents elements reguladors de la via de Notch en la formació de patrons d'inhibició lateral. Tots els elements reguladors que estudiem han estat motivats per evidències experimentals recents. El nostre estudi parteix d'un model dinàmic introduït per Collier i col·legues (1996), sent aquest el primer model matemàtic proposat per entendre la inhibició lateral [10]. En aquesta Tesi reformulem aquest model incloent-hi aquests altres elements reguladors en la dinàmica de Notch.

D.1.1 El model de referència per a la inhibició lateral: el model de Collier

El model de Collier es basa en dues equacions diferencials no lineals ordinàries per cèl·lula que modelitzen a un nivell fenomenològic el que els autors anomenen l'activitat del receptor Notch i del lligand Delta. En aquest model, l'activitat de Delta en una cèl·lula i és reprimida per l'activitat de Notch en aquesta cèl·lula, i aquesta és activada pel promig dels nivells d'activitat de Delta en les cèl·lules veïnes. El model és el següent:

$$\frac{\mathrm{d}s_i}{\mathrm{d}t} = f\left(\langle l_i\rangle\right) - s_i \tag{D.1a}$$

$$\frac{\mathrm{d}l_i}{\mathrm{d}t} = v\left\{g(s_i) - l_i\right\} \quad , \tag{D.1b}$$

on l_i i s_i són les activitats de Delta in Notch en la cèl·lula i, $\langle l_i\rangle$ és l'acoblament espacial entre cèl·lula i cèl·lula, i representa el promig d'activitat de lligand en cèl·lules adjacents (primeres veïnes) a la cèl·lula i ,

$$\langle l_i\rangle = \frac{1}{\omega}\sum_{j\in nn(i)} l_j \quad , \tag{D.2}$$

essent ω el nombre de primers veïns d'una cèl·lula ($\omega = 6$ en una xarxa hexagonal), i $j \in nn(i)$ es refereix a tots les j-cèl·lules adjacents a la cèl·lula i. Les funcions reguladores g i f són funcions de Hill definides com

$$f\left(\langle l_i\rangle\right) = \frac{\langle l_i\rangle^k}{a + \langle l_i\rangle^k}, \quad g(s_i) = \frac{1}{1 + bs_i^h} \quad . \tag{D.3}$$

a està relacionat amb la quantitat d'activitat promig de Delta en les cèl·lules veïnes requerit per a l'activació de l'activitat de Notch en una cèl·lula, b controla la força d'inhibició de l'activitat de Delta per part de l'activitat de Notch (com més fort sigui b, més forta serà la inhibició), k i h són els exponents de Hill que conferiran més o menys linealitat en la funció d'activació f i d'inhibició g respectivament, i v és la raó de les degradacions de l'activitat de Delta en relació a l'activitat de Notch.

En aquest model, petites diferències inicials en les concentracions d'activitat entre cèl·lules veïnes són amplificades mitjançant el *feedback* positiu que s'estableix entre cèl·lules (Fig. D.1 (A)). Com a resultat, si la interacció trans entre

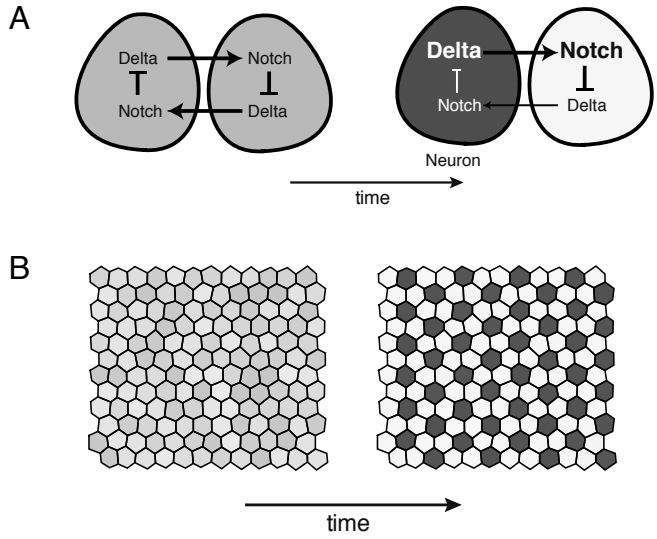

Figura D.1: Formació del patró fi d'inhibició lateral. (A) La inhibició lateral mútua entre cèl·lules veïnes dóna lloc a un *feedback* intercel·lular positiu. Aquest *feedback* amplifica les diferències inicials entre cèl·lules que són inicialment equivalents (esquerra) donant lloc a dos estats diferents (dreta). Lletres més grans (petites) dins de les cèl·lules indiquen nivells elevats (baixos) d'activitat. (B) Inhibició lateral actuant en un teixit de cèl·lules precursores equivalents amb petita variabilitat (esquerra) dóna lloc a un patró ordenat fi de dos tipus cel·lulars (dreta). Instantànies mostrant la creació del patró a partir de resultats de simulació del model de Collier (Eqs. 1.1) en una xarxa irregular de cèl·lules amb condicions periòdiques de contorn **[II,V]**. Al principi de la simulació, les cèl·lules tenen quantitats equivalents d'activitat de Notch i Delta, i això resulta en la formació d'un patró de cèl·lules amb nivells alts d'activitat en Delta (baixos en Notch), rodejades per cèl·lules amb nivells baixos d'activitat en Delta (alts en Notch) (dreta). Anomenarem aquest patró com el patró normal d'inhibició lateral donat que és el que típicament es troba en la natura.

cèl·lula i cèl·lula és suficientment forta, cèl·lules amb activitat alta de Delta (i baixa de Notch) vidran rodejades per cèl·lules amb activitat baixa de Delta (i alta de Notch), resultant en un patró ordenat fi (Fig D.1 (B)), el que anomenem el patró típic o normal d'inhibició lateral. Mitjançant aquest model es proposà per primera vegada aquest *feedback* com a responsable de la formació del patró. Collier i col·legues demostraren que la dinàmica proposada fa que l'estat homogeni inicial sigui linealment inestable, resultant en el patró esmentat [10].

D.2 Resum de resultats originals

Primerament, començarem amb les contribucions metodològiques que s'han fet en aquesta Tesi. Després, resumirem els resultats científics originals (seccions D.2.2-D.2.5).

D.2.1 Contribucions metodològiques

En aquesta Tesi hem utilitzat tècniques estàndard i també tècniques més noves que hem aplicat als nostres models. En aquesta secció presentem les contribucions metodològiques més importants i esmentarem quin tipus de resultats n'hem extret.

En la Tesi hem proposat un mètode nou que permet avaluar les solucions exactes d'estats de patrons periòdics en xarxes cel·lulars hexagonals **[I,II,IV,V]**. Mitjançant aquest mètode hem pogut trobar que la formació de patrons mitjançant la inhibició lateral succeeix en una regió de l'espai de paràmetres més àmplia que el que es prediu per anàlisi d'estabilitat lineal. Aquesta regió addicional l'hem anomenat regió biestable donat que almenys hi ha dues solucions espacialment exteses que són linealment estables: la solució homogènia i la solució del patró d'inhibició lateral. En vàries ocasions hem mostrat que, en aquestes regions biestables on l'estat homogeni és linealment estable, la inestabilització de l'estat homogeni és possible per diferents mecanismes, donant lloc a la formació d'un patró. La nova metodologia ha permès buscar en els espais de paràmetres de forma sistemàtica i àgil les regions biestables, i ha facilitat notablement l'obtenció dels diagrames de bifurcació corresponents. Hem pogut constatar que els diferents models emprats també presenten aquesta regió biestable. Aquestes re-

gions biestables han tingut la seva rellevància a l'hora d'entendre la formació de patrons dels nostres sistemes.

Gràcies al coneixement de les solucions exactes de patró, també hem pogut donar estimacions teòriques d'un paràmetre d'ordre o la funció d'estructura en patrons periòdics, cosa que ha facilitat diferents tasques en les simulacions numèriques **[I,V,VII]**.

Aquesta metodologia també ha permès la cerca de solucions exactes d'altres patrons regulars i l'estudi d'aquestes en diagrames de bifurcació i en l'espai de paràmetres **[V]**.

En la Tesi hem pogut desenvolupar una tècnica d'anàlisi d'estabilitat lineal sobre solucions de patró. Aquesta metodologia ens ha permès establir fàcilment l'estabilitat de varis patrons periòdics en l'espai de paràmetres i hem vist un acord pràcticament total amb resultats numèrics de simulacions. Això ha donat lloc a resultats remarcables, com per exemple el descobriment de l'existència de regions on més d'un patró periòdic és estable en el context de la inhibició lateral. L'anàlisi d'estabilitat d'estats de patró és menys estàndard en el camp de sistemes discrets espacialment extesos.

Al llarg de la Tesi hem hagut de tractar amb la solució d'arrels simples i múltiples d'equacions algebraiques, i també amb la integració numèrica dels nostres models, d'una manera eficient i sistemàtica. És per això que hem escrit els nostres propis programes per a la realització extensiva d'aquestes tasques en espais de paràmetres, explorant diferents ordres de magnitut per a diferents paràmetres. Hem aplicat els nostres programes d'integració numèrica a dinàmiques deterministes i estocàstiques en xarxes hexagonals bidimensionals regulars i en xarxes bidimensionals irregulars.

D.2.2 Progressió de fronts de diferenciació cel·lular

El primer treball de la Tesi se centra en l'estudi de la propagació d'un patró d'inhibició lateral i en la interacció d'aquest amb l'estat del teixit homogeni que és envaït pel patró. En particular, ens hem centrat en el cas de la neurogènesi (*i.e.* la diferenciació de cèl·lules neuronals) en la retina d'embrions de vertebrats **[II,III]**. En aquest cas, la formació de patró s'inicia en un únic domini circular creixent de diferenciació en el qual la capacitat d'inhibició lateral del teixit envaït

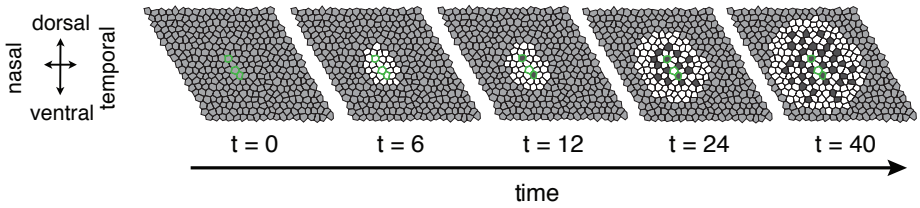

Figura D.2: Instantànies de simulacions on es mostra la seqüència de resultats en el temps, emulant l'emergència del patró d'inhibició lateral en la retina de vertebrats. Gris: cèl·lules no neurogèniques, *i.e.* sense dinàmica d'inhibició lateral; blanc: cèl·lules neurogèniques amb la dinàmica d'inhibició lateral; negre: cèl·lules neurogèniques que ja s'han diferenciat en neurona. Les tres cèl·lules centrals amb un contorn verd en tots els panells assenyalen les fonts inicials de morfogen. Detalls de la simulació estan descrits en **[II].**

s'estableix progressivament, deixant al seu pas el patró fi.

Hem proposat un model de propagació del patró autorregulat en el que hem pogut generar de forma robusta el creixement d'un simple domini de patró **[II]** (veure Fig. D.2). Dos dominis diferents en el teixit han estat establerts. Un domini interior creixent anomenat neurogènic, en el qual la inhibició lateral i la formació de patró succeeixen, i un domini exterior, el teixit envaït anomenat no neurogènic, el qual inicialment no té dinàmica d'inhibició lateral. Aquesta divisió de dominis ha estat motivada per les evidències experimentals existents i aportades pel nostre col·laborador José María Frade (Institut Cajal, CSIC, Madrid). Una proteïna que difón anomenada morfogen pot convertir aquest teixit no neurogènic en teixit neurogènic que començarà a tenir dinàmica d'inhibició lateral. Aquest morfogen és secretat per les cèl·lules que es diferencien en neurones en el domini neurogènic interior. Aquest front és autorregulat donat que (i) la diferenciació neurogènica allibera un morfogen i (ii) aquest morfogen envaeix teixit no neurogènic i fa que s'hi estableixi una dinàmica d'inhibició lateral.

Evidències experimentals han motivat estudiar el que passaria si el teixit envaït no tingués capacitat d'inhibir el teixit neurogènic, i per tant si no hi hagués lligand en el teixit envaït inhibint la diferenciació en el front d'ona neurogènic. Hem efectuat una exploració sistemàtica en l'espai de paràmetres mitjançant simulacions numèriques. Els nostres resultats mostren que les propietats del front

de propagació i el patró que es forma depenen fortament de la presència de lligand davant del front de diferenciació. En particular, aquesta expressió de lligand fa més robust el patró fi en l'espai de paràmetres (per exemple impedint la sobreproducció de neurones quan les interaccions trans són febles), impedeix una inestabilitat de la morfologia del front i ralentitza la progressió del front en el teixit envaït. Aquests resultats han pogut ésser utilitzats per explicar observacions prèvies en la retina d'embrions de ratolí, estant en acord amb diferents evidències experimentals [153]. Per altra banda, hem trobat resultats similars en el creixement d'un front pla que pretén emular la progressió de l'anomenat solc morfogenètic en l'ull embrionari de la mosca *Drosophila* [148]. Així doncs, aquests resultats apunten a un mecanisme de regulació de fronts neurogènics **[II,III]**, i cap a un nou principi de disseny d'un mecanisme més general de desenvolupament.

D.2.3 Formació de patrons considerant un lligand difusiu que activa a Notch

A continuació, hem analitzat l'efecte d'un lligand que és capaç de difondre en l'espai extracel·lular i activar el receptor Notch [116, 117, 174] **[I]**. Mitjançant l'anàlisi d'estabilitat lineal hem trobat que la combinació d'aquest lligand amb la seva repressió mediada per Notch no fa possible la generació de patrons fins.

Hem proposat un segon model en el qual un lligand difusiu activa a Notch i és combinat amb el circuit de Collier d'inhibició lateral. Les nostres eines analítiques i numèriques ens han servit per veure com aquest lligand difusiu afecta en la formació del patró. En particular, hem trobat que aquest lligand difusiu suavitza el patró, i en últim terme, destrueix el patró (*e.g.* quan considerem alts valors de la difusió). Els nostres resultats també han mostrat que la difusió del lligand té un efecte constructiu en la formació de patró: difusions moderades poden suprimir els defectes del patró que emergeixen quan la dinàmica d'acoblament espacial és només mediada per la inhibició lateral de Collier. Aquest efecte constructiu de la difusió és més visible en sistemes petits. Tots aquests resultats es troben en la publicació **[I]**.

D.2.4 Interaccions cis en formació de patrons d'inhibició lateral i en la dinàmica de cèl·lules individuals

En el següent treball de la Tesi explorem l'efecte de les interaccions de lligand i receptor en una mateixa cèl·lula, anomenades interaccions cis [47, 72]. El nostre treball s'ha basat en l'efecte de les interaccions cis que dónen lloc a una producció de senyal de Notch (el que Collier anomenava com activitat de Notch) [81, 180], en combinació amb una font de senyalització alternativa. Això ho hem desenvolupat en dues situacions diferents: (i) en un escenari multicel·lular, on la font de senyalització alternativa prové de les interaccions trans, i (ii) en un escenari de cèl·lules individuals, on la font de senyalització alternativa prové d'una producció basal de senyal de Notch que és independent del lligand [188, 189]. Hem proposat un model simple, similar al de Collier, que captura aquests dos escenaris amb la mencionada fenomenologia. En aquest estudi hem utilitzat tant eines analítiques com numèriques.

En ambdues situacions, hem predit que les interaccions cis poden donar lloc a un règim que s'anomena d'inhibició cis, corresponent a una inhibició efectiva de la producció de senyal de Notch, quan la font de senyalització cis és dèbil en comparació amb una font de senyalització més forta. Aquest fet il·lustra un cas en què el mecanisme mol·lecular (cis produeix senyal de Notch) no determina el comportament emergent dinàmic (cis a nivell effectiu inhibeix senyal de Notch), però és la interacció dels diferents components de la xarxa el que revelen aquest comportament [208]**[V]**. Hem trobat que aquest comportament no intuïtiu és degut a l'existència d'un efecte de competència entre les fonts de senyalització. Aquesta competició és deguda a que ambdues fonts necessiten el mateix tipus de receptor per a senyalitzar, i també degut a que les fonts tenen diferents forces de senyalització (*i.e.* ritmes de senyalització).

El nostre treball mostra que la inhibició deguda a cis en l'escenari de cèl·lules individuals dóna lloc a biestabilitat, i per tant a nivell teòric obtenim interruptors cel·lulars en el context de cèl·lules individuals.

En el cas multicel·lular, hem trobat que incrementant la quantitat d'interaccions cis en el règim en que cis inhibeix el senyal a nivell efectiu, la proporció de cèl·lules amb nivells alts de lligand en el teixit incrementa gradualment. Hem justificat aquest efecte amb una prova analítica que mostra que les cèl·lules en

règim d'inhibició cis són més insensibles al senyal, essent més difícil d'inhibir la seva producció de lligand, cosa que distorsiona l'efecte d'inhibició lateral. Aquest és un efecte no lineal, donat que l'anàlisi d'estabilitat lineal prediu que les interaccions cis no poden canviar la longitud característica del patró a efectes lineals. Mitjançant simulacions i treball analític hem trobat que en el règim d'inhibició cis es promou la multiestabilitat, i per tant altres patrons regulars poden formarse. També hem trobat efectes de formació de patrons localitzats en una part de l'espai de paràmetres en el règim d'inhibició cis. En aquesta regió, l'emergència de patrons és més sensible a les condicions inicials i és on la biestabilitat que trobem per cèl·lules individuals sembla estar actuant més intensament.

També hem pogut comprovar en un model més realista que el que plantegem inicialment pot reproduir alguns dels resultats claus que hem presentat, donant més solidesa a les nostres troballes.

Aquests resultats originals es poden trobar en **[V]**.

D.2.5 Formació de patrons en l'oïda interna de pollastre mitjançant dos lligands diferents actuant en modes oposats

L'últim tema de la Tesi se centra en el procés de diferenciació de les cèl·lules sensitives en l'oïda interna d'embrions de pollastre. En aquest context, el mecanisme de Notch opera en dos modes diferents: inducció lateral i inhibició lateral. La inducció lateral es pot entendre com el fet que un lligand en una cèl·lula activi la producció de lligand en les cèl·lules veïnes. Ambdós règims d'inducció i inhibició lateral succeeixen durant el desenvolupament de l'orella interna de vertebrats, on el primer és propi de la formació de dominis prosensorials i el segon és propi del procés de diferenciació neuronal i de les cèl·lules sensorials a l'oïda interna [18].

En aquesta part de la Tesi hem abordat la qüestió de com en l'oïda interna es passa del règim d'inducció lateral al règim d'inhibició lateral. Evidències experimentals apunten a que primerament, en el domini prosensorial, el lligand Jag1 (Jagged1) actua en mode d'inducció lateral [57] i posteriorment, en l'etapa de diferenciació de les cèl·lules sensorials, el lligand Dl1 (Delta1) s'expressa en el teixit i passa a dominar la inhibició lateral [18]. Per modelitzar aquesta situació hem proposat un model per a dos lligands, Jag1 i Dl1, en el qual imposem que

quan els lligands actuen pel seu compte, Jag1 dóna lloc a inducció lateral mentres que Dl1 dóna lloc a inhibició lateral. Quan ambós lligands actuen junts, el circuit emergent pot donar lloc al patró fi que s'observa en el teixit embrionari.

El nostre treball prediu que les forces de senyalització relatives de Jag1 i Dl1 quan s'uneixin al receptor Notch són crítiques per la transició entre inducció lateral i inhibició lateral. Per una banda, una quantitat de senyalització mínima deguda a Jag1 és necessària per a la generació d'una ona de propagació de lligand en el teixit (règim d'inducció lateral). Per altra banda, forces de senyalització molt altes de Jag1 respecte la força de senyalització de Dl1 no permeten l'emergència del patró d'inhibició lateral en la fase posterior. La predicció de la diferència en les forces de senyalització ha set corroborada experimentalment. A més a més, hem predit que en l'estadi de determinació de les cèl·lules sensorials hi ha un efecte de competència entre els lligands Dl1 i Jag1 degut a que (i) els dos lligands interaccionen amb el mateix tipus de receptor (Notch) i també (ii) la força de senyalització de Jag1 és més dèbil que la de Dl1 al interaccionar amb Notch. En particular, aquesta competència fa que l'increment de Jag1 en una cèl·lula interaccioni en forma trans amb el receptor Notch que està en cèl·lules veïnes, impedint que interaccionin amb Dl1, cosa que a nivell efectiu redueix la quantitat de senyal en aquestes cèl·lules veïnes. Per aquesta raó, Jag1 introdueix a nivell efectiu un *feedback* intercel·lular positiu d'inhibició mútua, contribuint a l'efecte d'inhibició lateral. Per tant, Jag1 actua en mode d'inducció lateral en absència de Delta, mentre que actua en règim d'inhibició lateral en presència de Dl1. Aquesta predicció indica que la pèrdua de funció de Jag1 en l'estadi sensorial destrueix el patró.

Aquests resultats originals han pogut ser obtinguts mitjançant eines analítiques i simulacions numèriques, i estan recollits en **[IV]**.

Aquest resultats estan actualment essent testejats pel grup experimental del Prof. Fernando Giraldez (UPF-PRBB, Barcelona, Spain).

D.3 Perspectives

Els nostres resultats han obert una sèrie de qüestions noves, i hem pogut començar a investigar algunes d'elles. A continuació resumim alguns d'aquests fronts oberts.

En el context del front de diferenciació neuronal, quan no hi ha lligand davant

del front, hem vist que pot sorgir una inestabilitat morfològica. La causa última que dóna lloc a aquesta inestabilitat és encara un misteri. En el capítol 3 hem proposat l'existència d'una progressió anòmala del front, que hem detectat en simulacions numèriques, com a possible mecanisme inestabilitzador del front. L'estudi i la quantificació apropiada d'aquesta progressió anòmala possiblement acabarà de desvetllar la causa de la inestabilitat, i en particular esperem poder predir en quin règim dels paràmetres emergeix la inestabilitat morfològica.

Avui en dia és sabut de l'existència lligands i altres molècules que poden difondre en l'espai extracel·lular i que al interactuar amb el receptor Notch causen una producció de senyal (que acabarà inhibint la producció de lligand), o al contrari, simplement el bloquegen [117]. Amb els resultats teòrics que hem obtingut en l'estudi de les interaccions cis, això porta a pensar que pot ser força revelador estudiar diferents forces (o ritmes) de senyalització relativa del lligand difusiu quan interactua amb el receptor respecte la força de senyalització que s'obté de les interaccions trans. Probablement, senyalitzacions febles degut al lligand difusiu donaran lloc a efectes interessants no trivials, donat que s'establiran *feedbacks* locals positius que actuaran conjuntament amb acoblament espacial mitançant les interaccions trans i les interaccions difusives.

L'interruptor cel·lular que proposem en el context de les interaccions cis és possiblement un nou mecanisme per a prendre decisions a nivell cel·lular. La cerca experimental d'aquest interruptor en cèl·lules reals podria desvetllar funcions fins ara desconegudes per la via de senyalització de Notch. Per altra banda, seria interessant estudiar com l'efecte de biestabilitat d'aquest interruptor por reflectirse en processos d'inhibició lateral, i pot estar actuant en combinació amb altres agents reguladors de la via de Notch.

En el mateix context d'inhibició cis hem pogut trobar l'existència d'altres patrons periòdics estables. Això porta a processos de competència entre possibles patrons en un mateix punt de l'espai de paràmetres, i per tant obra nous interrogrants de com un patró pot ser seleccionat. L'implementació de noves dependències espacio-temporals en els models proposats podrien proporcionar mecanismes de control per a la selecció de patrons **[VII]**.

En el context del desenvolupament de l'oïda interna de vertebrats, és encara desconegut el mecanisme en què Jag1 és activat per Notch. Dades recents on es veuen els agents directament regulats per Notch (el que s'anomenen els gens diana

de Notch) en aquest context podrien ajudar a entendre aquesta qüestió **[IV]**. També, diferents escenaris de competició entre aquests agents podrien ajudar a entendre el mecanisme d'activació.

En aquesta Tesi hem pogut presentar dos casos en que la competició de dues fonts de senyalització pot canviar el rol efectiu de les components en la xarxa genètica reguladora en qüestió (Fig. D.3), cosa que podria apuntar a un mecanisme genèric de competició en xarxes genètiques. Seria interessant poder testejar aquest efecte de competició amb experiments. De fet, hi ha altres escenaris en la via de senyalització de Notch en els quals diferents elements bàsics poden donar lloc a competició, resultant en altres comportaments efectius. Per exemple, altres efectes competitius desconeguts podrien sorgir en una gran varietat de situacions on hi ha més d'un lligand actuant simultàniament en les mateixes cèl·lules, o bé quan altres elements moleculars més desconeguts (anomenats molècules no-canòniques) poden suposar altres fonts de senyalització al interactuar amb el receptor Notch [117]. Aquests possibles escenaris de competició podrien ajudar a entendre diferències de comportament que mostra la via de Notch en actuar en contextos diferents.

Sorprenentment, els efectes que hem trobat de competició no depenen del nivell de saturació del receptor. Per entendre millor aquest fenomen s'haurà de prosseguir amb un estudi teòric més profund de la competició, per exemple utilitzant models cinètics més realistes.

Finalment, seria interessant estudiar des d'un punt de vista teòric diferents tipus de fenòmens competitius que poden ocórrer en petites xarxes regulatòries genètiques a nivell transcripcional i post-transcripcional. El disseny de petites xarxes amb elements competitius podria donar lloc a nous mòduls genètics multifuncionals constituïts d'un nombre força reduït d'elements, cosa que podria ser utilitzat per exemple en el camp de la biologia sintètica. Per altra banda, aquest estudi podria ajudar a entendre efectes antagònics que una mateixa xarxa genètica pot presentar en diferents contextos.

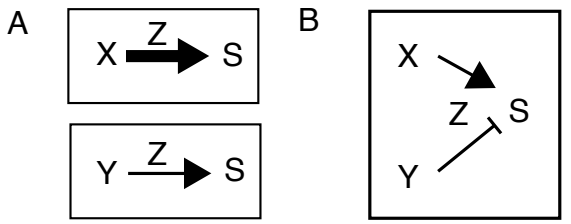

Figura D.3: Un possible mecanisme genèric de competició en xarxes regulatòries genètiques. X i Y són dues fonts de senyalització, que mitjançant un mediador o substrat Z produeixen un senyal S amb diferents intensitats quan X i Y actúen (A) per separat o bé (B) conjuntament. La competició entre X i Y pot sorgir si X i Y comparteixen el mateix substrat Z (en el nostre cas, el receptor). Per exemple, X representa la concentració de lligand que serà utilitzat per les interaccions trans, i Y representa la concentració de lligand que serà utilitzat per les interaccions cis. Per altra banda, X pot representar la concentració de lligand Delta que activa a Notch mitjançant trans i Y pot representar la concentració de Jag1 que activa a Notch mitjançant trans. En el primer cas, quan les interaccions cis emeten un senyal dèbil comparat amb les interaccions trans, poden tenir un efecte inhibidor. En el segon cas, si Jag1 al interaccionar de forma trans amb Notch produeix un senyal dèbil respecte el que es produeix mitjançant la interacció trans de Dl1, llavors Jag1 pot estar contribuint en la inhibició de senyal de les cèl·lules adjacents. La identificació i caracterització d'aquests i altres motius que duen a fenòmens competitius podrien ajudar a entendre diferents comportaments antagònics que pot presentar una mateixa xarxa genètica en diferents contextos.

D.4 Llistat de publicacions

I. Pau Formosa-Jordan and Marta Ibañes (2009) Diffusible ligand and lateral inhibition dynamics for pattern formation. J. Stat. Mech. P03019

II. Pau Formosa-Jordan, Marta Ibañes, Saúl Ares, and José María Frade (2012) Regulation of neuronal differentiation at the neurogenic wavefront. Development, 139, 2321-2329 doi:10.1242/dev.076406

III. Pau Formosa-Jordan, Marta Ibañes, Saúl Ares, and José María Frade. Lateral inhibition and neurogenesis: novel aspects in motion. The International Journal of Developmental Biology, en premsa.

IV. Jelena Petrovic*, Pau Formosa-Jordan*, Juan Camilo Luna, Marta Ibañes, Joana Neves and Fernando Giraldez. Lateral induction and lateral inhibition depend on Notch signal strength in the developing inner ear (Manuscrit en procés de revisió en la revista Development)

V. Pau Formosa-Jordan and Marta Ibañes. Competition in Notch signaling dynamics with cis enriches cellular decision making (Manuscrit)

VI. Pau Formosa-Jordan*, Norma Fàbregas*, Ana Confraria*, Ana I. Caño-Delgado and Marta Ibañes. Auxin influx carriers control vascular differentiation in *Arabidopsis* (En preparació)

VII. David Palau, Pau Formosa-Jordan, José María Sancho and Marta Ibañes. Dynamical selection of coexisting patterns (En preparació)

*Contribucions iguals

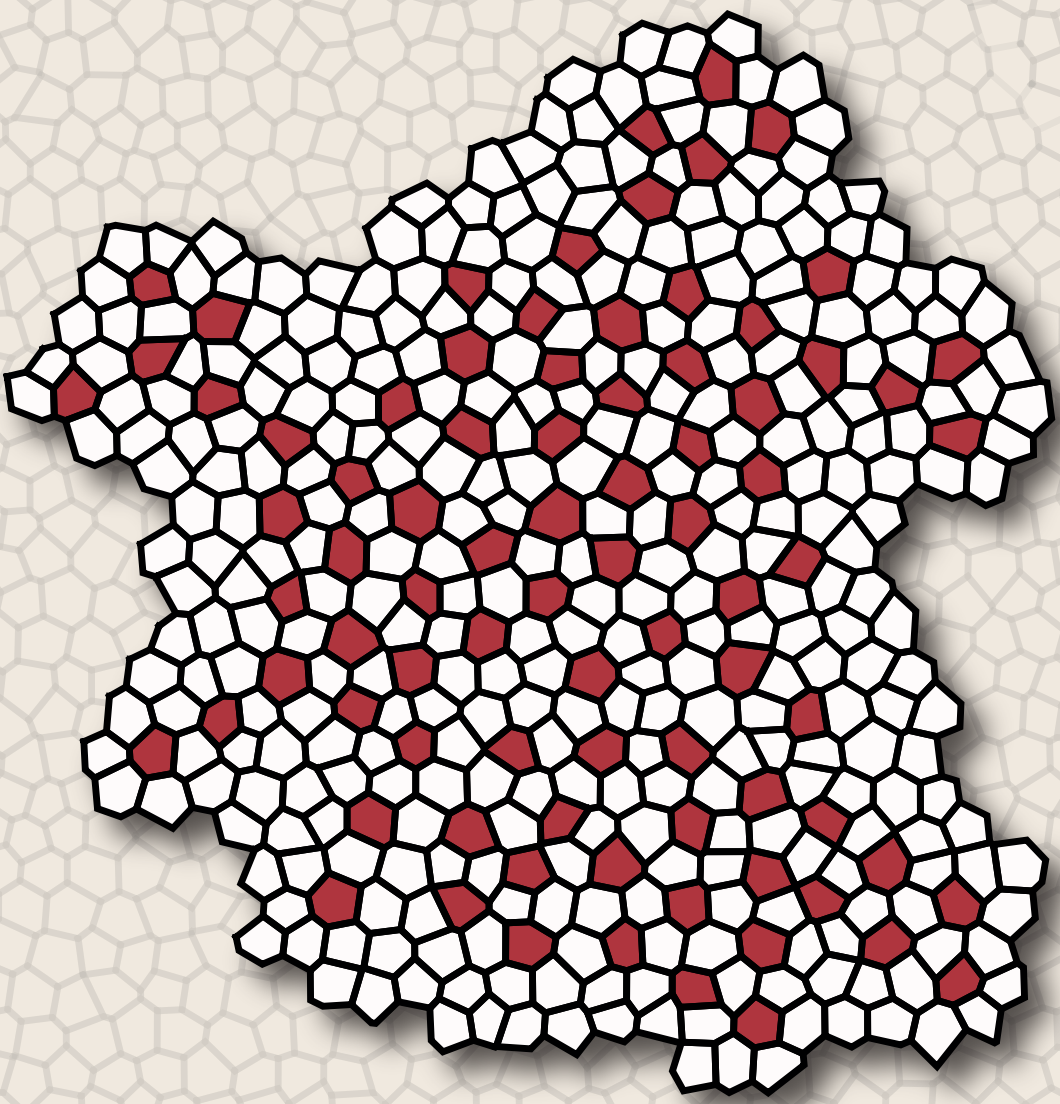

Universitat de Barcelona